Purdue University
Purdue e-Pubs

Open Access Dissertations | Theses and Dissertations

Fall 2013

Technology Agnostic Analysis and Design for Improved Performance, Variability, and Reliability in Thin Film Photovoltaics

Sourabh Dongaonkar
Purdue University

Follow this and additional works at: https://docs.lib.purdue.edu/open_access_dissertations

Part of the Electrical and Computer Engineering Commons, and the Oil, Gas, and Energy Commons

Recommended Citation
Dongaonkar, Sourabh, "Technology Agnostic Analysis and Design for Improved Performance, Variability, and Reliability in Thin Film Photovoltaics" (2013). *Open Access Dissertations*. 207.
https://docs.lib.purdue.edu/open_access_dissertations/207

This document has been made available through Purdue e-Pubs, a service of the Purdue University Libraries. Please contact epubs@purdue.edu for additional information.

Graduate School ETD Form 9
(Revised 12/07)

PURDUE UNIVERSITY
GRADUATE SCHOOL
Thesis/Dissertation Acceptance

This is to certify that the thesis/dissertation prepared

By Sourabh Dongaonkar

Entitled
Technology Agnostic Analysis and Design for Improved Performance, Variability, and Reliability
in Thin Film Photovolatics

For the degree of Doctor of Philosophy

Is approved by the final examining committee:

MUHAMMAD A. ALAM
Chair

MARK S. LUNDSTROM

RAKESH AGRAWAL

RICHARD J. SCHWARTZ

To the best of my knowledge and as understood by the student in the *Research Integrity and Copyright Disclaimer (Graduate School Form 20)*, this thesis/dissertation adheres to the provisions of Purdue University's "Policy on Integrity in Research" and the use of copyrighted material.

Approved by Major Professor(s): MUHAMMAD A. ALAM

Approved by: M. R. Melloch 08-15-2013
Head of the Graduate Program Date

TECHNOLOGY AGNOSTIC ANALYSIS AND DESIGN FOR IMPROVED PERFORMANCE, VARIABILITY, AND RELIABILITY IN THIN FILM PHOTOVOLTAICS

A Dissertation

Submitted to the Faculty

of

Purdue University

by

Sourabh Dongaonkar

In Partial Fulfillment of the

Requirements for the Degree

of

Doctor of Philosophy

December 2013

Purdue University

West Lafayette, Indiana

आई बाबा यांस

To my parents

ACKNOWLEDGMENTS

I would like to first acknowledge the help, support, and guidance from my thesis advisor Prof. Muhammad A. Alam, who provided the structure and direction to my graduate research, while allowing enough intellectual freedom for creating thinking. While working with him, I have learned how to approach completely new problems and research areas, by solving one problem at a time. In addition to building my technical expertise, under his guidance I have learned how to talk to convey my ideas best, and perhaps more importantly how to listen to absorb others' insights fully.

I also wish to thank Prof. Mark S. Lundstrom for his constant help and support throughout my time at Purdue. As a student and a collaborator, I have benefited greatly from his knowledge and insights about semiconductor physics and technology, as well as his vision on research and learning. I must also thank Prof. Rakesh Agrawal for being generous with his time regarding any help or advice (technical and otherwise) that I approached him for. His passion for research has always motivated me to do better and aim higher. My sincere thanks also to Prof. Richard J. Schwartz for agreeing to be a part of my thesis committee in spite of his busy schedule, and for his insightful feedback which has helped improve this thesis considerably.

For my graduate research, I have collaborated extensively with many researchers who have provided experimental data, and offered useful insights, which has helped strengthen my thesis considerably. I am particularly indebted to Prof. Souvik Mahapatra from IIT Bombay, Dr. Michel Frei and Dr. Dapeng Wang from Applied Materials, Prof. Mark A. Ratner and Prof. Tobin J. Marks from Northwestern University, and Dr. Chris Deline and Dr. Steve Johnston from NREL for generously sharing their experimental expertise and data. Special thanks are also due to my student collaborators and co-authors particularly, Dr. Jonathan D. Servaites, Dr. Grayson M. Ford, Karthik Y., Stephen Loser, Erik J. Sheets, Charles J. Hages, Nathan J. Carter,

Elif S. Mungan, James E. Moore, Raghu V. Chavali, and Katherine Zaunbrecher, for their active help in variety of technical matters, as well as with writing and reviewing many manuscripts.

I would also like to acknowledge the courteous help I received from Vicky Johnson, Matt Golden, Angela Rainwater, and Michelle Wagner, regarding all administrative matters. I also gratefully acknowledge research funding from Applied Materials and Semiconductor Research Corporation (SRC), which made this work possible; and the computing resources from Network for Computational Nanotechnology (NCN), and experimental facilities at the Birck Nanotechnology Center (BNC).

For making my time at Purdue memorable and enjoyable, I thank my past and present research group members and many other friends and colleagues at Purdue. I must mention Ankit Jain, Biswajit Ray, Sambit Palit, Piyush Dak, Xufeng Wang, Dr. Ahmed E. Islam, and Dr. Pradeep R. Nair in particular for the constant help, support and camaraderie which has kept me going for so long.

Finally, I would like to acknowledge the debt of gratitude I owe to my family. My parents with their endless sacrifices, and unwavering support, are the guiding lights of my life, and like all my achievements this thesis is dedicated to them.

TABLE OF CONTENTS

Page

LIST OF TABLES ix
LIST OF FIGURES x
ABSTRACT xxvi
1 INTRODUCTION 1
1.1 Introduction to Thin Film Photovoltaics 2
1.1.1 A Historical Perspective 2
1.1.2 The Case for TFPV Technologies 3
1.1.3 Thin Film Solar Cell Landscape 5
1.2 Technology Agnostic Features of Thin Film PV 10
1.2.1 Device Physics of TFPV Cells 10
1.2.2 Module Manufacturing Process 12
1.2.3 Reliability and Module Lifetime 14
1.2.4 Challenges Unique to Thin Film PV 16
1.3 Outline of the Thesis 17
1.3.1 Research Direction and Philosophy 17
1.3.2 Detailed Outline 18
1.4 List of Associated Publications 19
2 DEVICE PHYSICS OF THIN FILM SOLAR CELLS 23
2.1 Introduction 23
2.2 Intrinsic Light and Dark IV 27
2.2.1 Solution without Bulk Recombination 28
2.2.2 Calculation of Bulk Recombination Current 32
2.2.3 Poisson Equation under Light 34
2.3 Parasitic Shunt Current 35

Page

2.3.1 Diode vs. Shunt Current Components 36
2.3.2 Phenomenology of Shunt Current 38
2.3.3 Space-Charge-Limited Model for Shunt Current 38
2.3.4 Single Carrier Injection 42
2.4 Universal non-Ohmic Shunt Conduction 42
2.4.1 Thickness Dependence of Shunt Conduction 44
2.5 External Series Resistance 46
2.6 Thin Film Solar Cell Equivalent Circuit 47
2.7 Conclusions 47
3 VARIABILITY AND RELIABILITY IN THIN FILM SOLAR CELLS . 50
3.1 Performance Variability in Solar Cells 51
3.2 Universal Statistics of Shunt Conduction 54
3.2.1 Shunt Magnitude Distribution 54
3.2.2 Spatial Shunt Statistics 59
3.2.3 Origin of Universal Shunt Statistics 63
3.3 Solar Cell Reliability 63
3.4 Effect of Reverse Bias Stress in Thin Film Cells 65
3.4.1 Diode Degradation Kinetics 66
3.4.2 Metastable Shunt Switching in a-Si:H 69
3.4.3 Metastable Shunt Behavior in CIGS 72
3.5 Conclusions 76
4 CELL TO MODULE PERFORMANCE AND DESIGN 78
4.1 Grain Variation and Cell Efficiency 78
4.1.1 SPICE Simulation Setup 79
4.1.2 Cell Efficiency with Grain Variation 81
4.2 TFPV Module - Effect of Sheet Resistance 82
4.2.1 Resistive Loss in Sheet Conductors 83
4.2.2 Optimized Series Connected Module 86

Page

4.3 Shunt Variability and Cell to Module Gap 89
4.3.1 2D SPICE Simulation Framework 91
4.3.2 Cell to Module Efficiency Gap 93
4.3.3 Impact of Shunts on Module Performance 96
4.4 Strategies for Shunt Loss Mitigation 98
4.4.1 Process Solutions for Shunt Removal 99
4.4.2 Scribing Isolation Techniques 100
4.4.3 Comparison of Scribing Isolation Techniques 106
4.5 Conclusions 111
5 SHADOW STRESS AND SHADE TOLERANT DESIGN 114
5.1 Introduction 114
5.2 Partial Shading at System Level 116
5.2.1 Partial Shading and Reverse Bias Stress 116
5.2.2 String Operation Under Shading 118
5.3 2D Shadow Stress in TFPV Modules 120
5.3.1 Asymmetric Shadow Stress 120
5.3.2 Origin of Asymmetric Stress 124
5.3.3 Experimental Validation of Asymmetric Stress 126
5.3.4 Effect of Shadow Size And Orientation 130
5.3.5 Long Term Reliability Prediction 136
5.4 Shade Tolerant Module Design 137
5.4.1 Design Rules for Shade Tolerance 138
5.4.2 Radial Design with Triangular Cells 140
5.4.3 Spiral Design with Curvilinear Cells 142
5.4.4 Effect of Shadow Position 144
5.4.5 Module Efficiency Comparison 146
5.4.6 Practical Considerations 150
5.5 Conclusions 152

Page

6 SUMMARY AND FUTURE WORK 154
6.1 Summary 154
6.2 Future Work 158
LIST OF REFERENCES 160
A ANALYTICAL SOLUTION FOR P-I-N SOLAR CELL 177
A.1 Semiconductor Equations 177
A.2 Solution without Recombination 178
A.3 Bulk Recombination 180
B SPACE-CHARGE-LIMITED CURRENT IN SOLIDS 182
B.1 Ideal Semiconductor - Mott-Gurney Law 182
B.2 With Exponential Distribution of Shallow Traps 183
C SHEET RESISTANCE AND ASYMMETRIC SHADOW STRESS 186
C.1 Typical Scenario - Metal and TCO contacts 186
C.2 Translucent Module - TCO on Both Sides 188
C.3 Current Rearrangement in 2D 190
C.4 Asymmetric Shadow Stress 191
D NON-RECTANGULAR MODULE GEOMETRIES 193
D.1 Construction of Module Geometries 193
D.1.1 Radial Geometry 193
D.1.2 Spiral Geometry 194
D.2 Shading Simulation for Different Geometries 195
VITA 198

LIST OF TABLES

Table Page

1.1 Summary of TFPV materials and associated manufacturing technologies. 8

3.1 A partial summary of performance variability sources in thin film solar cells. 51

3.2 Partial list of relevant front end reliability issues in representative thin film PV technologies. The listed back end reliability issues are common to all PV technologies and concern module or systems level. 64

4.1 Highest reported cell performance metrics for a-Si:H technology, and the model parameter used for fitting these metrics using the equivalent circuit model discussed in Sec. 2.11. 89

4.2 Sub-cell parameters for highest reported cell efficiencies for different TFPV technologies. The module parameters for the respective technologies are taken from manufacturer datasheets, as listed. 95

LIST OF FIGURES

Figure Page

1.1 Estimated cost breakdown for an installed PV system in $/W for commercial c-Si technology (for 2010 fiscal taken from [18]), showing that module cost accounts for half of the electricity cost ($1.70). The breakup of module cost shows that a significant fraction ($0.55) comes from high Silicon cost, and the rest is combination of cell manufacturing ($0.45 for metals, dopants, chemicals etc.), and module manufacturing ($0.70 for glass, EVA, frame etc.). 4

1.2 Schematic showing thin film PV materials and structures, comparing the substrate and superstrate configurations, and the absorber and contact materials 6

1.3 Schematics showing the device structures, and layer thicknesses, of 3 major TFPV cell types namely, (a) a-Si:H p-i-n solar cell with Aluminum doped ZnO (AZO) and Fluorinated SnO_2 (FTO) contacts; (b) organic bulk heterojunction (BHJ) with Al and Indium doped SnO_2 (ITO) contacts; and, (c) CdS/CIGS solar cell with Molybdenum (Mo) and ITO contacts. . . 9

1.4 Typical band diagrams of the three TFPV cells shown in Fig. 1.3; showing the (a) p-i-n homojunction for a-Si:H and nc-Si:H cells, (b) Type II heterojunction between the two organic materials in OPV, and (c) CdS/absorber Type I heterojunction for the chalcogenide cells. 10

1.5 Side view of a TFPV module under step by step fabrication marked as, P1 - metal deposition followed by laser scribing (arrows), P2 - absorption deposition and scribing, and finally, P3 - TCO deposition and scribing. This leads to series connected cells in a module, with current flow direction shown by dashed arrows. 14

1.6 Schematic of the thesis outline showing the sequential development from device physics in chapter 2, leading to physics and statistics of variability and reliability in chapter 3; both of which are then used in analysis of module performance in chapter 4, and finally shading problem at system level in chapter 5. 18

Figure Page

2.1 (a) Schematic band diagram of a typical p-n junction solar cell, showing the photogeneration and recombination processes, along with the carrier transport. (b) Schematics of the generation profile $G(x)$, and recombination profile $R(x)$ inside the solar cell shown in the area plot. The difference between the area under these curves determines the output current of the solar cell (c) Typical equivalent circuit used for solar cells which show superposition. The photocurrent is represented by constant current source J_{photo}, in parallel to the dark diode current J_{diode}. The parasitic shunt R_{SH} and series R_s resistances are also shown. 25

2.2 The measured dark (blue) and light (green) IV of a a-Si:H solar cell, compared to the IV calculated from superposition principle in Eq. 2.3 (red), showing the failure of conventional superposition in TF solar cells. . . . 26

2.3 (a) Schematic band diagram of an a-Si:H p-i-n solar cell, showing the various generation and recombination fluxes. (b) Photo and dark current components assuming no bulk recombination, showing that J_{photo} is voltage dependent even for this ideal case. (c) Recombination currents from first order perturbation, with the dark and generation dependent bulk recombination components. (d) The sum of all current components J_{total} closely matches the simulated IV (symbols) curve. 31

2.4 (a) Plot of measured dark current for four nominally identical a-Si:H cells (symbols), showing excess leakage current in reverse and low forward bias region, which varies significantly for each cell, and deviates from the expected exponential diode current (line). (b) Plot of $|I_{dark}|$ vs. $|V|$ showing symmetric shunt current (crosses) overlaps the measured forward current (squares) for the same 4 cells. The deviation from expected I_{diode} (black line) at low biases is highlighted. (c) Cleaned forward current obtained after subtraction of the symmetric shunt current (circles) shows the expected exponential behavior (compare with line). (d) Empirical CDF comparing the calculated ideality factors n_{calc} before (squares) and after (circles) subtracting the shunt component, showing that cleaned n_{calc} values are closer to the expected value of 2 (red line). 35

2.5 (a) Symbols show the voltage symmetry of I_{SH}, for 3 cells (i) (scaled for clarity). (ii) The distribution of symmetry ratio $\alpha = I_{SH}(0.3V)/|I_{SH}(-0.3V)|$ for 60 identical cells. (b) (i) Non-Ohmic voltage dependence of shunt current for same 3 cells. (ii) the power exponent β for most of the 60 cells lies between 2 and 3. (c) (i) Temperature dependent dark IV (symbols), showing the weak temperature dependence of I_{SH} compared to activated diode current (solid lines). (ii) I_{SH} temperature coefficient $\alpha_T = I_{SH}(T_2)/I_{SH}(T_1)$ for T_2/T_1=85°C/45 °C (solid lines), and T_2/T_1=120 °C/45 °C (dashed lines) for 23 cells. 37

Figure Page

2.6 (a) Symmetric MSM structure for SCL conduction showing single carrier (hole) injection. (b) Proposed localized parasitic p-i-p structure in otherwise ideal p-i-n structure. (c) Dark IV from the 2D simulation showing that the shunt (red), and diode (blue) dominate in different voltage regimes to give the total dark current (green). Quiver plots contrast localized current distribution in shunt dominated regime at low biases (i), with the uniform diode current conduction at higher biases (ii). 40

2.7 Extracted characteristic slope of band tails E_0 is ∼40 meV for 61 devices, which is very close to the valence band tail slope in a-Si:H, as expected from the p-i-p shunt hypothesis. 41

2.8 (a) Schematics showing the likely shunt formation in a-Si:H, OPV and CIGS cells, due to contact metal diffusion through emitter. (b) From the localization of shunt current, we can separate the shunt and diode current paths, simplifying the 2D picture in part (a). (c) Simulations combining the 1D shunt in parallel to a diode for all 3 cell types, can reproduce the measured voltage and temperature dependencies, using typical material parameters. 43

2.9 I_{SH0} vs. L_{abs} plots showing the scatter plot of individual cell I_{SH0} values (black crosses) for (a) a-Si:H and (b) OPV cells. The overlaid box-and-whisker plots show the median (circles), inter-quartile range (blue bars), and min/max data values (whiskers) for each L_{abs}. The inverse power law (red line) holds true for mean of $\ln I_{SH0}$. 44

2.10 (a) 3D schematic of current flow in a p-i-n solar cell, showing that the photocurrent (arrows) must flow laterally through the metal and TCO layers to reach the terminals. (b) Side view of the p-i-n cell, showing the external series resistance contributions due to contact resistances at the metal-semiconductor contacts (R_{c1} and R_{c2}), as well as the sheet resistance of TCO $R_{\square}^{TCO}$ and metal $R_{\square}^{metal}$ layers. 45

2.11 Equivalent circuit incorporating the intrinsic (orange box) and extrinsic (blue box) current components. The intrinsic components include voltage dependent collection J_{photo}, generation enhanced recombination $J_{rec,G}$, and exponential dark current J_{diode}. And, the extrinsic components are represented by elements (I_{SH}) and series resistance (R_s). 48

3.1 (a) Schematic of a polycrystalline (CdTe) solar cell with multiple grains, and grain boundaries. The recombination profile for this structure is shown below, highlighting the impact of grain structure. (b) Simulation of 100 micro-cells (10 μm × 1 μm) with varying grain sizes obtained from full TCAD device simulation (after [129]). (c) The resulting efficiency distribution due to grain structure, shows a heavy tailed distribution. 52

Figure Page

3.2 (a) Measured I_{dark} (squares) can be represented by a parallel combination of diode with series resistance I_{diode} (green), and a parasitic shunt component I_{SH} (red), with a symmetric (around $V = 0$) non-Ohmic voltage dependence. (b) Measured dark IV characteristics of 8 a-Si:H solar cells (dots) on same substrate, fabricated under identical conditions, showing large variation in shunt current (near 0 V point), while the diode component is identical and matches the simulation (line). 53

3.3 QQ plots for $\hat{X}$ values for four different TFPV cells (symbols) show very good fit to the theoretical standard normal quantiles (red line) for (a) a-Si:H, (b) OPV, (c) CIGS, and (d) CdTe technologies. For all technologies, the MLE of mean $\hat{\mu}_X$, and standard deviation $\hat{\sigma}_X$ of the scaled variable $\hat{X}$ are 0 and 1, respectively, with standard errors of these estimates shown in insets. 56

3.4 (a) Calculated KS statistic (bottom) for the four data sets assuming log-normal distribution (bars), compared to the cut-offs (dots), showing that the log-normal hypothesis cannot be rejected at 95% confidence level. (b) Log-likelihood ratios (bars) comparing log-normal and Weibull distributions with MLE parameters, and corresponding p values (dots) 58

3.5 (a) Original grayscale reverse DLIT image from [150] showing the bright shunt spots scattered across the cell surface. (b) The size of each bright spot can be calculated from this modified binary image which identifies the spots in black. (c) The location (centroid) of each spot (red stars) and some of their pairwise distances (lines) are also available, from the binary image. 60

3.6 (a) Normalized spot size distributions for DLIT images of a-Si:H [150], CIGS [137], and mc-Si [124] solar cells, from literature show same log-normal behavior. Normalized spot size is defined as $N_{pixel,spot}/N_{pixel,image}$. (b) The distribution of pairwise distances between spot locations, for same three images normalized to unit square (bars), closely follows the PDF obtained from a CSR process in a unit square (line), given in Eq. 3.6. . 61

3.7 (a) Schematic of parasitic shunt formation due to local metal incursion, resulting in parasitic MSM path for a-Si:H case, showing the shunt and diode current paths. Top view of solar cell with local shunts as seen in DLIT images, with the spots distributed on the surface. (b) Simulated grain structure for the top TCO layer, with the grains having high shunt formation probability highlighted in red. 62

Figure Page

3.8 (a) Initial (squares) and post stress (circles) dark IV, after a stress voltage $V_R = -5$ V has been applied for 10^4 s. Measured dark current I_{dark} increases with stress, both in $I_{SH}(t, V_R)$ dominated (highlighted magenta) as well as in the $I_{diode}(t, V_R)$ dominated (highlighted red) regimes. (b) Time dependent increase in I_{diode} under moderate reverse stress for 3 cells (symbols), shows a power law in time $\Delta I_{diode} \propto t^{\alpha}$ with $\alpha \sim 0.2 - 0.26$. (c)The power exponent of the time dependence is independent of stress voltage, but the voltage acceleration of diode current degradation has a weak linear dependence. (d) Time evolution of Dark IV at reverse stress of -5 V for 10^4 s, for a small area device with $I_{SH} = 0$, shows disproportionately high increase in the dark current at low biases, with power exponent of the power law degradation decreasing monotonically from $\alpha \approx 0.95$ to $\alpha \approx 0.25$ depending on measurement voltage. 67

3.9 (a) Pre-stress (squares), post-stress (circles) and relaxed (triangles) dark IV, showing that the diode current relaxes to its original with time, but the increase in shunt current is permanent. The stress (b) and relaxation (c) time dependencies of δI_{diode} show similar power law features with power exponent independent of stress voltage. 68

3.10 (a) Initial dark IV characteristic (blue squares) switches to the low I_{SH} state after voltage sweep (green circles) and increases again after subsequent current sweep (red triangles). (b) Abrupt switching transitions during voltage sweep showing the OFF transition (blue) and current sweep showing the ON transition (red). (c) Scatter plot showing that the values of $P_{Critical}$ and $V_{Critical}$ are similar for eight devices. (d) Power exponent of the SCL shunt current β, in the high (after ON) and low (after OFF) shunt current states remains close to 2.5, showing that the SCL nature of shunt is preserved during the nonvolatile switching. 70

3.11 (a) Simulation showing the change in reverse current at the location of shunt formation, as a function of distance of Al incorporation. As Al gets past the 20 nm n-layer, the current changes significantly Schematics in the inset show the corresponding transition from a p-i-n diode to a p-i-p shunt in the local region. (b) Self-consistent simulations of the 2-D shunt structure at reverse bias of -7.5 V, showing (i) localized shunt current and (ii) local heating effect (temperature scale in K) caused by the fast reverse sweep. 72

Figure Page

3.12 (a) Reverse current hysteresis for 0 to -3 V sweep, showing reduction in dark current with stress (arrows show sweep direction). (b) Dark IV before and immediately after stress shows similar decrease. The dark IV, however, relaxes to its original value after storage in dark for extended period. (c) Similar reverse sweep to -3 V in another cell, results in abrupt *increase* in current, limited by compliance (arrows mark sweep direction). (d) Comparison of dark IV also mirrors the corresponding increase in current, but this increase in current does not relax to initial value even after extended storage. For all the plots, refer legend on top for reference. 73

3.13 (a) Stress IV for OFF transition, showing sweep direction, and the transient measurement points (circles). (b) Time-dependent relaxation of shunt current after stress shows a fast transient (<0.1 s), and a slow transient component ($\sim 10^4$ s), after which the current saturates close to its pre-stress value. Arrows show the direction of change in current with time.(c) Threshold current for OFF transition for all 6 cells is close to 20 mA. (d) The ON transition is voltage triggered, with a threshold voltage of about 3 V reverse bias. 75

4.1 (a) Top view of a typical lab scale cell showing the current flow towards the collecting terminal. This cell is sub-divided into micro-cells for simulating the grain size effect (dashed lines). (b) Side view of the cell, showing the current entering the bottom contact and leaving the top contact, with dashed lines showing micro-cells. (c) Each micro-cell (with a number grains) is simulated using detailed TCAD device simulations, which account for the electronic properties of bulk and grain boundary regions. (d) The resulting 2D mesh equivalent circuit representation of the cell, with each equivalent circuit representing one micro-cell. 80

4.2 (a) IV curves of the micro-cells (lines), compared to the cell IV obtained from the circuit simulation (circles), shows that cell performance is between the worst case micro-cells. (b) The cell efficiency (vertical line) is actually equal to the mean of micro-cell efficiency distribution (histogram). (c) CDF of cell efficiencies (black line), obtained from Monte-Carlo circuit simulations of $1mm^2$ cells, compared to the distribution of micro-cell efficiencies (blue line), shows that the effect of grain variability is averaged out for larger areas. 82

Figure		Page
4.3	(a) Top view of N_{series} rectangular series connected cells in a TFPV module, each of them with width W_{module}. (b) Side view cross section of the module, across the XX' axis, shows the series connection created through successive laser scribes (marked P1, P2, P3). The cell length l_{cell} and width of the dead region created by the scribes w_{dead} are also shown. (c) 3D schematic showing the current flow pattern in a typical cell, with current entering the bottom metal contact, and collected at the far edge of the top TCO contact. The other schematic shows the continuity equations to be solved in the TCO layer, when photocurrent is being injected at all points.	84
4.4	(a) The top schematic shows a rectangular sheet conductor with current collecting edge at the top (line), other sides of the rectangle are open circuited, and the current flows in y direction. The bottom plot shows the power dissipation density from Eq. 4.5 as a color plot, showing that the dissipation increases near the collecting edge (red regions). (b) Plot of the module efficiency as a function of increasing number of cells N_{series} (bottom axis); or equivalently, reducing cell length l_{cell} (top axis), for typical a-Si:H technology. The output change due to sheet resistance loss only (squares), dead area loss only (circles), and total (triangles) are as shown. The typical value of $l_{cell} = 1$ cm, for the a-Si:H is near the optimal, (marked with a star).	87
4.5	(a) Physical equivalent circuit for a TFPV 1 cm^2 cell discussed in Sec. 2.6, with a variable non-Ohmic shunt current $I_{SH} = I_{SH0}V^{\alpha}$ highlighted in red. (b) Simulated IV curves from the equivalent circuit shown in part (a), as a function of increasing I_{SH0} values. The MPP voltage and current drop significantly for larger shunt current values (marked with stars). (c) Simulated cell efficiency as a function of I_{SH0} (line), deviates from maximum (η_{max} marked red) for large I_{SH0} values. The points corresponding to part (b) are also marked. On the right axis, the histogram shows measured log-normal distribution of I_{SH0}, showing that the low efficiency "shunted" cells comprise the tail of this distribution.	90

Figure Page

4.6 (a) Schematic of a TFPV module ($L_{module} \times W_{module}$), with N_{series} series connected cells, and the current direction denoted by arrow. Each cell is subdivided into $N_{parallel}$ sub-cells (squares), each represented by the TFPV equivalent circuit, discussed in Sec. 2.6. These sub-cells are connected using the contact sheet resistances of the TCO (blue), and metal (gray) layers, to create a 2D circuit representation of the module, as shown in (b). All sub-cells are assumed identical across the module, except the shunt (in red) which is varied according to the measured log-normal distribution. The sub-cell power output P_{sub}, and operating voltage V_{sub}, as shown in the schematic, can be monitored across the module. 92

4.7 (a) CDF plot of module efficiency obtained from the Monte-Carlo simulations of a-i:H modules in presence of log-normal distribution of parasitic shunt current (blue), compared to the best sub-cell efficiency (η_{sub}), and highest possible module efficiency η_{module}. The relative contributions of sheet resistance loss $\Delta\eta_{R_{sq}}$, and $\Delta\eta_{I_{SH}}$, are also highlighted. (b) Bar plot comparing the best cell efficiencies of various TFPV technologies (red), with the module efficiency obtained from circuit simulation (blue), accounting for sheet resistance and shunt current losses, shows that these two factors can account for most of the cell to module efficiency gap in TFPV technologies. 94

4.8 (a) Color plot of I_{SH0} distribution in an example simulation of 11×11 cm^2 sub-module, with only three shunted sub-cells (numbered), each assigned different I_{SH0} magnitude. All other sub-cells are assumed to be at η_{max}, with negligible shunt current. (b) Distribution of sub-cell voltages V_{sub} as a color plot (color bar in V), at the sub-module MPP bias shows that the shunted sub-cells can lower the operating point of their neighboring “good” sub-cells in parallel (marked with dashed box). (c) The distribution of sub-cell power output P_{sub}, shows that a heavily shunted sub-cell (circled) can *consume* ($P_{sub} < 0$ in this sign convention) the power output of its neighboring sub-cells (color bar in mW). 97

4.9 Schematic of the series connected cells in a module (top), with two isolating (open circuit) scribes shown as solid black lines. Bottom schematic shows the side view along the YY’ axis, showing that overlapping P1 and P3 lasers can be used to ablate all layers and create isolating scribe lines, after [187]. 100

Figure Page

4.10 (a) Color plot of I_{SH0} for the same 11×11 cm^2 sub-module, with three shunted sub-cells (numbered), now showing periodic lengthwise isolating scribes (dashed lines), which limit the parallel connections to 2 sub-cells only. (b) Distribution of sub-cell voltages V_{sub} as a color plot (color bar in V), at the sub-module MPP bias shows that the shunted sub-cells can now influence only 1 neighboring "good" sub-cell within the vertical scribe lines (marked with dashed box), as the others are disconnected by the isolating scribes. (c) The distribution of sub-cell power output P_{sub}, shows that the power output of all sub-cells is now positive (dashed box) as the scribing isolation reduces the mismatch due to shunting (color bar in mW). . . 102

4.11 (a) Color plot of I_{SH0} for the same $11 \times 11 cm^2$ sub-module, with three shunted sub-cells (numbered), showing targeted partial isolation using parallel isolating scribes on either side of the shunted sub-cell (dashed lines). The scribe length can be varied according to shunt magnitude at a particular location. (b) Distribution of sub-cell voltages V_{sub} as a color plot (color bar in V), at the sub-module MPP bias shows that the shunted sub-cells can now only influence sub-cells in *series* within the vertical scribes, pushing them to slightly higher forward bias, as all sub-cells in parallel are now disconnected from the shunted one. (c) The distribution of sub-cell power output P_{sub}, shows that the power output of all sub-cells is higher after the partial isolation of shunts, as the effect of shunted sub-cells on others in series is weaker than on those in parallel (color bar in mW). . 104

4.12 (a) Color plot of I_{SH0} for the same 11×11 cm^2 sub-module, with three shunted sub-cells (numbered), showing targeted full isolation using an enclosed (box) created using isolating scribes the shunted region sub-cell (black square), which ensures that the shunt is completely isolated from all neighboring sub-cells. (b) Distribution of sub-cell voltages V_{sub} as a color plot (color bar in V), at the sub-module MPP bias shows that the operating points of all sub-cells improves considerably, and only a slight mismatch remains due to the large dead area loss inside scribed region. (c) The distribution of sub-cell power output P_{sub}, shows that the power output of all sub-cells also improves significantly after full isolation of shunts (color bar in mW), showing that the mismatch caused by increased dead area in shunted cells is minimal compared to the mismatch due to parasitic shunts. 105

Figure Page

4.13 Plot comparing the efficiency of a typical 7.22% a-Si:H module with parasitic shunts (horizontal line), after the module is treated using different scribing isolation techniques. For the periodic lengthwise isolating scribes (triangles), the efficiency improves with more vertical scribe lines (N_{scribe}), but the efficiency gains remain modest due to large dead area penalty. The efficiency enhancements are significantly better if selective scribing is used to isolated more and more shunted sub-cells (increasing N_{iso}/N_{sub}) for both partial (circles) and full (squares) isolation case. In case of partial isolation, the efficiency improves for larger L_{scribe}, due to better isolation, but ultimately limited by dead area losses (squares). For full isolation, the dead area losses are determined by the ratio A_{scribe}/A_{sub}, which limits the efficiency enhancements obtained due to reduced shunt effects. 108

4.14 CDF plots of module efficiency distribution for typical case (blue), lengthwise periodic scribing (magenta), partial shunt isolation after detection (green), and full shunt isolation after detection (red). The improvement in mean efficiency ($\bar{\eta}_N$), and reduction in standard deviation s_N are apparent from the values shown in inset. The full isolation of shunts can yield efficiency values close to the maximum possible module efficiency (black). 110

5.1 (a) Schematic showing partial shading caused by nearby modules, usually when sun is at shallow angles during morning or evening. An example photograph of this shading in an installed array is shown at the bottom. (b) On rooftop systems shadows from nearby objects are also important, as shown schematically at the top, and example image at the bottom. (* Photos taken from google images) 115

5.2 (a) An example circuit of 3 series connected solar modules supplying a resistive load. It illustrates the effect of partial shadow on one of the modules, with or without bypass diode (gray). (b) Schematics of the module (dashed lines) and string (solid lines) IV curves for the example circuit. Under normal operation (green), all operating points are positive (green squares), and the array power output is high (green rectangle). After middle module is shaded, its operating point shifts to negative value (red circles), in order to maintain current continuity, and it starts *dissipating* power (red rectangle). In presence of a bypass diode, the shaded module voltage is clamped near zero (gray circle), preventing module damage. . 117

Figure Page

5.3 (a) Schematic of typical TFPV string configuration connected to a DC bus, which is considered here for shading simulations. Each module has an external bypass as shown. (b) 1D simulation of partial shading for $V_{string} = 505$ V DC, showing the string (solid) and bypass diode (dashed) currents for increasing shade on one of the modules. The change in operating points of the string (squares), and bypass diode (circles) with increasing shade is shown with arrows. (c) IV curves for individual shaded (solid) and unshaded (dashed) modules in the string, with operating points (circles shaded, squares unshaded) changing for different shading conditions, so that the string current remains continuous (horizontal lines). The operating points stop moving after the shaded module voltage becomes negative, and the bypass diode turns on (see arrows). 119

5.4 Schematic of a typical TFPV module, with active area dimensions, and partial shadow covering a fraction of some cells at the bottom. 121

5.5 2D color plots of 26 rectangular cells (y-axis scaled for clarity) in a TFPV module with a partial shadow covering left half of 5 cells at the bottom (arrow shows direction of current flow, and the color bar on the top denotes the values). (a) The photo-generated current I_{abs} in sub-cells is reduced for left half of cells 1 to 5 (marked region 1), while their right half (marked region 2), and cells 6 and above (marked region 3) are fully illuminated. (b) The distribution of sub-cell voltage (V_{sub}) in this scenario shows that all sub-cells in the 5 partially shaded cells are reverse biased with $V_{sub}^{shaded} \approx$ 8.8 V across the cell width (regions 1 and 2), but the fully illuminated cells continue to operate in forward bias so that $V_{sub}^{illum} \approx 0.76$ V. (c) The sub-cells current I_{sub} shows asymmetric behavior, and I_{sub} in region 2 increases to ~ -16 mA, to compensate for the low $I_{sub} \approx -4$ mA in region 1, to ensure current continuity with fully illuminated cell where $I_{sub}^{illum} \approx$ -10 mA. (d) As a consequence of the voltage and current redistribution in cells 1 to 5, the sub-cell power dissipation P_{sub} in region 2 is four times that of region 1 (positive values in this sign convention), while the fully illuminated cells 6 and above continue to produce power (negative values in this sign convention). 122

Figure Page

5.6 (a) Schematic showing a pair of cells at the edge of the shaded and unshaded regions for the shade considered in Fig. 5.5 namely, fully illuminated cell 6 in region 3 (green) in series with the partially illuminated cell 5 (blue), with a shaded region 1 (red) and unshaded region 2 (purple). (b) The IV curves of half cells, including the shaded (red), unshaded (purple), and fully illuminated (green) halves, show that as the current in region 1 drops the current in region 2 must increase beyond even $I_{cell}/2$ to maintain current continuity. (c) The full IV curves of the cells (solid lines) showing that the total current through partially shaded illuminated 5 (blue) is same as the fully illuminated cell 6 (green), and their respective operating voltages determined by the amount of photocurrent reduction in the shaded cell. 125

5.7 (a) IR thermal image of fully illuminated series connected modules under normal operating conditions showing roughly uniform operating temperature of 32-34 °C (color bar on the right indicates temperature in °C). The hot spot at the top appears in all modules, due to placement of the connectors in that region resulting in current crowding and local heating. The module dimensions for these vertically oriented modules, and positions of regions 1, 2, 3 as defined in Fig. 5.5 are also shown. (b) An image of the same module under partial shade using a translucent shading cloth with 27% transmittance. The shade dimensions, direction of current flow and cell orientation are also marked. (c) The IR thermal image immediately after removal of the shade showing a slight temperature rise to 34-36 °C shaded region 1, but the temperature in unshaded region 2 is noticeably higher at 39–41 °C, and the temperature of fully illuminated region 3 is largely unchanged, as anticipated by theory. 127

5.8 (a) Schematic of partially shaded module showing the electrical (Q_e) and insolation heat (Q_s) flux components in the three regions of interest. (b) IR thermal image of module in steady state at V_{OC} showing roughly uniform temperature across the module surface, with relatively small extrinsic variation. This is then subjected to the identical shading conditions as in Fig. 5.7. (c) IR thermal image immediately after the partial shade is removed does not show any significant difference in temperatures between regions 1, 2, and 3; demonstrating that the differential heading due to insolation is essentially negligible. 129

5.9 Schematic showing a partially shaded module with module and shadow dimensions, along with the simplified 3-element equivalent circuit with blocks for the shaded and unshaded fractions of the partially shaded cells, and fully illuminated cells of the module. The current and voltage scaling parameters, as well as equivalent resistance values are shown. 131

Figure Page

5.10 IV characteristics comparing the full 2D simulations (blue dashes) with the simplified 1D case (green dotted) for the partial shading scenario considered in Section 2. The 1D and 2D cases are virtually indistinguishable, showing that the (a) string output, (b) module output for shaded and unshaded modules, as well as (c) characteristics of the shaded and unshaded halves of the partially shaded cells, are identical. 132

5.11 Schematics at the top highlight the important shading scenarios, with consequences shown in plots below. (a) Color plot showing the worst case reverse bias (color bar in V) across a cell in the shaded region for shadows of different length (y-axis) and width (x-axis). Note that unlike the symmetric edge shading (marked 2), the asymmetric edge shadow (marked 3) causes reverse breakdown of shaded cells, but typical shadow stresses (marked 4) are fairly moderate. (b) String output power (color bar in W) as a function of varying shadow sizes, shows that small edge shadows (2 and 3) do not cause significant drop in output power, which only happens for large shadow sizes. 134

5.12 Role of external bypass diodes is explored by comparing the cases with or without bypass diodes. (a) ΔV_{cell}^{bypass} is the difference between worst case reverse stresses (color bar in V) in presence and absence of external bypass is plotted for different shadow sizes, showing that external bypass only marginally (by about 1 V) reduces the shadow induced stress, typically for larger shadows. (b) The difference in string power output $\Delta P_{string}^{bypass}$, due to external diodes (color bar in W) shows that while there is no impact for smaller shadows, for large shadows external bypass diodes can limit the string DC output loss by about 200 W. 136

5.13 (a) Schematic representation of repeated shadow stresses during operation resulting in I_{Dark} degradation. (b) Flowchart showing the simulation method used for estimating the statistical degradation mechanism. (c) Due to this parametric shadow degradation, the expected efficiency loss over 25 year operation of module with 2 hours of partial shadow each day, for different shading scenarios. 137

Figure Page

5.14 (a) Schematic of a typical TFPV module with rectangular cells. Arrows show the direction of current flow in N_{series} series connected cells, each with area A_{cell} (see bottom for 3D current flow patter at cell level). 2D color plots of (b) minimum cell voltage V_{cell}^{min}, and (c) string output power (P_{string}) for all possible rectilinear shadows on a typical rectangular module. Each point on the plot corresponds to a shadow of length L_{sh} and width W_{sh}, and the color denotes the worst case reverse stress V_{cell}^{min}, or power output P_{string} (see color bar). The dashed box highlights the cases where external bypass is on. Schematic in (a) also defines symmetric shadow (purple), and asymmetric shading (red); the corresponding V_{cell}^{min} and P_{string} are highlighted with arrows on respective plots. 139

5.15 (a) Schematic showing the radial design for TFPV modules, with triangular half-cells arranged in a radial pattern, with terminals along diagonals. Each cell comprises 2 triangles with of area $A_{cell}/2$, so that the total cell area is the same (marked green e.g.). There are 2 types of triangular half-cells, depending on whether the current is collected at longer (2) or shorter (1) edge (3D current flow shown in the schematic below). (b) Color plot showing that the worst case V_{cell}^{min} value for this design is restricted to -4.7 V (see color bar), for all possible rectilinear shadows as before. (c) The color plot of P_{string} values for radial modules also shows improvement for smaller shadow sizes. The cases when external bypass turns on are highlighted by the dashed polygon. The radial symmetry of design is also apparent in shade response (marked by arrows). 141

5.16 (a) Schematic showing the spiral design of TFPV module, with N_{series} cells in series. Each cell consists of two half-cells (marked green e.g.) shaped like concave polygons, requiring curved terminals as shown, and resulting in the current flow direction marked by arrows. The schematic below shows 3D current flow pattern in half-cells with current flowing towards outer (1) and inner (2) edges. (b) Color plot of V_{cell}^{min} values for this spiral module, for various shadow sizes, shows the worst case value to be restricted to -4.2 V (see color bar). (c) The color plot of string output power P_{string} also shows marked improvement. The cases when external bypass turns on are highlighted by the dashed polygon. The directional symmetry of radial design is also retained (marked by arrows). 143

Figure Page

5.17 Schematics showing the shading cases considered for the three designs, where shadow effect is evaluated as function of (a) horizontal, (b) vertical, and (c) diagonal orientations as shown.(a) Plot of V_{cell}^{min} vs. x position for long vertical shadow (best case for the rectangular geometry), comparing the three geometries (colors as shown in inset). (b) Plot of V_{cell}^{min} vs. y position for a horizontal shadow (worst case of rectangular design) comparing the three designs.(c) Plot of V_{cell}^{min} vs. position d for a diagonal shadow, which is the worst case for radial design. These results show that the spiral design works well in all cases and prevents shadow stress completely. 145

5.18 PDE simulation results for rectangular, radial, and spiral sub-modules, showing distribution of resistive power dissipation per unit area in the TCO layer (color bar in mW/cm^2). Plot at the bottom shows power loss in each of the 128 cells for radial (P_{dis}^{rad}) and spiral (P_{dis}^{spi}) designs, compared to the dissipation in rectangular cells (P_{dis}^{rec}) which is same for all cells. The annotations highlight the fact that thin long cells near diagonals, have lower power dissipation (purple); while the wider cells near the center have significantly higher power dissipation (red), for both the designs. . 148

5.19 Change in module efficiency compared to the rectangular design for the radial (dashed lines) and spiral (solid lines) designs, for different sheet resistance values and dead regions widths (legend in microns). The analysis shows, that spiral design usually improves the net module efficiency, except for very wide dead regions and/or very low sheet resistances. The filled symbols show the efficiency change for the state of the art parameters used in this study. 149

A.1 a-Si:H p-i-n solar cell band diagram, showing the thicknesses and built-in potential. 178

B.1 (a) Band diagram of an MSM structure with single carrier (hole) injection setup, showing the change in potential due to injected charge. (b) Schematic showing the exponential trap distribution (band tails) near the valence band edge. 184

C.1 (a) Color plot of sub-cell voltages for 20 cells ($y - axis$), where left half of 5 cells at the bottom is shaded (color bar in V). (b) The sub-cell voltages across the cell width for 2 shaded cells (no. 1 and 5), and 2 unshaded cells (no. 6 and 20). (c) Color plot of sub-cell current for 20 cells ($y - axis$), where left half of 5 cells at the bottom is shaded (color bar in mA). (d) The sub-cell current across the cell width for 2 shaded cells (no. 1 and 5), and 2 unshaded cells (no. 6 and 20). 187

Figure Page

C.2 (a) Color plot of sub-cell voltages for 20 cells ($y - axis$), where left half of 5 cells at the bottom is shaded (color bar in V). (b) The sub-cell voltages across the cell width for 2 shaded cells (no. 1 and 5), and 2 unshaded cells (no. 6 and 20). (c) Color plot of sub-cell currents for 20 cells ($y - axis$), where left half of 5 cells at the bottom is shaded (color bar in mA). (d) The sub-cell currents across the cell width for 2 shaded cells (no. 1 and 5), and 2 unshaded cells (no. 6 and 20). 189

C.3 Horizontal current flow through the bottom (metal/TCO) contact of different cells for (a) $R_{\square}^{metal} = 0.1\Omega/\square$ case and (b) $R_{\square}^{TCO2} = 10\Omega/\square$ case, showing the horizontal current flow responsible for redistribution of sub-cell current between sub-cells of partially (cells 1 and 5) and fully (cells 6 and 20) illuminated cells. Sub-cell power output (or dissipation) for the 2 shaded cells (no. 1 and 5), and 2 unshaded cells (no. 6 and 20), for the typical case with $R_{\square}^{metal} = 0.1\Omega/\square$ (c) vs. high $R_{\square}^{TCO} = 10\Omega/\square$ on both contacts (d). 191

D.1 (a) Schematic of rectangular module with cell area A. (b) Transformation of each rectangular cell into two triangles, with different angles, keeping the base and height the same. The resulting triangles arranged in radial pattern to create the module with same dimensions, and same cell area. 193

D.2 (a) Schematic of a square module with radial design showing two half-cells with equal areas. (b) The dashed lines are drawn as shown to bisect the triangle areas. (c) The successive triangles are exchanged so that triangles have one axis of bending. (d) This process repeated for all cells results in the spiral design with equal area half-cells, with once axis of twist. . . . 194

D.3 (a) Schematics showing the same size shadow on different module designs, showing the number of shaded cells (N_{sh}), and shaded areas $A_{sh,i}$ (identical for rectangular designs, but different for others). (b) Schematic of 1D equivalent circuit of the partially shaded module (with external bypass), using the calculated J_{sh} values from the respective A_{sh} values for each cell. The individual cell voltages are shown, and minimum V_{cell} is calculated at each shading condition for all the designs. 196

ABSTRACT

Dongaonkar, Sourabh Ph.D., Purdue University, December 2013. Technology Agnostic Analysis and Design for Improved Performance, Variability, and Reliability in Thin Film Photovoltaics. Major Professor: Muhammad A. Alam.

Thin film photovoltaics (TFPV) offer low cost alternatives to conventional crystalline Silicon (c-Si) PV, and can enable novel applications of PV technology. Their large scale adoption however, requires significant improvements in process yield, and operational reliability. In order to address these challenges, comprehensive understanding of factors affecting panel yield, and predictive models of performance reliability are needed. This has proved to be especially challenging for TFPV for two reasons in particular. First, TFPV technologies encompass a wide variety of materials, processes, and structures, which fragments the research effort. Moreover, the monolithic manufacturing of TFPV modules differs significantly from that of c-Si technology, and requires new integrated approaches to analysis and design for these technologies.

In this thesis, we identify a number of features affecting the variability and reliability of TFPV technologies in general, and propose technology agnostic design solutions for improved performance, yield, and lifetime of TFPV modules. We first discuss the universal features of current conduction in TFPV cells, for both intrinsic dark and light currents, and parasitic (shunt) leakage. We establish the universal physics of space-charge-limited shunt conduction in TFPV technologies, and develop physics based compact model for TFPV cells. We examine the statistics of parasitic shunting, and demonstrate its universal log-normal distribution across different technologies. We also evaluate the degradation behavior of cells under reverse bias stress, and identify different degradation mechanisms for intrinsic and parasitic components.

We then embed the physics and statistics of cell operation and degradation, in a circuit simulation framework to analyze module performance and reliability. With this integrated circuit-device simulation, we establish log-normal shunt statistics as a major cause of module efficiency loss in TFPV, and develop a in-line technique for module efficiency and yield enhancement. Finally, we study the features of TFPV module reliability under partial shading using this circuit simulation, and propose a geometrical design solution for shade tolerant TFPV modules.

The most important theme of this thesis is to establish that TFPV technologies share many universal performance, variability, and reliability challenges. And, by using a technology agnostic approach for studying these problems, we can achieve fruitful cross coupling of ideas and enable broadly applicable solutions for important technological challenges in TFPV.

1. INTRODUCTION

Importance of the sun as ultimate source of energy has been appreciated since ancient times [1]. As the primary energy source, the sun contributes 99.97% of entire energy budget of earth [2]. The remaining 0.03% comes from the stored heat of earth's core as geothermal, and from the nuclear decay of radioactive elements. Consequently, all renewable and nonrenewable energy sources, excepting nuclear and geothermal, are, in fact, derivative forms of solar energy. It therefore stands to reason that entire human energy requirements can be met easily, even if a fraction of solar energy can be tapped directly [3]. Solar energy has been used for heating, cooking, and cooling since ancient times [4]. More recently, large scale, high temperature collectors have been investigated, for large scale electricity production [5]. The chief challenge for this technology is its dependence on water supply, an increasingly scarce commodity in the world [6]. Advent of semiconductor technology in 1950s enabled direct conversion of sunlight to electricity for the first time, using photovoltaic (PV) effect [7]. This remains the most direct way of converting light to electricity, as it involves no moving parts and is the only major electricity generation technology that does not require large moving parts. This also enables 'point of use' generation of electricity, a key advantage for rural electrification in underdeveloped countries [8]. Note that thermoelectric, piezoelectric, and electrochemical converters are also capable of solid state electricity generation, and require no moving parts, but their large scale applicability is under question.

Because of such promise of solar PV technology, it has been actively researched since 1950s. As a result, individual solar cell efficiencies have increased from $\sim 1\%$ efficient crystalline Silicon (c-Si) cell in 1951 [9], to latest record of 28.8% for single junction Gallium-Arsenide (GaAs) based cell [10]. Although higher efficiencies and improved processing have reduced the price of PV cells; the cost of solar electricity in

$/kWh, has remained high compared to conventional energy sources [11]. A significant portion of the cost in conventional crystalline semiconductors based PV systems is materials and processing cost, both in terms of capital as well as energy [12]. Therefore, solar cells made from amorphous and polycrystalline materials, deposited at low temperatures on large area substrates, have been actively researched [13], as low cost alternatives to c-Si based PV. Since, the active semiconductor layers in these cells is typically $\sim 0.2-2\ \mu$m thick,as opposed to $\sim 100\ \mu$m for c-Si cells, they have acquired the collective name *Thin Film Photovoltaics* (TFPV).

1.1 Introduction to Thin Film Photovoltaics

We begin with a brief survey of the history and present status of TFPV technology, illustrating the relevant scientific and technical highlights, and continuing challenges.

1.1.1 A Historical Perspective

Although TFPV technologies are considered an alternate to 'conventional' crystalline silicon (c-Si) PV, their development, in fact, started at the same time. The first heterojunction thin film solar cell based on Cu_2S/CdS structure, and with 6% efficiency [14] was reported in 1954, the same year as the 6% efficiency c-Si solar cell from Bell Labs [15]. By 1960s CdTe heterojunction solar cells, with 6% efficiency, were also developed [16]. The research and development in various TFPV materials and cells has been going on in parallel to the c-Si and later GaAs cells. It is therefore apparent that the discovery of photovoltaic effect was not a differentiating factor between c-Si and TF cells. The primary reason behind the success of c-Si based PV were primarily technological, as it was deemed more reliable and manufacturable, making them suitable for space applications, which was the primary application for solar cells in early days [17]. Moreover, c-Si PV also benefited from the tremendous advances in Si processing and manufacturing techniques, brought about by the developments in microelectronic industry over the decades.

The development of TFPV technologies at an industrial scale started only after PV technologies were considered serious contenders for terrestrial electricity generation on a large scale. In order to achieve this goal, huge quantities of solar cells and modules would be required to cover km^2 of land area. In this new role, the cost of solar cells became an important concern. And, as c-Si material and processing costs were very high to enable large scale adoption of PV electricity [12], a fresh incentive to pursue cheaper materials and processes was created. This led to a greater interest in TFPV technologies as they offered a promise for lower cost in terms of $/kWh, even though their cell efficiency had lagged behind crystalline cells.

1.1.2 The Case for TFPV Technologies

The cost of PV electricity generation can be sub-divided into three main components namely, module, inverter, and balance of systems (cabling, installation, permits etc.) costs. As shown in Fig. 1.1, according to the 2010 estimates [18], the total installed cost of c-Si PV system was $3.40/W, half of which ($1.70/W) was due to the module cost. The module cost in turn depends on various manufacturing steps, which can be classified according to cost of material (Si in this case), cost of cell manufacturing, and rest for module manufacturing. For the c-Si technology, these values are $0.70/W for module manufacturing (includes glass, EVA, frame, tooling, capital, and labor), $0.45/W for cell manufacturing (includes metallization, dopants, chemicals, capital and labor), and $0.55/W for Silicon itself (includes feedstock, and processing) [18]. This shows that despites the significant improvements in c-Si manufacturing, the cost of Si itself still forms a significant chunk of overall cost of PV electricity.

The high material cost of c-Si is the biggest motivation for pursuing low cost absorber materials. Besides cheaper feedstock, the cost advantage in TFPV arises from about 100 fold lower material consumption in thin film absorber layers [19]. Moreover, these thin film materials are typically deposited using low temperature

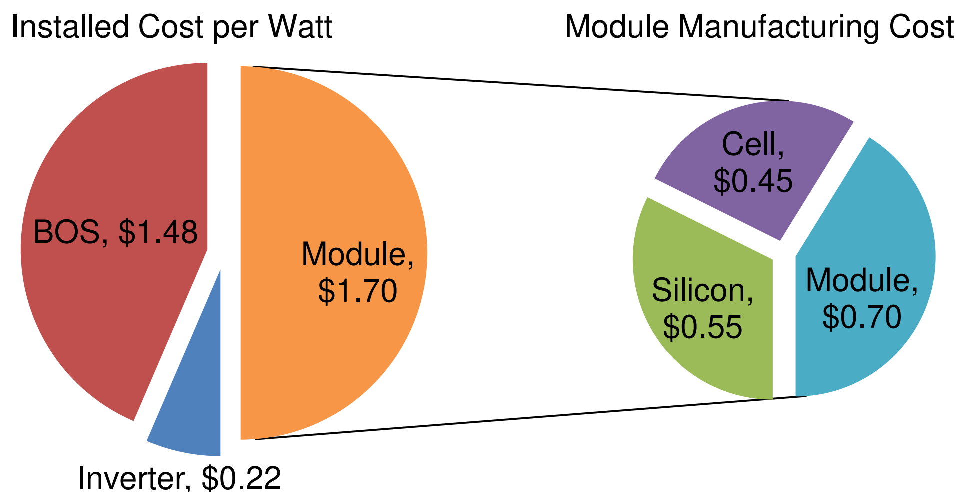

Fig. 1.1. Estimated cost breakdown for an installed PV system in $/W for commercial c-Si technology (for 2010 fiscal taken from [18]), showing that module cost accounts for half of the electricity cost ($1.70). The breakup of module cost shows that a significant fraction ($0.55) comes from high Silicon cost, and the rest is combination of cell manufacturing ($0.45 for metals, dopants, chemicals etc.), and module manufacturing ($0.70 for glass, EVA, frame etc.).

processes, resulting in lower energy budget and hence lower cost [20]. Another aspect of the cost argument for TFPV arises from monolithic manufacturing of TFPV modules, which enables large area, high volume manufacturing of TFPV modules [21, 22]; and, in case of flexible TFPV, the roll-to-roll fabrication of modules [23, 24]. Both these capabilities, which are only possible for TFPV technologies, allow for higher throughput, thereby lowering manufacturing costs.

It must be noted that the balance of system (BOS) costs of PV technologies includes the cost of land for an installation. Owing to their lower efficiency, TFPV technologies require larger area installation resulting in higher BOS costs, which in turn undermines their economic advantage [25]. Moreover, the rapid drop in c-Si module prices in recent years, driven by commercial factors, has nearly voided the cost advantage of TFPV technologies [18, 26]. There are, however, technical advantages that continue to make TFPV attractive. These include,

- Most TFPV technologies exhibit better low light performance, and smaller sensitivity to operating temperature, resulting in better relative energy yield over the operating lifetime in many environments [27].

- Owing to their adaptability to various substrates and module shapes, TFPV is ideally suited for building integrated (BIPV) applications, which is a growing segment of overall PV market [28].

- And, their amenability to flexible substrates, means that TFPV can enable new applications of PV technology, as well as lower the installation costs at system level [29].

These advantages continue to drive the TFPV research, and a host of different approaches and materials are being pursued.

1.1.3 Thin Film Solar Cell Landscape

We now survey the materials, processes, and device structures for the various TFPV technologies.

Absorber Materials

The term TFPV encompasses a range of different technologies in terms of materials, structures, and processes used [13]. The moniker 'thin film', however, refers to the thin absorber layers in these cells, of which there are a many types. A brief summary of the most important absorber layer materials used in TFPV technologies, classified according to the material structure can be given as follows:

- inorganic amorphous (includes amorphous (a-Si:H) and nanocrystalline (nc-Si:H) silicon);

- inorganic polycrystalline (mostly binary (CdTe), ternary (CISe), and quaternary (CIGSe, CZTSe) chalcogenides); and

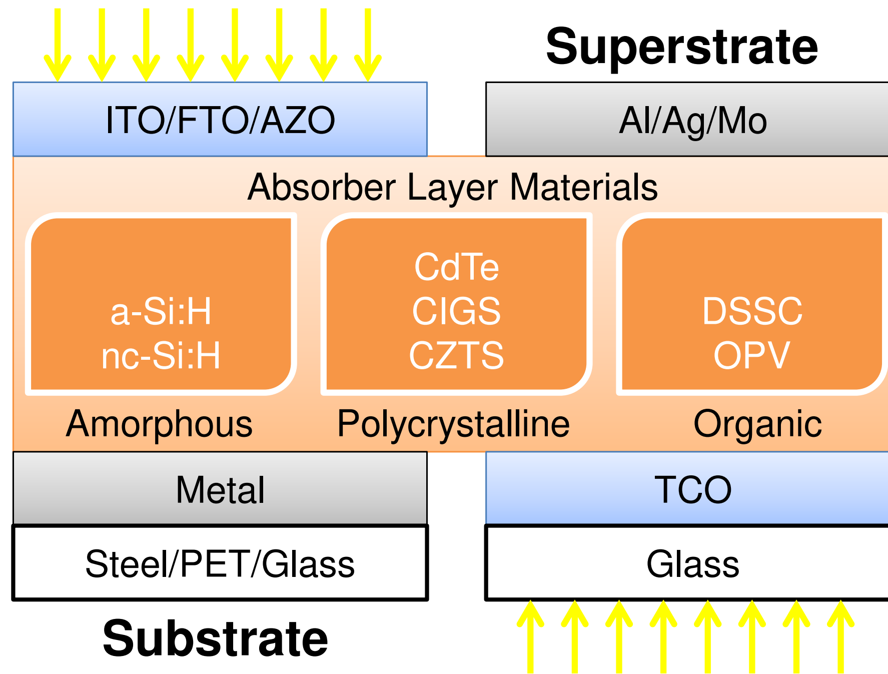

Fig. 1.2. Schematic showing thin film PV materials and structures, comparing the substrate and superstrate configurations, and the absorber and contact materials

- organic (includes small molecule and polymeric organic semiconductors (OPV) and dye sensitized (DSSC)).

This classification is based on material structure, and is shown schematically in Fig. 1.2. There are other differences in these materials due to chemical composition as well, most notably in the variety of polymers and small molecules used for OPVs [30]. Another difference arises in stoichiometry of multicomponent materials, most notably chalcogenides, which allows control of the absorber properties, but also leads to challenges in controlling material quality over large areas [24, 31].

Contact Layers

Besides the absorber materials, all TFPV technologies require a transparent conductor to serve the dual purpose of collecting generated photocurrent while allowing

the light to reach the active material (as shown Fig. 1.2). The family of Transparent Conducting Oxides (TCOs), including fluorinated SnO_2, Al doped ZnO (AZO), and Indium Tin Oxide (ITO) are the most commonly used materials for this purpose [32]. A variety of new transparent conductors, however, are being actively researched for replacing these somewhat expensive materials in TFPV manufacturing [33, 34]. For all TFPV technologies, the other electrical contact is provided by a metal layer, which also acts as the mirror (Fig. 1.2). Again, a variety of metals are used for different technologies, including Ni-Cu alloy for CdTe [35], Mo for CIGS [36], and Al/Ag for a-Si:H [37] and OPV [38] cells.

Depending on the order of deposition the TFPV cells can either be made in substrate, or superstrate configuration [39], as shown in Fig. 1.2. The choice of supersatrate or substrate configuration depends on materials processing constraints, as well as choice of the substrate. The superstate configuration is is used for CdTe [21], a-Si:H/nc-Si:H [40] and OPV technologies [41], as good quality CdTe, a-Si:H, and organic layers can be deposited on the TCO coated glass substrate. For CIGS and CZTS on the other hand, the absorbers are best deposited on Mo coated substrate, thereby requiring a substrate configuration for these materials.

Deposition Methods

Not only there is a large array of materials used in TFPV technologies, there is also a huge variety of deposition techniques used in their manufacturing. Table 1.1 compiles a partial list of the various deposition techniques used for deposition of the materials used in TFPV technologies. These include vacuum processes like chemical vapor deposition (CVD) [40], or different physical vapor deposition (PVD) techniques like sputtering, or thermal evaporation [13], which have been adapted for large area, in-line manufacturing processes. Another set of methods which are being actively developed for large area substrates, and roll-to-roll deposition, involve solution processing such as ink [42], sol-gel [43], electrodeposition [44], chemical bath deposition

Table 1.1
Summary of TFPV materials and associated manufacturing technologies.

	x-CVD	x-PVD	Solution	EPD	Spin
TCO	√	√	√		
x-Si	√				
CdTe		√		√	
CIGS		√	√		
OPV					√
Metal		√	√		

(CBD) [45], and spin and spray coating techniques [46]. This is only a partial list, which is continuously growing as newer materials and processes are being actively researched worldwide. Table 1.1, however, highlights the large spectrum of materials and processes being used for TFPV technologies.

For the a-Si:H (and nc-Si:H) technology for example, a superstrate configuration is used. The process starts with large area sputtering of the transparent contact (FTO in this case), followed by deposition of p/i/n a-Si:H using PECVD process. The back contact, which is a combination of AZO and Ag layers, is then deposited using sputtering. All these processes have been adapted for large area manufacturing, and have been used to produce $2.2m \times 2.6m$ a-Si:H modules [47].

Device Structure

Finally, we consider the specific structures used to form TFPV cells. Fig. 1.3 shows the schematics of three representative TFPV cells, along with the thicknesses of various layers. As apparent from the schematics, the layer thickness can vary from $\sim$100 nm for a-Si:H and OPV, to $\sim 1-2\mu$m for CIGS and CZTS and $\sim 3-5\mu$m for CdTe. The layers used for junction formation in these cells are also quite different. For a-Si:H and nc-Si:H, the doping can be changed easily to create p and n layers for

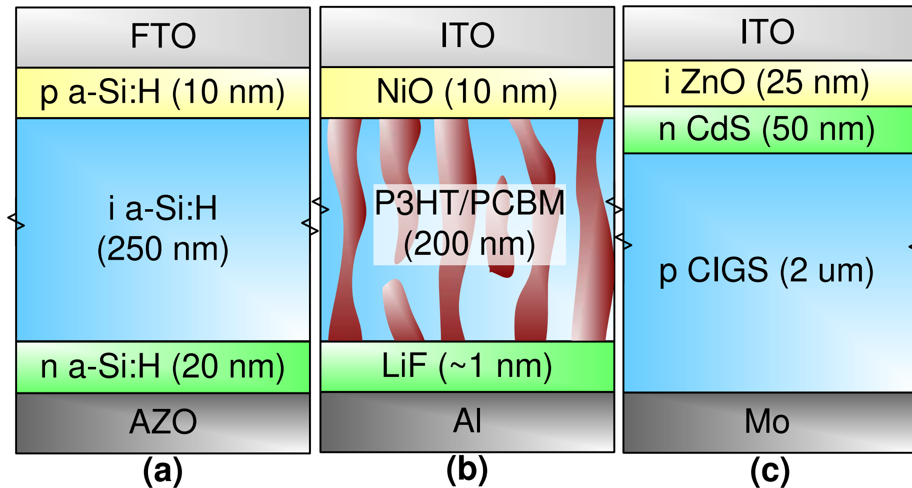

Fig. 1.3. Schematics showing the device structures, and layer thicknesses, of 3 major TFPV cell types namely, (a) a-Si:H p-i-n solar cell with Aluminum doped ZnO (AZO) and Fluorinated SnO_2 (FTO) contacts; (b) organic bulk heterojunction (BHJ) with Al and Indium doped SnO_2 (ITO) contacts; and, (c) CdS/CIGS solar cell with Molybdenum (Mo) and ITO contacts.

junction formation (see Fig. 1.3 (a)). In OPV, the built-in field is created by using metals/TCO of different work function, typically Al and ITO for most cells, as shown in Fig. 1.3(b). Chalcogenide materials,are intrinsically p-type, and the junction is created using thin CdS/ZnO layer, which are intrinsically n-type materials.

As the layers used for junction formation are very different, the diode junctions that form TFPV cells are very different from the typical p-n homojunction in c-Si cells. This leads to different electronic band profiles, which can be summarized as,

- p-i-n homojunction for a-Si:H and nc-Si:H cells (Fig. 1.4(a));
- type II, bulk heterojunction between donor-acceptor materials in phase segregated OPV cells (Fig. 1.4(b));
- type I n-p heterojunction for CdS/CIGS, and CdS/CdTe junctions in case of chalcogenides (Fig. 1.4(c))

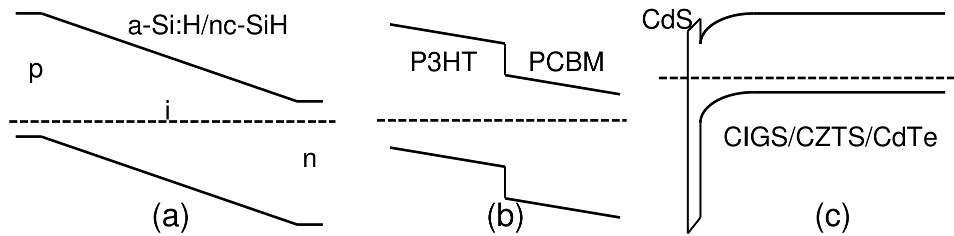

Fig. 1.4. Typical band diagrams of the three TFPV cells shown in Fig. 1.3; showing the (a) p-i-n homojunction for a-Si:H and nc-Si:H cells, (b) Type II heterojunction between the two organic materials in OPV, and (c) CdS/absorber Type I heterojunction for the chalcogenide cells.

The material parameters of metal and TCO layers in each case, and electrical properties at different material interfaces also play an important role in determining the operation of each type of solar cell.

1.2 Technology Agnostic Features of Thin Film PV

From the discussion in previous sections, we can see that the term TFPV encapsulates a wide array of PV technologies, with different materials, processes, and structures. Moreover, this list is continually growing due to the active research in the TFPV, which are exploring many pathways for improving TFPV efficiency. It is therefore easy to see why these technologies typically have been viewed as separate from each other, and studied individually. In this work, however, we will show that despite the glaring differences, there are conceptual commonalities in all TFPV technologies; and by focusing on these unifying features important insights can be obtained into the performance, variability, and reliability of all TFPVs in general.

1.2.1 Device Physics of TFPV Cells

Fig. 1.3 shows the schematics of three major types of TFPV cells, with significant differences in materials and structure, leading to very different optical and electronic

behavior for each of them. There are, however, some important aspects of the device physics that are common across all these cells.

Opto-electronic properties

Owing to the low temperature processing, all TFPV materials have large density of electronic defects leading to relatively low carrier lifetime values (typically $\lesssim$10 ns) [48, 49]. Moreover, the amorphous and polycrystalline nature of these materials, leads to significantly low effective free carrier mobilities; e.g. $\sim 10^{-4} - 10^{-3}$ cm^2/Vs for organic [30], $\sim 0.1 - 1$ cm^2/Vs for a-Si:H [50], and $\sim 10 - 100$ cm^2/Vs for CIGS/CdTe [48]. This low value of mobility-lifetime ($\mu\tau$) product, results in low diffusion lengths for photogenerated carriers; which means that the built-in electric field must be used to ensure good carrier collection in all TFPV cells. Therefore, in all TFPV technologies either the electric field region is equal (in a-Si:H and OPV), or comparable (in CIGS and CdTe), to the total film thickness, as seen in Fig. 1.3. This has important consequences, as the carrier collection becomes voltage dependent [51], and contribution from bulk recombination must be treated carefully [52, 53]. This is a key factor differentiating the operation of TFPV cells from c-Si cells, and therefore most of the understanding of carrier transport developed for c-Si cells is not directly applicable in TFPV. Fortunately, all TFPV materials behave as direct bandgap materials, and usually have high absorption coefficients [54]. This ensures good optical absorption and photocurrent, even for these thin absorber layers. Often, however, optical or plasmonic light trapping designs are needed for enhancing the absorption, especially in a-Si:H and OPV cells [55]. This is the primary reason for the use of 'thin' (usually $\lesssim 1\mu$m) absorber layers made from these materials.

Solar cell structure

All solar cells require a built-in electric field to separate the photocarriers, and is created by the semiconductor junction formed by different doping and/or different

materials. As apparent from Fig. 1.3, another common feature in all TFPV cells is that the 'emitter' layers responsible for junction formation (n/p layers in a-Si:H, CdS layer in CIGS/CdTe, and NiO blocking layer in OPV) are very thin. These layers must be kept very thin ($\lesssim$ 50 nm), in order to allow more light to reach to absorber layers [56]. Additionally, these thin layers must be deposited over large area absorber layers with rough surfaces [45], using low temperature processes. Therefore, it is more than likely that local defects like pinholes can form in these layers, leading to parasitic defects.

Another structural aspect common to TFPV cells, which distinguishes it from c-Si cells is the use of a transparent conductor for providing the ohmic contact for the photocarriers, while allowing light to reach the absorber layer. In c-Si cells, the sparsely spaced metal fingers or grids are deposited on the top surface for current collection, and the absorber layer is exposed to light in between the grid lines [57]. This is possible because the conductivity of the emitter layer in c-Si is very high, and the photocarriers can reach the grid lines without significant voltage drop, and get collected. In TFPV cells, however, the low conductivity and small thickness of emitter layers, which means that the photocarriers cannot drift through the emitter to reach metal grid lines. Therefore, these carriers must be collected as soon as they reach the emitter, which necessitates the use of a transparent conductor. These transparent conductors need to fulfill the dual requirement of high conductivity *and* high transparency, which means that the performance of all TFPV cells and modules is limited by the TCO properties [32].

1.2.2 Module Manufacturing Process

The output current of a solar cell is proportional to its area, so in order to obtain large output currents for practical use, we simply need to use large area cells. The voltage of all solar cells, however, is limited to approximately 1 V, and in order to obtain useful operating voltage, many cells must be connected in series, to form a

PV module. In c-Si technology, this is accomplished by manufacturing individual cells first, and then soldering them together in series to form a typical sized module with $\sim 60-100$ cells in series, and operating voltage of $\sim 40-60$ v. This series connection is done after the solar cell fabrication is finished, thereby separating the cell and module manufacturing processes.

Owing to the stark difference in materials and processes, the module and cell manufacturing are intertwined, and TFPV modules are made directly in a 'monolithic' process. This is also an important factor in realizing the promise of low cost thin film PV, because it enables high throughput module production [20]. This monolithic manufacturing is made possible by techniques for large area (typically $\gtrsim 1\text{m}^2$) deposition of active materials in a batch [58], or roll-to-roll [29] process. In order to make the series connected cells inside the module, the large area film deposition is coupled with an integrated approach for creating these series connections. This is accomplished by interspersing the film deposition steps with laser scribing to create the series connections required to form a module in a monolithic fashion [59]. Fig. 1.5 shows the manufacturing steps of a TFPV module in side view. Each layer deposition is followed by a laser scribing process step, which ablates the active material and forms well defined grooves. By repeating this process with well placed scribes, one obtains the desired series connection. This process is used for almost all TFPV technologies, and is required for their commercial success. This top down series connection, however, precludes any addition or changes in module circuitry to improve their performance or reliability, as is common practice in c-Si modules [60].

Understandably, this large area deposition of very thin layers poses significant challenges in terms of process control [61], and parametric yield [62]. Two subtleties of this monolithic manufacturing must be noted in this regard. First is the drop in TFPV efficiency suffered, while going from cell to module level [63]. This is by no means a problem unique to TFPV; and all PV technologies have a 2-5% (absolute) gap in efficiency between best reported efficiencies at scell and module level [10]. Unlike crystalline PV, however, the monolithically made TFPV modules do not have

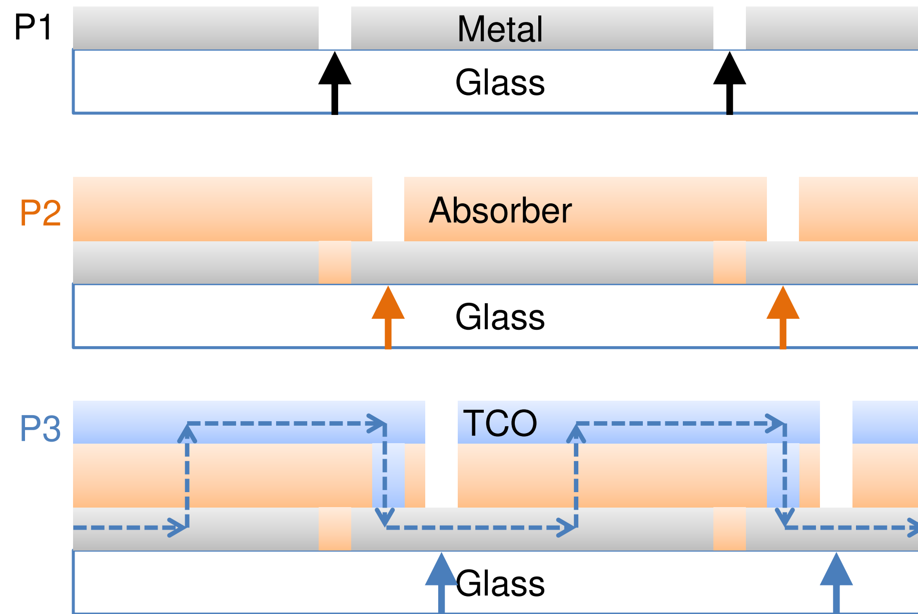

Fig. 1.5. Side view of a TFPV module under step by step fabrication marked as, P1 - metal deposition followed by laser scribing (arrows), P2 - absorption deposition and scribing, and finally, P3 - TCO deposition and scribing. This leads to series connected cells in a module, with current flow direction shown by dashed arrows.

a clear demarcation of front end (wafer level), and back end (module level) issues [64]. This means that the cell and module cannot be optimized independently to achieve higher efficiency. Moreover, it is not possible to manage the process variability by binning individual wafers, a common practice for c-Si [64]. Because of the direct module fabrication, the effect of process variability must be assessed and tackled at the module level itself. These two factors require a new integrated approach for variability analysis, which can scale from cell to module level.

1.2.3 Reliability and Module Lifetime

Long term performance reliability is a critical factor in success of any technology or product. This, however, is doubly important for PV technologies, because the amortization of capital costs depends on the module lifetime [11]. Therefore, better

predictive reliability models for TFPV are also important from the point of view of making them commercially competitive. Owing to its importance, PV reliability has been studied extensively [65]. The reliability literature, however, has been divided into two distinct categories namely, [66]

- *back end* reliability which concerns the packaging and structural materials and is determined by environment factors, and
- *front end* reliability which is determined by degradation in the active semiconductor layers.

The back end reliability encompasses performance degradation due to environmental and operational effects, which is common to *all* PV technologies. These have remained the limiting factors for most TFPV technologies; and therefore, the majority of IEC 61646 qualification tests are centered around extrinsic reliability [67]. Front end reliability, on the other hand, refers to material and device degradation mechanisms unique to each technology or material system. These degradation mechanisms are fundamental, and would remain even if all environmental factors could be controlled fully. Consequently, these have been explored from a physics perspective; the most famous examples of which are light induced degradation (LID) in a-Si:H [68], and copper diffusion in CdTe [35].

While most front end reliability issues are cell or material specific, a universal front end reliability challenge arises from partial shading of modules during normal operation, which can cause shaded cells to go into reverse bias [69]. This is a universal problem for all PV technologies, but can be solved for c-Si modules by incorporating protective circuit elements (bypass diodes) inside the module [70]. This is possible because for c-Si modules the cell and module manufacturing are separate, and extra circuitry can be added to the modules during series connection of individual cells. This is not possible for TFPV because, the monolithic module structure does not allow inclusion of external circuit element inside the modules. Moreover, the shape and orientation of series connected cells in TFPV modules is very different from c-Si

case. And, a fresh approach towards analysis of shading effect in TFPV modules and cells is required, incorporating the understanding of shadow induced reverse bias stress, as well as the physics of degradation of TF solar cells under reverse stress [71].

1.2.4 Challenges Unique to Thin Film PV

In the previous sections, we have summarized the state of research on TFPV performance, variability and reliability. Based on this discussion, we can now identify certain challenges that are unique to TFPV, and approaching them in a unified manner may be helpful in streamlining their understanding. These are summarized briefly as:

- Due to low mobility and lifetime in TFPV absorber materials, the field dependent collection and recombination is a common feature in TF solar cell operation, and must be understood in a coherent manner to assess their performance limitations.
- Thin emitter layers with TCO/metal contacts are used in all TFPV technologies, and their relation to parasitic defect formation should be analyzed in a universal fashion.
- There is no distinction between cell and module performance variability of TFPV because of their monolithic processing, and new approaches must be developed for understanding and solving these problems in TFPV.
- Reliability issues associated with partial shading require a combined cell, module, and system level analysis for TFPV, owing to the monolithic structure and unique material degradation characteristics.

1.3 Outline of the Thesis

1.3.1 Research Direction and Philosophy

From this introduction, we make two important observations. First, we saw that the research in TFPV and c-Si started at the same time, and at the same level; but, the factors which limited the success of TFPV were technological rather than scientific. This means that c-Si cells were able to make the transition from laboratory scale to industrial production much earlier, because the critical problems of production yield, and long term reliability in c-Si were addressed earlier. TFPV could only become a viable contender many decades later, when these manufacturing and operational challenges were finally addressed for them. A full quantitative assessment of these issues, however, is still lacking for TFPV; due in part, to the various materials and processing factors distinguishing it from c-Si technology. Owing their critical importance in commercial success of TFPV technologies, in this work therefore, we will focus on these very aspects of module performance loss and variability, caused by random parasitic defects, and long term performance reliability in TFPV, affected by partial shading of modules.

The second important observation concerns the universal features of TFPV materials, devices, and modules, outlined in the previous section. These commonalities suggest that it must be possible to obtain universal trends in operation, variability and reliability issues in TFPV cells, to a certain degree. This will enable a cross coupling of ideas and lead to technology agnostic solutions to common problems in TFPVs. We therefore, will focus on these common aspects of variability and reliability challenges, and strive to make our analysis and solutions generally applicable to TFPV as a whole.

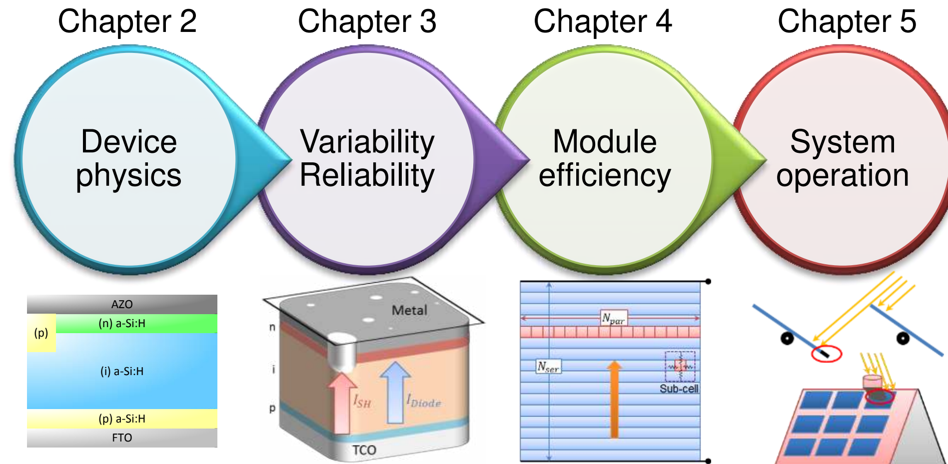

Fig. 1.6. Schematic of the thesis outline showing the sequential development from device physics in chapter 2, leading to physics and statistics of variability and reliability in chapter 3; both of which are then used in analysis of module performance in chapter 4, and finally shading problem at system level in chapter 5.

1.3.2 Detailed Outline

In the following chapters, the results obtained will be discussed at length. This development is depicted schematically in Fig. 1.6, and is summarized as:

- In chapter 2, we discuss the universal physics of dark and light current in TFPV cells, including the intrinsic as well as parasitic components. We isolate the parasitic shunt current, and establish its universal physics, and conduction mechanisms. We embed this physical understanding in an equivalent circuit for module level analysis.

- In chapter 3, we consider the sources of performance variation in TFPV cells, focusing in particular on the universal statistics of parasitic shunt current in TFPV cells, and provide empirical evidence for the same. We also evaluate the physics of solar cell degradation under reverse stress, and identify the various mechanisms responsible for the degradation of intrinsic and parasitic components.

- In chapter 4, we develop a detailed circuit module for incorporating statistical fluctuations in module level simulations, to gain insight into module performance variability. Based on these insights, we propose a technology agnostic solutions for reducing cell to module efficiency gap, using the laser scribing technique for reduction shunt losses at module level.

- Finally, in chapter 5, we discuss shadow induced reliability effects, and identify the unique features of shadow stress in TFPV modules. We also establish the geometrical features of shadow stress, and use it to propose shade tolerant module designs, which can be created using the monolithic module fabrication processes.

- In Chapter 6, we summarize the work, and suggest directions for future work.

1.4 List of Associated Publications

Chapter 2

- *S. Dongaonkar*, Karthik Y., D. Wang, M. Frei, S. Mahapatra, and M. A. Alam, "On the Nature of Shunt Leakage in Amorphous Silicon p-i-n Solar Cells", IEEE Electron Device Letters, 31(11), 1266-1268, 2010.

- *S. Dongaonkar*, J. D. Servaites, G. M. Ford, S. Loser, J. Moore, R. M. Gelfand, H. Mohseni, et al., "Universality of non-Ohmic shunt leakage in thin-film solar cells", Journal of Applied Physics, 108(12), 124509, 2010.

- C. J. Hages, J. Moore, *S. Dongaonkar*, M. A. Alam, M. Lundstrom, and R. Agrawal, "Device Limitations and Light-Soaking Effects in CZTSSe and CZTGeSSe", 38th IEEE Photovoltaic Specialits Conference (PVSC), pp. 002658-002663, 2012.

- *S. Dongaonkar*, and M. A. Alam, "PV Analyzer", Retrieved March 2012, from `http://nanohub.org/tools/pvanalyzer`

Chapter 3

- *S. Dongaonkar*, S. Loser, E. J. Sheets, K. Zaunbrecher, R. Agrawal, T. J. Marks, and M. A. Alam, "Universal statistics of parasitic shunt formation in solar cells, and its implications for cell to module efficiency gap", Energy & Environmental Science, vol. 6, pp. 782787, 2013.

- *S. Dongaonkar*, Karthik Y., S. Mahapatra, and M. A. Alam, "Physics and Statistics of Non-Ohmic Shunt Conduction and Metastability in Amorphous Silicon p.i.n Solar Cells", IEEE Journal of Photovoltaics, 1(2), 111-117, 2011.

- *S. Dongaonkar*, E. J. Sheets, R. Agrawal, and M. A. Alam, "Reverse Stress Metastability of Shunt Current in CIGS Solar Cells", 38th IEEE Photovoltaic Specialists Conference (PVSC), pp. 000868-000872, 2012.

- *S. Dongaonkar*, Karthik Y., S. Mahapatra, and M. A. Alam, "A Physical Model for Non-ohmic Shunt Conduction and Metastability in Amorphous Silicon p-i-n Solar Cells", 37th IEEE Photovoltaic Specialists Conference (PVSC), 2011.

- M. A. Alam, *S. Dongaonkar*, Karthik Y., S. Mahapatra, D. Wang, and M. Frei, "Intrinsic reliability of amorphous silicon thin film solar cells", 2010 IEEE International Reliability Physics Symposium (IRPS), pp. 312-317, 2010.

Chapter 4

- *S. Dongaonkar* and M. A. Alam, "Thin Film Photovoltaic Panels and Repair Methods", U.S. Patent Appl. 13/761,9142013.

- *S. Dongaonkar* and M. A. Alam, "In-Line Post-Process Scribing for Reducing Cell to Module Efficiency Gap in Monolithic Thin Film Photovoltaics", (*Under Review*).

- M. A. Alam, B. Ray, M. R. Khan, and *S. Dongaonkar*, "The essence and efficiency limits of bulk-heterostructure organic solar cells: A polymer-to-panel perspective", Journal of Materials Research, vol. 28, no. 04, pp. 541557, 2013.
- *S. Dongaonkar* and M. A. Alam, "Reducing the Cell to Module Efficiency Gap in Thin Film PV using In-line Post-Process Scribing Isolation", 39th IEEE Photovoltaic Specialists Conference (PVSC), 2013.
- E. S. Mungan, *S. Dongaonkar*, and M. A. Alam, "Bridging the Gap: Modeling the Variation due to Grain Size Distribution in CdTe Solar Cells", 39th IEEE Photovoltaic Specialists Conference (PVSC), 2013.
- *S. Dongaonkar*, and M. A. Alam, "End-to-End Modeling for Variability and Reliability Analysis of Thin Film Photovoltaics", 2012 IEEE International Reliability Physics Symposium (IRPS), pp. 4A.4.1 - 4A.4.6, 2012.
- M. Alam, B. Ray, and *S. Dongaonkar*, "The Essence and Efficiency Limits of Bulk-Heterostructure Organic Solar Cells", MRS Fall Meeting, p. 1390, 2012.
- *S. Dongaonkar*, and M. A. Alam, "PVpanel Sim", Retrieved March 2012, from `http://nanohub.org/tools/pvpanelsim`

Chapter 5

- *S. Dongaonkar* and M. A. Alam, "Shade Tolerant Thin Film Photovoltaic Panel", U.S. Patent Appl. 61/6446532012.
- *S. Dongaonkar*, C. Deline, and M. A. Alam, "Performance and Reliability Implications of Two Dimensional Shading in Monolithic Thin Film Photovoltaic Modules", IEEE Journal of Photovoltaics, 2013 (*in press*).
- *S. Dongaonkar* and M. A. Alam, "Geometrical Design of Thin Film PV Module for Improved Shade Tolerance and Performance", Progress in Photovoltaics: Research and Applications, 2013 (*in press*).

- *S. Dongaonkar* and M. A. Alam, “Partial Shading in Monolithic Thin Film PV Modules: Analysis and Design”, Photovoltaic Module Reliability Workshop (PVMRW) 2013.

- *S. Dongaonkar*, and M. A. Alam, “A Shade Tolerant Panel Design for Thin Film Photovoltaics”, 38th IEEE Photovoltaic Specialists Conference (PVSC), pp. 002416-002420, 2012.

- *S. Dongaonkar*, Karthik Y., D. Wang, M. Frei, S. Mahapatra, and M. A. Alam, “Identification, Characterization and Implications of Shadow Degradation in Thin Film Solar Cells”, 2011 IEEE International Reliability Physics Symposium (IRPS), pp. 5E.4.1 - 5E.4.5, 2011.

2. DEVICE PHYSICS OF THIN FILM SOLAR CELLS

In this chapter, we discuss the physics of operation of thin film solar cells. We consider typical laboratory scale cells with dimensions less than 1 cm^2; and analyze the dark and light current voltage (IV) characteristics, including the fundamental and parasitic current components. This chapter is organized as follows: In Sec. 2.2, we analyze the *intrinsic* solar cell response with and without illumination, and clearly identify the respective current components. Next, in Sec. 2.3 [1], we focus on the parasitic shunt current component. We isolate the diode and shunt current contributions in measured data, and explore their voltage and temperature dependencies in detail. Finally, in Sec. 2.6, we combine the models of intrinsic and parasitic currents, to create a physics based equivalent circuit for thin film solar cells.

2.1 Introduction

At the fundamental level, all solar cells operate by separating the photogenerated carriers using a built-in electric field, as shown schematically for a p-n junction solar cell in Fig. 2.1(a). All solar cells, however, suffer from bulk and surface recombination, which results in the loss of some of these carriers before they can be collected at the contacts. Therefore, current density in an illuminated solar cell can be written most generally, as a difference between total generation ($G(x)$) and net recombination ($R(x)$), integrated over the cell, so that [74],

$$J_{total}(V) = q\int_{cell} G(x)dx - q\int_{cell} R(x,V)dx. \tag{2.1}$$

This is shown schematically as the area under the generation $G(x)$ and recombination $R(x,V)$ profiles in Fig. 2.1(b). The dependencies of J_{total} are determined by the

[1]Text and figures in this section are taken from [72] ©AIP 2010 and [73] ©IEEE 2010

voltage and photogeneration dependence of the recombination profile $R(x, V)$. In typical c-Si cells, the density of photogenerated carriers due to AM1.5G illumination is many orders of magnitude below the doping levels in the absorber layer, so that low-level injection conditions are preserved under illumination. In this scenario, the carrier concentrations at cell *boundaries* are determined by applied voltage V only [74]. Therefore, we can write the recombination profile under light $R_{illum}(x, V)$ in terms of recombination under dark $R_{dark}(x, V)$ as

$$R_{illum}(x, V) = R_{dark}(x, V) + \zeta G(x), \tag{2.2}$$

where ζ is a proportionality constant dependent on the minority carrier lifetime of the absorber layer. In this regime, the integrals in Eq. 2.1 separate two terms, one which depends on photogeneration only, and the other on voltage only so that we get

$$J_{total} = J_{photo}(G) + J_{diode}(V), \tag{2.3}$$

where $J_{diode}(V)$ is the exponential diode current under dark, and the constant photocurrent J_{photo} is equal to the short circuit current density J_{SC}. This is known as the superposition principle in solar cells, and is applicable to most crystalline PV technologies [75]. This IV relation is usually represented by a current source and diode as shown by the 'intrinsic' portion of the equivalent circuit shown in Fig. 2.1(c). In general, however, the photocurrent can depend on the applied voltage, and the *dark* diode current which is determined by the carriers injected from the contacts can also be modified due to illumination J_{diode}^{illum}, so we should write total current as

$$J_{total} = J_{photo}(G, V) + J_{diode}^{illum}(G, V). \tag{2.4}$$

In case of thin film solar cells, the carrier lifetimes and mobilities are low, and it is known that superposition relation of Eq. 2.3 does not hold true [39, 76–78]. Fig. 2.2 shows the measured dark and light IV curves of a typical a-Si:H solar cell. The light IV is also compared with the calculated IV obtained from the superposition principle in Eq. 2.3. Note that there is a considerable difference between the

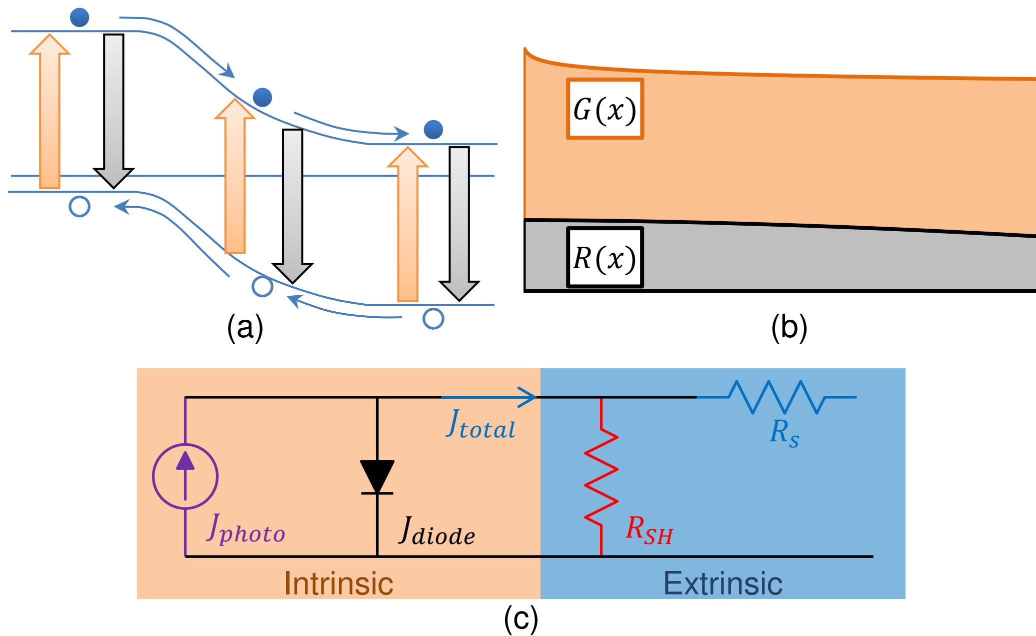

Fig. 2.1. (a) Schematic band diagram of a typical p-n junction solar cell, showing the photogeneration and recombination processes, along with the carrier transport. (b) Schematics of the generation profile $G(x)$, and recombination profile $R(x)$ inside the solar cell shown in the area plot. The difference between the area under these curves determines the output current of the solar cell (c) Typical equivalent circuit used for solar cells which show superposition. The photocurrent is represented by constant current source J_{photo}, in parallel to the dark diode current J_{diode}. The parasitic shunt R_{SH} and series R_s resistances are also shown.

measured and calculated light IV demonstrates that photocurrent in TF solar cells cannot be assumed constant. It is therefore crucial to account for the correct voltage dependence of photocurrent when analyzing TFPV cells. This, in general, can only be done numerically [53, 79] because the transport equations are usually non-linear in these cells. Although, analytical solutions to the transport equations in TFPV have been obtained in the past [52, 80], they are only valid in certain limited operating range. Our first task in this chapter, is to solve the transport equations for a-Si:H p-i-n cells under reasonable assumptions, to obtain closed form expressions for the dark and photocurrent components. We identify the contributions of generation and

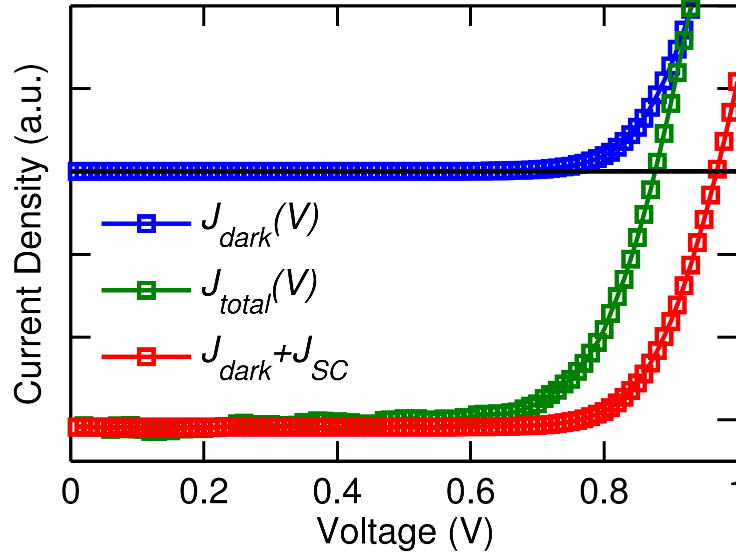

Fig. 2.2. The measured dark (blue) and light (green) IV of a a-Si:H solar cell, compared to the IV calculated from superposition principle in Eq. 2.3 (red), showing the failure of conventional superposition in TF solar cells.

recombination processes to find the expression for $J_{photo}(G, V)$, and highlight their relationship to various material and device parameters. We will also consider the situation when the injected current (usually equal to the dark current) is affected by illumination, which results in failure of superposition. By including the correct physics of intrinsic and extrinsic conduction for TF solar cells, we will develop an enhanced version of the equivalent circuit shown in Fig. 2.1(c), which is applicable for TFPV cells.

In addition to the above intrinsic (fundamental) current components, in a realistic solar cell structure we must also account for the extrinsic (parasitic) components. Fig. 2.1(c) shows the parasitic components as represented in typical solar cells using shunt resistance R_{SH} in parallel, and series resistance R_s from contact layer, which must be reevaluated for TFPV cells. In TFPV cells, the series resistance R_s is largely due to the sheet resistance $R_{\square}$ of TCO contact layer [81]. Other contributions due to

intrinsic semiconductor resistivity [82], and metal grid lines [83] may also be important in certain cases. The shunt current is also typically represented as a parallel resistor R_{SH} in solar cell equivalent circuits [84], but the physical origin of this parasitic shunt is not well understood [85]. We therefore focus on the characterization and modeling of I_{SH} with following goals:

- establishing the common phenomenological features of shunt conduction;
- developing of a universal physical model for I_{SH}, and
- identifying the physical origin of shunt path formation.

Finally, we embed this understanding of intrinsic and extrinsic current components in a physics based equivalent circuit, which can be used for analyzing module level phenomena.

2.2 Intrinsic Light and Dark IV

As discussed in the previous section, the assumptions required for the superposition described by Eq. 2.3 to hold are almost never satisfied for TFPV cells. Two important reasons are responsible for this difference; first, the important role of built in electric field in photocarrier collection in TFPV [52] (especially for p-i-n or m-i-m structures); second, the low mobility and lifetime of carriers in TFPV materials lead to modified boundary conditions under illumination. Therefore, in thin film cells, we must account for the following aspects of carrier transport carefully:

- Field dependent collection of carriers;
- Bulk recombination under illumination; and
- Modification of band diagram under illumination.

For the different solar cells types shown in Fig. 1.4 the analysis of dark and light IV characteristics has been reported for a-Si:H cells in [51, 86], for OPV cells in [87],

and for chalcogenides in [88]. While these focused approaches effectively address the individual aspects of each solar cell type, we will be focusing on the important current transport phenomena in TFPV cells, which distinguish them from good quality c-Si cells. We choose the a-Si:H cells as our model system, as it is possible to solve the transport equations analytically for a typical a-Si:H p-i-n solar cell under reasonable assumptions, and this solution offers important insights into the various components and their dependencies.

In the following sections, we derive analytical expressions for the various current fluxes for a-Si:H p-i-n solar cells. This analysis also leads to correct expressions of the dark current components, and their relationship with surface and bulk recombination. Since, the transport equations cannot be solved analytically in presence of recombination, we adopt a first order perturbation approach (based on the carrier profile obtained for $R(x) = 0$ case). The detailed, step-by-step, derivation of IV characteristics is provided in Appendix A.

2.2.1 Solution without Bulk Recombination

For a p-i-n cell the drift-diffusion equations can be solved analytically in absence of bulk recombination, under the following assumptions:

(a) the thickness of i-layer is much larger than the p/n layers, i.e. $d \approx d_i$, where d_i is the thickness of i-layer;

(b) electric field inside the i-layer is constant and is given by $\mathcal{E} = (V - V_{bi})/d_i$, where V_{bi} is the built in potential;

(c) the generation rate can be approximated by a constant G_{eff} is constant across i-layer.

With these assumptions, the drift diffusion equations for electrons and holes become decoupled, and the resulting electron and hole profiles are a linear combination of the dark and generation dependent terms (see Eq. A.10). As a result the electron

and hole currents, and the total current, also separates into two terms namely, photocurrent (J_{photo}) and 'ideal' diode current (J_{D1}) components. See Sec. A.2 for the full derivation.

Dark diode current

As shown in Sec. A.2 of the appendix the solution of semiconductor equations in these yields an exponential diode current. The full expression obtained from this solution is given as,

$$J_{D1} = q\left(\mu_p \frac{n_i^2}{N_D} + \mu_n \frac{n_i^2}{N_A}\right)\left(\frac{(V - V_{bi})/d}{e^{(q(V-V_{bi})/k_B T)} - 1}\right)\left[\exp\left(\frac{qV}{k_B T}\right) - 1\right]. \tag{2.5}$$

Here, q is electron charge, N_D and N_A are the doping densities of n and p layers respectively, μ_n and μ_p denote the electron and hole mobilities, n_i is the intrinsic carrier density in a-Si:H, k_B is the Boltzmann constant, and T is absolute temperature. For $V < V_{bi}$, the middle term is close to 1, and the equation simplifies to familiar ideal diode equation (with ideality factor 1, and saturation current density J_{01}), i.e.

$$J_{D1} \approx \underbrace{q\left(\frac{D_p}{d}\frac{n_i^2}{N_D} + \frac{D_n}{d}\frac{n_i^2}{N_A}\right)}_{J_{01}}\left[\exp\left(\frac{qV}{k_B T}\right) - 1\right], \tag{2.6}$$

which is same as an ideal diode injection current [89] (black arrows in Fig. 2.3(a)). Note that this equation is exactly like the ideal diode equation, except the electron and hole diffusion lengths are replaced by the i-layer thickness. Equation 2.5 remains valid for $V > V_{bi}$, where the equation simplifies to a linear function of applied voltage

$$J_{D1} \approx \underbrace{q(\mu_n N_D + \mu_p N_A)}_{\sigma}\underbrace{\frac{V - V_{bi}}{d}}_{\mathcal{E}}, \tag{2.7}$$

as expected in the series resistance limited regime. We must emphasize that this current is due to intrinsic resistivity of a-Si:H layer, and external series must be accounted for separately.

Voltage dependent collection

As expected from the assumptions the dark current component does not change under illumination. The current under light is an algebraic sum of J_{D1} and a photocurrent term dependent on generation G_{eff} as,

$$J_{photo} = qG_{eff}d\left[\coth\left(\frac{q(V-V_{bi})}{2k_BT}\right) - \frac{2k_BT}{q(V-V_{bi})}\right]. \tag{2.8}$$

This shows that the photocurrent in an *ideal* (no bulk recombination) p-i-n cell is also voltage dependent [51]. This means that unlike crystalline cells, photocurrent in TFPV cells is fundamentally voltage dependent, and the only parameters affecting it are total generation and built-in potential. The reason behind this can be understood intuitively from magenta arrows in Fig. 2.3(a), which show that photogenerated carriers can either be collected by electric field, or jump over the diode barrier and recombine at the wrong contact. As the applied voltage increases, the built-in field reduces proportionally, and the fraction of carriers getting to wrong contact increases and the collection reduces. As the applied bias becomes equal to built-in potential V_{bi}, the photocurrent becomes zero, as there is no electric field to separate the photogenerated carriers. Above this voltage, the electric field inside the device changes sign, and the carriers flow to opposite contacts, resulting in a *positive* photocurrent. Note that this behavior of the voltage dependent collection of photocarriers also explains the widely reported dark and light IV crossover in thin film solar cells [90, 91]. Fig. 2.3(b) shows the calculated dark and photocurrent components, in relation to the total absorption current $qG_{eff}d$.

This result shows that superposition relation in Eq. 2.3 is not valid for a-Si:H cells, *even without any bulk recombination.* Although, the closed form expression in Eq. 2.8 is derived for a p-i-n cell; the photocurrent will always be voltage dependent for any solar cell which relies on electric field assisted collection of photocarriers. Because, in all such cells, the fraction of carriers going to the wrong contact, will increase with applied bias (see Fig. 2.3(a)). Since the electric field region in all TFPV

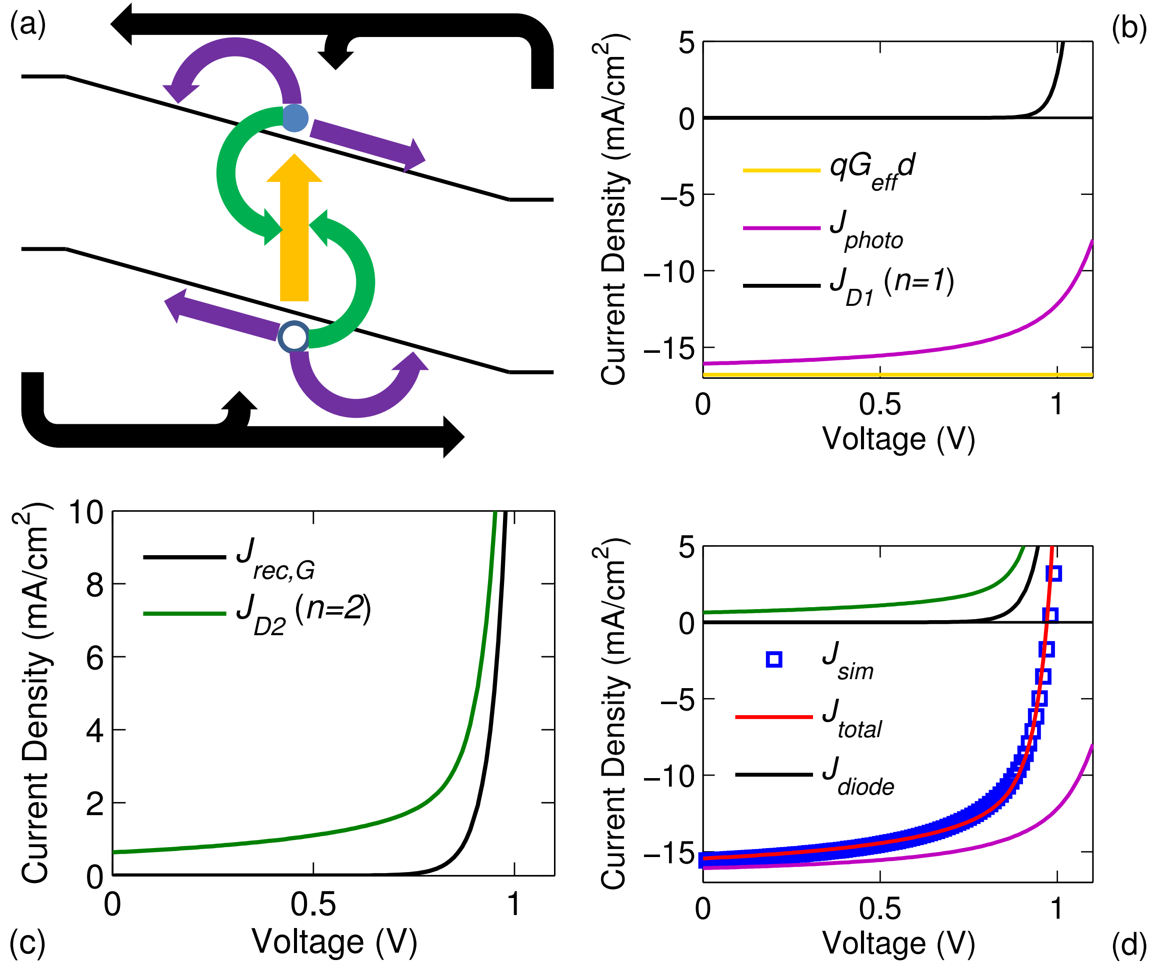

Fig. 2.3. (a) Schematic band diagram of an a-Si:H p-i-n solar cell, showing the various generation and recombination fluxes. (b) Photo and dark current components assuming no bulk recombination, showing that J_{photo} is voltage dependent even for this ideal case. (c) Recombination currents from first order perturbation, with the dark and generation dependent bulk recombination components. (d) The sum of all current components J_{total} closely matches the simulated IV (symbols) curve.

cells is either equal to or comparable to absorber layer thickness, all TFPV cells will exhibit a fundamentally voltage dependent photocurrent.

2.2.2 Calculation of Bulk Recombination Current

In order to incorporate the effect of bulk recombination we use the first order perturbation approach [76]. We get the electron and hole profiles from the exact solution obtained without recombination in the previous section, and calculate the recombination current [86] using

$$J_{rec} = \int_{0}^{d} R(x)dx. \tag{2.9}$$

With this method we can calculate the bulk recombination current in presence of light. In order to obtain useful closed form expressions, however, a further approximation of minority carrier dominated recombination in different regions is needed (see Sec. A.3 for details). With these approximations, the recombination current also separates into a generation dependent component $J_{rec,G}$ and dark a component J_{D2}.

Dark recombination current

The generation independent term of recombination current calculated from Eq. 2.9 can be approximated as

$$J_{D2} \approx \underbrace{q\frac{n_i}{\tau_{eff}}d\frac{2k_BT/q}{V_{bi}-V}}_{J_{02}} \exp\left(\frac{qV}{2k_BT}\right), \tag{2.10}$$

for $V < V_{bi}$, with saturation current density J_{02} and ideality factor 2. This dark current is very similar to bulk recombination current of p-n diode, and depends on the effective recombination lifetime τ_{eff} and width of depletion region d, which is equal to the thickness of i-layer, and slight modification due to constant electric field [89].

Generation dependent recombination

The other component of recombination depends explicitly on photogeneration, and for $V < V_{bi}$ it is approximated by

$$J_{rec,G} \approx \frac{qG_{eff}d^3}{4\mu_{eff}\tau_{eff}(V_{bi} - V)}. \tag{2.11}$$

This component depends on net generation G_{eff}, built-in potential V_{bi}, and effective mobility-lifetime product $\mu_{eff}\tau_{eff}$. As seen 2.3(c), the bulk recombination is enhanced by the generated carriers, and acquires another component under light. This is because, under illumination, the carrier densities inside the depletion region are enhanced significantly; and, consequently, the bulk recombination current ($\propto np/(n+p)$ in forward bias) also increases proportionally. In order to understand this result intuitively, we can reformat Eq. 2.11 as

$$J_{rec,G} \approx qG_{eff}d\frac{d/2}{2\mu_{eff}\tau_{eff}\mathcal{E}} = qG_{eff}d\frac{d/2}{2l_{drift}}. \tag{2.12}$$

This shows that the enhancement in bulk recombination due to photogeneration is proportional to total absorption ($qG_{eff}d$), as well as the ratio between i-layer thickness and twice the effective *drift length* of the carriers. The drift length in this case is defined as $l_{drift} = \mu_{eff}\tau_{eff}\mathcal{E}$, and denotes the distance traveled by photocarriers in presence of an electric field, before they recombine. Understandably, as the mobility-lifetime product of the material is improved, the carriers can travel farther and get collected with higher probability, therefore the recombination losses due to $J_{rec,G}$ would be lower, and vice versa. This result shows that the dark current ($J_{D1} + J_{D2}$) is not a complete representation of recombination under solar cell operating conditions.

Fig. 2.3(d) compares the light IV J_{Sim} of a-Si:H cells obtained from full device simulations using commercial TCAD program, with the derived compact model current J_{Total}; which is obtained by summing over the dark diode (J_{D1}, J_{D2}) and light ($J_{photo}, J_{rec,G}$) components. Note that for typical a-Si:H parameters, the compact model can accurately describe the intrinsic IV characteristics of the solar cell. Therefore, we can be confident that the approximations used for obtaining the analytical expressions are physically justifiable.

2.2.3 Poisson Equation under Light

In the preceding sections, we analyzed the modifications in carrier transport equations under illumination, and analyzed the dependencies of various current components resulting from them. Throughout that analysis, however, we had assumed that the Poisson equation remains unchanged under light and with changing bias. This is a significant approximation, which is not always satisfied in for different TFPV technologies. Relaxing these assumptions will result in the *dark* injection component ($J_{diode}(G,V)$) getting modified due to photogeneration.

Most thin film PV materials are deposited at low temperature, resulting in large defect density. With illumination the occupancy of these traps can change, and the corresponding change in charge density will modify the band profile [42, 78]. Also, due to the lower doping densities in many of these materials, injected charges at high applied bias or illumination can affect the band bending and result in the modification of injection current. Although important in analyzing thin film solar cells, these effects cannot be modeled analytically, and more detailed numerical simulations are needed to assess these effects on a case by case basis.

From the analysis in previous sections, we expect that the dark current in a p-i-n cell to be a combination of exponential diode currents $J_{D1} + J_{D2}$, with ideality factors 1 and 2, respectively. In practice, this is commonly approximated by a single exponential equation as

$$J_{diode} = J_0 \left[\exp\left(\frac{qV}{nk_BT} \right) - 1 \right], \tag{2.13}$$

and the diode saturation current density J_0 and ideality factor n are adjusted to account for the relative magnitudes of injection (Eq. 2.5) and bulk recombination (Eq. 2.10) currents. The relationship of J_0 and n to material parameters has been a subject of active investigation for a variety of TFPV technologies, and considerable progress has been made in this regard [92–96].

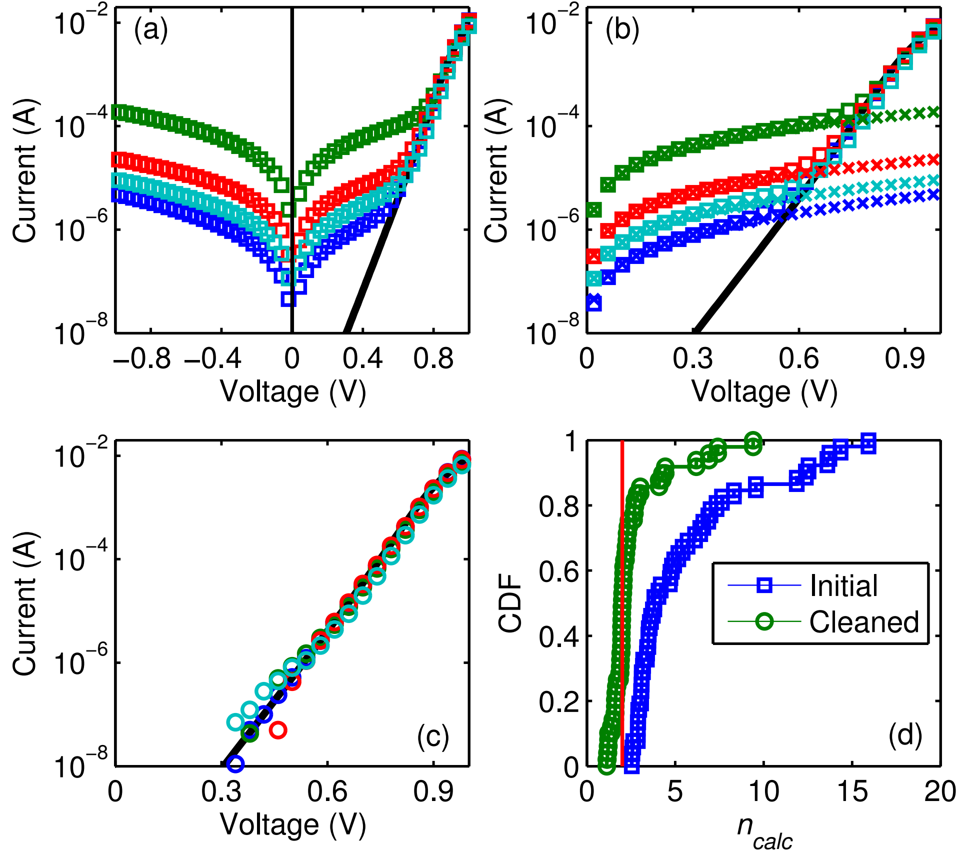

Fig. 2.4. (a) Plot of measured dark current for four nominally identical a-Si:H cells (symbols), showing excess leakage current in reverse and low forward bias region, which varies significantly for each cell, and deviates from the expected exponential diode current (line). (b) Plot of $|I_{dark}|$ vs. $|V|$ showing symmetric shunt current (crosses) overlaps the measured forward current (squares) for the same 4 cells. The deviation from expected I_{diode} (black line) at low biases is highlighted. (c) Cleaned forward current obtained after subtraction of the symmetric shunt current (circles) shows the expected exponential behavior (compare with line). (d) Empirical CDF comparing the calculated ideality factors n_{calc} before (squares) and after (circles) subtracting the shunt component, showing that cleaned n_{calc} values are closer to the expected value of 2 (red line).

2.3 Parasitic Shunt Current

The measured dark current in TFPV cells, however, deviates significantly from Eq. 2.13 at low forward and reverse biases, as seen in Fig. 2.4(a). Moreover, unlike

I_{diode}, the excess leakage at low biases fluctuates significantly from cell to cell, even when all cells are processed identically [73, 97, 98]. That is why, this deviation from exponential I_{diode} is generally attributed to an extrinsic parasitic shunt, and I_{dark} is represented as sum of I_{diode} and I_{SH}. We will focus on the electrical aspects of shunt conduction in this section, and explore the statistical nature of this magnitude fluctuation in detail in chapter 3.

2.3.1 Diode vs. Shunt Current Components

As apparent from Fig. 2.4(b), this shunt current is symmetric with respect to voltage, i.e., $|I_{SH}(V)| = |I_{SH}(-V)|$. Therefore, the forward and reverse bias current in shunt dominated regimes overlap when plotting $|I_{dark}|$ vs. $|V|$. While this is generally modeled using a parallel parasitic shunt resistance R_{SH} [84, 99]; for thin film solar cells I_{SH} shows a non ohmic voltage dependence [73, 100]. This non-Ohmic I_{SH}, however, remains symmetric with respect to voltage [73, 101].

We can use this voltage symmetry of I_{SH} to subtract out the shunt component and obtain the forward diode current, i.e. $I_{diode} \approx I_{dark} - I_{SH}$. We know that in reverse bias $|I_{dark}(V)| \approx |I_{SH}(V)|$ for $V < 0$, as $|I_{diode}(V)| \approx I_0 \ll |I_{SH}(V)|$ in reverse bias. From the voltage symmetry, we know that $I_{SH}(V) = |I_{SH}(-V)| \approx |I_{dark}(-V)|$, and therefore we can write $I_{diode} \approx I_{dark}(V) - |I_{dark}(-V)|$. Fig. 2.4(c) shows the I_{diode} for $V > 0$ obtained using this subtraction scheme. Note that the diode current so obtained, follows Eq. 2.13 very closely. Moreover, as shown in Fig. 2.4(c), the large spread in measured dark IV is also eliminated as soon as the shunt is subtracted out, as expected from I_{diode} of identically processed cells. We check the validity of this technique by applying it to measured dark IV of 50 identical cells. We compare the empirical ideality factors before and after the subtraction step to check its effectiveness. These empirical ideality factors are calculated as $n_{calc} = q\left(V_2 - V_1\right)/k_B T \ln\left(I_2/I_1\right)$, with V_2 =0.7 V and V_1 =0.4 V. Fig. 2.4(d) shows that for the raw $I_{dark}(V)$, n_{calc} lies between 3 and 16 for all cells, because the forward current

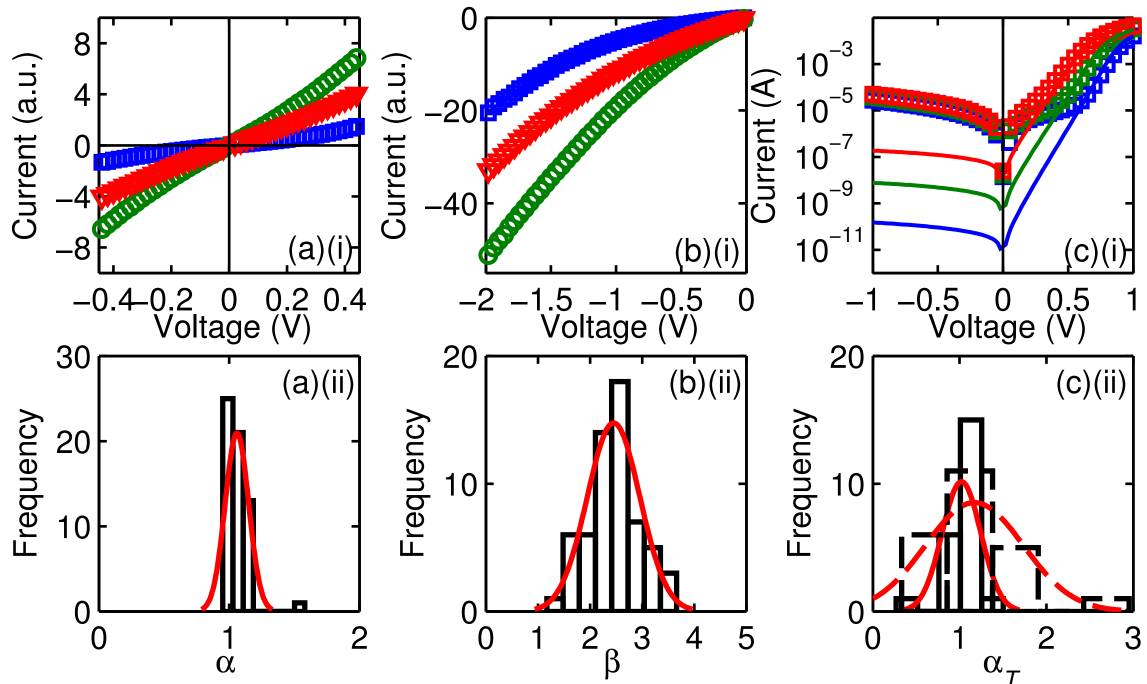

Fig. 2.5. (a) Symbols show the voltage symmetry of I_{SH}, for 3 cells (i) (scaled for clarity). (ii) The distribution of symmetry ratio $\alpha = I_{SH}(0.3V)/|I_{SH}(-0.3V)|$ for 60 identical cells. (b) (i) Non-Ohmic voltage dependence of shunt current for same 3 cells. (ii) the power exponent β for most of the 60 cells lies between 2 and 3. (c) (i) Temperature dependent dark IV (symbols), showing the weak temperature dependence of I_{SH} compared to activated diode current (solid lines). (ii) I_{SH} temperature coefficient $\alpha_T = I_{SH}(T_2)/I_{SH}(T_1)$ for T_2/T_1=85°C/45 °C (solid lines), and T_2/T_1=120 °C/45 °C (dashed lines) for 23 cells.

is corrupted by randomly varying I_{SH}. But once this parasitic shunt is subtracted off, 85% of n_{calc} values converge around 2, as expected for a-Si:H cells [102]. The deviation from 2 in the rest, is mainly to subtraction errors. An automated tool for dark IV analysis utilizing this subtraction scheme has been made available on nanoHUB [103].

2.3.2 Phenomenology of Shunt Current

The subtraction scheme is an elegant and robust technique for isolating the underlying device characteristics, by subtracting off the shunt component. Exploring the nature of shunt current itself, however, will allow a better understanding of this parasitic phenomenon. In order to do so, we begin by systematically observing the key features of shunt current.

Fig. 2.5(a)(i) shows the voltage symmetry of 3 identically processed cells, zoomed in and scaled for clarity. We verify this symmetric behavior by comparing the ratio $\alpha \equiv I_{dark}(0.3V)/|I_{dark}(-0.3V)|$, for 60 identically processed cells. Fig. 2.5(a)(ii) shows that this ratio is very close to 1 for all these cells, thus affirming the observation. We also find that I_{SH} has a non-Ohmic voltage dependence, as apparent from Fig. 2.5(b)(i), which shows the scaled $I_{dark}(V)$ ($\approx I_{SH}$ for $V < 0$) of the same 3 cells. In fact, we find that shunt current has a power law voltage dependence, i.e. $I_{SH} \propto V^{\beta}$, where $\beta \sim 2-3$. This is again a very robust trend, as seen in Fig. 2.5(b)(ii), which shows that $\beta \sim 2-3$ for 60 cells. Finally, I_{SH} also has markedly weak temperature dependence, compared to the temperature activated diode current component, as shown in Fig. 2.5(c)(i). Fig. 2.5(c)(ii) shows the temperature ratio $\alpha_T \equiv I_{SH}(T_2)/I_{SH}(T_1)$, for two different temperature ratios for 60 cells. This shows that the distinguishing features of I_{SH} are statistically robust and reproducible. Based on these observations we can construct a physical model of parasitic shunt current.

2.3.3 Space-Charge-Limited Model for Shunt Current

The symmetry, power law voltage dependence, and weak temperature dependence of I_{SH}, suggest that the most likely mechanism for shunt conduction is a Space-Charge-Limited (SCL) current [89]. SCL current occurs in a Metal-Semiconductor-Metal (MSM) structure, when both metal work functions are close, and allow only one carrier to be injection in the semiconductor, as shown in Fig. 2.6(a). In such cases the buildup of injected charge from the contacts modifies the internal electric field,

and results in a non-Ohmic current, so that $I_{SCL}^{ideal} \propto V^2$ [104]. For materials with shallow, exponentially distributed, traps the expression for SCL current depends on the density of shallow traps, and is written as [105],

$$I_{SCL} = \epsilon \mu_c(\gamma) A \frac{V^{\gamma+1}}{L^{2\gamma+1}}. \tag{2.14}$$

Here, ϵ is the material permittivity, μ_c is the carrier mobility, A is the cross-sectional area, and L is the film thickness. The parameter γ is a function of trap distribution inside the bandgap, and is usually between 1-2 [105, 106]. The expressions for SCL current in a defect free semiconductor (Mott-Gurney Law) [104], and for semiconductor with exponential distribution of shallow traps [107] are derived in Appendix B. It is easy to see that Eq. 2.14 can qualitatively capture the features of I_{SH} discussed earlier. The expression is symmetric in voltage, and the measured power exponent $\beta \equiv \gamma + 1$ is also in the expected range. Finally, note that the weakly temperature activated mobility μ_c is the only temperature dependent term in Eq. 2.14 [49,50,108]; which means that this equation can also capture the observed weak temperature dependence of I_{SH}. Therefore, we can write the shunt current in thin film cells, using the non-Ohmic relation

$$I_{SH} = I_{SH0} \frac{V^{\gamma+1}}{L_{abs}^{2\gamma+1}}; \tag{2.15}$$

where I_{SH0} denotes the shunt current magnitude depending on shunt defect area, and L_{abs} is the absorber layer thickness of the solar cells.

Formation of SCL Shunt Paths

In addition to explaining the shunt phenomenology, the SCL picture can also help in understanding the physical origin of I_{SH}. In case of a-Si:H cells, the most likely mechanism of shunt path formation is through contact metal diffusion into i-layer [72]. Aluminum is known to diffuse inside a-Si:H matrix at relatively low temperatures [109, 110], and it can counter dope the n-a-Si:H layer p-type [111]. The schematic in Fig. 2.6(b) shows one such possibility where a local metal incursion from the top contact results in a parasitic p-i-p path in parallel to the bulk p-i-n

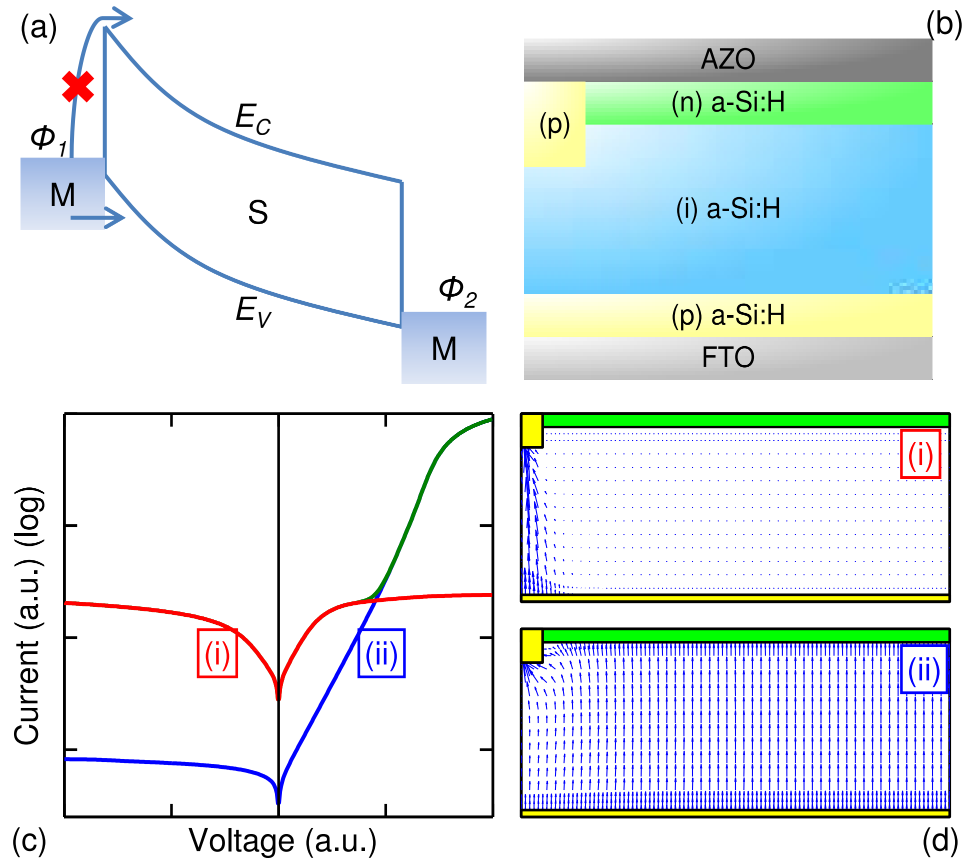

Fig. 2.6. (a) Symmetric MSM structure for SCL conduction showing single carrier (hole) injection. (b) Proposed localized parasitic p-i-p structure in otherwise ideal p-i-n structure. (c) Dark IV from the 2D simulation showing that the shunt (red), and diode (blue) dominate in different voltage regimes to give the total dark current (green). Quiver plots contrast localized current distribution in shunt dominated regime at low biases (i), with the uniform diode current conduction at higher biases (ii).

solar cell. Such a structure can form if the metal from top AZO contact diffuses past the thin ($\sim$10 nm) n-layer, or due to absence of n-doping locally. We can use 2D device simulations to explore the effect of such a parasitic path. Fig. 2.6(c) shows the simulated dark IV obtained by simulating the 2D structure in Fig. 2.6(b). Note that this structure with a local p-i-p path readily reproduces the qualitative features of measured dark IV, with the shunt and diode dominated regions. We can gain better

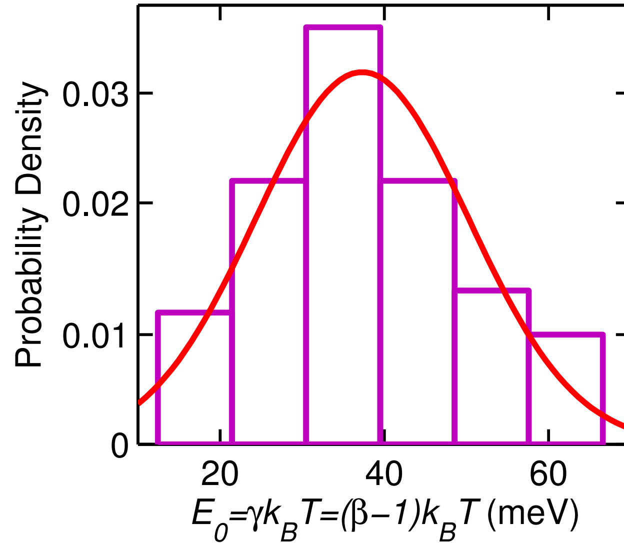

Fig. 2.7. Extracted characteristic slope of band tails E_0 is ∼40 meV for 61 devices, which is very close to the valence band tail slope in a-Si:H, as expected from the p-i-p shunt hypothesis.

insight into the current transport, by looking at the quiver plots of current density in Fig. 2.6(d). At low forward bias and at revers bias (Fig. 2.6(d)(i)), almost all current flows through the p-i-p region, because the diode current through the bulk is small. This current shows the SCL behavior expected from its symmetric structure, with only holes being injected in i-layer. As we increase the forward bias, the exponential diode current, through bulk p-i-n region takes over (Fig. 2.6(d)(ii)). These conduction paths are according to the observed shunt and diode like characteristics in Fig. 2.6(c). Besides providing the physical insight into shunt formation, Fig. 2.6(d) also shows that the shunt and diode current components are spatially isolated. Therefore, a computational simplification can be made by simulating 1D p-i-p shunt and p-i-n diode separately, and adding their respective contributions.

2.3.4 Single Carrier Injection

SCL conduction is a result of single carrier injection in the semiconductor layer [104, 105]. In case of a-Si:H cells, the proposed model for shunt formation suggests metal incursion from top contact, causing p-type counter-doping, and formation of a p-i-p shunt, as shown in Fig. 2.6(b) [72]. Therefore, in a-Si:H cells, only holes are injected in the shunt region, and will determine I_{SH}. We can indirectly establish the dominance of hole transport in I_{SH} by examining the voltage power exponent $\beta = \gamma + 1$. In materials with exponentially distributed shallow traps ($N_t = (N_{t0}/E_0)\exp((E_V - E)/E_0)$), it has been shown that the parameter $\gamma \approx E_0/k_B T$ [105], where E_0 is the characteristic energy of the exponential trap distribution, and E_V is the valence band edge. This feature of SCL current has previously been used to characterize the shallow band-tail states in a-Si:H [112]. Using this approach, we calculate the characteristic energy E_0 from the measured I_{SH} of 61 cells (Fig. 2.7), and find it to be ∼40 meV. This value is very close to the *valence* band tail slope in a-Si:H, suggesting that I_{SH} is mainly a hole current. Note that the characteristic slope of the valence band tail in a-Si:H is ∼40 meV, as opposed to the conduction band-tail slope of ∼20 meV [49, 113]. This affirms that the SCL shunt current is primarily caused by injection of holes in the i-layer, in accordance with the of the p-i-p shunt hypothesis [114].

2.4 Universal non-Ohmic Shunt Conduction

We have seen that parasitic shunt current in a-Si:H cells is likely to be caused by local metal incursion through the thin n-layer. This situation can potentially arise in all TFPV cells, owing to similarities in their structure and processing. All TFPV cells have a thin (∼10–100 nm) emitter layers deposited on the absorber to create the solar cells [39]. Moreover, the deposition of absorber as well as emitters are done at low temperatures over large area substrates [63, 115], leading to surfaces [45], and voids [111] or grain boundaries [116] in the material. Because of this, local

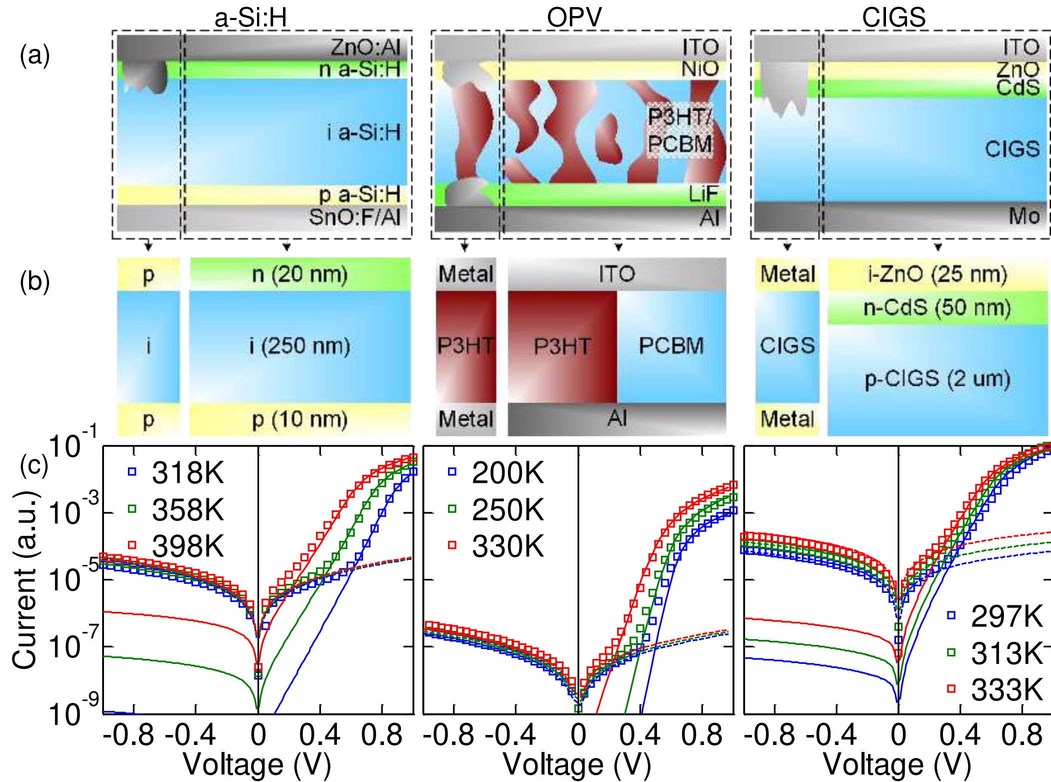

Fig. 2.8. (a) Schematics showing the likely shunt formation in a-Si:H, OPV and CIGS cells, due to contact metal diffusion through emitter. (b) From the localization of shunt current, we can separate the shunt and diode current paths, simplifying the 2D picture in part (a). (c) Simulations combining the 1D shunt in parallel to a diode for all 3 cell types, can reproduce the measured voltage and temperature dependencies, using typical material parameters.

shunt formation through metal incorporation through pinholes in emitter, or through contact metal diffusion, is quite likely.

Fig. 2.8 shows the schematic representation of local shunt paths formed due to metal incorporation through thin emitter layers for 3 different TFPV technologies. For a-Si:H we have seen that such local shunts give rise to *local* SCL shunt currents (Fig. 2.6(d)). Using this current localization, we can separate the diode and shunt current paths for all 3 types of cells, as shown in Fig. 2.8(b), and simulate the diode and shunt independently. Fig. 2.8(c) shows that such a 1D simulation of shunts and

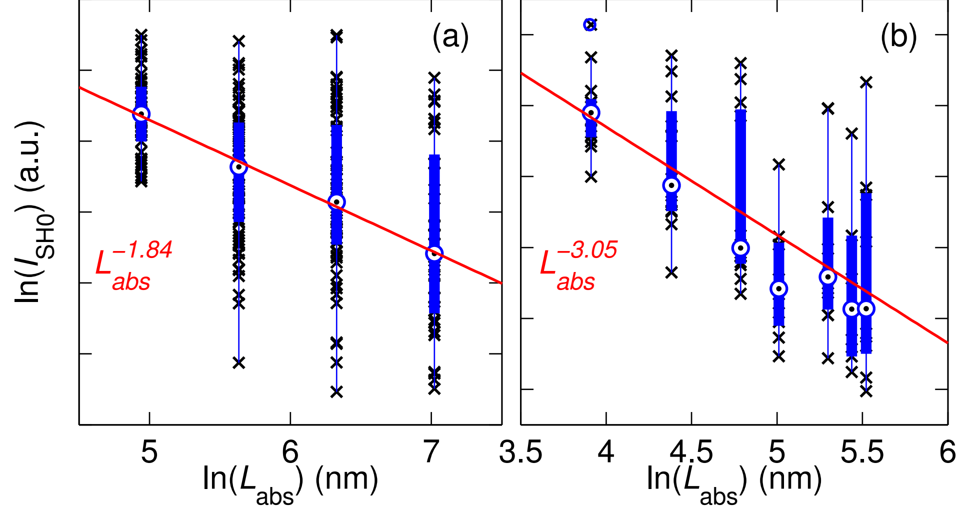

Fig. 2.9. I_{SH0} vs. L_{abs} plots showing the scatter plot of individual cell I_{SH0} values (black crosses) for (a) a-Si:H and (b) OPV cells. The overlaid box-and-whisker plots show the median (circles), interquartile range (blue bars), and min/max data values (whiskers) for each L_{abs}. The inverse power law (red line) holds true for mean of $\ln I_{SH0}$.

diodes separately, readily reproduces the observed voltage and temperature dependencies for all 3 TFPV technologies, *without requiring additional fitting parameters* [72]. This not only establishes the universal SCL features for shunt current in these different technologies, but also illuminates the possible cause of shunt formation in these cells. A detailed discussion and validation of universality of shunt characteristics can be found in [72].

2.4.1 Thickness Dependence of Shunt Conduction

In Sec. 2.3, we showed that shunt current varies significantly from one cell to the next. Understanding and accounting for this variability in shunt magnitude is essential for properly exploring the physics of shunt current. An important prediction of SCL shunt current model discussed in Sec. 2.3.3 is power law thickness dependence

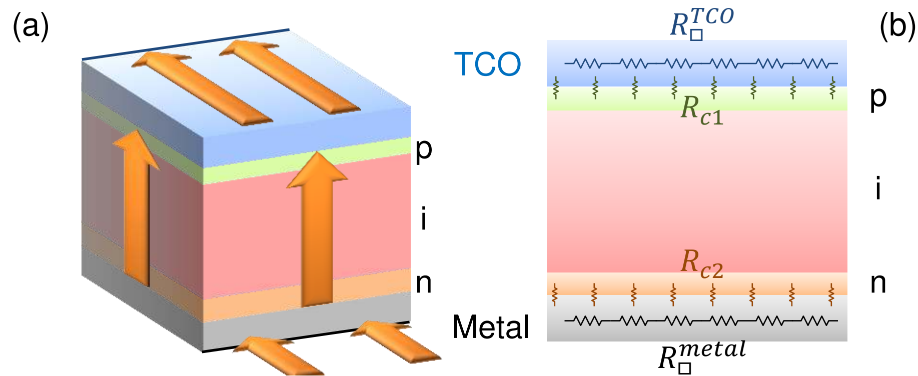

Fig. 2.10. (a) 3D schematic of current flow in a p-i-n solar cell, showing that the photocurrent (arrows) must flow laterally through the metal and TCO layers to reach the terminals. (b) Side view of the p-i-n cell, showing the external series resistance contributions due to contact resistances at the metal-semiconductor contacts (R_{c1} and R_{c2}), as well as the sheet resistance of TCO $R_{\square}^{TCO}$ and metal $R_{\square}^{metal}$ layers.

($I_{SH} \propto L^{-2\gamma-1}$). We now present *statistically robust* data that validates this prediction.

It is apparent from the SCL current expression in Eq. 2.15 that I_{SH} scales inversely with semiconductor layer thickness (L_{abs}) as a power law [105]. In order to check this prediction,we measured 356 a-Si:H devices with i-layer thicknesses 140 nm, to 1120 nm (89 devices each). For OPV cells, we measured devices with absorber thicknesses ranging from 50 nm to 250 nm, with 12-13 devices for each layer thickness. We then plot the distribution of extracted I_{SH0} values, in a box-plot shown in Fig. 2.9, along with the raw data of all I_{SH0} values (symbols in Fig. 2.9). Here, each cross represents the I_{SH0} of separate cell; and the box plot shows that the geometric mean of the I_{SH0} distribution for each absorber thickness follows the inverse power-law behavior [114, 117]. This trend is statistically robust for both a-Si:H and OPV cells, and therefore affirms the second major prediction of the proposed SCL shunt model.

2.5 External Series Resistance

The second important parasitic component in solar cells is external series resistance, which arises from the finite size of the cells. Because of this, the current must flow a certain distance before reaching the terminals, and the finite resistance of the contact layers then causes extra output power loss. Note that this series resistance is in addition to the intrinsic resistivity of the semiconductor layers under high forward bias, which was described in Sec. 2.2.

As shown in Fig. 2.10(a) for a p-i-n cell, the current generated in semiconductor layers is collected by metal and TCO contacts, and then flows laterally to reach the terminals. The contributions to external series resistance due to this distributed current flow are shown in Fig. 2.10(b), which distinguishes the contributions from contact resistances (R_{c1} and R_{c2}), and contact layer sheet resistances ($R_{\square}^{TCO}$ and $R_{\square}^{metal}$) to the total series resistances. The contact resistance is a distributed resistance arising from the metal-semiconductor or TCO-semiconductor junctions. The contact materials are often chosen because of their ability to minimize contact resistance. This is the determining factor in using Mo for CIGS [118], and Ni/Cu for CdTe cells [35].

The sheet resistance is often, however, higher, and limits the size of the solar cells used at the module level [21], as it arises from the lateral current flow in metal/TCO layers. For TFPV technologies, where at least one contact is always made from a transparent conductor (TCO), the TCO sheet resistance is the largest component of the overall series resistance, as for most TFPV technologies $R_{\square}^{TCO} \approx 10 - 20\ \Omega/\square$ and $R_{\square}^{metal} \approx 0.1 - 0.5\ \Omega/\square$. The TCO layers must fulfill dual purpose of high transparency at low resistivity, which makes design of transparent conductors a very challenging but active research problem [33, 119]. In some cases, where metal grids are used in addition to TCO layers, the additional resistance of grid lines must also be considered [120].

2.6 Thin Film Solar Cell Equivalent Circuit

The compact analytical expressions for the intrinsic and parasitic current components, discussed in the previous sections, allow one to create a physical equivalent circuit which can then be used in module level simulations. Fig. 2.11 shows the equivalent circuit for TFPV cells which accurately accounts for the intrinsic and extrinsic current components. The intrinsic elements are as follows:

- The voltage dependent photocurrent J_{photo} accounts for the loss of carriers at the wrong contact. It is given by Eq. 2.8 and depends only on generation G_{eff}, and built in potential V_{bi}.
- The generation dependent recombination current $J_{rec,G}$ accounts for the enhanced bulk recombination effect under light. It is given by Eq. 2.11 and depends on V_{bi}, G_{eff}, and net recombination, which is proportional to $\mu_{eff}\tau_{eff}$.
- The exponential dark current J_{diode} can be approximated by Eq. 2.13, with $1 < n < 2$. It is combination of minority carrier injection J_{D1} (Eq. 2.5), which depends on doping (N_A, N_D) and carrier mobilities (μ_n, μ_p); and bulk recombination J_{D2} (Eq. 2.10), which is a function of effective lifetime τ_{eff}.

This equivalent circuit also captures the extrinsic effects caused by shunt current and series resistances.

- The non-Ohmic parasitic shunt current discussed in Sec. 2.3, is incorporated by using a power law relation $I_{SH} = I_{SH0}V^{\beta}$ for shunt current.
- Finally, the external series resistance due to contact sheet resistance $(R_{\square})$ is incorporated in R_s.

2.7 Conclusions

In this chapter, we developed a consistent understanding of dark and light currents in TFPV cells. We began with a thorough analysis of photocurrent and dark current

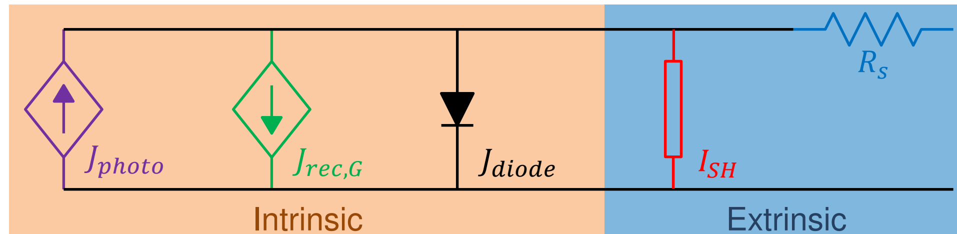

Fig. 2.11. Equivalent circuit incorporating the intrinsic (orange box) and extrinsic (blue box) current components. The intrinsic components include voltage dependent collection J_{photo}, generation enhanced recombination $J_{rec,G}$, and exponential dark current J_{diode}. And, the extrinsic components are represented by elements (I_{SH}) and series resistance (R_s).

components and their distinct dependencies, in an idealized cell with no parasitic elements. The next step was to isolate and analyze the non-Ohmic shunt conduction mechanism. Finally, these various conduction mechanisms were incorporated into a spice equivalent circuit, which can be used for module and system level circuit simulations. We can draw the following major insights from this chapter:

1. Intrinsic dark and light IV in TFPV cells

   (a) The photocurrent in a TFPV cell is not constant even for ideal no recombination case. Moreover, the bulk recombination is enhanced by photogeneration, and cannot be estimated by dark current alone.

   (b) In case of a-Si:H p-i-n solar cells, analytical expressions for these current components can be obtained, using a first order perturbation approach; which can reproduce the numerical simulations well.

2. Universal parasitic shunt current

   (a) The symmetric parasitic shunt current I_{SH} can be isolated from the intrinsic diode current I_{diode}, using a simple subtraction scheme. This enables more physical characterization of both current components, by avoiding mutual contamination of IV data.

(b) The parasitic shunt current in thin film cells has a symmetric non-Ohmic voltage dependence, and weak temperature dependence. These features are explained by a phenomenological SCL shunt current in parallel to the exponential diode current.

(c) This SCL shunt current behavior is identical across a-Si:H, CIGS, and OPV solar cells. The primary reason for this similarity is the thin emitter layers in these cells; which can allow the formation of parasitic MSM structures, resulting in an SCL shunt current.

(d) Single carrier injection, and power law thickness dependence predicted by SCL shunt current model were verified for a-Si:H and OPV cells, using statistically robust measurements.

(e) This characterization and modeling allows us to create a physics based equivalent circuit for a-Si:H cells, which can be used for accurate module level simulations.

In the next chapter, we analyze the variability and reliability issues associated with TF solar cells, and identify the sources of these problems.

3. VARIABILITY AND RELIABILITY IN THIN FILM SOLAR CELLS

In chapter 2, we analyzed the physics of as-fabricated thin film solar cells, including both the intrinsic and extrinsic (parasitic) components. We now turn to more practical issues encountered in producing and deploying this technologies. The first is performance variability in solar cells, due to a variety of parameter fluctuation from sample to sample [63]; and the other concerns long term reliability of the solar cell output, stemming from time dependent output degradation during operation [65]. These two aspects could be thought of as consequences of spatial and temporal fluctuations, for solar cells, respectively; and determine the practical utility of any technology under consideration. In this chapter, we will carefully analyze both these aspects, using detailed characterization, aided by tightly coupled simulations.

We begin by surveying the sources of variability in TFPV technologies, and classify them according to feature sizes. In Sec. 2.3, we had seen that the shunt current varies significantly from cell to cell, and the statistical fluctuation in shunts is also prominently reflected in the validation of SCL shunt model in Sec. 2.4.1. In this chapter, we build upon this aspect to establish a universal statistical model for shunt formation in TFPV and its origin in Sec. 3.1[1]. We then turn to performance reliability of TFPV in Sec. 3.3[2], by analyzing the solar cell degradation under reverse bias stress, and identify the degradation mechanisms for intrinsic and parasitic components separately.

[1]Text and figures in this section are taken from [117], Reproduced by permission of The Royal Society of Chemistry ©RSC 2013

[2]Text and figures in this section are taken from [121] ©IEEE 2011, [114] ©IEEE 2011, and [122] ©IEEE 2012

Table 3.1
A partial summary of performance variability sources in thin film solar cells.

	Intrinsic	Process
Macroscopic (∼m)	Composition variation [24]	Film thickness [123]
Mesoscopic (∼cm)	Parasitic shunting [117]	Scratches or dust [124]
Microscopic ($\sim \mu$m)	Grain Size Variation [125]	Micro-cracks [126]

3.1 Performance Variability in Solar Cells

All thin film solar cell technologies are use low temperature, large area deposition of active materials [63], in amorphous or poly-crystalline form [20]. These constraints mean that many material and device properties will fluctuate over the solar cell area, resulting in performance variation in the solar cells. Besides the material or technology specific variability sources, there are many which are common across all technologies. These can be classified according to their feature sizes as *microscopic* ($\sim \mu$m feature size), *mesoscopic* (≤cm feature size), or *macroscopic* (∼m feature size), and are summarized in Table 3.1. Some of these factors can be controlled with better process control; others, however, are *intrinsic*, and stem from the nature of thin film material or device itself.

The most prominent source of macroscopic process variations arise from the challenges of depositing thin films over large area ($\sim$ m^2 in area) substrates, for monolithic module production. This results in issues of film thickness variation [127], composition fluctuation in compound semiconductors [24], and sheet resistance variation in TCO layers [128]. Mitigation and control of these issues is an active area of research, as it directly determines the process yield, and is critically important of successful manufacturing of any PV technology.

At the mesoscopic level, performance fluctuations can arise from extrinsic fabrication issues like scratches of dust on the film surface, which lead to localized defect formation. These can be controlled with better cleaning and handling of substrates

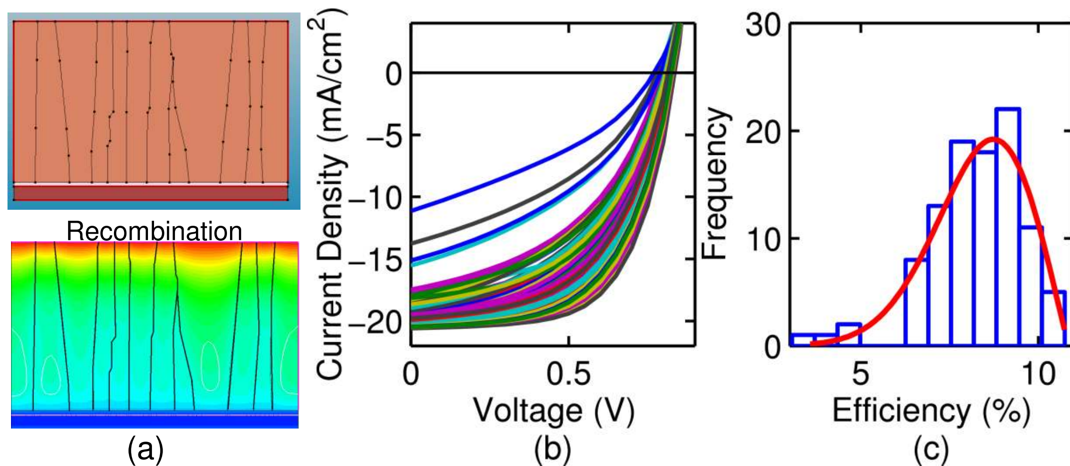

Fig. 3.1. (a) Schematic of a polycrystalline (CdTe) solar cell with multiple grains, and grain boundaries. The recombination profile for this structure is shown below, highlighting the impact of grain structure. (b) Simulation of 100 micro-cells (10 μm $\times$ 1 μm) with varying grain sizes obtained from full TCAD device simulation (after [129]). (c) The resulting efficiency distribution due to grain structure, shows a heavy tailed distribution.

and cells or modules. In addition to process induced defects, there are additional fluctuations caused by *intrinsic* parasitic shunting, due to SCL shunt paths as described in Sec. 2.3.3. These shunts are considered intrinsic because they arise from the morphology and material parameters of the semiconductor and contact layers, and are present even in cells with no visible defects like scratches or pinholes. The statistics of these intrinsic shunts, which results in large variations in I_{SH}, will be explored in detail in following sections.

At the other end of the spectrum, microscopic fluctuations can arise from thin film deposition on rough substrates, resulting in micro-crack formation in nc-Si:H films [126]. These can be alleviated with further process optimization. There are, however, other fundamental sources of variability, arising from grain size distribution in polycrystalline materials [125], phase separation in multi-phase systems [79, 130], or micro-voids during film formation [131]. These inherent sources of variation cannot be avoided by process improvement alone, because they are caused by thermodynamic

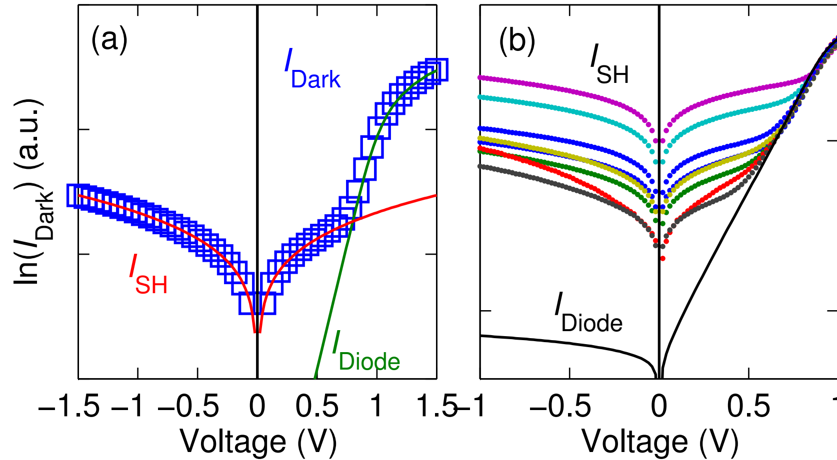

Fig. 3.2. (a) Measured I_{dark} (squares) can be represented by a parallel combination of diode with series resistance I_{diode} (green), and a parasitic shunt component I_{SH} (red), with a symmetric (around $V = 0$) non-Ohmic voltage dependence. (b) Measured dark IV characteristics of 8 a-Si:H solar cells (dots) on same substrate, fabricated under identical conditions, showing large variation in shunt current (near 0 V point), while the diode component is identical and matches the simulation (line).

constraints of film growth and nucleation. Fig. 3.1(a) shows an example simulation of a polycrystalline CdTe solar cell, showing the effect of grain structure on the recombination profile. A simulation of multiple micro-scale cells, with few grains shows a significant performance variation (Fig. 3.1). Consequently, the efficiency of the cells varies over 3% to 12%. These microscopic defects provide additional locations for SRH recombination, and cause efficiency loss in solar cells [79, 126] by increasing the dark diode current I_{diode} of the solar cells, but are not correlated with shunt current magnitude I_{SH} (see Fig. 3.2(a)).

Interestingly, due to the small size of these defects, however, their effect averages out over a larger ($mm^2 - cm^2$) area (to be discussed in Chapter 4), and their contribution to performance variation is small [129]. This is apparent from Fig. 3.2(b), which shows that for the 8 measured cells, the I_{diode} is virtually identical, while the shunt current varies over orders of magnitude. This fluctuation in shunt currents is due to

mesoscopic defects, like pinholes, etc. In this section, we will analyze the statistical nature of shunt formation in TFPV cells, for obtaining better understanding of their formation mechanisms.

3.2 Universal Statistics of Shunt Conduction

Shunt formation in solar cells is a universal challenge for achieving reproducible, good quality, cell performance. Therefore, shunt formation has been studied extensively in literature, and many physical phenomena responsible for shunt formation like, edge effects [123], material properties [132], or pinhole formation [133] have been identified. These efforts, however, have either focused on the empirical processing aspects [134], or have been used to identify individual shunt locations [133, 135–138], so that the nature of that defect region can be explored in detail. These have been used for identification of pinholes, or surface roughness related defects, as well as locations of hotspot formation [139–141]. In this section, we use a combination of these electrical and optical characterization techniques to identify the statistical nature of shunt formation in TFPV cells.

3.2.1 Shunt Magnitude Distribution

We saw in Fig. 3.2 that $|I_{SH}|$ varies over many orders of magnitude, from cell to cell. However, as seen in Fig. 2.7(b) the mean of $\ln(I_{SH})$ shows the expected power-law thickness dependence. This observation suggests that the statistics of shunt formation does not follow a simple Gaussian distribution, and probably belongs to some exponential type of distribution. In order to explore the actual nature of shunt statistics, we analyze the dark IV data for cells with typical structures. For evaluating the nature of their I_{SH0} distribution, we use statistically significant number of nominally identical cells for each technology (a-Si:H 89 cells, OPV 72 cells, CIGS 59 cells, and CdTe 23 cells). In Fig. 2.7, we saw that the mean of $\ln(I_{SH0})$ shows

the inverse power law relation to L_{abs} expected from the SCL model. This leads us to speculate that the shunt statistics may exhibit a log-normal distribution.

The cumulative probability for log-normal distribution is given as [142],

$$F_X(I_{SH0};\mu,\sigma) = \frac{1}{2}\left[1 + \mathrm{erf}\left(-\frac{\ln I_{SH0} - \langle I_{SH0}\rangle}{\sqrt{2}\delta I_{SH0}}\right)\right]. \tag{3.1}$$

On rearranging this we can write

$$\underbrace{-\sqrt{2}\,\mathrm{erf}^{-1}\left(2F_X - 1\right)}_{Y} = \underbrace{\frac{\ln I_{SH} - \hat{\mu}}{\hat{\sigma}}}_{\hat{X}}, \tag{3.2}$$

Note that if I_{SH0} follows a log-normal distribution, the scale variable $\hat{X}$ should exhibit standard normal ($\mathcal{N}(0,1)$) behavior. This can be checked using a quantile-quantile (QQ) plot, which shows the quantiles of data vs. theoretical quantiles from a hypothesized distribution. This means that if I_{SH0} is indeed distributed log-normally then the plot with quantiles of scaled variable $\hat{X}$ (see Eq. 3.2), vs. theoretical quantiles of $\mathcal{N}(0,1)$ distribution would give a straight line. Here, $\hat{\mu}$ and $\hat{\sigma}$ are the maximum likelihood estimates (MLE) of the mean and standard deviations of $\ln(I_{SH0})$, respectively.

Fig. 3.3 shows that the QQ plot of $\hat{X}$ vs. theoretical quantiles of $\mathcal{N}(0,1)$, shows a very good agreement with the hypothesized log-normal behavior, for all four technologies. The line shows that the best fit to scaled variable $\hat{X}$ for all technologies is a $\mathcal{N}(0,1)$ distribution, as expected for a log-normal distribution of I_{SH0}. Note that since $\hat{X}$ is on a log scale, this agreement with hypothesis actually extends over orders of magnitude in I_{SH0} values [117].

The standard errors in the MLEs of mean and variance of these scaled distributions, as shown in Fig. 3.3, are very small, lending credence to the hypothesis. Understandably, the standard errors (SE) in these estimates are larger for the CdTe data set because of its smaller size. A deviation from log-normal behavior is visible for the lower quantiles, most prominently for the CIGS data (Fig. 3.3(c)). This is a consequence of the fact that for very small values of I_{SH0}, the reverse current is determined by the reverse saturation current I_0, which manifests itself as an apparent

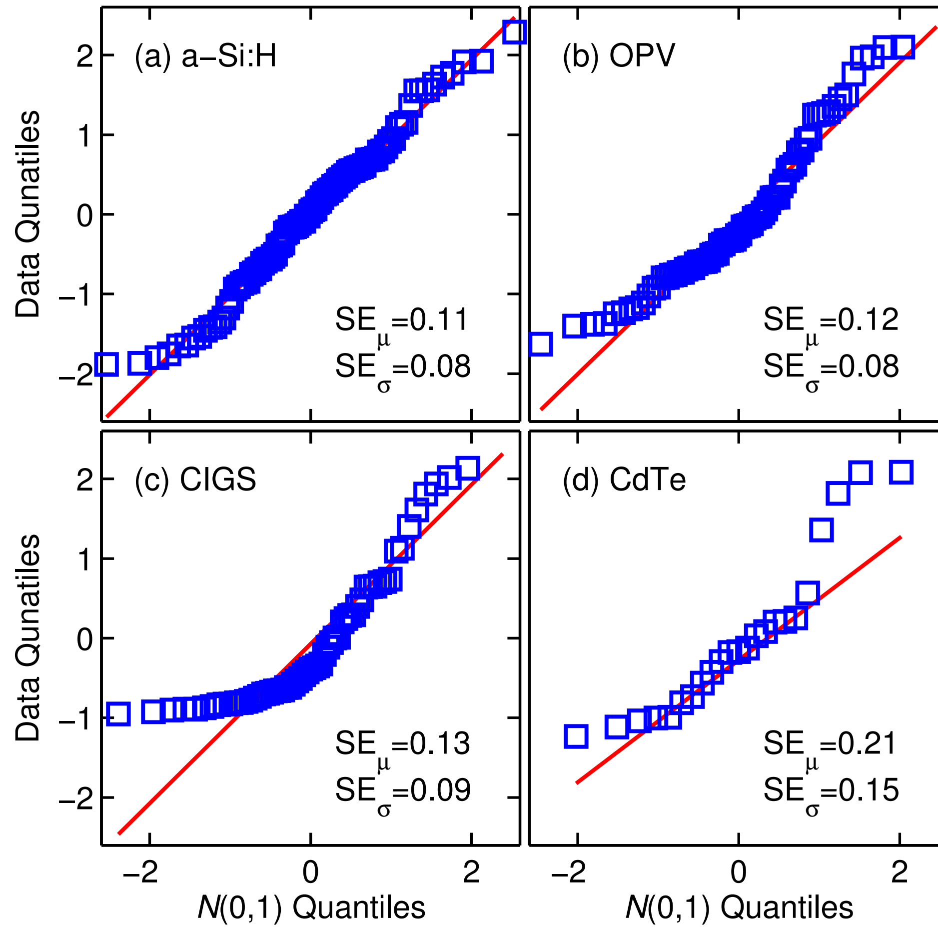

Fig. 3.3. QQ plots for $\hat{X}$ values for four different TFPV cells (symbols) show very good fit to the theoretical standard normal quantiles (red line) for (a) a-Si:H, (b) OPV, (c) CIGS, and (d) CdTe technologies. For all technologies, the MLE of mean $\hat{\mu}_X$, and standard deviation $\hat{\sigma}_X$ of the scaled variable $\hat{X}$ are 0 and 1, respectively, with standard errors of these estimates shown in insets.

minimum of I_{SH0} values. In order to affirm the log-normal nature of I_{SH0} distribution, we use goodness of fit tests and direct comparison of distributions to rule out other possibilities.

Kolmogorov-Smirnov Goodness-of-Fit Test

The Kolmogorov-Smirnov (KS) test can be used to compare the data to a hypothesized continuous distribution. The test checks the null hypothesis that the given data set comes from the hypothesized distribution. The test statistic for a data set with n observations is defined as $D_n = \sup |F_n(x) - F(x)|$, where F is the hypothesized CDF, and sup stands for supremum of the set of distances. The null hypothesis is rejected at a confidence level of (assumed 95% here) if

$$\sqrt{n}D_n > K_\alpha; \Pr(K \leq K_\alpha) = 1 - \alpha, \tag{3.3}$$

where K stands for Kolmogorov distribution [143]. Fig. 3.4(a) shows that when hypothesized distribution (F) is log-normal, the KS statistic ($\sqrt{n}D_n$) is smaller than the cut-off values (K_α) for all four technologies (except for CIGS where it is close). It shows that for all technologies except CIGS, the null hypothesis that the I_{SH0} distribution is log-normal cannot be rejected. While this gives more confidence in the nature of the distribution, we still need to eliminate the other likely heavy tailed distribution such as Weibull distribution.

Likelihood Ratio Test

In order to make a more direct comparison between the other possibility of a Weibull distribution, we use the likelihood ratio test [144]. The log-likelihood ratio $\mathcal{R}$, for n observations is defined as

$$\mathcal{R} = \ln\left[\prod_{i=1}^{n} \frac{p_1(x_i)}{p_2(x_i)}\right] = \sum_{i=1}^{n} \left[\ln(p_1(x_i)) - \ln(p_2(x_i))\right], \tag{3.4}$$

where p_1 and p_2 stand for the PDFs of two distributions under consideration. The sign of log-likelihood can be used to infer which distribution offers a better fit to the data; i.e., $\mathcal{R} > 0$ will imply p_1 is more likely than p_2, and vice-versa. To ensure that

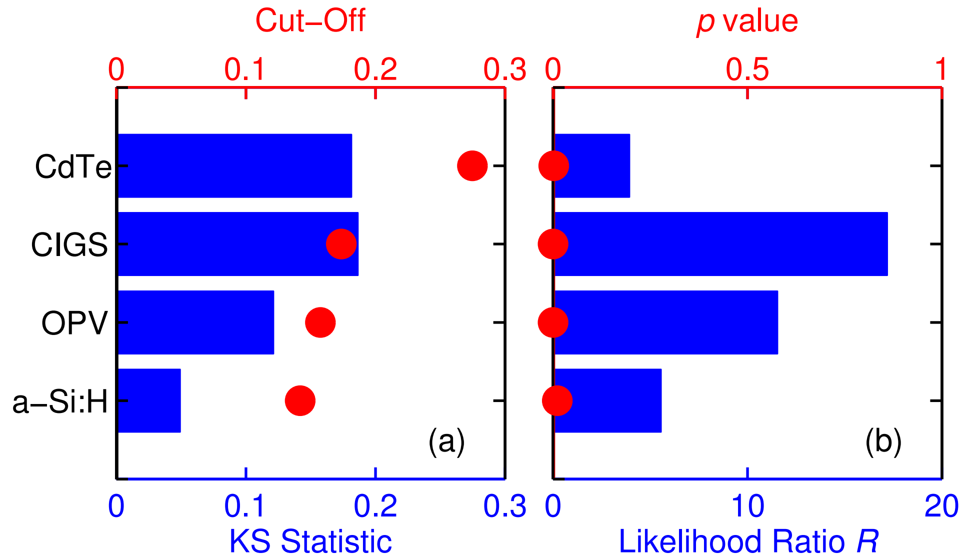

Fig. 3.4. (a) Calculated KS statistic (bottom) for the four data sets assuming log-normal distribution (bars), compared to the cut-offs (dots), showing that the log-normal hypothesis cannot be rejected at 95% confidence level. (b) Log-likelihood ratios (bars) comparing log-normal and Weibull distributions with MLE parameters, and corresponding p values (dots)

this statistic is not a result of statistical fluctuation we need to calculate the p value as

$$p = \mathrm{erfc}\left(\frac{|\mathcal{R}|}{\sqrt{2n}\sigma_l}\right), \tag{3.5}$$

where σ_l is the empirical standard deviation of this calculation. A large p value means that the sign of $\mathcal{R}$ could be a result of statistical fluctuation, and the test is not sufficient to distinguish between the two distributions. Fig. 3.4(b) shows the $\mathcal{R}$ and p values for all four data sets comparing log-normal and Weibull distributions. All data sets give a large positive value of $\mathcal{R}$, and all p values are close to zero, affirming the log-normal hypothesis. Based on the statistical analysis, we can be sure that the magnitude of shunt current follows a log-normal distribution for all four TFPV technologies. It is a remarkably universal trend, especially considering

the substantial differences between these technologies, ranging from cell structures, materials, fabrication processes, and even the variety of sources of these data sets.

3.2.2 Spatial Shunt Statistics

A closer investigation of shunt behavior is possible through imaging techniques, several of which have been developed over the years, including Dark Lock-In Thermography (DLIT) [145], Electro-luminescence (EL) [146], Photo-luminescence (PL) [147], among others. These methods allow us to identify the physical location of shunt defects on the cell surface. In this section we analyze the statistics of shunting, using imaging data from literature. This analysis provides an independent check for the shunt statistics obtained from electrical measurements.

In order to analyze the spatial aspects of shunt statistics, we will use data from DLIT imaging [136]. The DLIT technique takes thermal images of solar cells, when subjected to pulsed reverse bias under dark conditions. As bulk diode is "off" in reverse bias, only shunt paths conduct significant current, and the resultant local temperature rise due to Joule heating can be imaged using thermal imaging [148]. In this technique the local shunt paths appear as bright spots distributed across the cell surface [135, 149].

We use image processing techniques on these DLIT images to explore their statistical features. Fig. 3.5(a) shows a DLIT image for a-Si:H submodule from [150], showing the bright spots at shunt locations. The image is scaled to a unit square, for calculating the statistics. We transform this grayscale image to binary image with the bright spots represented by zeros (black patches in Fig. 3.5(b)). We can then count the number of pixels, and divide by total number of pixels in the image, to obtain the distribution of spot sizes normalized to unity. Another important statistic identifiable from the image is the location of these shunt paths. We define the shunt location as the centroid of each bright spot, shown with red stars in Fig. 3.5(c). We can then

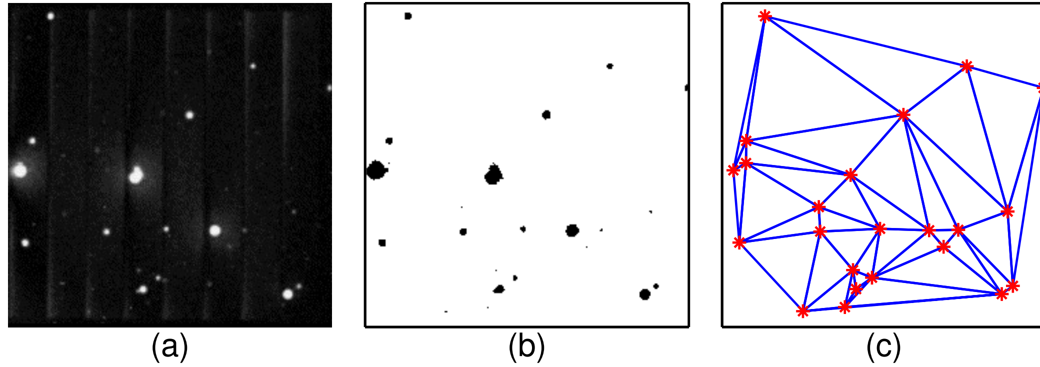

Fig. 3.5. (a) Original grayscale reverse DLIT image from [150] showing the bright shunt spots scattered across the cell surface. (b) The size of each bright spot can be calculated from this modified binary image which identifies the spots in black. (c) The location (centroid) of each spot (red stars) and some of their pairwise distances (lines) are also available, from the binary image.

calculate all their pairwise distances, shown with lines in Fig. 3.5(c). We show next that these size and position statistics show robust, technology independent, trends.

Validation of Log-normal Statistics

Fig. 3.6(a) shows the distribution of spot sizes obtained from a DLIT images of a-Si:H [150], CIGS [137], and even multi-crystalline Si [124]. Remarkably, the spot size distribution shows identical log-normal behavior for all technologies (Eq.3.2), despite the fact that these are fabricated using entirely different materials, processes, and structures. Moreover, note that the spot sizes are proportional to the local heat generation, which in turn is proportional to the local shunt current magnitude [136]. Therefore this log-normal spot size distribution correlates very well with log-normal magnitude of shunt current observed in electrical measurements on a-Si:H cells. Having seen the empirical evidence for shunt magnitude distribution, we explore the statistics of their locations next.

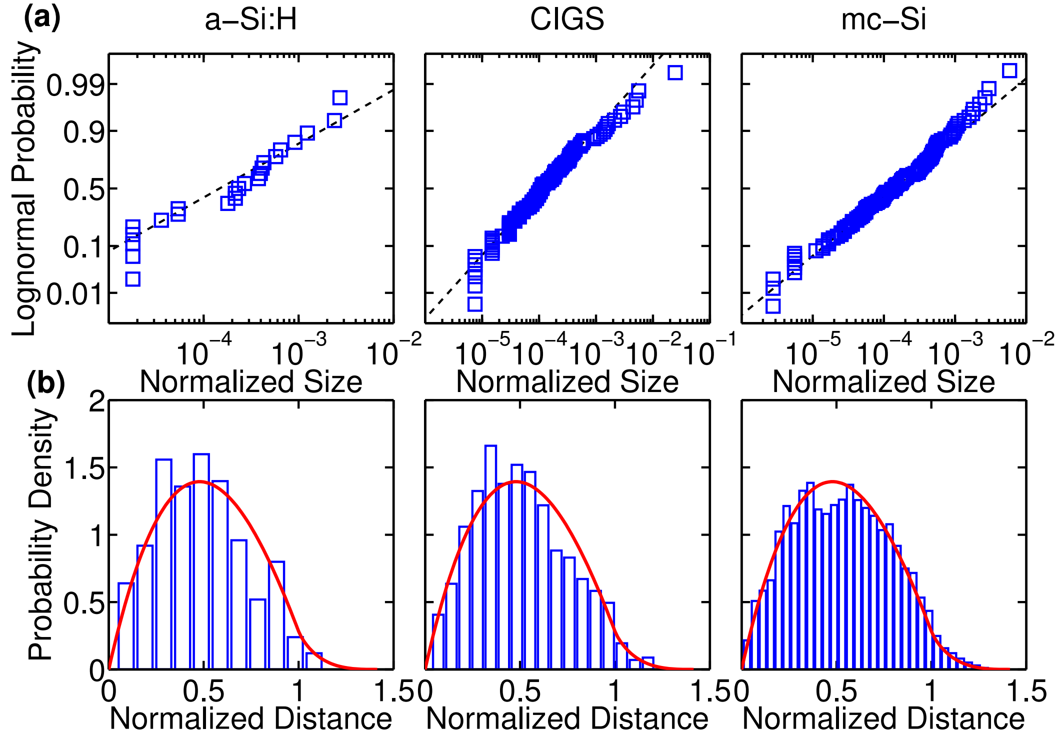

Fig. 3.6. (a) Normalized spot size distributions for DLIT images of a-Si:H [150], CIGS [137], and mc-Si [124] solar cells, from literature show same log-normal behavior. Normalized spot size is defined as $N_{pixel,spot}/N_{pixel,image}$. (b) The distribution of pairwise distances between spot locations, for same three images normalized to unit square (bars), closely follows the PDF obtained from a CSR process in a unit square (line), given in Eq. 3.6.

Position Statistics

Fig. 3.6(b) shows the probability density of the pairwise distances between the centroids (Fig. 3.5(c)), for all three cell types. This position statistics is also very similar for all cell types, and follows the PDF of a Complete Spatial Randomness (CSR) process [151]. Complete Spatial Randomness here refers to distribution of dots inside a unit square in (xy) plane, such that $x \sim \mathcal{U}(0,1)$ and $y \sim \mathcal{U}(0,1)$. For this CSR case, the PDF of pairwise distances between the dots d, defined as $d_{ij} = \sqrt{(x_i - x_j)^2 + (y_i - y_j)^2}$, is given by [152, 153],

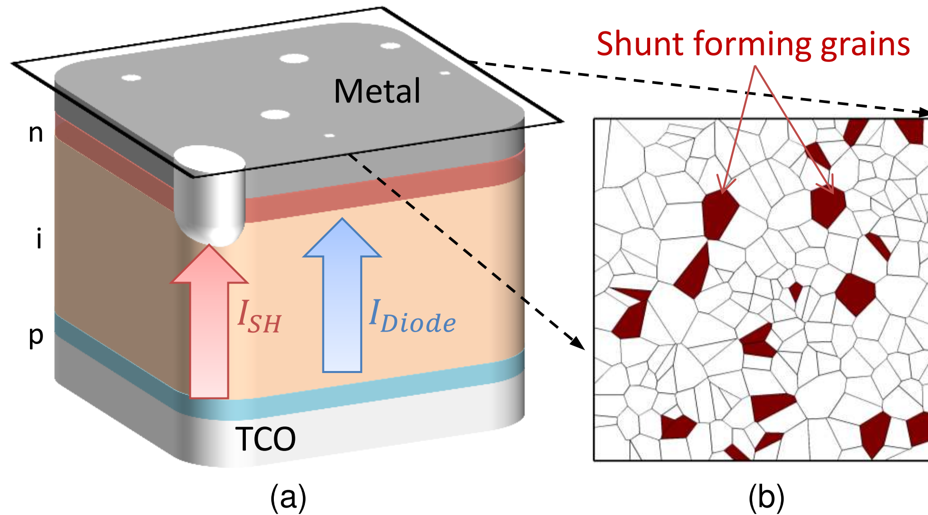

Fig. 3.7. (a) Schematic of parasitic shunt formation due to local metal incursion, resulting in parasitic MSM path for a-Si:H case, showing the shunt and diode current paths. Top view of solar cell with local shunts as seen in DLIT images, with the spots distributed on the surface. (b) Simulated grain structure for the top TCO layer, with the grains having high shunt formation probability highlighted in red.

$$f(d) = \begin{cases} 4d\left[\frac{\pi}{2} - 2d + \frac{d^2}{2}\right] & d \leq 1 \\ 4d\left[\sin^{-1}\left(\frac{1}{d}\right) - \cos^{-1}\left(\frac{1}{d}\right) - 1 - \frac{d^2}{2} + 2\sqrt{d^2-1}\right] & 1 < d \leq \sqrt{2}. \end{cases} \tag{3.6}$$

Fig. 3.6(b) shows that the empirical PDF follows the theoretical distribution given by Eq. 3.6 very closely, regardless of the cell type. This is a strong indication of uncorrelated shunt formation, which means that the formation of individual shunt paths does not affect the probability of shunt formation in its immediate vicinity [151]. This uncorrelated nature of shunt formation has very significant consequences for the gap between cell and module efficiencies, as discussed in following sections.

3.2.3 Origin of Universal Shunt Statistics

Based on the discussion in previous sections, we can arrive at the possible cause for these universal statistical features of shunt conduction in solar cells. It has been previously reported that shunt resistance in multi-crystalline silicon solar cells also shows a log-normal distribution [154], which we now show extends to TFPV as well. This remarkable universality of the statistics of shunt formation in solar cells leads us to believe that a common mechanism may underlie this behavior. It is well known that grain size (area) distribution in polycrystalline films is log-normal [155], regardless of the material of choice. Moreover, we note that while all TFPV cells use different absorber materials and processing techniques, the materials and deposition methods for contact layers are relatively similar (e.g., evaporation of TCO or metal layers), shown schematically in Fig. 3.7(b). In addition to this, the universal phenomenological SCL model of shunt conduction in TFPV cells also points to the role of contact layers in shunt formation [72]. This is also reinforced by the fact that interlayers, most notably in OPVs [156] and CIGS [157], are used for reduction of parasitic shunting (see Fig. 3.7(a)). Therefore, it is likely that the universal log-normal shunt statistics may be linked to the universal log-normal grain size distribution of metal/TCO layers (see schematic in Fig. 3.7(c)). A similar link may also be possible for multi-crystalline silicon, where shunt formation in mc-Si cells has been linked to impurity precipitates [145, 158]. A similar statistical analysis of I_{SH0} in other technologies, including mono-crystalline silicon, will help in narrowing down the possibilities in this regard. While more work is needed to establish this link quantitatively, we believe that the log-normal grain size distribution can be a good starting point for exploring the origin of this universal log-normal nature of shunt statistics.

3.3 Solar Cell Reliability

The next important challenge for a PV technology is its long term reliability, as it must survive under operating conditions for up to 25 years or more. In order to

Table 3.2
Partial list of relevant front end reliability issues in representative thin film PV technologies. The listed back end reliability issues are common to all PV technologies and concern module or systems level.

	Front End	Back End
a-Si:H	Light-induced degradation [159]	Glass fracture [160]
	Annealing instabilities [68]	Moisture ingress [161]
OPV	Phase segregation [162]	Delamination [163]
	Polymer oxidation [164]	TCO corrosion [161]
CIGS	Radiation instabilities [165]	Connector failure [65]
	Sulfur diffusion [166]	DC arcing [65]
CdTe	Copper diffusion [167]	Inverter reliability [168]
	Back contact stability [169]	Bypass diode failure [170]

predict the solar cell performance over such long periods, a deep understanding of the degradation mechanisms responsible for performance loss, as well as information about the operating conditions is essential. Owing to its importance, PV reliability at cell, module and systems level has been actively researched over the years.

The reliability issues associated with PV technologies can be classified as *back end*, which arise from issues with the passive elements in the module like encapsulation, sealant, glass, and frame materials. A Brief summary of these factors is provided in Table 3.2. As expected, these factors are usually common across all PV technologies, and depend on encapsulant materials (e.g., moisture, or delamination), or system components or setup (e.g., inverter reliability, and ground faults). Many of them lie under the purview of industries allied to PV namely, materials suppliers, and power system companies. Another common aspect of these issues is that they are determined or influenced by external factors, like humidity, wind, hail, snow, dust amongst others. Therefore, a significant effort in understanding or predicting these failure mechanisms involves weather modeling and prediction.

On the other hand, *front end* reliability issues arise from degradation in the solar cell active material directly. These reliability issues will be present even when the cell is operating under a hermetically sealed environment, because they arise from the degradation in active material directly. These issues are more fundamentally tied to the solar cell materials or structure, and must be solved for any PV technology before it can be commercialized. Understandably, these issues are typically technology, or material specific. See Table 3.2 for a representative list of front end reliability issues associated with TFPV technologies of choice.

3.4 Effect of Reverse Bias Stress in Thin Film Cells

In this chapter we focus on a front end reliability issue, arising from partial shading of PV modules under operation. This partial shading of the modules can result in shaded cells being reverse biased, and can cause permanent damage to the solar cells. In this aspect, partial shading is a module/system level, as well as cell level challenge. We will analyze the module level aspects of shading in greater detail in Chapter 4. Here, we focus instead on the effect of reverse stress caused by shading, on the performance of the solar cell itself. We will use careful characterization techniques to identify the reverse stress induced degradation in intrinsic and parasitic components alike.

We begin by analyzing the degradation mechanisms in a-Si:H solar cells, under moderate reverse stress voltages (¿ -10 V). We observe the time dependent degradation by subjecting the cells to long (up to 10^5 s) and constant reverse stress voltage (V_R), with periodic measurements of full dark IV to determine the stress effect. As shown in Fig. 3.8(a), the bulk diode current I_{diode} and parasitic shunt current I_{SH} increase significantly due to the stress (shunt and diode dominated regions of I_{dark} are highlighted). The degradation behavior of I_{diode} and I_{SH} can be monitored separately by observing reverse bias I_{dark} (as $I_{dark} \approx I_{SH}$ here), and *cleaned* I_{dark} in forward bias (as $I_{dark} \approx I_{diode}$ here). This allows us to identify and characterize the

degradation of these current components separately [171]. We identify two distinct mechanisms affecting the diode and shunt part separately, with different voltage and time dependencies as discussed next.

3.4.1 Diode Degradation Kinetics

We first focus on the degradation mechanism of diode current I_{diode}, and anlayze its time and stress dependencies. In order to identify the features in a robust manner, 22 devices were subjected to stresses ranging from -3 V to -7 V for a duration of 10^5 s each. Fig. 3.8(b) shows that time dependent increase in diode current $\Delta I_{diode}(t)$ for various reverse biases is described by robust power-law time dependence, i.e. $\Delta I_{diode} \propto t^{\alpha}$. The power exponent α of the power law is $\sim 0.2 - 0.26$, across 22 devices measured. The stress voltage acceleration of I_{diode} can be obtained from the pre-factor ($K(V_R)$) of the power-law fit ($I_{diode} = K(V_R)t^{\alpha}$) of the time dependent data. Interestingly, we find that the power exponent α is independent of stress voltage V_R (see top half of Fig. 3.8(c)) [121]. We find that the dependence of I_{diode} on stress voltage (V_R) is rather weak, but it approximately shows a linear dependence (bottom half of Fig. 3.8(c)). In order to explore diode degradation in greater detail, we measured 14 small area devices, which exhibited no shunt current ($I_{SH} = 0$). This allowed us to probe the diode current in the voltage range (-1 V to 1 V), without any contamination from I_{SH}. For these small area devices, we observe an asymmetrically high increase in I_{diode} at low biases (Fig. 3.8(d)). The current increase at low biases is much faster compared to higher biases, as apparent from the semi-log plot in Fig. 3.8(d). This is reflected clearly in the power exponent of $\Delta I_{diode}(t)$ at different values of measurement voltage V_m. The power exponent α decreases monotonically from about 0.95 for $V_m = -0.8$ V, to 0.25 for $V_m = 0.8$ V. Note that the power exponent value of 0.25 at measurement voltage of 0.8 V, obtained from these devices with $I_{SH} = 0$, coincides well with the power exponent obtained from the large area

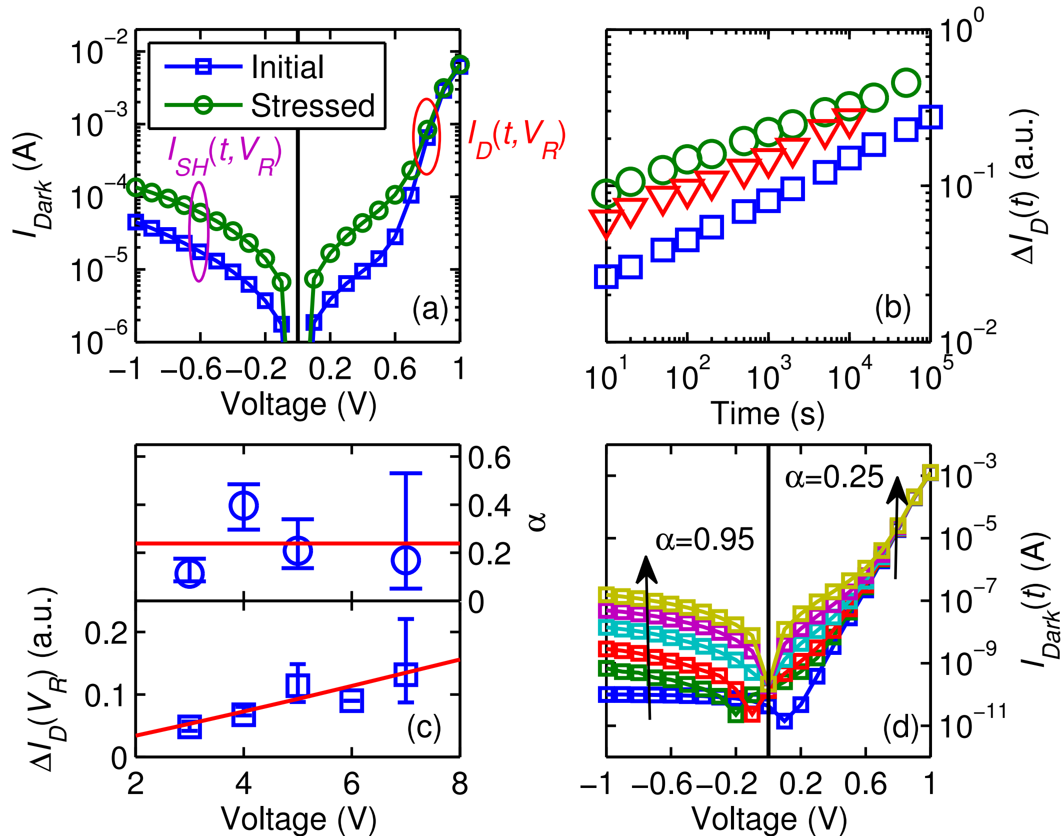

Fig. 3.8. (a) Initial (squares) and post stress (circles) dark IV, after a stress voltage $V_R = -5$ V has been applied for 10^4 s. Measured dark current I_{dark} increases with stress, both in $I_{SH}(t, V_R)$ dominated (highlighted magenta) as well as in the $I_{diode}(t, V_R)$ dominated (highlighted red) regimes. (b) Time dependent increase in I_{diode} under moderate reverse stress for 3 cells (symbols), shows a power law in time $\Delta I_{diode} \propto t^{\alpha}$ with $\alpha \sim 0.2 - 0.26$. (c)The power exponent of the time dependence is independent of stress voltage, but the voltage acceleration of diode current degradation has a weak linear dependence. (d) Time evolution of Dark IV at reverse stress of -5 V for 10^4 s, for a small area device with $I_{SH} = 0$, shows disproportionately high increase in the dark current at low biases, with power exponent of the power law degradation decreasing monotonically from $\alpha \approx 0.95$ to $\alpha \approx 0.25$ depending on measurement voltage.

devices through "cleaning" the shunt current. This underscores the usefulness of the cleaning technique in reliability characterization experiments.

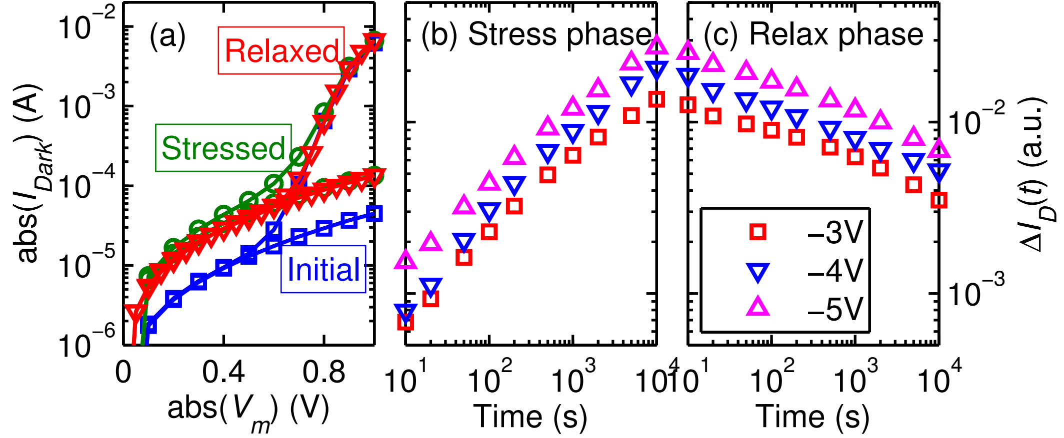

Fig. 3.9. (a) Pre-stress (squares), post-stress (circles) and relaxed (triangles) dark IV, showing that the diode current relaxes to its original with time, but the increase in shunt current is permanent. The stress (b) and relaxation (c) time dependencies of δI_{diode} show similar power law features with power exponent independent of stress voltage.

Another feature of the I_{dark} degradation is the distinct relaxation behaviors of diode and shunt current components. We find that diode current I_{diode} relaxes to its original value after extended storage in dark. The shunt current degradation on the other hand, appears to be permanent, as shown in Fig. 3.9(a) for the measured IV curves in pristine, stressed and relaxed states. Interestingly, the relaxation kinetics of I_{diode} also shows power-law time dependence, similar to the one observed for degradation kinetics, with similar time exponents and voltage acceleration factors (compare the behavior of Fig. ΔI_{diode} in Fig. 3.9(b) and (c)).

Diode current in a-Si:H cells is dominated by recombination in i-layer, as evident from the diode ideality factor close to 2 [94]. Therefore, it is likely that the parametric increase in I_{diode} is a consequence of parametric increase in midgap defect density in the i-layer [172, 173]. The similarity of reverse degradation kinetics to the kinetics of light-induced-degradation (LID) in a-Si:H solar cells [174], also suggests that a similar physical process may be responsible for reverse degradation. However, as apparent from Fig 3.8(d), the current increase at reverse and low biases is much larger than the

high bias regime. This asymmetry in the degraded diode current cannot be explained through increased recombination in the i-layer alone. Further experimental studies are required to clarify this degradation mechanism further.

3.4.2 Metastable Shunt Switching in a-Si:H

Unlike the parametric degradation and recovery kinetics of I_{diode}, shunt current shows an abrupt and non-volatile change on application of reverse stress [114]. Threshold switching of shunts in a-Si:H solar cells, under reverse bias, has been reported in the literature and is used in industry for *shunt busting* [175, 176]. This involves application of pulses of reverse voltage on finished cells, in order to reduce their net shunt current. However, our measurements show that this switching is actually *metastable*. We observe that during reverse voltage sweep, I_{SH} decreases abruptly by about 1-2 orders of magnitude (OFF transition), analogous to the shunt busting (see Fig. 3.10(a)). This change in the shunt current is nonvolatile during subsequent IV measurements. However, I_{SH} increases again (ON transition), after a subsequent reverse current sweep, and stays at the higher value thereafter. The abrupt transitions of I_{SH} during the two sweeps are shown in Fig. 3.10 (b). Both these metastable states of the shunt current are nonvolatile and remain stable for many days under room temperature storage.

In order to investigate the physical features of this switching behavior, we measured 16 nominally identical devices under reverse voltage and current stress. Consecutive voltage sweeps of -5 V, -6 V, and -7 V, and reverse current sweeps of 0.5 mA, 5 mA, and 50 mA were applied to all devices. Eight devices were subjected first to voltage sweeps followed by the current sweeps, and the other eight were stressed in the opposite order. The sweep rate was kept at the fastest possible, with the typical sweep time below 1 s (i.e., $>$ 10 V/s). Of the 16 devices measured, eight did not exhibit any switching transition in I_{SH} . For the other eight, which show metastability, the switching showed distinct dependences for ON and OFF transitions. We

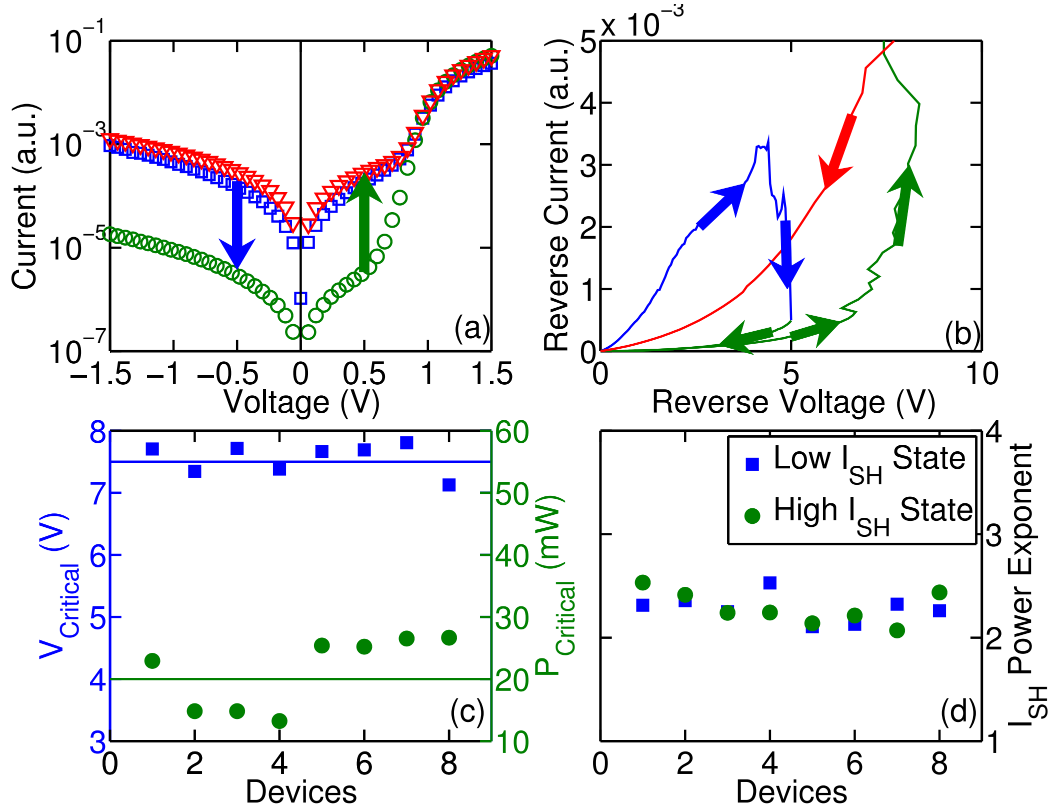

Fig. 3.10. (a) Initial dark IV characteristic (blue squares) switches to the low I_{SH} state after voltage sweep (green circles) and increases again after subsequent current sweep (red triangles). (b) Abrupt switching transitions during voltage sweep showing the OFF transition (blue) and current sweep showing the ON transition (red). (c) Scatter plot showing that the values of $P_{Critical}$ and $V_{Critical}$ are similar for eight devices. (d) Power exponent of the SCL shunt current β, in the high (after ON) and low (after OFF) shunt current states remains close to 2.5, showing that the SCL nature of shunt is preserved during the nonvolatile switching.

found that the decrease in I_{SH} (OFF transition) was determined by a power threshold $P_{Critical}$, and the increase in I_{SH} (ON transition) was triggered at a threshold voltage $V_{Critical}$. These thresholds were independent of the order of the sweeps (i.e., first voltage and then current, or vice versa). In Fig. 3.10(c), we show that the threshold voltage and power values for all the eight metastable shunts are ~ -7.5 V and ~ 20 mW, respectively. Finally, in Fig. 3.10(d), we compare the SCL power exponent β

of the shunt current in high and low-current states, respectively, showing them to be roughly equal. This shows that the SCL nature of I_{SH} shunts does not change before and after switching.

ON Transition

Note that the ON transition is a voltage (analogously electric field) driven process, as seen in Fig. 3.10(c). These observations suggest that the positively charged Al ions might be hopping through the Si matrix under the influence of the electric field and migrating into the a-Si:H layer. The voltage-driven contact metal migration in a-Si:H has been studied extensively for a-Si:H based nonvolatile resistive switching memories, as it forms the basis of their operation [177, 178]. Also, we know from Sec. 2.3.3, that only a small Al incursion of ~ 20 nm is sufficient to create the local shunt. As Al gets past the thin n-layer, it will destroy the n-i junction locally and form a p-i-p shunt, in place of a p-i-n diode (see insets in Fig. 3.11(a)). Correspondingly, the current in this local region will jump by many orders of magnitude. As shown in Fig. 3.11(a), the current increases by many orders, as a function of Al incorporation in a-Si:H layer. Therefore, we propose that the ON transition happens because of the formation of a new shunt path because of Al migration from the top AZO contact.

OFF Transition

Unlike the ON transition, the OFF transition is controlled by a power threshold, as seen in Fig. 3.10(d). This suggests that the most probable cause of the OFF transition is the dissolution of the small Al filament because of local heating. We discussed, in Sec. 3.2.2 , that the largest shunt path in a cell carries most of the current. Moreover, since the sweep rates are high, the local heating at the largest shunt can be significant. Fig. 3.11(b)(i) shows the 2D simulation of a p-i-n cell, with a p-i-p shunt at high reverse bias. As the reverse current is concentrated at local p-i-p shunt region, it leads to significant Joule heating in that region, leading

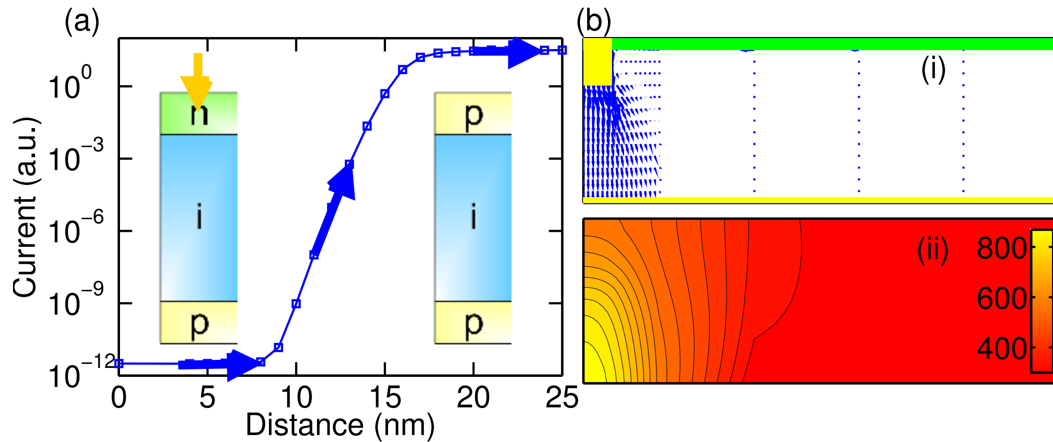

Fig. 3.11. (a) Simulation showing the change in reverse current at the location of shunt formation, as a function of distance of Al incorporation. As Al gets past the 20 nm n-layer, the current changes significantly Schematics in the inset show the corresponding transition from a p-i-n diode to a p-i-p shunt in the local region. (b) Self-consistent simulations of the 2-D shunt structure at reverse bias of -7.5 V, showing (i) localized shunt current and (ii) local heating effect (temperature scale in K) caused by the fast reverse sweep.

to a large temperature increase (see Fig. 3.11(b)(i)). Therefore, it is likely that the largest Al filament might dissolve/disperse at these temperatures, resulting in the OFF transition. And, due to the log-normal distribution of shunt magnitudes, the total current is then determined by the next largest shunt, which is 1-2 orders of magnitude lower than the original shunt current, resulting in the OFF transition.

3.4.3 Metastable Shunt Behavior in CIGS

We have also repeated the reverse stress measurement in CIGS cells, and found that they show similar metastable change in I_{SH} values on application of stress. We subjected 18 similarly processed cells to a 3 step measure-stress-measure cycle, with increasing reverse stress. The stress step involved a reverse voltage sweep with increasing magnitude (-2 V, -3 V, and -4 V). Each stress sweep was preceded and followed by a measurement step, in which the dark current (I_{dark}) was measured from

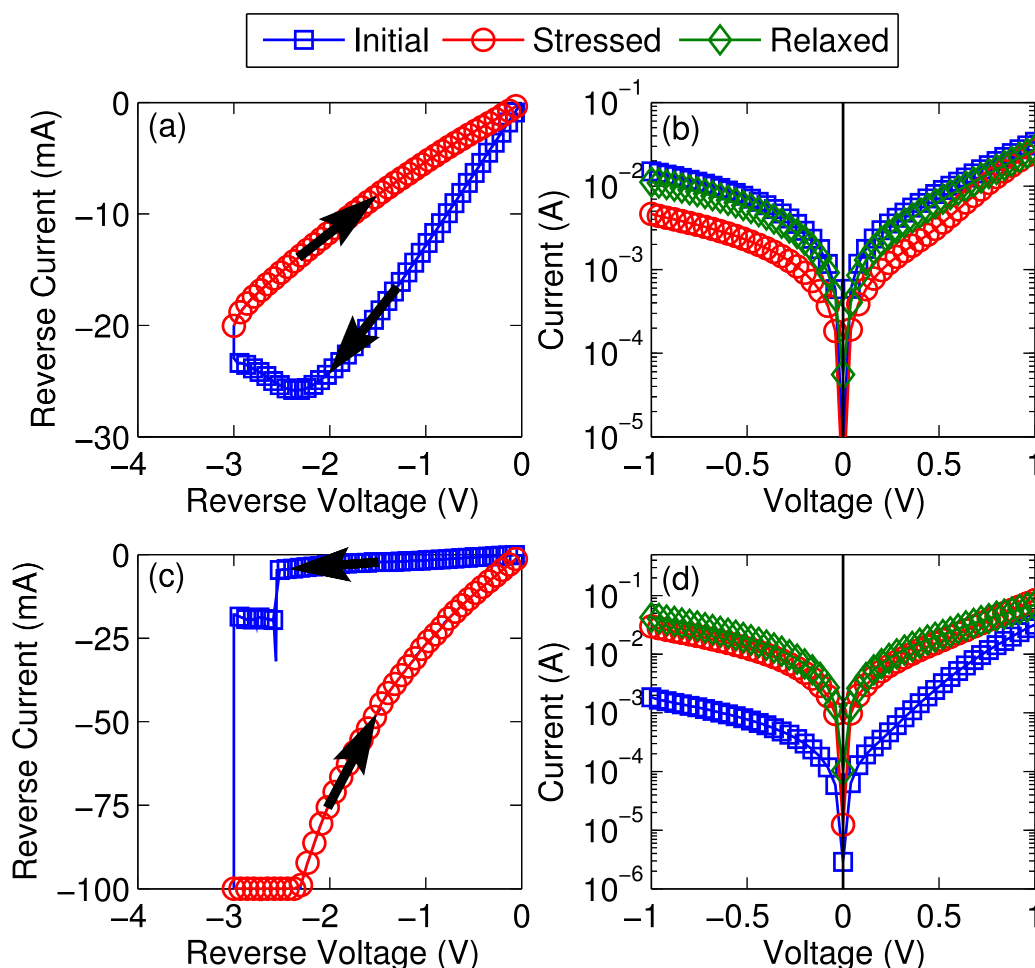

Fig. 3.12. (a) Reverse current hysteresis for 0 to -3 V sweep, showing reduction in dark current with stress (arrows show sweep direction). (b) Dark IV before and immediately after stress shows similar decrease. The dark IV, however, relaxes to its original value after storage in dark for extended period. (c) Similar reverse sweep to -3 V in another cell, results in abrupt *increase* in current, limited by compliance (arrows mark sweep direction). (d) Comparison of dark IV also mirrors the corresponding increase in current, but this increase in current does not relax to initial value even after extended storage. For all the plots, refer legend on top for reference.

-1 V to 1 V. Finally, the samples were allowed to relax in dark (without stress) for several weeks, and the dark and light IV were measured again to check if the observed

effects of stress are permanent. We find that characteristics of some cells revert to press-stress values.

Features of Switching Transitions

We observe that on application of reverse bias, the dark current shows pronounced hysteresis, and the current reduces by a factor of 2-3 as the bias is swept from 0 to -3 V, shown in Fig. 3.12(a). The effect of this reverse stress is also reflected in the low-voltage dark IV measured immediately before and after the stress, as shown in Fig. 3.12(b). We have used the cleaning method discussed in the last chapter, to isolate the diode and shunt components after each measurement step, and ensured that all changes observed with stress, are affecting the shunt component only. This is qualitatively analogous to the OFF transition observed for shunts in a-Si:H cells [114], and in non-volatile resistive switching memories (ReRAM) [179].

On the other hand, some cells show an abrupt increase in current on application of reverse bias. As shown in Fig. 3.12(c), the current jumps by about an order of magnitude during similar 0 to -3 V sweep. This change is also reflected in the low-voltage dark IV curves before and after the stress, which are compared in Fig. 3.12(d). We note that OFF transitions, where reverse current decreases are qualitatively similar for all samples, however, these OFF transitions are less abrupt compared to ON transition. Similarly, the ON transitions, where the increase in I_{dark} is very abrupt are also qualitatively consistent across different samples. This suggests that distinct physical processes are probably driving these transitions.

Difference from a-Si:H Switching

Unlike the shunt switching in a-Si:H case, which is nonvolatile for both ON and OFF transitions; the OFF transitions for CIGS are volatile, and I_{dark} increases to its original value after storage in the dark (see Fig. 3.12(b)); but the ON transitions remain nonvolatile (see Fig. 3.12(d)). In order to explore the relaxation behavior

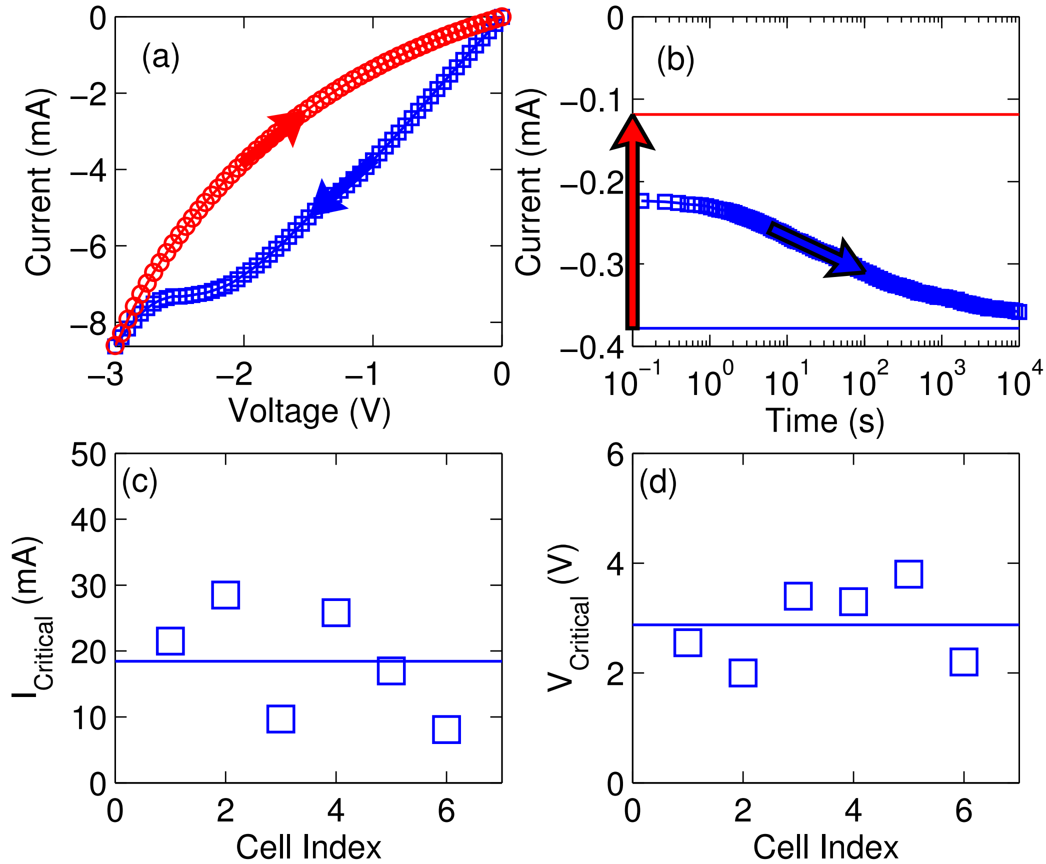

Fig. 3.13. (a) Stress IV for OFF transition, showing sweep direction, and the transient measurement points (circles). (b) Time-dependent relaxation of shunt current after stress shows a fast transient (<0.1 s), and a slow transient component ($\sim 10^4$ s), after which the current saturates close to its pre-stress value. Arrows show the direction of change in current with time.(c) Threshold current for OFF transition for all 6 cells is close to 20 mA. (d) The ON transition is voltage triggered, with a threshold voltage of about 3 V reverse bias.

after OFF transition, we performed transient measurements by observing the post stress reverse current as a function of time. This was done by observing the time dependent reverse current (at -0.1 V), immediately following the reverse stress sweep (Fig. 3.13(a)). Fig. 3.13(b) shows the reverse current transient after stress in perspective with the pre and post stress currents. It seems that the relaxation in I_{SH} after stress happens in two stages. The fast transient has a time constant <0.1 s and

recovers about half the change in I_{SH}. The slower transient, which is easily measurable, lasts for about 10^4 s, at the end of which I_{SH} recovers almost completely. These observations regarding the recovery kinetics suggest that the OFF transition is probably a result of charge trapping rather than trap generation because of the low to moderate time constant of recovery [180]. Moreover, the ON and OFF transitions show distinct current and voltage thresholds for switching. We found that all OFF transitions appear to be triggered at a reverse *current* threshold of approximately $20mA$ (Fig. 3.13(c)), while ON transitions are apparently controlled by the magnitude of reverse stress *voltage* with a threshold of approximately 3 V (Fig. 3.13). We note that this metastable behavior is most apparent in low to medium efficiency samples, which distinguishes these further from the switching behavior in a-Si:H cells.

3.5 Conclusions

In this chapter, we focused on analysis and quantification of important sources of variability and reliability in thin film solar cells. We used a-Si:H technology as our example case, but showed that most conclusions can be adapted for other TFPV technologies as well. For both variability and reliability analysis, we chose issues which have been overlooked traditionally, and provided solid experimental and theoretical framework for these problems. For the variability, we analyzed the problem of parasitic shunts, and established their universal statistical nature. In the next chapter, we will explore the implications of this statistical fluctuation on cell to module efficiency gap in TFPV technologies. In reliability, we focused on the effect of reverse stress on long term solar cell performance, and outlined the interesting physics behind degradation of various components under stress. This will inform our exploration of various aspects of partial shading in large area TFPV modules and systems, to be discussed in chapter 5. The key results from this chapter 5 can be summarized as.

1. Shunt variability in thin film solar cells

(a) The shunt current magnitude in a-Si:H, OPV, CIGS, and CdTe cells, exhibits universal statistical distribution from one cell to the next.

(b) We used statistical techniques to establish that this universal distribution in log-normal regardless of technology of choice.

(c) This log-normal shunt distribution is corroborated by independent analysis of optical imaging data, in which the spot sizes also show a log-normal distribution for different PV technologies.

(d) DLIT image analysis also shows that shunt formation is a Completely Spatially Random (CSR) process, implying that it is an uncorrelated process.

2. Reverse stress behavior of solar cells

(a) Diode and shunt current components of dark IV, in a-Si:H solar cells, show different degradation mechanisms with distinct stress and time dependencies.

(b) Diode current shows a parametric degradation and follows a power-law in time, most likely a result of increasing midgap defect density with time.

(c) The shunt current shows abrupt *metastable* switching on application of reverse stress, because of shunt formation and dissolution due to Al migration and local heating, respectively.

(d) Shunt current in CIGS cells also shows a metastable behavior under reverse stress, with statistically robust features.

(e) Shunt switching in CIGS differs from a-Si:H, as the OFF transition is volatile, suggesting different mechanisms responsible for shunt stress behavior.

4. CELL TO MODULE PERFORMANCE AND DESIGN

In the previous chapters, we analyzed the physics and statistics of thin film solar cell operation, variability, and reliability. We can now utilize this information to analyze the impact of these factors at module and systems level. In order to translate our understanding at the microscopic and mesoscopic level into module characteristics, however, we need a modeling approach which can scale to large size modules. Typical module are $\sim$m^2 in size, and are formed by connecting many small size cells in series (and parallel). Therefore, we need a more coarse-grained model, in which to embed the cell level physics and statistics. For this purpose, we use the solar cell equivalent circuit developed in chapter 2, and connect it in series and parallel to simulate large scale modules using SPICE circuit simulation.

In this chapter, we will analyze the effect of cell variability on the performance of large area cells and modules. We first analyze the effect of grain size fluctuations on a typical laboratory size cell in Sec. 4.1[1]. We then use the same approach in Sec. 4.3[2], to analyze the effect of shunt variability at the module level, and show how the parasitic shunt conduction is responsible for a significant portion of the efficiency gap between cell and module level. Finally, in Sec. 4.4[3], we describe an in-line, post-process technique of reducing the cell-to-module efficiency gap, by containing the effect of parasitic shunts.

4.1 Grain Variation and Cell Efficiency

In Sec. 3.1, we saw that the microscopic grain size variation in polycrystalline absorber layers like CIGS and CdTe, can lead to a significant performance variation.

[1]Text and figures in this section are taken from [129] ©IEEE 2013
[2]Text and figures in this section are taken from [181] ©IEEE 2012
[3]Text and figures in this section are taken from [182] ©IEEE 2013

In this section, we will use a hybrid device-circuit simulation approach to evaluate the effect of the grain size distribution in the absorber layer at cell level.

4.1.1 SPICE Simulation Setup

Simulating the effect of grain size distribution for a large cell, using a detailed physics based TCAD simulator becomes computationally expensive, as any laboratory cell with dimensions as small as 1 mm $\times$ 1 mm, will have more than $\sim 10^6$ grains. In order to assess the effect of grain sizes at cell level, therefore, we simulate a smaller cell (size 100 μm $\times$ 100 μm), by sub-dividing it into 1000 micro-cells, each 10 μm $\times$ 1 μm, shown schematically in Fig. 4.1(a,b). In this way, each micro-cell contains $\leq$ 10 grains on average, and is simulated using commercial Synopsys Sentaurus device simulator [129]. These detailed simulations, accurately capture the physics of carrier transport in these complex structures, as shown in Fig. 4.1(c). We generate 100 micro-cells with varying grain structures, obtained from reported distribution of grain sizes in literature [125]. A full device simulation of these micro-cells then results in 100 IV curves with varying efficiencies, as shown in Fig. 3.1(b). For simulating the cell IV, these are then connected in parallel, to form a circuit network representation of the cell, as shown in Fig. 4.1(d). Although, we need 1000 micro-cells to create the 100 μm $\times$ 100 μm cell, we can resample these 100 IV curves, to generate the 1000 micro-cell IVs required for the cell simulation, which reduces the computational expense by another order of magnitude.

Bootstrap Resampling of Micro-cell Data

In order to generate the required 1000 micro-cell IV curves, we use non-parametric bootstrap resampling with replacement [183], from the distribution of 100 micro-cell simulations. In the non-parametric bootstrap with replacement technique, a uniform distribution is assumed for the indices of the micro-cells. A random sample of 1000 is then generated from this uniform distribution with replacement, and the micro-cells

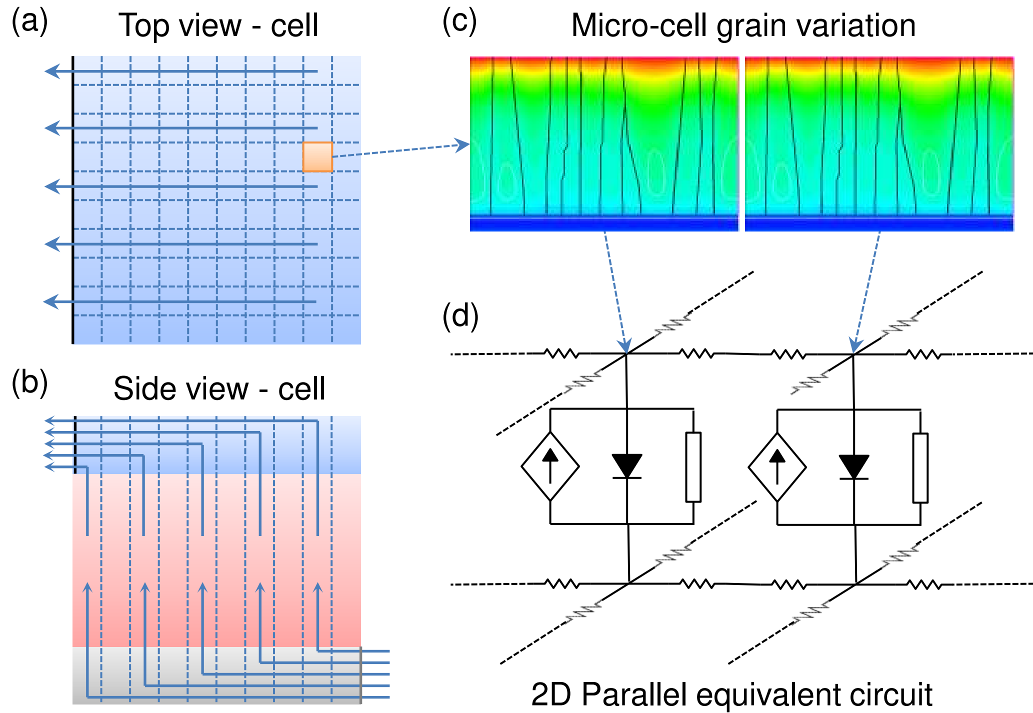

Fig. 4.1. (a) Top view of a typical lab scale cell showing the current flow towards the collecting terminal. This cell is sub-divided into micro-cells for simulating the grain size effect (dashed lines). (b) Side view of the cell, showing the current entering the bottom contact and leaving the top contact, with dashed lines showing micro-cells. (c) Each micro-cell (with a number grains) is simulated using detailed TCAD device simulations, which account for the electronic properties of bulk and grain boundary regions. (d) The resulting 2D mesh equivalent circuit representation of the cell, with each equivalent circuit representing one micro-cell.

in the circuit are placed according to the generated random indices. This ensures that the larger cell is formed from the simulated micro-cells only, and no statistical error is introduced by fitting the micro-cell characteristics for generating new random samples.

Micro-cell IV Characteristics

In this simulation scheme, we can represent the micro-cells using an equivalent circuit of choice; this, however, introduces extra fitting parameters. We, therefore, represent each micro-cell as a single voltage-controlled-current-source (VCCS). The voltage dependence of this VCCS element is given by a polynomial fit of the micro-cell IV characteristic obtained from device simulations. This ensures that each micro-cell is one circuit element, which contains all the physics of the grain structure, and no additional fitting errors are incurred by avoiding an equivalent circuit.

4.1.2 Cell Efficiency with Grain Variation

Once the cell equivalent circuit is setup, we can evaluate the effect of grain size distribution at the cell level. Fig. 4.2(a) compares the IV characteristics of micro-cells, and the large area cell obtained from the SPICE simulation. As expected the cell performance is somewhat in between the best and worst case micro-cells. Interestingly, however, we find that the cell efficiency is actually *exactly equal to* the mean efficiency of the micro-cells (see Fig. 4.2(b)). This is a consequence of the scale of grain variation. Since, the grains are a few microns in size, their individual current outputs are quite small. As a result, in a cell with multiple micro-cells, there is little voltage variation across the micro-cells, and almost all of them operate at the same applied voltage. In other words, the operation of the micro-cells is essentially independent of the behavior of its neighbors. This is why, a circuit simulation of cell performance in presence of grain fluctuation, results in an averaging of the micro-cell outputs.

Another consequence of this averaging appears in the statistical variation of cell performance itself. In order to evaluate this, we perform a Monte-Carlo simulation of cell efficiency, by generating 100 cell equivalent circuits, each with 1000 micro-cells, using the bootstrap resampling. The efficiency distribution of these cells is compared with the efficiency distribution of micro-cells in Fig. 4.2(c). Notice that due to this

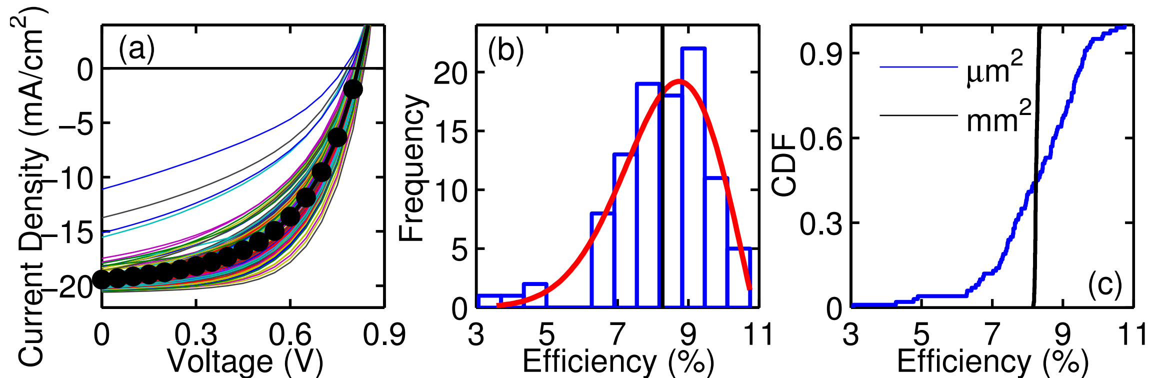

Fig. 4.2. (a) IV curves of the micro-cells (lines), compared to the cell IV obtained from the circuit simulation (circles), shows that cell performance is between the worst case micro-cells. (b) The cell efficiency (vertical line) is actually equal to the mean of micro-cell efficiency distribution (histogram). (c) CDF of cell efficiencies (black line), obtained from Monte-Carlo circuit simulations of $1mm^2$ cells, compared to the distribution of micro-cell efficiencies (blue line), shows that the effect of grain variability is averaged out for larger areas.

averaging of micro-cell characteristics, the cell efficiency distribution is very tightly centered around the mean value. This demonstrates that the grain size fluctuations at the micron scale cannot cause cell efficiency variation in relatively large area (mm^2–cm^2) cells. The observed variation in cell performance in experiments [125], therefore, must arise from other processing or material issues. This is also validated in our own measurements of dark IV (discussed in 3.1) where the diode component shows little variation across various samples.

4.2 TFPV Module - Effect of Sheet Resistance

So far, we have looked at the performance of individual cells at mm–cm scale. In order to extract any meaningful power output from a PV system, however, we need higher output voltages. This is accomplished by connecting many cells in series (each with typical operating voltage $V_{out} \approx 1$V), so that their output voltages add

up. The output current, on the other hand, is proportional to the total area of individual cells. Thus, it is easy to see that if a PV module of total area $A_{module} = L_{module} \times W_{module}$ consists of only 1 cell, the total output power in an *ideal* case will be $P_{out} = A_{module} \times J_{photo} \times V_{out}$. If this module is sub-divided into N_{series} cells which are connected in series (as shown in the schematic in Fig. 4.3(a)), the power output will remain unchanged as $P_{out} = (A_{module}/N_{series}) \times J_{photo} \times (N_{series}V_{out})$, assuming no area penalty for the creating the series connections.

Most TFPV technologies use a monolithic process for creating the series connected cells in the module. As shown in Fig. 4.3(a), this results in a module composed of N_{series} series connected rectangular cells, all of which span the width of the module W_{module}. The series connection is achieved by a successive deposition and scribing steps, using lasers, as shown in the side view cross section schematic in Fig. 4.3(b). This view shows the finite width of the scribed region which is responsible for the series connection as w_{dead}, because this region does not produce any power. The cell length of individual cell is shown as $l_{cell} = (L_{module}/N_{series}) - w_{dead}$. The arrows in Fig. 4.3(a, b) show the direction of current flow in the series connected configuration. In this arrangement, the current has to flow through TCO and metal layers to be collected at the edge.

4.2.1 Resistive Loss in Sheet Conductors

The schematic in Fig. 4.3(b) shows that for longer cell length (same as smaller N_{series}, because $l_{cell} = L_{module}/N_{series}$), the path length for current in the TCO and metal layers increases, resulting in higher resistance. In order to increase N_{series}, however, we need to create more scribe lines, resulting in increased dead area, as $A_{dead} = N_{series} \times (w_{dead} \times W_{module})$. In order to evaluate this trade-off we need to calculate the relative losses associated with sheet resistance, and dead area. Since the current flow in the TCO and metal layers is 2D, with photocurrent being injected at

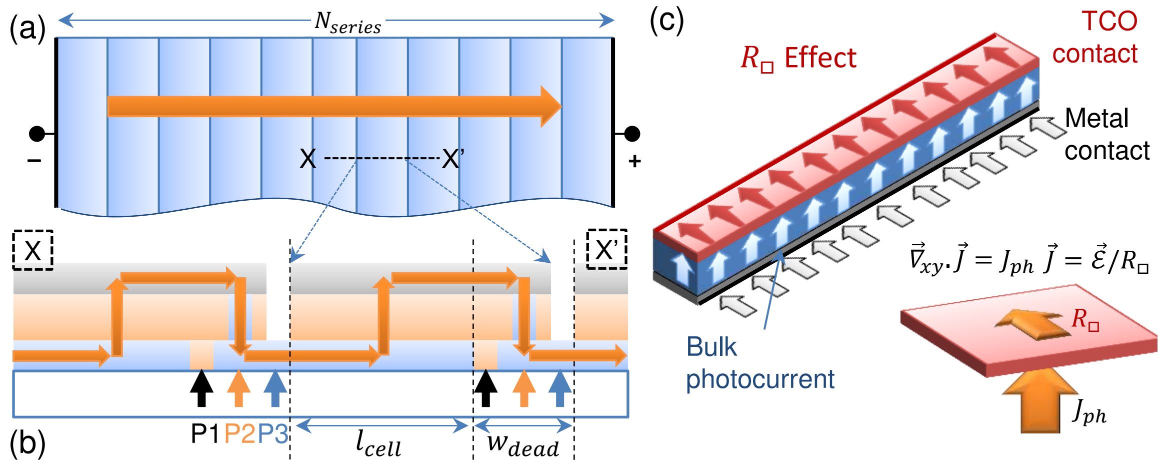

Fig. 4.3. (a) Top view of N_{series} rectangular series connected cells in a TFPV module, each of them with width W_{module}. (b) Side view cross section of the module, across the XX' axis, shows the series connection created through successive laser scribes (marked P1, P2, P3). The cell length l_{cell} and width of the dead region created by the scribes w_{dead} are also shown. (c) 3D schematic showing the current flow pattern in a typical cell, with current entering the bottom metal contact, and collected at the far edge of the top TCO contact. The other schematic shows the continuity equations to be solved in the TCO layer, when photocurrent is being injected at all points.

all points (as shown in the 3D schematic in Fig. 4.3(c)), we need to use the continuity equations to calculate the effect of current flow through sheet conductors.

Continuity Equation Formulation

In order to solve the current flow in sheet conductors rigorously, we need to solve a system of coupled equations, which account for the TCO and metal layers, with a forcing function given by voltage dependent photocurrent,so that

$$\begin{bmatrix} \vec{\nabla}_{xy}.\vec{J}_{xy}^{TCO} \\ \vec{\nabla}_{xy}.\vec{J}_{xy}^{metal} \end{bmatrix} = \begin{bmatrix} J_{photo}(\phi_{TCO} - \phi_{metal}) \\ -J_{photo}(\phi_{TCO} - \phi_{metal}) \end{bmatrix}. \tag{4.1}$$

Here, $\vec{\nabla}_{xy}$ is the divergence in 2D, $\vec{J}_{xy}$ is the sheet current per unit width (in A/cm), and J_{photo} is the photocurrent density in A/cm^2, which is being injected in plane at all points on the TCO or metal. This is a generalization of the distributed sheet resistance effect formulation reported in [184], and the details have been discussed in [185]. The negative sign of J_{photo} denotes current exiting the metal layer into the solar cell, and the positive sign reflects current entering the TCO layer from the solar cell. The local magnitude of the photocurrent is a function of local potential difference between the TCO and metal, as described by the solar cell IV characteristics.

This system of equations, however, is non-linear, and cannot be solved analytically for a completely general case with voltage dependent photocurrent at each point $J_{photo}(V, x, y)$. An approximate analytical solution, however, can be obtained with few reasonable assumptions namely, (a) The metal conductivity is significantly larger than that of the TCO, so that metal layer can be treated as an equipotential surface, and (b) the photocurrent is relatively voltage insensitive near the cell maximum power point (MPP), so that $J_{photo}(V_{mpp}) \approx J_{photo}^{mpp}$. For typical parameter values in TFPV technologies, these assumptions do not affect the calculations of current flow and power dissipation significantly (see [185] for further discussion). Under these assumptions, the equation for the 2D sheet current in TCO layer $\vec{J}_{xy}$ simplifies to

$$\vec{\nabla}_{xy}.\vec{J}_{xy} = J_{photo}^{mpp}. \tag{4.2}$$

We then write, $\vec{J}_{xy} = \sigma\vec{\mathcal{E}}_{xy} = \vec{\mathcal{E}}_{xy}/R_{\square}$, where $R_{\square}$ is the sheet resistance of the TCO layer. Finally, expressing the 2D electric field as $\vec{\mathcal{E}}_{xy} = -\nabla_{xy}\phi$ in terms of the potential $\phi(x, y)$, we get

$$\nabla_{xy}^2\phi = -J_{photo}^{mpp}R_{\square}. \tag{4.3}$$

This equation can be solved to get the potential/field profile across the TCO layer, and the resistive power dissipation in the layer can then be calculated as

$$P_{\square}^{dis} = \int_{A_{cell}} \vec{J}_{xy}.\vec{\mathcal{E}}_{xy}dS = \int_{A_{cell}} |\vec{\mathcal{E}}_{xy}|^2/R_{\square}dS, \tag{4.4}$$

where $\int_{A_{cell}} dS$ denotes the surface integral over the entire cell area A_{cell}.

Sheet Conduction in Rectangular Cells

For typical rectangular cells described in Fig. 4.3, the simplified continuity equation (Eq. 4.3) can be solved analytically to obtain the 2D potential and electric field, using the right boundary conditions. For the cell structure shown in Fig. 4.3(c), we fix the voltage at the current collecting edge (Dirichlet condition, so that $\phi(x, l_{cell}) = \phi_{cell}^{mpp}$), for a cell biased at its MPP voltage. All other boundaries are at open circuit (Neumann condition, so that $\vec{J}_{xy}(x, 0) = 0$ etc.), as shown in Fig. 4.4(a). The solution to Eq. 4.3 in this case is given by

$$\phi(x, y) = -\frac{J_{photo}^{mpp} R_{\square}}{2} y^2 + Ay + B, \tag{4.5}$$

where A, and B are the constants of integration, to be determined by the boundary conditions. From Eq. 4.5, we get $\vec{\mathcal{E}}_{xy} = -\nabla_{xy}\phi = (J_{photo}^{mpp} R_{\square} y + A)\hat{y}$. Applying the boundary condition at $y = 0$, we get $\vec{J}_{xy}(x, 0) = \sigma\vec{\mathcal{E}}_{xy}(x, 0) = 0$, which gives $A = 0$. The result is plotted in Fig. 4.4(a) on a color plot, showing increased dissipation near the current collecting edge at the top. Now, we can use Eq. 4.4 to get the total resistive power dissipation as

$$\begin{aligned} P_{\square}^{cell} &= \frac{1}{R_{\square}} \iint_{0,0}^{w_{cell}, l_{cell}} {J_{photo}^{mpp}}^2 R_{\square}^2 y^2 dxdy \\ &= \frac{{J_{photo}^{mpp}}^2 R_{\square} w_{cell}}{3} l_{cell}^3 = \frac{{J_{photo}^{mpp}}^2 R_{\square} W_{module}}{3} \frac{L_{module}^3}{N_{series}^3}. \end{aligned} \tag{4.6}$$

This equation is obtained by using $w_{cell} = W_{module}$, and $l_{cell} = L_{module}/N_{series}$. Finally, the total resistive power dissipation in a module with N_{series} identical series connected cells is then $P_{\square}^{mod} = N_{series} \times P_{\square}^{cell}$.

4.2.2 Optimized Series Connected Module

From the previous section, it is clear that increasing the number of cells in a module will reduce the resistive power losses because $P_{\square}^{mod} \propto N_{series}^{-2}$ from Eq. 4.6. This requires higher number of scribe lines of finite width w_{dead}, which will increase

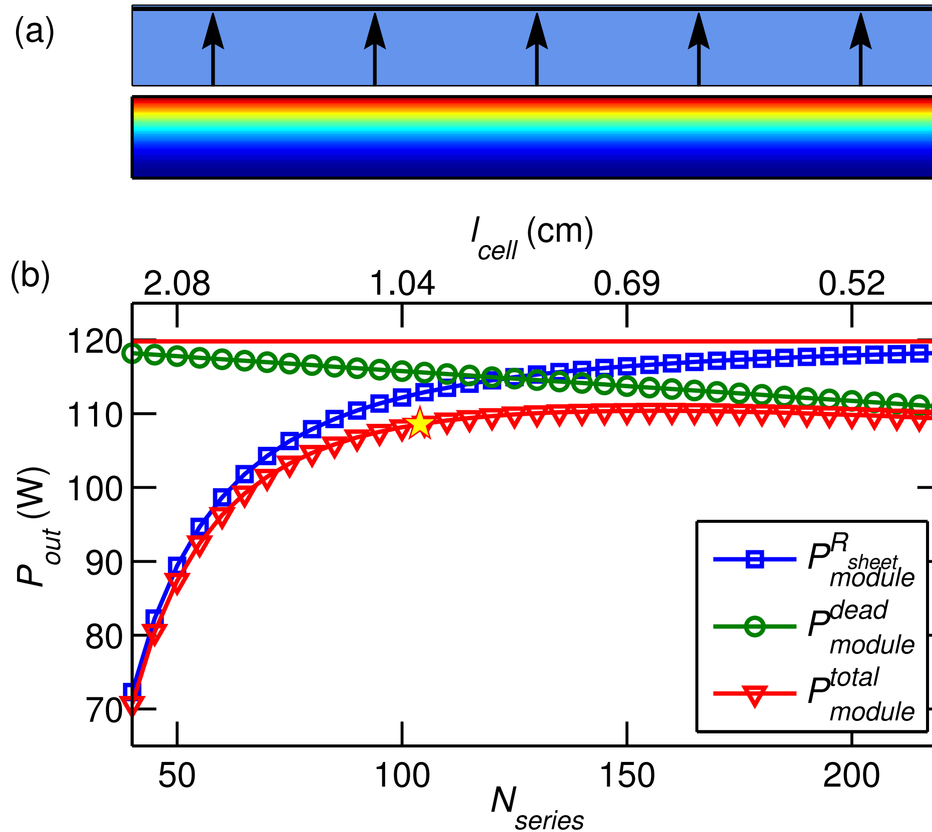

Fig. 4.4. (a) The top schematic shows a rectangular sheet conductor with current collecting edge at the top (line), other sides of the rectangle are open circuited, and the current flows in y direction. The bottom plot shows the power dissipation density from Eq. 4.5 as a color plot, showing that the dissipation increases near the collecting edge (red regions). (b) Plot of the module efficiency as a function of increasing number of cells N_{series} (bottom axis); or equivalently, reducing cell length l_{cell} (top axis), for typical a-Si:H technology. The output change due to sheet resistance loss only (squares), dead area loss only (circles), and total (triangles) are as shown. The typical value of $l_{cell} = 1$ cm, for the a-Si:H is near the optimal, (marked with a star).

the dead area loss. This means that the number of series connected cells must be

chosen carefully to optimize the module output. Using Eq. 4.6, we can write the total output power loss in creating the series connections as

$$\begin{aligned} P_{out}^{loss} &= N_{series} P_{\square}^{cell} + P_{dead} \\ &= \frac{{J_{photo}^{mpp}}^2 R_{\square} W_{module} L_{module}^3}{3 N_{series}^2} + \underbrace{N_{series} W_{module} w_{dead}}_{A_{dead}} J_{photo}^{mpp} V_{cell}^{mpp}. \end{aligned} \tag{4.7}$$

In order to minimize this loss term we can differentiate the above equation with respect to N_{series} and equate it to zero, to obtain the optimal number of series connected cells as

$$N_{series}^{opt} = \left(\frac{2 J_{photo}^{mpp} R_{\square}}{3 V_{cell}^{mpp} w_{dead}} \right)^{1/3} L_{module}. \tag{4.8}$$

The above equation nicely illustrates the trade-offs involved in optimizing the number of series connected cells for any given TFPV technology. The sheet resistance loss is determined by current at the MPP voltage; therefore, a high J_{photo}^{mpp} and low V_{cell}^{mpp} technology (e.g., CIGS [157]) will require more series connections so N_{series}^{opt} will be higher, and *vice versa*. Similarly, if the sheet resistance is higher, and dead area penalty smaller, the output power loss is minimized by larger N_{series}^{opt}. Therefore, depending on the TFPV technology of choice, we need to choose the N_{series} to minimize the power loss at module level.

For typical a-Si:H technology, we can use $\eta_{cell} = 9.6\%$ with $J_{photo}^{mpp} = 13$ mA/cm^2 [186], $R_{\square}^{FTO} = 10\ \Omega/\square$ [32], $L_{module} = 104$ cm, $W_{module} = 120$ cm [47], and $w_{dead} = 350\ \mu$m [187]. We can now compare the contributions of various loss mechanisms quantitatively, and obtain the optimal N_{series}. Fig. 4.4(b) plots the module output power for the a-Si:H technology for various N_{series} (alternately l_{cell}) values, showing the relative impact of sheet resistance loss which decreases with N_{series}, and the dead area loss which decreases with N_{series}. The ideal output power, without any losses is marked (red line) for reference. This results in an optimal module output for $N_{series} \approx 100$ ($l_{cell} \approx 1$ cm), which is exactly what is used in manufacturing [47]. Similar analysis can be repeated for other TFPV technologies, to obtain the optimal N_{series} value, depending on material and performance parameters.

Table 4.1
Highest reported cell performance metrics for a-Si:H technology, and the model parameter used for fitting these metrics using the equivalent circuit model discussed in Sec. 2.11.

a-Si:H sub-cell parameters [47]			
J_{SC} (mA/cm^2)	V_{OC} (V)	FF (%)	η_{sub} (%)
15.87	0.89	68.3	9.6
Model parameters			
J_{abs0} (mA/cm^2)	V_{bi} (V)	$(\mu\tau)_{eff}$ (cm^2/Vs)	$R_{\square}$ ($\Omega/\square$)
15	1.1	10^{-8}	10

4.3 Shunt Variability and Cell to Module Gap

In Sec. 3.2, we used careful statistical analysis to establish the log-normal nature of I_{SH0} distribution. In order to understand its importance for cell efficiency, we first use a physical equivalent circuit model (discussed in 2.6) to simulate the effect of I_{SH0} magnitude on individual (lab scale ~ 1 cm^2) cell efficiencies. The intrinsic equivalent circuit parameters namely, voltage dependent photocurrent (I_{photo}) [51], generation enhanced recombination ($I_{rec,G}$) [86], and the dark diode current I_{diode} [188] (see Fig. 4.5(a)), can be obtained by fitting the highest reported cell efficiency for a-Si:H [186]. The parameter set obtained from this fitting is summarized in Table 4.1.

We now use this calibrated equivalent circuit, to evaluate the effect of shunt variability by varying the shunt current magnitude I_{SH0}. The result of the circuit simulations are shown in Fig. 4.5(b), demonstrating that the reduction in cell efficiency with for higher I_{SH0}, is caused by a sharp drop in fill factor, and V_{OC} values of the cell. The IV characteristics of these heavily shunted cells have often been described using a 'weak diode' in CIGS [139] and CdTe [189] literature. We, however, don't consider the weak diodes separately, as the non-Ohmic shunt conduction automatically captures the characteristics attributed to weak diodes.

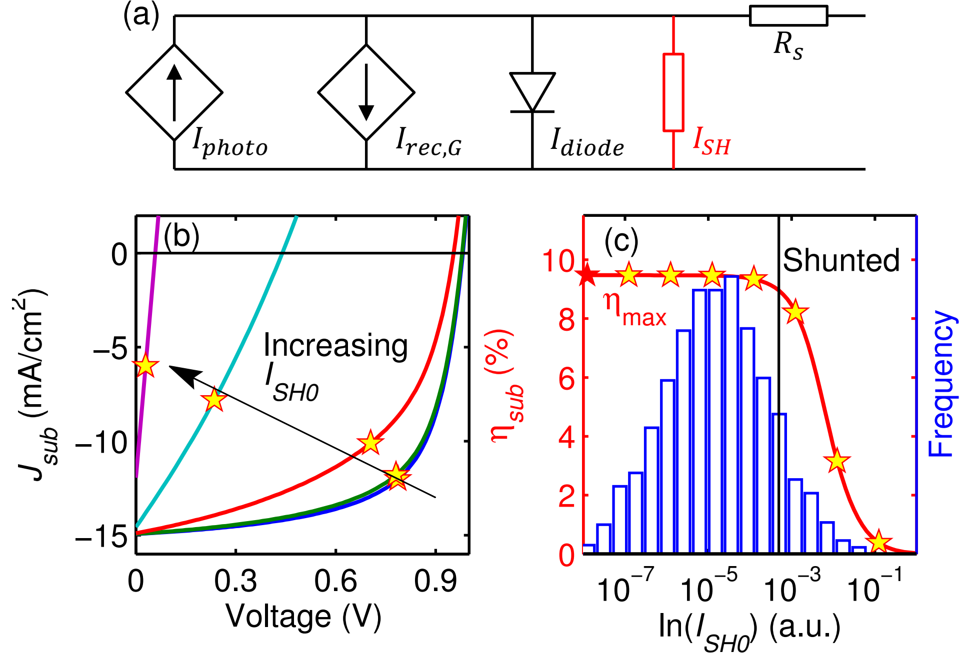

Fig. 4.5. (a) Physical equivalent circuit for a TFPV 1 cm^2 cell discussed in Sec. 2.6, with a variable non-Ohmic shunt current $I_{SH} = I_{SH0}V^{\alpha}$ highlighted in red. (b) Simulated IV curves from the equivalent circuit shown in part (a), as a function of increasing I_{SH0} values. The MPP voltage and current drop significantly for larger shunt current values (marked with stars). (c) Simulated cell efficiency as a function of I_{SH0} (line), deviates from maximum (η_{max} marked red) for large I_{SH0} values. The points corresponding to part (b) are also marked. On the right axis, the histogram shows measured log-normal distribution of I_{SH0}, showing that the low efficiency "shunted" cells comprise the tail of this distribution.

A more quantitative comparison is shown in Fig. 4.5(c), which demonstrates that the cell efficiency drops significantly below η_{max} (record efficiency) only for $I_{SH0} \geq$ 1 mA. This asymmetric relation between cell efficiency and I_{SH0} means that only a small fraction of cells, with the log-normally distributed I_{SH0} values, will be affected significantly by the shunt leakage. This is visible from the overlapping histogram in Fig.4.5(c), plotting the measured log-normal I_{SH0} distribution for a-Si:H cells. Comparing these two plots, it is obvious that low efficiency "shunted" cells constitute the higher tail of the I_{SH0} distribution. This analysis seems to suggest that only a

small fraction of cells would suffer from efficiency loss due to parasitic shunting, and their impact on the module efficiency would be small. In a typical module, however, many cells are connected in series and parallel. In order to assess the effect of parasitic shunts, in this interconnected system, we use equivalent circuit approach discussed next.

4.3.1 2D SPICE Simulation Framework

Fig. 4.6(a) shows the schematic of a TFPV module, with dimensions L_{module} and W_{module}. Typically, these dimensions are $1-2$ m each, so that module areas range from $1-5$ m^2. As seen in the schematic, the module is formed by N_{series} series connected cells. Consequently, the cell dimensions are $w_{cell} = W_{module}$, and $l_{cell} = L_{module}/N_{series}$, respectively. In order to capture the spatial variations, we further sub-divide each rectangular cell into $N_{parallel}$ sub-cells, so that $l_{sub} = l_{cell}$, and $w_{sub} = W_{module}/N_{parallel}$. As shown in Sec. 4.2, due to the sheet resistance constraints, $l_{cell} \approx 1$ cm for most TFPV technologies; and we adjust $N_{parallel}$ to obtain $w_{sub} \approx 1$ cm as well. Therefore, each sub-cell is similar in dimensions to a laboratory scale cell, and can be represented with the equivalent circuit in Sec. 2.6.

These equivalent circuits are connected in series and parallel using TCO and metal sheet resistances (marked $R_{\square}^{TCO}$ and $R_{\square}^{metal}$, respectively in Fig. 4.6(b)), to obtain a 2D mesh equivalent circuit representation of a full size TFPV module, as shown in Fig. 4.6(b)) [81,190]. We use this setup to circuit setup to evaluate the effect of shunt variability [191], by assuming that all sub-cell parameters are identical, and equal to the highest efficiency cell, and the only difference between the sub-cells is the shunt current. We know from Sec. 3.2 that I_{SH0} magnitude varies log-normally across sub-cells. Moreover, we saw in Sec. 3.2.2 that the position statistics of parasitic shunts is completely spatially random. Therefore, in order to assess the effect of shunt statistics, we will generate a random sample of I_{SH0} values from the log-normal magnitude distribution, and assign it randomly to different sub-cells across the module. This 2D

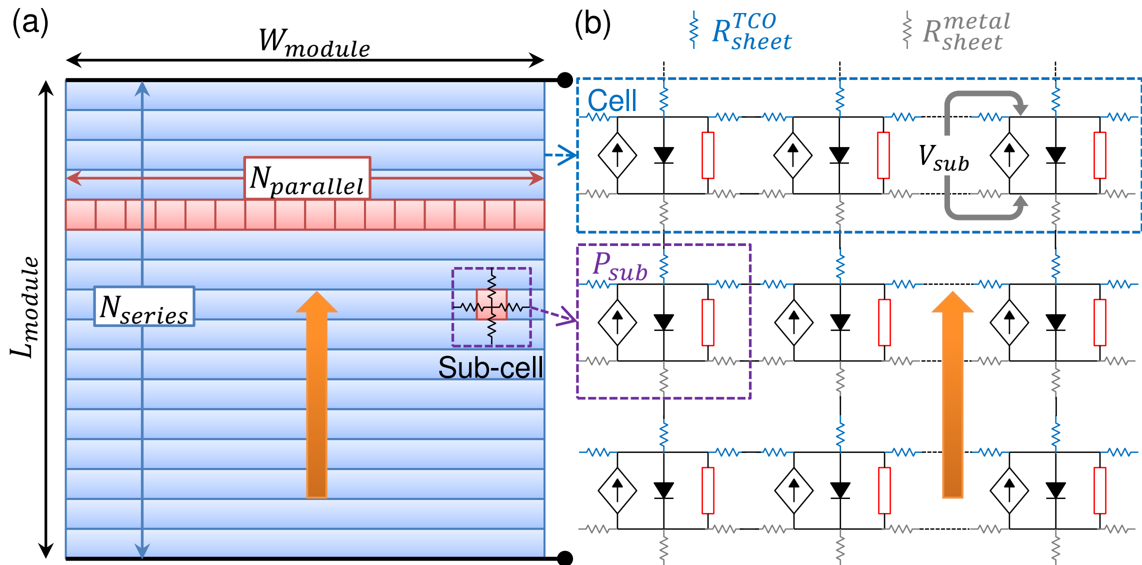

Fig. 4.6. (a) Schematic of a TFPV module ($L_{module} \times W_{module}$), with N_{series} series connected cells, and the current direction denoted by arrow. Each cell is subdivided into $N_{parallel}$ sub-cells (squares), each represented by the TFPV equivalent circuit, discussed in Sec. 2.6. These sub-cells are connected using the contact sheet resistances of the TCO (blue), and metal (gray) layers, to create a 2D circuit representation of the module, as shown in (b). All sub-cells are assumed identical across the module, except the shunt (in red) which is varied according to the measured log-normal distribution. The sub-cell power output P_{sub}, and operating voltage V_{sub}, as shown in the schematic, can be monitored across the module.

setup then allows us to look at the sub-cell operating parameters like output power P_{sub}, and operating voltage V_{sub} (as marked in Fig. 4.6(b)) across the module surface in presence of shunt variations. We have made available a version of this simulator is available as a web-enabled tool on nanoHUB [192].

Note that this framework simulates the more common monolithically manufactured modules for the four representative TFPV technologies, which does not allow for sorting/binning of defect cells before connecting them to form modules. In some cases, however, a roll-to-roll manufacturing on flexible substrates is used; which allows

individual cells to be cut from the larger role [63]. These cells can then be tested and sorted, and the modules are then formed separately by taking cells from a particular bin. While this may help in reducing the cell mismatch at module level, we must remember that the number of cells in each bin will still be determined by the log-normal shunt statistics, and will in turn determine the process yield of these technologies. Also, just like multi-crystalline Si cells, these roll-to-roll process cells will have certain amount of mismatch even after binning. These residual mismatches, although smaller than monolithic case, will lead to certain module efficiency loss. This can be analyzed using established 1D simulation method for crystalline modules [193]. In this work, we focus on the more common monolithic TFPV modules, which require a full 2D circuit simulation for analysis of variability effects.

4.3.2 Cell to Module Efficiency Gap

In order to examine the effect of shunt statistics for a typical TFPV module, we perform Monte-Carlo circuit simulations of module efficiency. This is done by generating multiple module circuits with log-normally distributed I_{SH0} values, and simulating these modules in SPICE to obtain the distribution of their efficiencies. For making consistent quantitative comparisons, we start with a-Si:H modules with dimensions L_{module} = 104 cm, W_{module} = 120 cm, and N_{series} = 104. We choose $N_{parallel}$ = 104, so that $l_{sub} = w_{sub}$ = 1 cm for the sub-cell. The sub-cell parameters for non-shunted sub-cells are given in Table 4.1, and the log-normal I_{SH0} distribution was chosen based upon the measured values in Sec. 3.2.

Fig. 4.7(a) shows the simulated distribution of module efficiency for a-Si:H, compared to best sub-cell efficiency η_{sub}(same as η_{max} in Fig. 4.5(b)), and the highest possible module efficiency η_{module}, for a module composed of identical sub-cells, each with efficiency η_{sub}. Note that the efficiency drop in going from η_{sub} to η_{module}, is solely due to the sheet resistance losses. As shown in Fig. 4.7(a), in presence of parasitic shunt distribution, the module efficiency is reduced further, and we get a

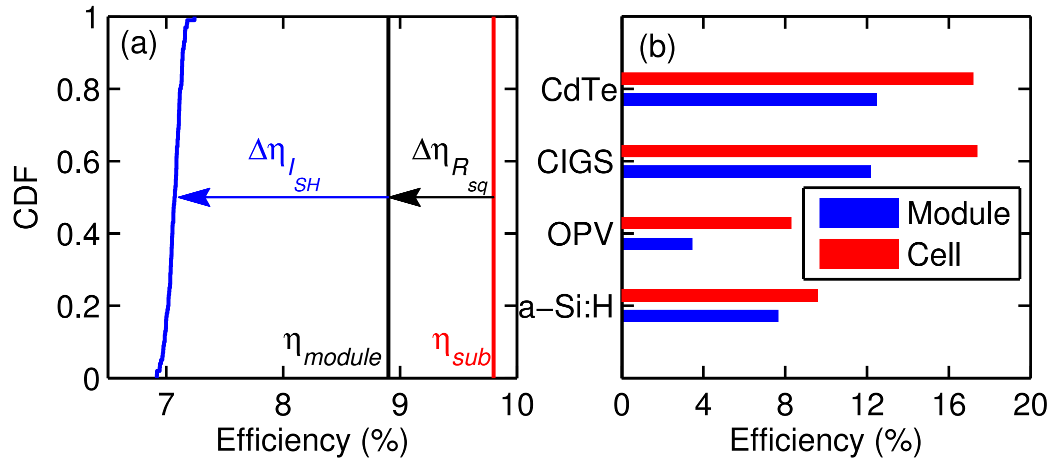

Fig. 4.7. (a) CDF plot of module efficiency obtained from the Monte-Carlo simulations of a-i:H modules in presence of log-normal distribution of parasitic shunt current (blue), compared to the best sub-cell efficiency (η_{sub}), and highest possible module efficiency η_{module}. The relative contributions of sheet resistance loss $\Delta\eta_{R_{sq}}$, and $\Delta\eta_{I_{SH}}$, are also highlighted. (b) Bar plot comparing the best cell efficiencies of various TFPV technologies (red), with the module efficiency obtained from circuit simulation (blue), accounting for sheet resistance and shunt current losses, shows that these two factors can account for most of the cell to module efficiency gap in TFPV technologies.

finite spread in the efficiency values, due the the statistical fluctuations. Note that the sheet resistance loss $\Delta\eta_{R_{sq}}$ taken together with shunt induced loss $\Delta\eta_{I_{SH}}$, can roughly reproduce the typical gap between cell and module efficiency for a-Si:H [10]. This suggests that the magnitude of module efficiency losses due to shunts, predicted by the Monte-Carlo simulations, is not a simulation artifact.

Note that the equivalent circuit in Fig. 4.5(a) was validated for a-Si:H cells [194], but it can also be used effectively as a semi-empirical equivalent circuit for other TFPV technologies [195]. Using this fitting approach, and including the shunt statistics data for other technologies, discussed in Sec. 3.2, we can repeat the module efficiency simulations for other TFPV technologies. The best reported cell efficiency metrics are taken from published literature [10], and module parameters from the respective manufacturers; these are summarized in Table 4.2.

Table 4.2
Sub-cell parameters for highest reported cell efficiencies for different TFPV technologies. The module parameters for the respective technologies are taken from manufacturer datasheets, as listed.

Sub-cell parameters [10]				
Technologies	J_{SC} (mA/cm^2)	V_{OC} (V)	FF (%)	η_{sub} (%)
OPV	16.4	0.82	70	8.3
CIGS	33.0	0.688	76.7	17.4
CdTe	27.1	0.827	76.6	17.2
Module parameters				
Technologies	L_{module} (cm)	W_{module} (cm)	N_{series}	$R_{\square}^{top}, R_{\square}^{bot}$ ($\Omega/\square$)
OPV (Konarka)	40	20	40	10, 10
CIGS (Solar Frontier)	150	115	90	10, 0.5
CdTe (First Solar)	116	56	116	10, 0.5

We repeat the Monte-Carlo simulations for the other TFPV technologies, using log-normal I_{SH0} distribution derived from the measured values in Sec. 3.2. Fig. 4.7(b) compares the simulated mean module efficiency obtained from the Monte-Carlo simulations to the respective record cell efficiency for each of the four technologies. We can see that by accounting for the losses due to log-normal shunt distribution, in addition to the sheet resistance loss, our simulations can reproduce the universal gap between cell and module efficiency in all TFPV technologies. It must be noted that these simulations indicate the lower limit of the cell to module efficiency gap, and inclusion of other sources of variability will only increase the gap.

Note that this is only a sample simulation, and the sub-cell efficiency data, module parameters, and shunt statistics data are collected from different sources. Therefore, the gap between cell and module efficiency obtained from this simulation is only

indicative. A precise assessment of impact of shunt statistics will require a controlled and calibrated data on physical parameters, as well as statistical distribution, from the same process. The purpose of this simulation is to demonstrate that it is possible to incorporate statistical variability into module simulations, and obtain useful results from the analysis. The calculation also reinforces the importance of the universality in shunt statistics, by showing that although the simulation is not exactly calibrated to the data; we are still able to obtain reasonable results just by accounting for the log-normal nature of shunt distribution.

4.3.3 Impact of Shunts on Module Performance

The discussion in previous sections appears to present a puzzle. This is because only few sub-cells are expected to suffer significant efficiency loss due to the log-normal shunt statistics (see Fig. 4.5(c)). The Monte-Carlo simulations, on the other hand, demonstrate that shunt distributions are responsible for a majority of cell-to-module efficiency loss. In order to resolve this issue, we need to take a closer look at the operation of 2D mesh equivalent circuit of the module. Fortunately, the detailed 2D model, allows us to evaluate the spatial variations during module operation, and pin point the source of shunt induced efficiency loss, as discussed next.

Non-Local Shunt Effect

For studying the effect of shunts in an interconnected module, we simulate a 11×11 cm^2 sub-module with 11 series connected cells. All sub-cells are identical in this example simulation, except 3 particular sub-cells which are assigned specific I_{SH0} values, shown numbered in the color plot in Fig. 4.8(a). We simulate this sub-module, and evaluate the distribution of sub-cell parameters at the *sub-module MPP voltage*. Fig. 4.8(b) shows the distribution of sub-cells voltages (V_{sub}) plotted as color plot (color bar is in volts). Note that depending on the shunt magnitude, the V_{sub} values of the shunted sub-cells, *as well as their neighbors* is lowered significantly. This is means

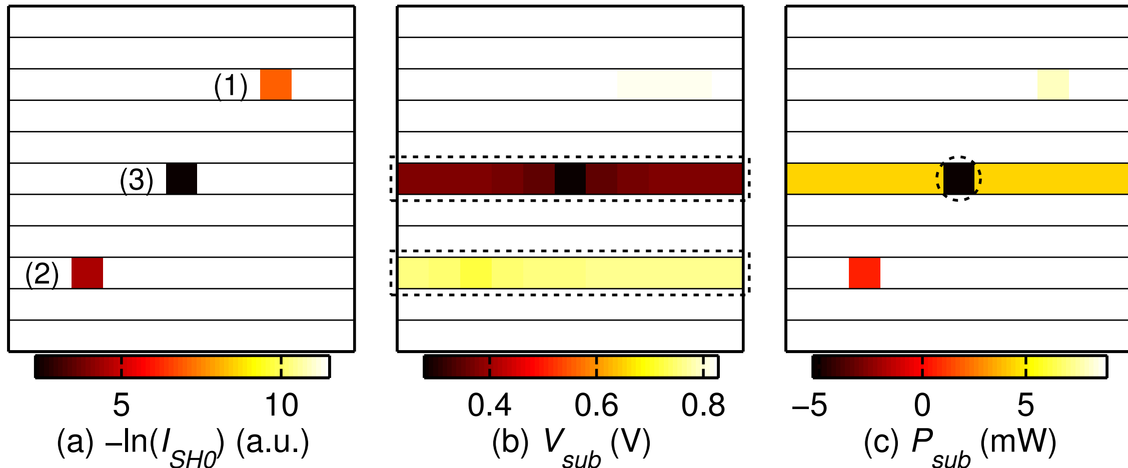

Fig. 4.8. (a) Color plot of I_{SH0} distribution in an example simulation of 11×11 cm^2 sub-module, with only three shunted sub-cells (numbered), each assigned different I_{SH0} magnitude. All other sub-cells are assumed to be at η_{max}, with negligible shunt current. (b) Distribution of sub-cell voltages V_{sub} as a color plot (color bar in V), at the sub-module MPP bias shows that the shunted sub-cells can lower the operating point of their neighboring "good" sub-cells in parallel (marked with dashed box). (c) The distribution of sub-cell power output P_{sub}, shows that a heavily shunted sub-cell (circled) can *consume* ($P_{sub} < 0$ in this sign convention) the power output of its neighboring sub-cells (color bar in mW).

that defect free sub-cells in parallel to a badly shunted sub-cell, operate away from their MPP voltage, reducing their power output. The number of neighboring sub-cells which suffer from lower operating voltage due to a shunted sub-cell, depends on the magnitude of the shunt, as well as the net sheet resistance of the metal/TCO contact layers (compare the highlighted cells in Fig. 4.8(b)). Note that this phenomenon of localized shunt defects causing a reduction in the operating voltage of defect free neighboring regions in parallel (same cell), has been observed experimentally using electroluminescence imaging [147,196]. This non-local effect of shunts in reducing the output of its neighboring is a major contributor towards module efficiency loss.

Another more peculiar effect of shunted sub-cells in this interconnected configuration, becomes apparent on plotting the distribution of sub-cell power output P_{sub}, at the sub-module MPP voltage. As seen in the middle cell highlighted in Fig. 4.8(c), a heavily shunted sub-cell can be biased in such a way so that it *dissipates* power under normal operation, instead of producing it. In this scenario, the power output of the sub-cells in parallel to the shunted sub-cell is dissipated in the defective region instead of flowing to the terminals. Thus, we have a twofold impact on module efficiency due to the effect of shunted sub-cells on their neighbors. First, the sub-cells adjacent to a shunted sub-cell can get biased away from their MPP voltage, and produce less power. Moreover, even this reduced power output may be dissipated in the shunted sub-cell. This is the reason why, even a few shunts can result in a significant reduction in the sub-module output power. This also explains the puzzle of how relatively few shunted sub-cells can cause significant reduction in the module efficiency, as demonstrated by the Monte-Carlo simulations. In Sec. 4.2.2, the cell sizes were optimized by minimizing sheet resistance losses. In this section, however, we saw that the non-local effect of shunts are worsened for lower sheet resistances. Therefore, a better strategy for module design would be simultaneous minimization of sheet resistance and parasitic shunt losses, because they can counterbalance each other in certain parameter ranges.

4.4 Strategies for Shunt Loss Mitigation

From the previous discussion, it is obvious that parasitic shunts are responsible for a significant portion of cell to module efficiency gap, as well as reducing the process yield due to variability. This problem of random parasitic defects and process variability is by no means limited to TFPV technologies. In conventional c-Si technology, however, the effect of shunt and other random defects can be alleviated by testing and sorting individual cells [170]. Then, only the cells in a particular efficiency 'bin' are soldered together to form a module, which reduces the effect of mismatches.

This still leaves the problem of process variability unsolved, because the modules formed from low efficiency cells lie in the low efficiency bin, and are sold at lower prices [197]. Such sorting is not possible for most TFPV technologies because the commonly used monolithic manufacturing of modules does not allow separation high and low efficiency cells or regions. Therefore, while shunt formation is a random process, alternative *post-process* treatments to reduce shunting in all PV technologies have been studied. In this section we overview these methods, and propose a new technology agnostic approach [198].

4.4.1 Process Solutions for Shunt Removal

In order to overcome the problem of shunt losses at module level, many process level solutions for different TFPV technologies have been proposed. Some of these methods have focused on process solutions for improving deposition uniformity [37], better substrate cleaning [124], or inclusion of resistive interlayer [156,157]. A number of post-process methods for shunt removal have also been reported. These include, shunt busting in a-Si:H cells [175], which uses application of high reverse bias on finished cells to burn-up or 'bust' the shunt paths. Another approach involves electrolytic treatment of finished solar cell under reverse bias [199], or under illumination [200] for passivating the shunt forming regions, or other non-uniformities on solar cell surface using electrolytic modification of the shunted regions.

All these techniques focus on modifying the properties of shunt paths, and reducing the leakage through those regions. Unfortunately, these techniques are indiscriminate, as the whole cell area is subjected to a particular treatment for shunt passivation. This increases the chances of adversely affecting other "good" regions. Finally, these techniques rely on specific, materials, or structures, used in each TFPV technology to achieve shunt passivation, thereby limiting their application to a single material or process. Next, we describe a general post-process technique for mitigating shunt effects, which differs from these earlier approaches in two specific aspects. First,

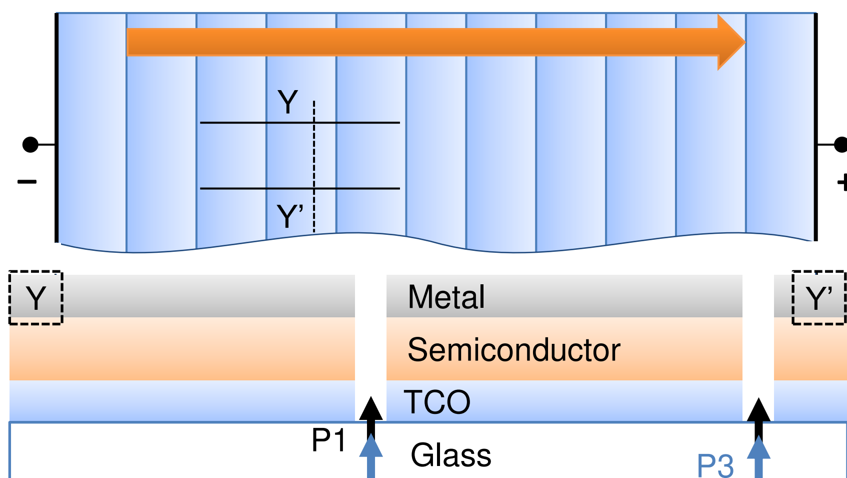

Fig. 4.9. Schematic of the series connected cells in a module (top), with two isolating (open circuit) scribes shown as solid black lines. Bottom schematic shows the side view along the YY' axis, showing that overlapping P1 and P3 lasers can be used to ablate all layers and create isolating scribe lines, after [187].

it does not rely on removing or passivating the shunts themselves, but on reducing the *effect* of shunted regions on their neighboring regions. Second, this approach is applicable to all TFPV technologies which use scribing and monolithic integration for module fabrication.

4.4.2 Scribing Isolation Techniques

From the 2D circuit simulations in the previous section, we observed that the significant reduction in module efficiency due to shunting arises from the non-local effect of shunted sub-cells on their neighbors. This implies that a significant portion of shunt induced efficiency losses can be recovered, if this interaction between the neighboring sub-cells can be suppressed *after* module fabrication.

Creating Isolating Scribes

Fortunately, the laser scribing method, used for creating the series connection in monolithic TFPV modules (as shown in Fig. 4.3), can be adapted to create isolating scribes; which act as open circuits, and can be used to mitigate shunt losses at module level. As shown in Fig. 4.9, these isolating scribes can be created by superposing P1 and P3 lasers to ablate all layers, which results in the region between two isolating scribes to be disconnected from other regions of the cell. The typical width of the scribe lines for these isolating scribes $w_{scrb} = 150$ μm, see [187] for details. Note that the isolating scribes in Fig. 4.9 are created in parallel to the direction of current flow in the module, which ensures that the normal module operation is not affected by adding these additional scribe lines, after the usual processing has been finished.

Lengthwise Periodic Scribing

The most straightforward method for shunt isolation using scribing involves creating full length isolating scribes in the direction of current flow in a TF module. These vertical scribes divide the rectangular cells in the module into columns of smaller width (shown as dashed lines in the plot of I_{SH0} values in Fig. 4.10(a)). These vertical scribes ensure that fewer parallel connections between sub-cells are possible. In case of the sub-module in Fig. 4.10(a), each sub-cell is connected in parallel to at most one other sub-cell. The advantage of this approach is that it does not require identification of the shunt locations beforehand. The scribe lines, however, need to span the entire module length, to ensure that regardless of the shunt location, the number of neighboring sub-cells in parallel it can influence is limited. Note that this full length scribing isolation at the sub-module level has been demonstrated earlier using mechanical scribing for edge shunt isolation in CIGS sub-module [201]. In this work, we propose to extend this approach and create periodic scribes for constraining shunt effect at all locations.

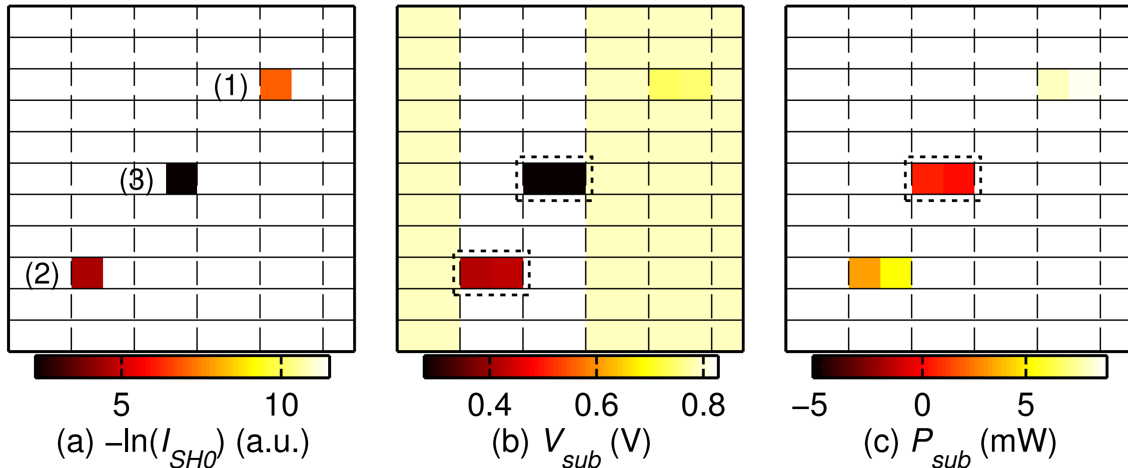

Fig. 4.10. (a) Color plot of I_{SH0} for the same 11×11 cm^2 sub-module, with three shunted sub-cells (numbered), now showing periodic lengthwise isolating scribes (dashed lines), which limit the parallel connections to 2 sub-cells only. (b) Distribution of sub-cell voltages V_{sub} as a color plot (color bar in V), at the sub-module MPP bias shows that the shunted sub-cells can now influence only 1 neighboring "good" sub-cell within the vertical scribe lines (marked with dashed box), as the others are disconnected by the isolating scribes. (c) The distribution of sub-cell power output P_{sub}, shows that the power output of all sub-cells is now positive (dashed box) as the scribing isolation reduces the mismatch due to shunting (color bar in mW).

In order to evaluate the impact of these periodic isolating scribes, we simulate the sub-module with 3 shunts in presence of 5 vertical scribes (as shown in Fig. 4.10(a)). The active area loss due to w_{scrb} is accounted for in the simulations by reducing the active area of the scribed sub-cells accordingly. We can then compare the V_{sub} and P_{sub} distributions obtained from the simulations at the MPP voltage of this modified sub-module. Note that in this scenario, the effective range of all shunted sub-cells is restricted to only one neighboring sub-cell in parallel. Consequently, the operating voltages of the 'good' sub-cells, which are now isolated from the shunted ones, is restored to normal values (see color plot on Fig. 4.10(b)). Note that the voltage of each column of sub-cells (between two isolating scribes), however, must

be equal. Therefore, the operating points of the sub-cells in *series* to the shunted sub-cells now move to slightly higher values (see columns containing shunted sub-cells marked (2) and (3) in Fig. 4.10(b)). In spite of this limitation, the blocking of parallel conduction paths results in all sub-cells producing power (i.e. $P_{sub} > 0$ even for the heavily shunted sub-cell (3) as highlighted in Fig. 4.10(c)). Therefore, we can see that this approach will lead to improved sub-module output.

Targeted Partial Scribing Isolation

It is easy to see from the previous discussion, that the requirement of full length scribes used in the previous section, end up scribing a lot of non-shunted sub-cells unnecessarily. A much better approach for scribing isolation of shunts, would be to use targeted scribing, by placing the scribes only where needed. This requires identification of shunt locations before the scribing step. In the literature, a number of imaging techniques have been reported, which are capable of detecting distributed shunt defects. These are either based on thermal imaging like DLIT [202], or luminescence from the active layer like EL [196]. The images obtained from these techniques can be fed to an image processing algorithm, similar to the one discussed in Sec. 3.2.2, to obtain the shunt locations, which in turn can guide the scribing step.

Once the shunt locations are known, we can use parallel isolating scribes on either side of the shunted sub-cells to isolate only the required sub-cells (shown with dashed lines for the I_{SH0} plot in Fig. 4.11(a)). Note that the scribe length (L_{scribe}) can be varied to control the degree of isolation needed. This ensures that the non-shunted sub-cells are not unnecessarily scribed. Fig. 4.11(b) shows the color plot V_{sub} values from the sub-module simulation, in presence of the scribes, at the sub-module MPP in this case. Note that the operating points of all sub-cells in parallel to shunted sub-cells improve close to MPP values, as the shunted sub-cell is fully isolated from other sub-cells in parallel. The V_{sub} values of the sub-cells in series to the shunted sub-cells, however, now increase slightly to ensure total sub-module voltage being same. The

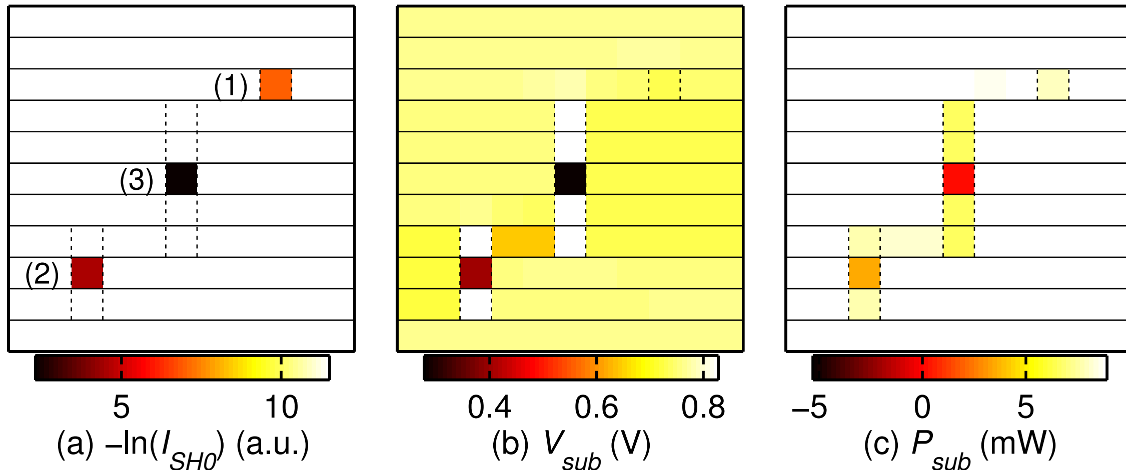

Fig. 4.11. (a) Color plot of I_{SH0} for the same $11 \times 11cm^2$ sub-module, with three shunted sub-cells (numbered), showing targeted partial isolation using parallel isolating scribes on either side of the shunted sub-cell (dashed lines). The scribe length can be varied according to shunt magnitude at a particular location. (b) Distribution of sub-cell voltages V_{sub} as a color plot (color bar in V), at the sub-module MPP bias shows that the shunted sub-cells can now only influence sub-cells in *series* within the vertical scribes, pushing them to slightly higher forward bias, as all sub-cells in parallel are now disconnected from the shunted one. (c) The distribution of sub-cell power output P_{sub}, shows that the power output of all sub-cells is higher after the partial isolation of shunts, as the effect of shunted sub-cells on others in series is weaker than on those in parallel (color bar in mW).

distribution of P_{sub} values, shown in Fig. 4.11(c), also shows the improvement in the output power of non-shunted sub-cells in parallel, at the cost of slight reduction in P_{sub} values for the non-shunted sub-cells enclosed by the scribe lines. Finally, note that the length of scribe lines used affects the degree of isolation, and accordingly, the efficiency improvement obtained at the cost of higher dead area loss.

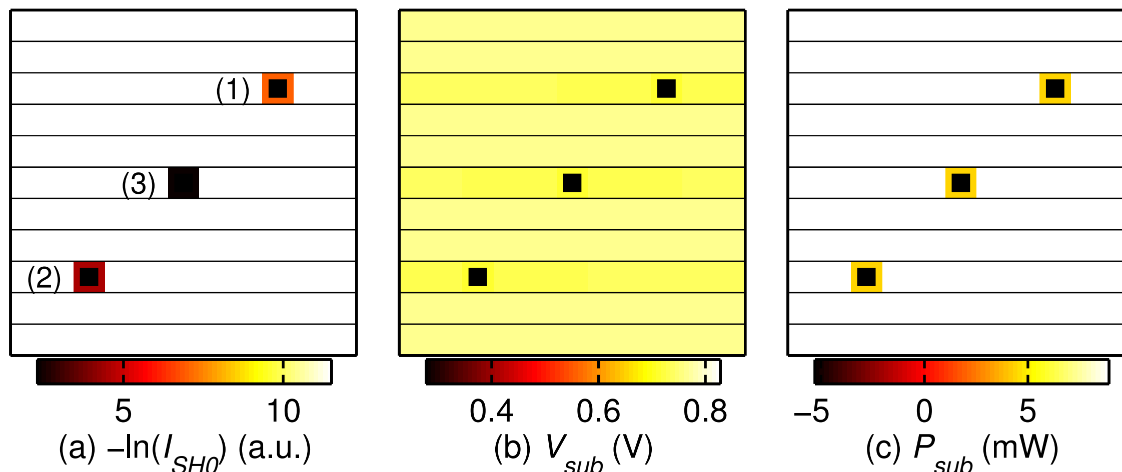

Fig. 4.12. (a) Color plot of I_{SH0} for the same 11×11 cm^2 sub-module, with three shunted sub-cells (numbered), showing targeted full isolation using an enclosed (box) created using isolating scribes the shunted region sub-cell (black square), which ensures that the shunt is completely isolated from all neighboring sub-cells. (b) Distribution of sub-cell voltages V_{sub} as a color plot (color bar in V), at the sub-module MPP bias shows that the operating points of all sub-cells improves considerably, and only a slight mismatch remains due to the large dead area loss inside scribed region. (c) The distribution of sub-cell power output P_{sub}, shows that the power output of all sub-cells also improves significantly after full isolation of shunts (color bar in mW), showing that the mismatch caused by increased dead area in shunted cells is minimal compared to the mismatch due to parasitic shunts.

Targeted Full Scribing Isolation

In the scribing techniques described so far, the shunted sub-cells are only partially isolated. And, even after the scribing isolation, the sub-cells in series with the shunted sub-cells are affected due to the requirement of series connection. The best solution to this would be to fully isolate the shunted region within a sub-cell, by enclosing it with isolating scribes (e.g. creating a box around the shunted region as shown in the plot of I_{SH0} values in Fig. 4.12(a)). This ensures that the shunt is not completely disconnected from all active areas of the module. This also, however, results in a

higher dead area loss, because the entire area enclosed by the scribes (A_{scribe}) is no-longer generating any power. And, from a practical standpoint, the full isolation of shunts requires more precise shunt location identification and positioning of the lasers to be effective.

The sub-module simulations are repeated, with full isolation with full isolation for the 3 shunts, as shown in Fig. 4.12(a); and, the distribution of P_{sub} and V_{sub} values obtained at the MPP voltage of this sub-module is plotted in Fig. 4.12(b) and (c), respectively. As seen in Fig. 4.12(b), the full isolation of shunts almost completely removes the V_{sub} fluctuation across the sub-module; except for a small mismatch between the cells containing the shunts and the defect free cell, due to a slight area mismatch. The isolated region is shown by dark squares, as it is completely cut-off from the module output. Correspondingly, all the non-shunted sub-cells now operate at their MPP voltage (see Fig. 4.12(c)). Depending on the total dead area inside the scribed region (A_{scribe}), some portion of the shunted sub-cells will still be generating power (see Fig. 4.12(c)), and the fraction of area lost to scribing per sub-cell (A_{scribe}/A_{sub}) will determine the eventual efficiency enhancement from this technique.

4.4.3 Comparison of Scribing Isolation Techniques

From the previous discussion, we can see that various scribing techniques improve the module performance by isolating the shunts to varying degrees, but the trade-off in terms of dead area loss is also different. We now analyze these trade-offs more quantitatively, for typical TFPV modules. We consider one of the a-Si:H modules from the Monte-Carlo simulation in Sec. 4.3.2, which has a particular I_{SH0} distribution resulting in $\eta_0 = 7.22\%$ due to the various module lossses. We will apply the different scribing schemes to this particular module (keeping the I_{SH0} distribution unchanged) and evaluate the improvement in efficiency obtained for different configurations. This will allow us to evaluate the effectiveness of these schemes under

realistic circumstances. In these simulations the module and sub-cell parameters are same as those used in Sec. 4.3.2, and we also use a realistic value for isolating scribe line width [187] to account for the dead area and mismatch losses correctly. The dead area loss in the scribed sub-cells is accounted for in the SPICE simulation directly, by modifying the active area of each cell, depending on the presence of isolating scribes. This also ensures that when evaluating the effect of scribing schemes any effects due to mismatches in sub-cell IV are accounted for.

Module Efficiency Enhancement

We now compare the various scribing isolation schemes, each of which have one or more design parameters, which need to be optimized for best result. For the periodic lengthwise scribing approach, it is apparent from Fig. 4.10 that an increase in the number of vertical scribes (N_{scribe}) will improve the module efficiency, by containing the effect of shunted sub-cells. These scribes, however, span the entire length of the module, resulting in significant increase in dead area penalty N_{scribe}. As shown in Fig. 4.13, the high dead area penalty limits the incremental gains in module efficiency with increasing N_{scribe}. The module efficiency improves to $\sim$ 7.6% for N_{scribe} = 30. The incremental gains for even larger N_{scribe} values, however, are very limited. Therefore, we can conclude that the periodic lengthwise scribing, while easiest to implement in practice, can offer less that 0.5% efficiency enhancement for the a-Si:H case.

In case of targeted shunt isolation after determination of shunt locations, we need to choose the number of shunted sub-cells to isolate (N_{iso}). This is also determined by the sensitivity of the detection scheme. As expected, when more and more shunted sub-cells out of the total N_{sub}, are isolated with scribing (increasing N_{iso}/N_{sub} in Fig. 4.13), the module efficiency improves significantly (shown as circles in Fig. 4.13). Again the improvements are limited by increased dead area loss with more scribing, and the curves saturate for larger N_{iso}/N_{sub} values. Interestingly, note that using

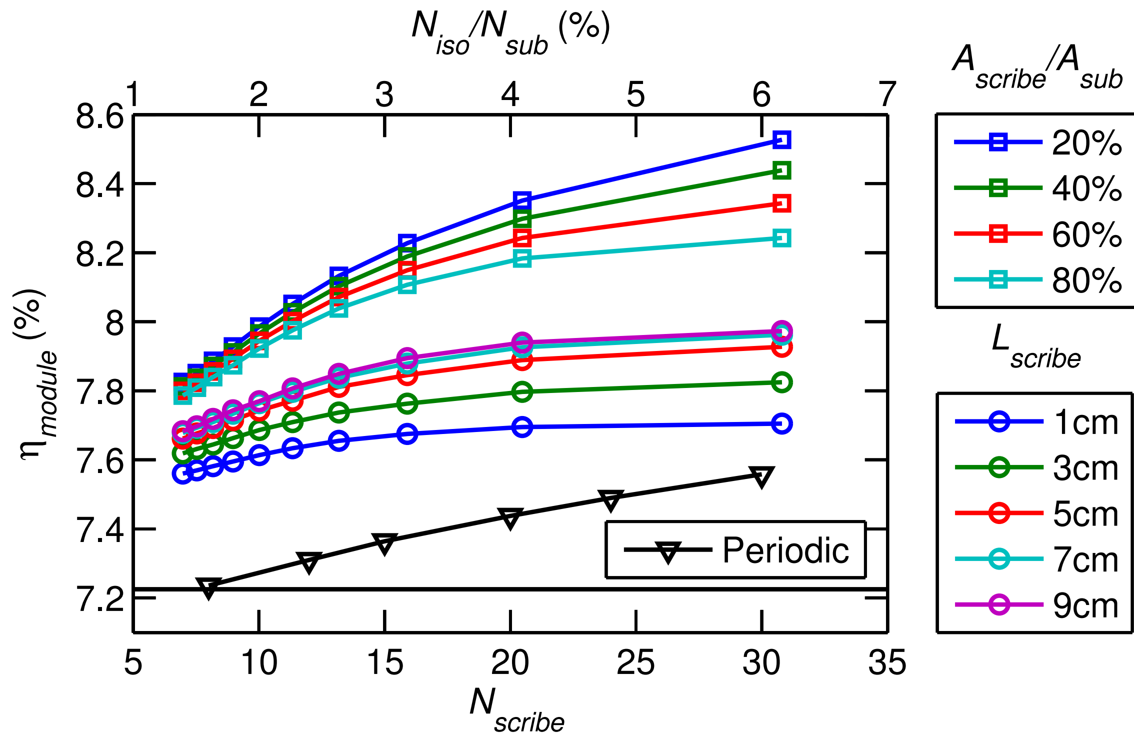

Fig. 4.13. Plot comparing the efficiency of a typical 7.22% a-Si:H module with parasitic shunts (horizontal line), after the module is treated using different scribing isolation techniques. For the periodic lengthwise isolating scribes (triangles), the efficiency improves with more vertical scribe lines (N_{scribe}), but the efficiency gains remain modest due to large dead area penalty. The efficiency enhancements are significantly better if selective scribing is used to isolated more and more shunted sub-cells (increasing N_{iso}/N_{sub}) for both partial (circles) and full (squares) isolation case. In case of partial isolation, the efficiency improves for larger L_{scribe}, due to better isolation, but ultimately limited by dead area losses (squares). For full isolation, the dead area losses are determined by the ratio A_{scribe}/A_{sub}, which limits the efficiency enhancements obtained due to reduced shunt effects.

the prior detection of shunts, it is possible to get $\eta_{module} \geq 7.6\%$ by partially or fully isolating just the largest 1% shunt defects. This is a consequence of the heavy tailed log-normal shunt distribution, which means that few largest shunts dominate the overall efficiency loss at the module level (see [117] for details). Therefore, we

can obtain significant improvements by focusing on these most critical parasitic defects. In case of partial isolation technique, another optimization parameter is the length of isolating scribes L_{scribe} used for each shunted sub-cell. Fig. 4.13 shows that longer scribe lines provide better isolation; therefore, more efficiency improvement is obtained for the same N_{iso}/N_{sub} value by increasing L_{scribe} (see legend in Fig. 4.13). Understandably, these gains are also limited by increasing dead area penalty; and therefore, the module efficiency for $L_{scribe} = 7$ cm vs. $L_{scribe} = 9$ cm are virtually identical.

Finally we repeat the analysis for full isolation of largest shunts. As shown by squares in Fig. 4.13 the efficiency enhancement is even greater in this case, due to complete isolation of shunt defects. We can see that this can increase the module efficiency to almost 8%, even for small values of N_{iso}/N_{sub}. The major factor limiting the efficiency gains is the ratio between scribed sub-cell area, and total sub-cell area A_{scribe}/A_{sub}. In a practical scenario, this ratio will depend on the accuracy of the shunt detection, and scribing head positioning. We consider a variety of scenarios, varying the dead area loss (A_{scribe}/A_{sub}) from 20% to 80% (see legend in Fig. 4.13), and show that regardless of the dead area loss associated with full scribing, the full shunt isolation provides highest module efficiency out of the three proposed techniques. This is because, this approach removes the effect of shunted sub-cells on all its neighbors (series or parallel) by fully isolating the shunts. Furthermore, the random distribution of shunts on a module surface ensures that the mismatches introduced by scribing area loss are not significant.

Module Variability Improvement

Based on the discussion so far, we observe that all three scribing techniques enable improvement in module efficiency. We now show that these results hold true in a statistical sense, and compare the change in module efficiency distribution for different scribing methods. In order to compare the techniques statistically, we take

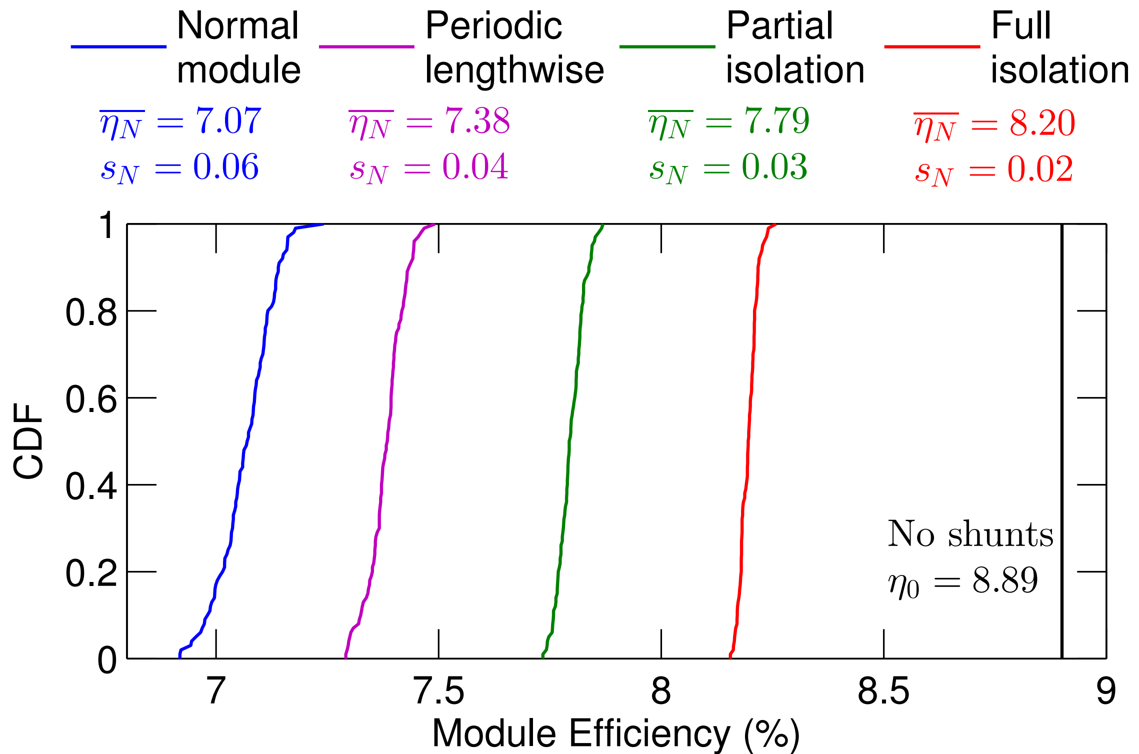

Fig. 4.14. CDF plots of module efficiency distribution for typical case (blue), lengthwise periodic scribing (magenta), partial shunt isolation after detection (green), and full shunt isolation after detection (red). The improvement in mean efficiency ($\bar{\eta}_N$), and reduction in standard deviation s_N are apparent from the values shown in inset. The full isolation of shunts can yield efficiency values close to the maximum possible module efficiency (black).

the modules structures used for Monte-Carlo simulation in Sec. 4.3.2, and apply the different scribing techniques for each module. The distribution of module efficiencies obtained after each scribing 'treatment' can then be compared to the distribution of module efficiencies for a typical module, shown in Fig. 4.7(a). Based in the discussion in previous section, we choose the optimal design parameters for each scribing scheme. For the lengthwise periodic scribing, we choose full length scribes 5 cm apart (i.e. $N_{scribe} = 24$). For both the selective scribing schemes we choose $N_{iso}/N_{sub} = 3\%$,

using $L_{scribe} = 5$ cm, and $A_{scribe}/A_{sub} = 40\%$ for the partial and full isolation, respectively. These numbers are chosen because, from Fig. 4.13 we note that the incremental improvement in module efficiency with scribing more shunts or using longer scribe is minimal. Moreover, these values are reasonable from a practical standpoint of implementing this strategy in a production environment. In practice, these quantities need to be optimized for the technology of choice, the shunting and scribing parameters of the process, and the required efficiency improvement.

Fig. 4.14 compares the CDFs of module efficiency without any scribing with those obtained for each scribing method. Note that as expected from previous sections, the mean module efficiency $\bar{\eta}$ improves by $\sim 0.3\%$ (absolute) for lengthwise periodic scribing, $\sim 0.7\%$ (absolute) for selective partial scribing, and $\sim 1.1\%$ (absolute) for selective full scribing isolation method. Interestingly, note that simply by isolating only 3% of the shunts, and even allowing for significant area penalty for each isolating box, we can bring the module efficiency very close to "ideal" module efficiency $\eta_0 = 8.9\%$, which is obtained for a module without any shunt defects. Equally importantly, along with the improved average module efficiency, the scribing isolation of shunts also leads to reduced standard deviation s_N of the module efficiency distribution, as shown in Fig. 4.14. This means that in addition to the improvement in overall module efficiency, the scribing techniques also reduce the performance variability associated with random shunt formation. This in turn will improve the overall yield of the manufacturing process, which is an important factor in PV manufacturing cost.

4.5 Conclusions

In this chapter, we developed hybrid device-circuit modeling approach for analyzing the effect of statistical fluctuations on cell and module performance. The key advantage of this approach is that it allows us to incorporate the correct physics and statistics of fluctuation in simulations, and provides a way of carefully evaluating their interdependencies during operation. We used this method to analyze variability

issues due to microscopic grain size fluctuations, and mesoscopic shunt magnitude variation. Having understood the mechanism by which these variations cause losses during operation, we proposed a technology agnostic solution for module efficiency enhancement, and evaluated its effectiveness in realistic scenarios. The key messages from this chapter can be summarized as follows:

1. Microscopic grain size variation
   (a) Grain size variability in polycrystalline TFPV cells results in a cell efficiency, which is in between the best and worst grain structure.
   (b) The cell efficiency is equal to mean efficiency of smaller polycrystalline micro-cells, because the micro-cells operate independently of each other.
   (c) Cell performance variability is not caused by the grain size variation, as these fluctuations are averaged out over length scales of few mm.
2. Mesoscopic shunt magnitude variation
   (a) Design of series connected cells in monolithic TFPV modules is dictated by the competition between sheet resistance loss, and dead area loss due to finite width of scribe lines used for creating series connection.
   (b) Mesoscopic shunt variation from cell to cell affects only small fraction of cells significantly, due to the asymmetric relationship between I_{SH0} and cell efficiency.
   (c) At the module level, parasitic shunt distribution in interconnected subcells, is responsible for a majority of cell to module efficiency gap, for the representative monolithic TFPV technologies.
   (d) The most severe effect of parasitic shunts on module efficiency arises because the shunted regions adversely affect the 'good' neighboring regions, and reduce their power output.

(e) Reduction of the interaction between shunted sub-cells and their neighbors, offers a powerful, technology agnostic, solution for improving the module output in presence of random shunts.

(f) An approach utilizing scribing isolation for reducing shunt losses can be implemented in different ways, with or without a detection step, to obtain 20-40% relative improvement in module efficiency for a monolithic TFPV technology.

(g) Scribing isolation of shunts can also improve the process yield of module manufacturing, by reducing the variation in module efficiency caused by parasitic shunting.

5. SHADOW STRESS AND SHADE TOLERANT DESIGN

In the previous chapter, we focused on the performance of 'as fabricated' TFPV cells and modules, and analyzed their performance and variability issues using a circuit simulation approach. Now, we turn our attention to the long term reliability and safety of TFPV modules. A brief survey of reliability issues associated with PV technologies was given in Sec. 3.3, covering both the *front end* and *back end* issues. We identified shading induced reverse bias stress as an important reliability concern, and discussed its impact on cell degradation in 3.4.

In this chapter, we will focus on the origin of this reverse stress under partial shading for TFPV modules, and provide a general solution mechanism for its prevention. We use the equivalent circuit approach developed in Chapter 4 to analyze the effect of partial shading in TFPV modules. We begin in Sec 5.2[1] by examining the effect of partial shading on cell operation, and discuss how it leads to reverse stress. We then extend this analysis to realistic TFPV modules in Sec. 5.3[2], and use full 2D circuit simulations to highlight the unique aspects of shading in TFPV modules, and validate our predictions with thermal imaging data. Finally, in Sec. 5.4[3], we propose a general design solution to the shadow problem, and evaluate its effectiveness for different shading scenarios.

5.1 Introduction

During the first deployment of solar cells for powering the satellites, it was recognized that a few partially shaded cells in a string of series connected cells, can lead to reverse bias across shaded cells, and there is a disproportionately large drop in string

[1]Text and figures in this section are taken from [181] ©IEEE 2012
[2]Text and figures in this section are taken from [194] ©IEEE 2013
[3]Text and figures in this section are taken from [185] ©John Wiley & Sons 2013

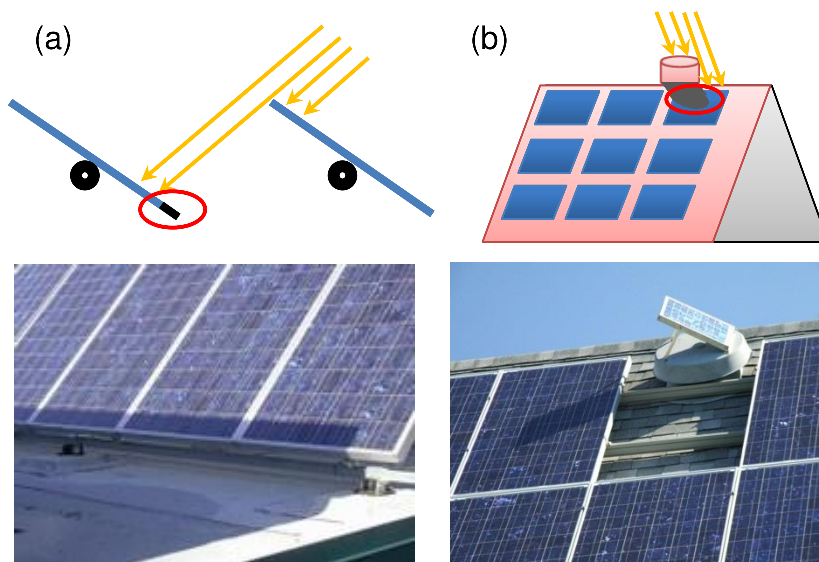

Fig. 5.1. (a) Schematic showing partial shading caused by nearby modules, usually when sun is at shallow angles during morning or evening. An example photograph of this shading in an installed array is shown at the bottom. (b) On rooftop systems shadows from nearby objects are also important, as shown schematically at the top, and example image at the bottom. (* Photos taken from google images)

output power [69]. In terrestrial solar arrays, shading is perhaps even bigger concern; and can arise from neighboring modules (see Fig. 5.1(a)), or other nearby objects (see Fig. 5.1(b)). The partial shading is a continuing challenge, as PV adoption increases to building integrated [28], and high population density environments.

Because of the large power loss associated with partial shading, a significant research effort has focused on analysis of system power loss for different shading scenarios [203], and strategies for tracking the system MPP value under shading [204]. At the module level, a significant body of research focuses on circuit techniques for mitigating shadow effects, using integrated bypass diodes inside the module [60]. In addition, several groups have focused on understanding the device breakdown mechanisms in detail [205, 206]. A majority of these research efforts have focused on c-Si modules and systems because of their dominant market share. A comprehensive

analysis of shadow effects in TFPV modules, however, is lacking. In particular we would like to address:

- Effect of shadow stress in the absence of integrated bypass diodes;
- Relationship of module and system architecture and shadow induced stress;
- Issues specific to TFPV modules with rectangular cell geometry; and
- Geometrical solution strategies for shade tolerant module design.

5.2 Partial Shading at System Level

In this section, we will explore the reasons behind shadow induced reverse stress in 1D string of series connected modules, to understand the origin of this behavior clearly. We first discuss the qualitative picture, and then evaluate the exact quantitative details. In this analysis, we will represent each module with a single equivalent circuit. The effect on individual cells inside the modules in this scenario will be considered in the next section.

5.2.1 Partial Shading and Reverse Bias Stress

In order to develop an intuitive understanding of partial shading, we begin by considering an example of a string of 3 modules in series supplying a resistive load, as shown in Fig. 5.2(a). We will analyze the behavior of this circuit when one of the modules is partially shaded. The schematic IV curves of the modules and the string as a whole are shown in Fig. 5.2(b). In this series connected configuration, under normal operation, the module voltages (dashed green line) are added to obtain the string output (solid green line). The load (black line) is choses so that the string supplies the load at maximum power point (green rectangle). In this scenario, all the modules are also biased at their MPP values in forward bias (green dots).

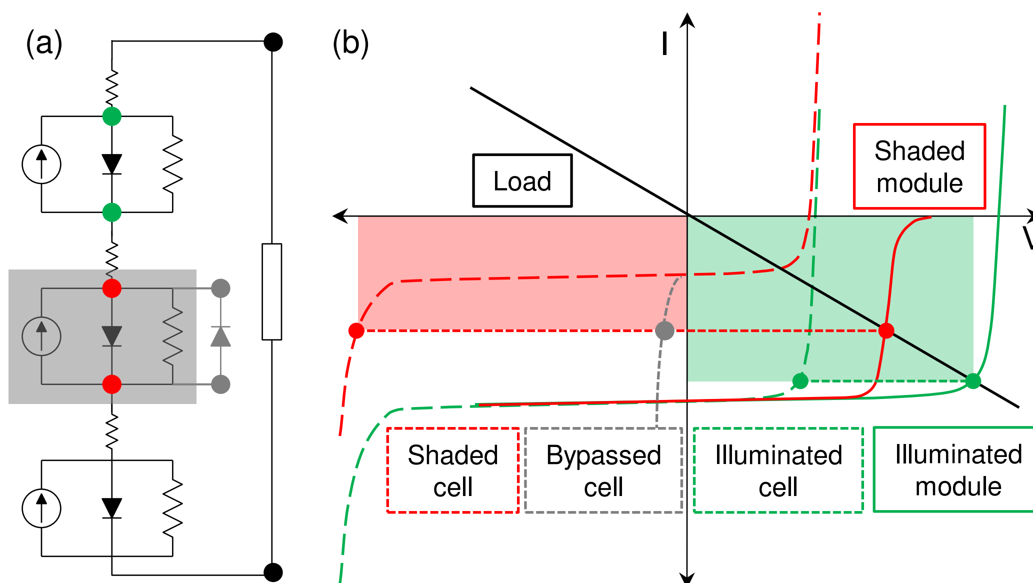

Fig. 5.2. (a) An example circuit of 3 series connected solar modules supplying a resistive load. It illustrates the effect of partial shadow on one of the modules, with or without bypass diode (gray). (b) Schematics of the module (dashed lines) and string (solid lines) IV curves for the example circuit. Under normal operation (green), all operating points are positive (green squares), and the array power output is high (green rectangle). After middle module is shaded, its operating point shifts to negative value (red circles), in order to maintain current continuity, and it starts *dissipating* power (red rectangle). In presence of a bypass diode, the shaded module voltage is clamped near zero (gray circle), preventing module damage.

Now, if the middle module is partially shaded, its photocurrent will drop, and its IV curve will shift upwards (dashed red line). Since the string output is the sum of one shaded (dashed red) and two unshaded (dashed green) curves, it will be modified as shown (solid red). Consequently, the new operating point will move to lower current values (red dots). If the shaded module, however, cannot supply this current in forward bias, its operating point may shift to reverse bias because the current must be continuous in series connected cells, possibly resulting in reverse breakdown (red dots). In this situation, the shaded module actually starts to *dissipate* power instead of producing any, as shown by the red rectangle, which causes a disproportionately

large output power loss, in addition to causing reliability problems due to reverse stress on the shaded module. The most straightforward approach for solving the problem of reverse stress is by putting a bypass diode, with reverse polarity across each module (shown in gray Fig. 5.2(a)). This bypass diode can supply the required current even if the shaded module cannot, and prevents the module voltage from going into reverse bias, as shown in by the gray dashed curve in 5.2(b).

5.2.2 String Operation Under Shading

In order to assess the impact of shading in realistic scenarios, we simulate a typical utility scale PV system with a string inverter topology [168]. The number of modules in the string is adjusted to obtain the required DC output voltage of 505 V. We use typical a-Si:H modules in this analysis, so that 7 modules are required to obtain the desired output as shown in the schematic in Fig. 5.3. The dimensions and output characteristics of the individual modules have been discussed in Sec. 4.3.2. It is assumed that the system DC voltage is kept constant at 505 V during operation. We will evaluate the effect of partial shading in one of the modules of this string, when all other modules are fully illuminated. Partial shade implies only diffused light is reaching the shaded area, which has ∼20% of the intensity of direct sunlight [207]. Therefore, for simulating the shadow we consider $J_{Photo,shade} = 0.2 J_{Photo,direct}$, in SPICE circuit described in Sec. 4.3.

We first perform a 1D simulation to evaluate the module and bypass diode operating points under shading. In this simulation, each module is represented as a series connection of 104 a-Si:H cells, each of which is represented using the equivalent circuit discussed in Sec. 2.6. Note that this simulation approach does not consider the width of individual cells, but only the number of shaded cells inside the module is varied. Fig. 5.3(a) shows the string output characteristics when increasing number of cells are shaded. Since the string voltage is kept fixed, its operating point shifts to lower current values, until the bypass diode current kicks in (see squares and circles

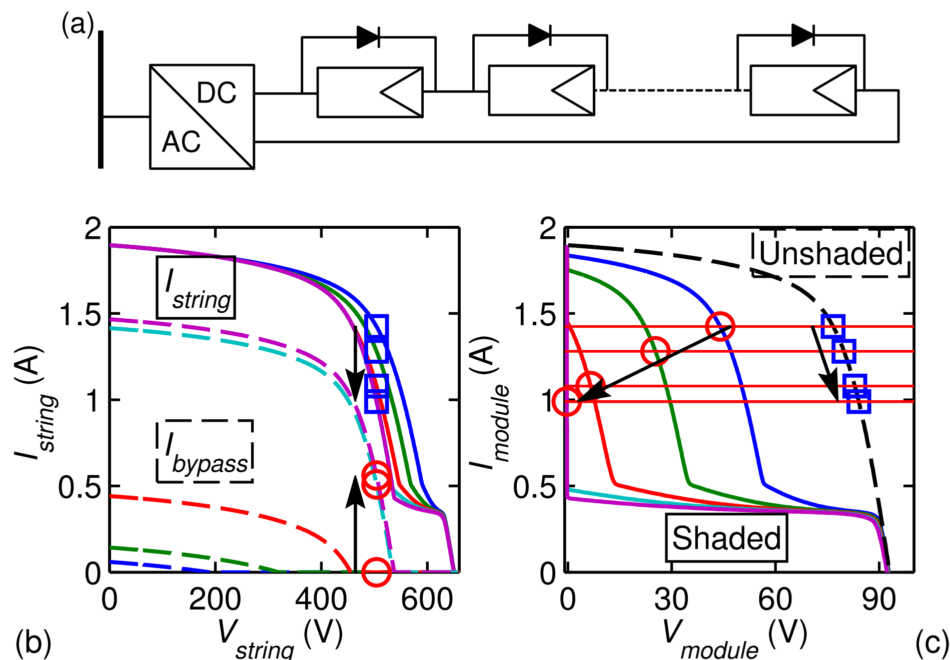

Fig. 5.3. (a) Schematic of typical TFPV string configuration connected to a DC bus, which is considered here for shading simulations. Each module has an external bypass as shown. (b) 1D simulation of partial shading for $V_{string} = 505$ V DC, showing the string (solid) and bypass diode (dashed) currents for increasing shade on one of the modules. The change in operating points of the string (squares), and bypass diode (circles) with increasing shade is shown with arrows. (c) IV curves for individual shaded (solid) and unshaded (dashed) modules in the string, with operating points (circles shaded, squares unshaded) changing for different shading conditions, so that the string current remains continuous (horizontal lines). The operating points stop moving after the shaded module voltage becomes negative, and the bypass diode turns on (see arrows).

in Fig. 5.3(a)) which prevents further output drop. Note that for smaller shadows the bypass diodes do not turn on, and the string output drops strongly with shading. The module IV curves of shaded and unshaded modules for different degrees of shading are compared in Fig. 5.3(b), showing that as the number of shaded cells increases, the output current drops, and the operating voltage of shaded and unshaded modules move in opposite directions to keep the total string operating voltage constant (see squares and circles in Fig. 5.3(b)). And, as the operating voltage of the shaded

module tries to become negative, the bypass diode turns on and clamps this voltage near zero. Throughout these changes the string current remains continuous, and the bypass diode turns on only for larger shading fractions. This means that the *external bypass diode does not turn on until a very large fraction of module area is shaded.* But, as we show next, the shaded cells can experience high reverse biases even for small shadows. And, since the output does not drop significantly for small shadows the external bypass diode remains off and cannot protect the shaded cells.

5.3 2D Shadow Stress in TFPV Modules

The 1D circuit simulation approach discussed above, is useful for analyzing the role of bypass diodes and understanding the string behavior. To understand the effects at cell level, however, we must consider the various shading configurations for shade dimensions and orientations. Fig. 5.4 shows the schematic of a typical TFPV module, with a partial shadow of length (L_{sh}) and width (W_{sh}) as shown. We will first examine the 2D effects of a shadow of a particular dimension ($L_{sh} \times W_{sh}$), and also vary the shadow dimension from 0 to module dimensions to account for all different shadow sizes. Note that in the simulations, the shadow position will be fixed to the bottom left corner of the module (as shown in Fig. 5.4), because it covers most of the typical shades caused by nearby objects (see Fig. 5.1)

We now evaluate the effect of shadow and cell shape for a typical TFPV module. We use the 2D SPICE circuit simulation setup discussed in 4.3, and assume all sub-cells to be identical. The partially shaded region is assumed to receive only diffused light, so that the total absorption flux in the shaded regions is reduced to 20% of the normal 1 Sun irradiation.

5.3.1 Asymmetric Shadow Stress

Because of the thin, long rectangular shape of cells in a monolithic TFPV module, the module will sometimes experience shadows that cover only a fraction of the cell

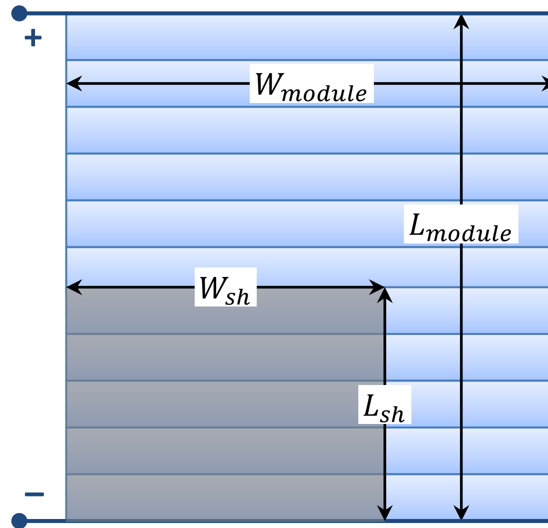

Fig. 5.4. Schematic of a typical TFPV module, with active area dimensions, and partial shadow covering a fraction of some cells at the bottom.

area (i.e., partial shadows), as shown in Fig. 5.4. In order to evaluate the impact of such partial shadows, we simulate the string of 7 modules with a shadow at the bottom left of one of the modules, such that $W_{sh} = W_{module}/2$, and $L_{sh} = 5$ cm. Fig. 5.5(a) shows the color plot of the photon absorption flux (I_{abs}) in each sub-cell in this shading scenario. For clarity, we plot only the results for bottom 26 cells of this module. In this situation, the photogeneration in left half of cells 1 to 5 is reduced by 80% (for $L \leq L_{sh}$ and $W \leq W_{sh}$, marked region 1), while the right half ($L \leq L_sh$ and $W > W_{sh}$, marked region 2), and all other cells from 6 to 104 ($L > L_{sh}$, marked region 3) remain fully illuminated. We perform the 2D circuit simulation for this shading scenario, assuming that all other modules in the string are fully illuminated.

We simulate this module at the string operating point to get the voltage across each sub-cell (V_{sub}) in the module. The simulation results are shown in Fig. 5.5(b) as a 2D color plot, showing that the reduced photocurrent in cells 1 to 5 have pushed them in reverse bias. Note, however, that this reverse bias voltage is essentially uniform at $V_{sub}^{shaded} \approx 8.8$ V across the entire width of the cell (regions 1 and 2),

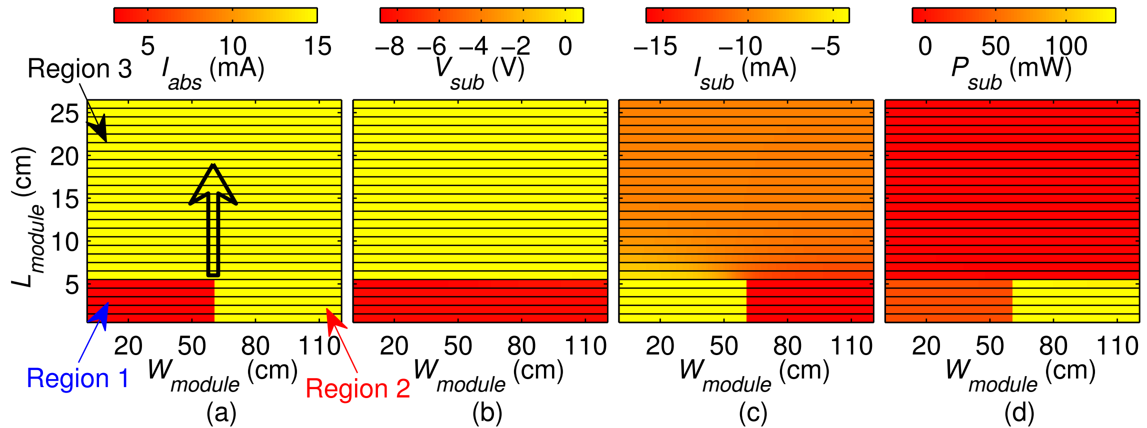

Fig. 5.5. 2D color plots of 26 rectangular cells (y-axis scaled for clarity) in a TFPV module with a partial shadow covering left half of 5 cells at the bottom (arrow shows direction of current flow, and the color bar on the top denotes the values). (a) The photo-generated current I_{abs} in sub-cells is reduced for left half of cells 1 to 5 (marked region 1), while their right half (marked region 2), and cells 6 and above (marked region 3) are fully illuminated. (b) The distribution of sub-cell voltage (V_{sub}) in this scenario shows that all sub-cells in the 5 partially shaded cells are reverse biased with $V_{sub}^{shaded} \approx 8.8$ V across the cell width (regions 1 and 2), but the fully illuminated cells continue to operate in forward bias so that $V_{sub}^{illum} \approx 0.76$ V. (c) The sub-cells current I_{sub} shows asymmetric behavior, and I_{sub} in region 2 increases to ~ -16 mA, to compensate for the low $I_{sub} \approx -4$ mA in region 1, to ensure current continuity with fully illuminated cell where $I_{sub}^{illum} \approx -10$ mA. (d) As a consequence of the voltage and current redistribution in cells 1 to 5, the sub-cell power dissipation P_{sub} in region 2 is four times that of region 1 (positive values in this sign convention), while the fully illuminated cells 6 and above continue to produce power (negative values in this sign convention).

while the fully illuminated cells in region 3 continue to operate in forward bias at $V_{sub}^{illum} \approx 0.76$ V. The sub-cell current direction in the partially shaded cells (regions 1 and 2), however, remains unchanged (therefore $I_{sub}^{shaded}, I_{sub}^{illum} < 0$), as shown in the color plot in Fig. 5.5(c). As a consequence, the shaded cells actually dissipate power (in our sign convention, this means $P_{sub}^{shaded} = V_{sub}^{shaded} \times I_{sub}^{shaded} > 0$), while

the fully illuminated forward-biased cells in region 3 continue to produce power, so that $P_{sub}^{illum} = V_{sub}^{illum} \times I_{sub}^{illum} < 0$, see Fig. 5.5(d). Note that this power dissipation ($P_{sub}^{shaded} > 0$) occurs in the semiconductor junction under reverse bias as $V_{sub}^{shaded} < 0$; as opposed to fully illuminated cells in forward bias, which produce useful output power ($P_{sub}^{illum} < 0$). This must not be confused with resistive power loss in the contact metal/TCO layers, which is much smaller and continues regardless of the presence of a shade.

This partial shading leading to reverse bias in shaded cells is well known issue and applies to all PV technologies [193]. In thin film PV, however, the thin long shape of the individual cells results in a large asymmetry in current flow through the partially shaded cell; so that the current in the unshaded part (region 2) of the partially illuminated cells increases to balance the loss of photocurrent in the shaded part (region 1). This is visible in the color plot of sub-cell current I_{sub} in Fig. 5.5(c); which shows that while the current through fully illuminated cells in region 3 is essentially uniform, there is a stark asymmetry in current flow between region 1 and region 2 of the partially shaded cells. In these cells, the current in shaded region 1 reduces due to reduced photogeneration, so that $I_{sub}^{shaded,1} \approx -4$ mA. In order to compensate for this decrease in region 1, the current in the sub-cells in region 2 increases to -16 mA. The most important consequence of this redistribution in I_{sub}^{shaded} is that the unshaded region 2 dissipates more power than the shaded region 1, and in our example $P_{sub}^{shaded,2} \approx 4P_{sub}^{shaded,1}$, as shown in Fig. 5.5(d), because $I_{sub}^{shaded,2} \approx 4I_{sub}^{shaded,1}$ while V_{sub}^{shaded} is equal in regions 1 and 2, as shown in Fig. 5.5(b). A sanity check for these simulation results can be done by ensuring that the total current flow in these series connected cells is equal, i.e., $I_{cell}^{illum} = I_{cell}^{shaded}$. For the fully illuminated cell (cells 6 to 104), $I_{sub}^{illum} \approx -10$ mA per sub-cell, so that for each cell with 120 sub-cells $I_{cell}^{illum} = 120 \times I_{sub}^{illum} \approx -1.2$ A. In the partially illuminated cells 1 to 5, the current in region 1 $I_{sub}^{shaded,1} \approx -4$ mA, and in region 2 $I_{sub}^{shaded,2} \approx -16$ mA (Fig. 5.5(c)). This ensures that net cell current in the shaded cells $I_{cell}^{shaded} = 60 \times I_{sub}^{shaded,1} + 60 \times I_{sub}^{shaded,2} \approx -1.2$ A, which is same as fully illuminated cells. Note that the sub-cell current in

region 2 (-16 mA) is higher than the photocurrent (-15 mA), because these sub-cells are in reverse bias where the dark and photocurrent are in the same direction.

5.3.2 Origin of Asymmetric Stress

In order to clarify the origin of this asymmetric stress in partially shaded cells, we compare the IV characteristics of fully and partially illuminated cells in the the module, as shown schematically in Fig. 5.6 for cell no. 5 (in regions 1 and 2) and 6 (in region 3). Under normal operating conditions (no shading anywhere) both cells will operate at their maximum power point (0.7 V, -0.72 A, so that $I_{cell} = -1.45$ A for all cells), marked with red asterisk in Fig. 5.6. Fig. 5.6(a) shows the IV characteristics of the shaded and unshaded *halves* of cell 5, and half the current of cell 6 ($I_{cell}/2$). Without shade these half cells are identical, which means that all sub cells are operating at their MPP, with $V_{sub} \approx 0.7$ V, and $I_{sub} \approx -12$ mA.

When the left half of cell 5 is shaded, the output current reduces to -1.2 A, so that the current through illuminated half of cell 6 (region 1, green) moves to -0.6 A (green circle). The current in region 1 (red) is suppressed below $I_{cell}/2$ due to shade (such that $I_{sub}^{shaded,1} \approx -4$ mA in this region); therefore the operating point of cell 5 shifts, so that the current in region 2 becomes higher than $I_{cell}/2$ (and $I_{sub}^{shaded,1} \approx -16$ mA), which pushes the shaded cell in reverse bias ($V_{cell}^{shaded} \approx -8.8$ V), such that the total current in half cells $I_{cell/2}^{shaded,1} + I_{cell/2}^{shaded,2} = I_{cell}$ (black dashed line). Comparing the total IV of cells 5 and 6 (solid lines in Fig. 5.6(b)), we observe that the operating point for the illuminated cell 6 (green) moves to lower current value on shading (red asterisk to green circle). However, since the current output of cell 5 (blue) has dropped, it must operate in a reverse bias (blue circle). The plot in Fig. 5.6(b) also highlights the role of reverse characteristics of the shaded cells in determining the operating point. As apparent from the figure, a less abrupt reverse characteristic (due to non-Ohmic shunts in TFPV cells) allows for more stable operating points at lower reverse voltages and alleviates some of the shade induced stress.

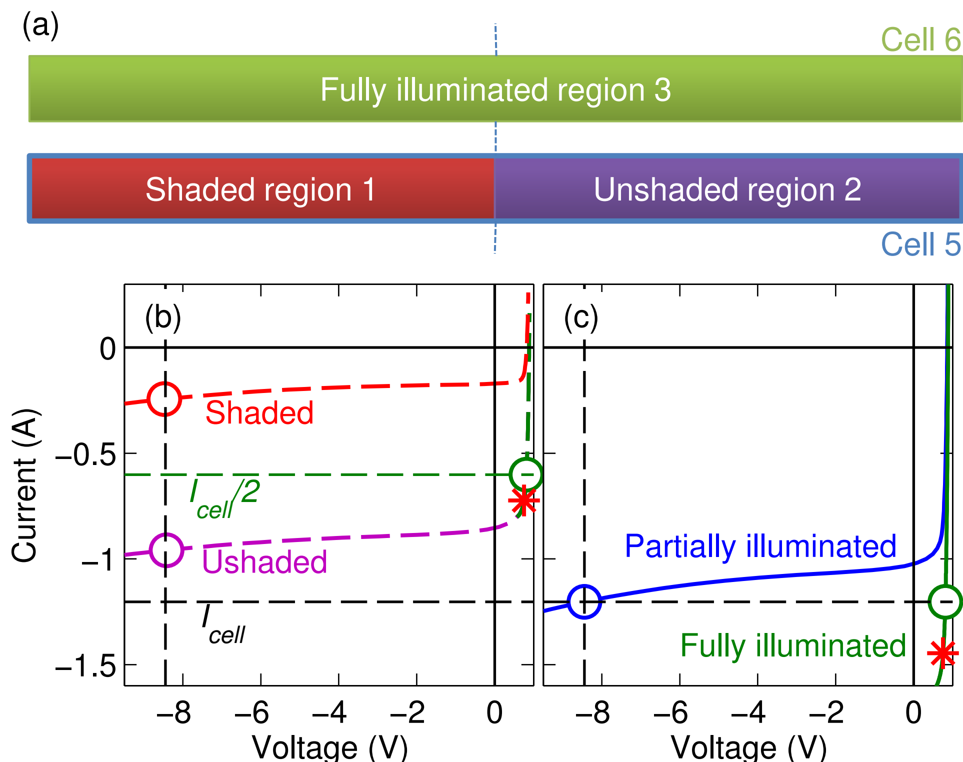

Fig. 5.6. (a) Schematic showing a pair of cells at the edge of the shaded and unshaded regions for the shade considered in Fig. 5.5 namely, fully illuminated cell 6 in region 3 (green) in series with the partially illuminated cell 5 (blue), with a shaded region 1 (red) and unshaded region 2 (purple). (b) The IV curves of half cells, including the shaded (red), unshaded (purple), and fully illuminated (green) halves, show that as the current in region 1 drops the current in region 2 must increase beyond even $I_{cell}/2$ to maintain current continuity. (c) The full IV curves of the cells (solid lines) showing that the total current through partially shaded illuminated 5 (blue) is same as the fully illuminated cell 6 (green), and their respective operating voltages determined by the amount of photocurrent reduction in the shaded cell.

Note that the transition of current flow from asymmetric distribution in the partially shaded cells (regions 1 and 2), to symmetric distribution in the fully illuminated cells (region 3) cannot occur abruptly, and must be spread over several cells. As seen in Fig. 5.5(c), the I_{sub}^{illum} in cells 6 to 8, which are nearest to the shaded cells, varies slightly along the width, in order to accommodate the asymmetric $I_{sub}^{shaded,1}$ and

$I_{sub}^{shaded,2}$ entering cell 6 from the partially shaded cell 5, while maintaining current continuity. This is made possible by a rearrangement in sub-cell voltages along the width of the fully illuminated cells nearest to the shaded regions, as dictated by the sheet resistance values of the metal and TCO contacts. This asymmetry of current flow in the fully illuminated cells, however, is reduced as we move away from the shaded regions (see Fig. 5.5(c)). This 2D rearrangement of sub-cell current and voltage, and its relation to sheet resistance, are discussed in greater detail in appendix C.

This observation also highlights the need to differentiate between reverse voltage stress (which is uniform for regions 1 and 2), and stress due to electrical heating due to power dissipation in the junction (which is substantially higher in region 2) in partially shaded cells in TFPV modules, as apparent from Fig. 5.5(d). Note that this "non-local" heating due to partial shade may occur in conventional c-Si cells as well, if only part of an individual cell area is shaded. The compact shape of c-Si cells, however, ensures that the 2D effects are much less pronounced and distribution of electrical heating due to partial shade is not readily observable in thermal images with limited resolution [170, 208]. In TFPV cells, however, this prominent distinction between shaded and unshaded portions of the partially shaded cells is a consequence of the thin long cell geometry and two-dimensional current flow in TFPV modules.

5.3.3 Experimental Validation of Asymmetric Stress

Although monolithic structure of TFPV modules makes it difficult to access individual cells inside for directly validating the simulation results of previous section, we can use noninvasive IR thermal imaging for assessing the impact of shading and evaluating the predicted behavior [170]. This imaging technique allows us to estimate the temperature in different regions of the module, in the event of shading for building a qualitative insight into the stress behavior. The modules used for this test are Shell Eclipse-80 CIGS modules installed in a grid-tied system at NREL's outdoor test facility. The system is composed of two series strings of seven modules each. As a

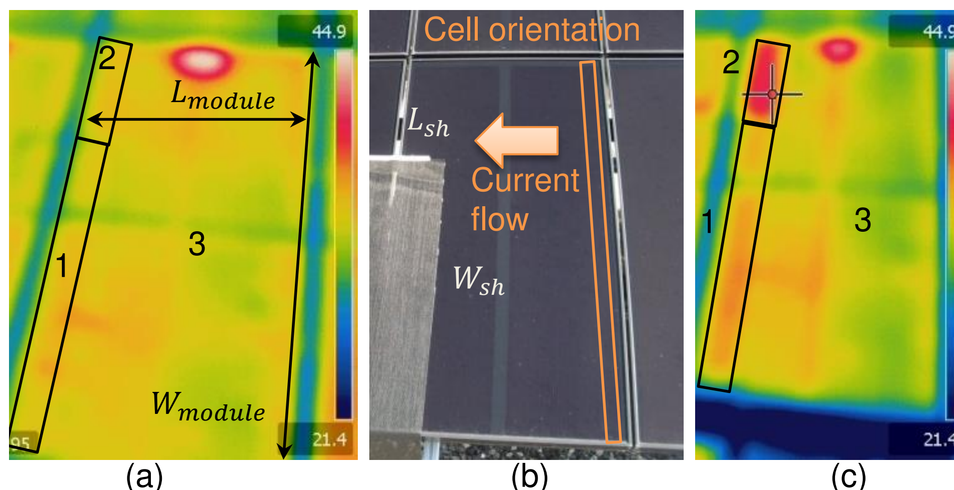

Fig. 5.7. (a) IR thermal image of fully illuminated series connected modules under normal operating conditions showing roughly uniform operating temperature of 32-34 °C (color bar on the right indicates temperature in °C). The hot spot at the top appears in all modules, due to placement of the connectors in that region resulting in current crowding and local heating. The module dimensions for these vertically oriented modules, and positions of regions 1, 2, 3 as defined in Fig. 5.5 are also shown. (b) An image of the same module under partial shade using a translucent shading cloth with 27% transmittance. The shade dimensions, direction of current flow and cell orientation are also marked. (c) The IR thermal image immediately after removal of the shade showing a slight temperature rise to 34-36 °C shaded region 1, but the temperature in unshaded region 2 is noticeably higher at 39–41 °C, and the temperature of fully illuminated region 3 is largely unchanged, as anticipated by theory.

monolithically constructed module, the Shell Eclipse-80 CIGS module has long, thin cells running the length of the module. Two separate sub-modules of 42 cells apiece are integrated into a single frame, individually protected by bypass diodes and placed in series with each other. Thermal imaging of the system was conducted with a FLIR SC640 hand-held thermal digital camera. The outdoor ambient temperature was 15–17 °C and incident plane-of-array irradiance was $86 - 92$ mW/cm^2 during experiment timeframe. We note that the temperatures recorded from these IR images are subject to a variety of extrinsic and environmental factors, and therefore qualitative

in nature [209]. We will therefore focus on the relative temperature differences across different regions of the module when analyzing the shadow effect.

Fig. 5.7(a) shows the thermal image of a series-connected module under normal operating conditions, indicating a roughly uniform temperature across the module, at around 32 °C. Note that the hot spot near the top of the module forms due to current crowding in that region, caused by the placement of connectors, and appears in all modules under normal operation. These modules are vertically oriented, as shown by the module dimensions marked in Fig. 5.7(a). The three regions as defined in Fig. 5.5 are also shown. For assessing the 2D shading effect, the module was shaded by partially covering few cells with a translucent cloth (with 27% transmittance). The shade dimensions are marked in Fig. 5.7(b), showing that $L_{sh} \approx 19$ cm and $W_{sh} \approx 0.75W_{module}$. The thermal image of the modules immediately after the removal of shading fabric is shown in Fig. 5.7(c), showing that the temperature of unshaded region 2 increased to 39-41 °C, which is noticeably higher than the shaded region 1 for the partially shaded cells, where the temperature increased to 34-36 °C. On the other hand, the temperature of fully illuminated cells in region 3 remains largely unchanged around 32-34 °C, as expected from the simulation results in Fig. 5.5. Note that the simulation predicts asymmetric electrical dissipation across the partially shaded cell (see Fig. 5.5(d)), while the fully illuminated cells continue to produce power. This is also apparent in Fig. 5.7(c), which shows that the overall temperature in fully illuminated cells (marked 3) does not change, but power dissipation in regions 1 and 2 of the partially shaded cells causes a temperature rise in these regions. Despite the local variations in temperature across the module surface due to manufacturing non-uniformities, as well as camera angle and reflections, the general trends in temperatures in regions 1, 2 and 3 are in good qualitative agreement with the simulation results.

In order to better understand the reasons behind this temperature change, we must consider the various heat fluxes on the module surface. Fig. 5.8(a) shows a schematic of the partially shaded module showing the insolation (marked Q_s) and electrical

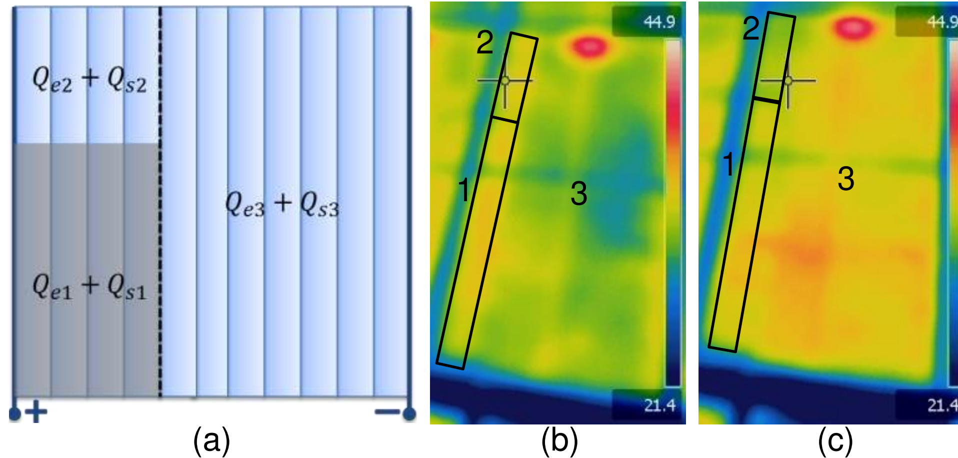

Fig. 5.8. (a) Schematic of partially shaded module showing the electrical (Q_e) and insolation heat (Q_s) flux components in the three regions of interest. (b) IR thermal image of module in steady state at V_{OC} showing roughly uniform temperature across the module surface, with relatively small extrinsic variation. This is then subjected to the identical shading conditions as in Fig. 5.7. (c) IR thermal image immediately after the partial shade is removed does not show any significant difference in temperatures between regions 1, 2, and 3; demonstrating that the differential heading due to insolation is essentially negligible.

(marked Q_e) heat flux components in different regions. The insolation heating Q_s is caused by incident radiation and is proportional to the light intensity falling on the module. Since regions 2 and 3 are illuminated, we have $Q_{s2} = Q_{s3} = Q_{s0}$, where Q_{s0} is equal to the fraction of incident light lost as heat under normal operation. Typically, this arises from non-radiative recombination and resistive losses in metal/TCO layers [209]. To a good approximation we can assume $Q_{s0} \approx 0.4 \times \phi_{inc} \approx 36$ mW/cm^2 [210], where ϕ_{inc} is the plane-of-array irradiance which is ≈ 90 mW/cm^2 in our case. And, due to the 27% transmittance of the cloth in region 1 $Q_{s1} = 0.27 Q_{s0} \approx 10$ mW/cm^2. From the difference in Q_{s1} and Q_{s2} it might appear that the asymmetric temperature rise in Fig. 5.7(c) may be caused in part due to the difference in insolation heating.

The total heat generated during shading, however, includes heating due to power dissipation in the shaded regions as calculated in Fig. 5.5(d) (note that electrical

power flux $Q_e = P_{sub}/A_{sub}$). Extrapolating from the simulations, we can estimate $Q_{e3} \approx -10$ mW/cm^2 for the forward biased cells in region 3 which are generating output power; and $Q_{e2} \approx 3Q_{e1} \approx 150$ mW/cm^2 for reverse biased regions 1 and 2 dissipating power for the duration of the shade. In this scenario $Q_{s2} + Q_{e2} =$ 186 mW/cm^2 $> Q_{s1} + Q_{e1} = 60$ mW/cm^2, which is consistent with the observations in Fig. 5.7(c).

In order to experimentally confirm that the actual contributions from insolation heating are small, we repeat the same shading experiment with IR thermal imaging while keeping the module at open circuit. At open circuit, no current flows through the module, so there is no reverse stress or electrical asymmetry ($I_{sub}(V_{OC}) = 0$ ensures that $Q_{e1} = Q_{e2} = Q_{e3}$), and we will be able to infer the differential contribution of Q_s alone. Comparing the thermal image of and open circuit module before shading (Fig. 5.8(b)), to the image taken immediately after the shade is removed (Fig. 5.8(c)), we find that the temperature difference between regions 1 and 2 is minimal, affirming that insolation alone cannot cause significant asymmetric heating. Thus, we can be confident that the temperature difference between regions 1 and 2 observed in Fig. 5.7(c) is indeed due to a rearrangement of current flow pattern, resulting in an asymmetric electrical heating, in qualitative agreement with the theoretical predictions of the previous section. Note that the exact heating contributions from various sources will depend on cell geometry, module configuration, contact resistances, etc.; however, key theoretical prediction regarding asymmetric heat generation in shaded cells will remain valid.

5.3.4 Effect of Shadow Size And Orientation

So far, we have considered a shadow of specific size and orientation, and examined its impact on the shaded cells. The shape and size of shadows, however, can change due to random events, or depending on the time of the day. Fortunately, all shadows do not result in reverse bias stress across shaded cells. In order to explore the effect of

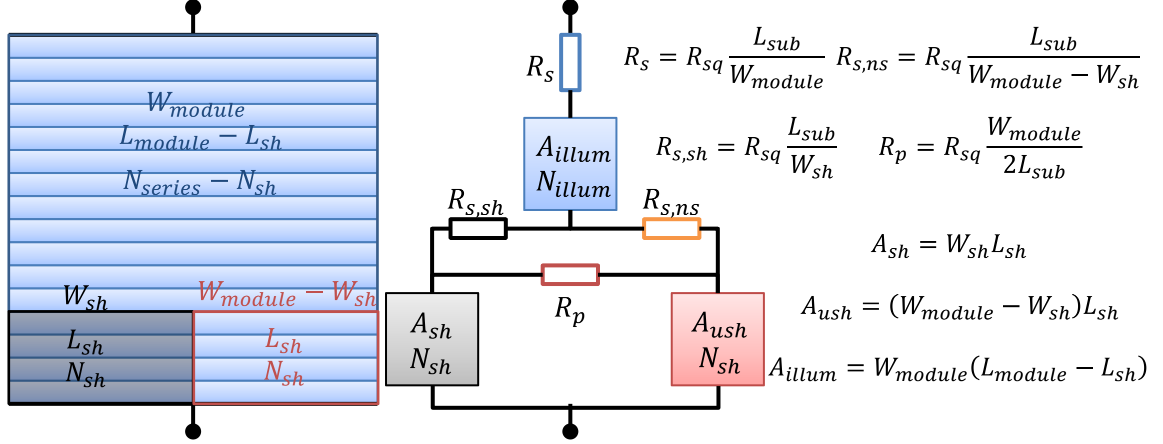

Fig. 5.9. Schematic showing a partially shaded module with module and shadow dimensions, along with the simplified 3-element equivalent circuit with blocks for the shaded and unshaded fractions of the partially shaded cells, and fully illuminated cells of the module. The current and voltage scaling parameters, as well as equivalent resistance values are shown.

different shadow sizes and shapes, we next vary the size and orientation of a shadow by changing L_{sh} and W_{sh}, and evaluate the corresponding reverse stress as well as output power loss, under different shading scenarios. In this section, we will be focusing on the overall cell voltage V_{cell} across the partially shaded cells. Therefore, we can simplify the large 2D circuit of sub-cells into a two element circuit, in which current and voltage outputs change with varying L_{sh} and W_{sh}, respectively.

Simplification of the 2D Circuit

In our simulations we have assumed that all the sub-cells have identical IV characteristics, representing the average performance. Therefore, we can simplify the circuit representation of a module and reduce it to a single equivalent circuit. For a module with N_{series} cells in series each with area A_{cell}, and module dimensions $W_{module} \times L_{module}$ (as shown in Fig. 5.4), we can use a single equivalent circuit by

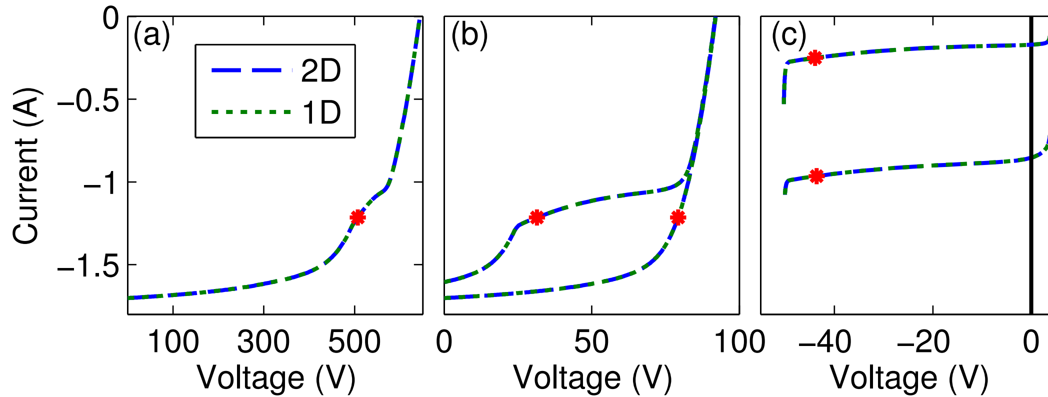

Fig. 5.10. IV characteristics comparing the full 2D simulations (blue dashes) with the simplified 1D case (green dotted) for the partial shading scenario considered in Section 2. The 1D and 2D cases are virtually indistinguishable, showing that the (a) string output, (b) module output for shaded and unshaded modules, as well as (c) characteristics of the shaded and unshaded halves of the partially shaded cells, are identical.

appropriately scaling the terminal voltage, current and series resistance; so that $V_{eq} = V_{terminal}/N_{series}$, $I_{eq} = A_{cell} \times J_{terminal}$, where $J_{terminal}$ is the total sub-cell current, and $R_{s,eq} = R_{\square} L_{module}/W_{module}$. These scaling relations are a straightforward consequence of series (addition of voltage) and parallel (addition of current) connection of individual sub-cells.

Similar simplification is possible for a partially shaded module, which can be divided into 3 equivalent circuits connected in series and parallel, as shown in Fig. 5.9. Based on the number of series connected cells in the region, the area of cells in the region, and the length and width of the region under consideration, we can use the same voltage, current and series resistance scaling as above (details in Fig. 5.9). We also need to include a parallel connection between the shaded and unshaded fraction at the bottom. This needs a parallel resistance from the midpoint of the shaded region to the midpoint of unshaded region on the right, as shown in Fig. 5.9.

Once the equivalent circuits and interconnections are set up with correct scale parameters, we can compare its output to the full 2D circuit simulation with partial

shading. For the shading conditions considered in the previous section, we plot the results obtained from the full and simplified simulations in Fig. 5.10. We find that the string level characteristics (Fig. 5.10(a)), as well as the module level characteristics for shaded and unshaded modules (Fig. 5.10(b)) are identical for 2D and 1D simulations. The characteristics across the shaded and unshaded halves are also the same (Fig. 5.10(c)), as are the operating points for the two simulations. This comparison shows that the simplified equivalent circuit approach does not compromise on the accuracy of the simulations, and allows us to sweep the shadow sizes at a much smaller computational expense.

Shadow Geometry and Reverse Voltage Stress

We first explore the relationship of shadow size with reverse bias stress on shaded cells. The top schematic in Fig. 5.11 identifies the important shading scenarios, which are also highlighted in the plots. Fig. 5.11(a) shows the worst-case cell voltage in a module, as a function of shadow width and length. Each point on the xy plane represents a shadow of certain width and length, with the minimum V_{cell}^{min} under those conditions displayed as corresponding color (color bar in V). In the absence of shadows, all cells operate at their maximum power point ($\sim$ 0.8 V), as expected (marked 1). The importance of shadow orientation can be illustrated by considering the case of thin wide shadows along the edges. Note that for asymmetric edge shadows, where a few cells are shaded fully along the width (marked 3), the shaded cells can go into severe reverse bias and breakdown ($\sim$ -10 V). On the other hand, a similar shadow oriented along the vertical edge is completely harmless, since all the cells are shaded equally and stay in forward bias after shading (marked 2). Most typical shadows, however, will be smaller than the module dimensions, and would result in moderate (-2 V to -5 V) reverse bias stress on shaded cells (marked 4). This orientation dependence of partial shading is in accordance with the module installation instructions from TFPV manufacturers.

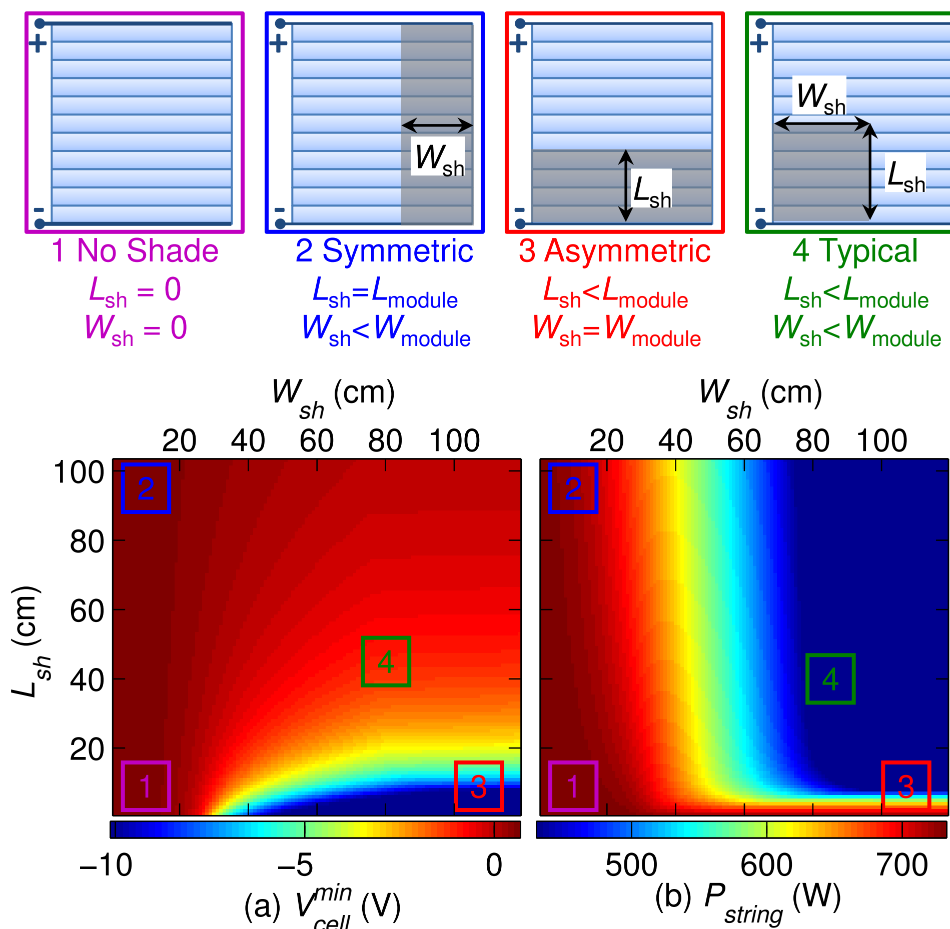

Fig. 5.11. Schematics at the top highlight the important shading scenarios, with consequences shown in plots below. (a) Color plot showing the worst case reverse bias (color bar in V) across a cell in the shaded region for shadows of different length (y-axis) and width (x-axis). Note that unlike the symmetric edge shading (marked 2), the asymmetric edge shadow (marked 3) causes reverse breakdown of shaded cells, but typical shadow stresses (marked 4) are fairly moderate. (b) String output power (color bar in W) as a function of varying shadow sizes, shows that small edge shadows (2 and 3) do not cause significant drop in output power, which only happens for large shadow sizes.

Shadow Geometry and Output Power Loss

We can also evaluate the impact of various shading scenarios on string DC output power loss. The plot in Fig. 5.11(b) shows the DC output power of the string, for

a variety of different shadow sizes. We can see that large shadows cause significant output power loss, but do not cause extreme reverse stress on individual cells, because the reverse bias is distributed across many shaded cells. On the other hand, the power loss is small for edge shadows, but the asymmetric edge shadow causes the worst reverse stress. This underscores the fact that loss of output power may not correlate with large reverse stress on shaded cells, as large shadows cause power loss but do not cause large stresses. This also brings into focus the role of external bypass diodes, and their ability to prevent output loss and/or reverse stress.

Limitations of External Bypass

In order to gauge the role of external bypass diodes, we perform the shading simulations for all shadow sizes, with and without external bypass. Fig. 5.12(a) plots the difference in worst case shaded cell voltages, with and without external bypass diode, i.e. $\Delta V_{cell}^{bypass} = V_{cell}^{bypass} - V_{cell}^{no,bypass}$. We find that for a majority of shading cases, the presence of external bypass has no impact on stress voltages. For a few cases, the reverse stress voltages are smaller in presence of external bypass. This improvement however, is small (< 1.5 V) in the best of cases. Moreover, it shows that the external bypass diodes become active only for large shadows, when the module operating voltage becomes negative. This means that for cases like asymmetric edge shadow (marked 3 in Fig. 5.11), which causes reverse breakdown in shaded cells (see Fig. 5.11(a)), the bypass diodes remain off. Therefore, external bypass diodes cannot provide any significant protection to individual cells from shadow stress.

External bypass diodes do, however, help in limiting the output power loss, as seen by plotting the difference in string output power in presence of external bypass ($\Delta P_{string}^{bypass} = P_{string}^{bypass} - P_{string}^{no,bypass}$). As shown in Fig. 5.12(b), we can get up to 200 W extra power output from the string, when modules have external bypass diodes, but this improvement is only obtained for large area shadows. Thus, we see that external

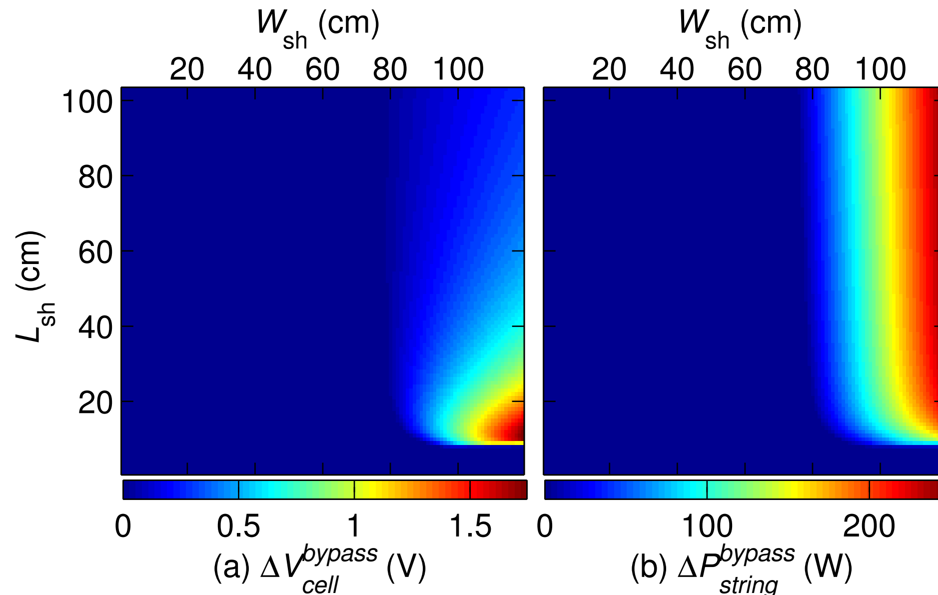

Fig. 5.12. Role of external bypass diodes is explored by comparing the cases with or without bypass diodes. (a) ΔV_{cell}^{bypass} is the difference between worst case reverse stresses (color bar in V) in presence and absence of external bypass is plotted for different shadow sizes, showing that external bypass only marginally (by about 1 V) reduces the shadow induced stress, typically for larger shadows. (b) The difference in string power output $\Delta P_{string}^{bypass}$, due to external diodes (color bar in W) shows that while there is no impact for smaller shadows, for large shadows external bypass diodes can limit the string DC output loss by about 200 W.

bypass diodes cannot protect individual cells from shadow-induced reverse stress and damage, but do limit the power loss in the case of large shadows on the module.

5.3.5 Long Term Reliability Prediction

Having looked at the device and circuit level implications of shadowing, we combine these insights to obtain predictive long term models of module reliability. We also propose design solution to shadow problems, based on insights from circuit analysis.

Over the operating lifetime of a module, a cell will be subjected to repeated shadow stresses of different magnitudes for random lengths of time. This would

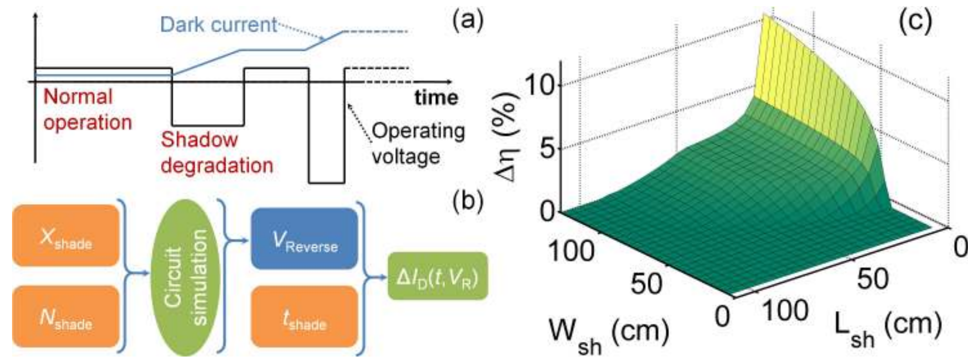

Fig. 5.13. (a) Schematic representation of repeated shadow stresses during operation resulting in I_{Dark} degradation. (b) Flowchart showing the simulation method used for estimating the statistical degradation mechanism. (c) Due to this parametric shadow degradation, the expected efficiency loss over 25 year operation of module with 2 hours of partial shadow each day, for different shading scenarios.

result in steady parametric increase in dark current due to increase in both I_{SH} and I_{diode} (shown schematically in Fig. 5.13(a)). In order to estimate the increase in I_{diode} during a particular shading event; we need to know the reduction in photo-current of the shaded cells, the number of shaded cells, and the duration of shading. We can use the shading fraction and number of shaded cells, and use the simulation discussed in Sec. 5.2 to obtain the reverse stress voltage V_R caused by the shadow. We can then use this stress voltage value and stress duration in the empirical relation of $I_D(t, V_R)$ shown in Fig. 3.8(a), to estimate the shadow-induced output degradation for each shading event. For a module lifetime of 25 years, with 2 hours of shadow per day, the degradation expected for various shading scenarios can be as high as 10% (Fig. 5.13(b)) [121], which is comparable to light induced degradation in a-Si:H cells [211].

5.4 Shade Tolerant Module Design

The 2D analysis of the origin and consequences of partial shading in TFPV modules, not only allows us to make accurate predictions of module degradation, as

discussed earlier, but also suggests a solution to the shading problem altogether. This idea of a shade tolerant module design originates from the geometry dependence of the shadow effect in TFPV modules discussed in the earlier sections.

In order to compare the module designs quantitatively, we chose a typical a-Si:H technology as a reference, similar to previous sections. For simplifying the geometrical transformations, however, we have assumed that the module is a square, with $L_{module} = W_{module} = 128$ cm, and $N_{series} = 128$ (although for a typical module $L_{module} = 104$ cm, $W_{module} = 120$ cm, with $N_{series} = 104$ [47]). This slight modification makes no difference to the conclusions of this work. Given the module geometry and cell parameters, 6 modules connected in a string produce an output voltage of 535 V DC, with all modules are operating at their maximum power points (as shown in Fig. 5.4). We consider the situation when one of the modules is partially shaded, and evaluate the worst case voltage developed across cells inside the shaded module, as well as the string output power under each shading scenario.

Fig. 5.14 shows the simulation results for partial shading in this square module with rectangular cells. The worst case reverse stress V_{cell}^{min} (Fig. 5.14(b)) at the cell level, and the string power output P_{string} (Fig. 5.14(c)), are plotted for all possible shadow sizes. The results are similar to the ones obtained for typical sized modules in Fig. 5.11, highlighting the high stress ≈ -10 V caused by asymmetric shading, and the region of bypass diode operation is also shown with dashed box. We will reevaluate these results for the shade tolerant design for a direct comparison of the improvements obtained.

5.4.1 Design Rules for Shade Tolerance

From the results shown in Fig. 5.11, we can see that if the geometry and arrangement of the cells inside a module could be altered, it might be possible to mitigate the effect of shading by distributing the shade over multiple cells. We can summarize these observations for shade tolerant design as:

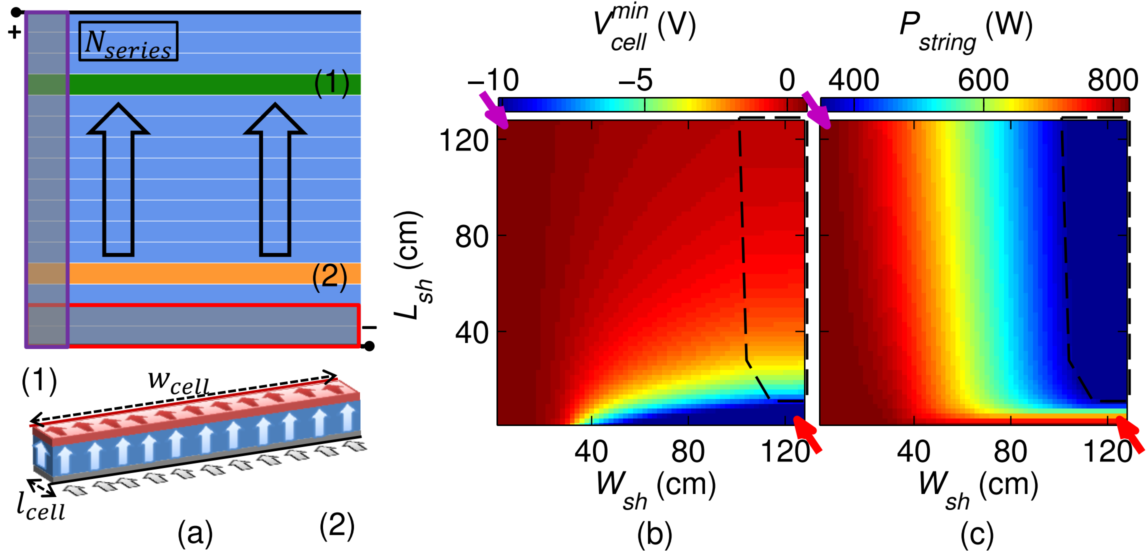

Fig. 5.14. (a) Schematic of a typical TFPV module with rectangular cells. Arrows show the direction of current flow in N_{series} series connected cells, each with area A_{cell} (see bottom for 3D current flow patter at cell level). 2D color plots of (b) minimum cell voltage V_{cell}^{min}, and (c) string output power (P_{string}) for all possible rectilinear shadows on a typical rectangular module. Each point on the plot corresponds to a shadow of length L_{sh} and width W_{sh}, and the color denotes the worst case reverse stress V_{cell}^{min}, or power output P_{string} (see color bar). The dashed box highlights the cases where external bypass is on. Schematic in (a) also defines symmetric shadow (purple), and asymmetric shading (red); the corresponding V_{cell}^{min} and P_{string} are highlighted with arrows on respective plots.

- The strong difference in effect of symmetric vs. asymmetric shading suggests that a shade tolerant design must be free from this orientation dependence.
- The worst case of thin asymmetric shadow shown in Fig. 5.11 must be avoided to prevent permanent damage.
- Shading of multiple cells together distributes the reverse bias, and if it can be utilized by the new design, permanent damage to shaded cells can be averted.

It is obvious that the series connected configuration of the solar cells forming the module must be preserved in any design. For example, it is easy to see that if the rectangular cells of TFPV modules could be arranged radially (like the blades of a fan), the worst case shadow stress can be reduced, because a rectangular shadow will now cover small areas of multiple cells. This, however, cannot preserve the series connection or the rectangular module shape. Fortunately, the monolithic fabrication allows us to change the cell shape in a way, which will satisfy all these constraints, and preserve the module shape and output characteristics at the same time.

The fundamental insight behind this is the observation that a good overlap of a rectangular shadow with rectangular cell is the cause of worst case shadow stress; and, while shadows are generally rectangular (buildings, poles etc.), the cells need not be. Their shape can be modified in a way which reduces the probability of perfect overlap between a rectangular shadow and a non-rectangular cell.

5.4.2 Radial Design with Triangular Cells

The simplest geometry which satisfies the design constraints outlined in the previous section is formed by modifying each rectangular cell into two triangular half-cells and arranging them in a radial pattern, as shown in Figure 5.15(a). The current flow patterns in two types of half cells are also shown for comparison. The terminals need to be put in diagonally, as shown in the schematic and the current flows in a curved path dictated by the series connection. Note that the triangle dimensions and orientations can be chosen to ensure that all cells are of equal area, number of series connected cells is the same, and the square module dimensions are preserved (see Sec. D.1.1 in the appendix for details on how to generate the radial geometry).

The new design can now be assessed using the same SPICE simulation framework (see Sec. D.2 in the appendix for details). The results of the simulation are shown in Fig. 5.15(b), which shows the color plot of V_{cell}^{min} under partial shading, for all different shadow sizes for the radial design. We find that the V_{cell}^{min} value for the radial

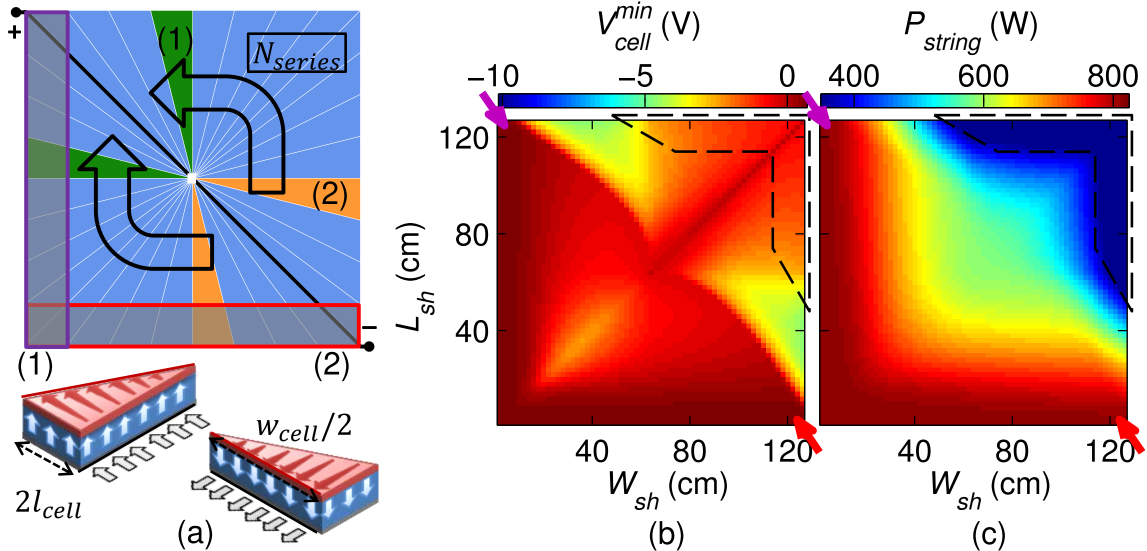

Fig. 5.15. (a) Schematic showing the radial design for TFPV modules, with triangular half-cells arranged in a radial pattern, with terminals along diagonals. Each cell comprises 2 triangles with of area $A_{cell}/2$, so that the total cell area is the same (marked green e.g.). There are 2 types of triangular half-cells, depending on whether the current is collected at longer (2) or shorter (1) edge (3D current flow shown in the schematic below). (b) Color plot showing that the worst case V_{cell}^{min} value for this design is restricted to -4.7 V (see color bar), for all possible rectilinear shadows as before. (c) The color plot of P_{string} values for radial modules also shows improvement for smaller shadow sizes. The cases when external bypass turns on are highlighted by the dashed polygon. The radial symmetry of design is also apparent in shade response (marked by arrows).

design is always above -4.7 V, thus preventing any permanent damage from partial shading [121]. Also, note that the radial symmetry ensures that there is no difference between symmetric and asymmetric shading scenarios (evident from the schematic in Fig. 5.15(a)). The corresponding P_{string} values for different shading scenarios for this design are shown in Fig. 5.15(c), showing marked improvement for smaller shadows, and values are comparable for large shadows. Moreover, Fig. 5.15(b),(c) show that for this radial design, only large shadows cause any significant output power loss or

reverse stress, but the more likely smaller shadows are rendered practically harmless. Thus, we see that the radial design can significantly improve the shade tolerance of the module.

So far, we have compared the shade tolerance of the design subjected to shadows that are anchored to the edge of the module, as would be typical for shadows cast by nearby modules or other objects (see Fig. 5.1) [121]. It is apparent from the schematics in Fig. 5.15(a), however, a thin long shadow, placed along the axis of any of the radial cells would be comparable to the worst case (asymmetric) shading for rectangular cells (see Figure 5.14). Such radial shadows are improbable in a properly installed system [28], but it does reflect a limitation of the radial design. We will explore various worst case scenarios for different shadow positions and orientations for different designs in Sec. , and illustrate this limitation of the radial design. Unfortunately, even this improved shade tolerance of radial design is achieved at a cost of higher resistive losses in the triangular cells. This is because the cells have to be wider near the base of the triangle, thereby increasing the path length for the photocurrent. A detailed analysis and comparison of the resistive losses is presented in Sec. 5.4.5.In order to reduce the resistive losses, we note that the average cell width should be reduced, so that photocurrent flows over shorter distances before being collected. This must be done while keeping the cell area constant; which will be possible by making the cell shape longer and thinner. And, the problem posed by diagonal shadows can be avoided if the cells themselves are non-rectilinear, so that the asymmetric shading will never arise. We show next that both these objectives are achieved by a spiral arrangement of curvilinear cells.

5.4.3 Spiral Design with Curvilinear Cells

Fig. 5.16(a) shows the schematic of the spiral design, with the same N_{series} series connected cells, with the curved positive and negative terminals. Each cell is a concave polygon with varying curvature, constructed so that their areas are identical, while

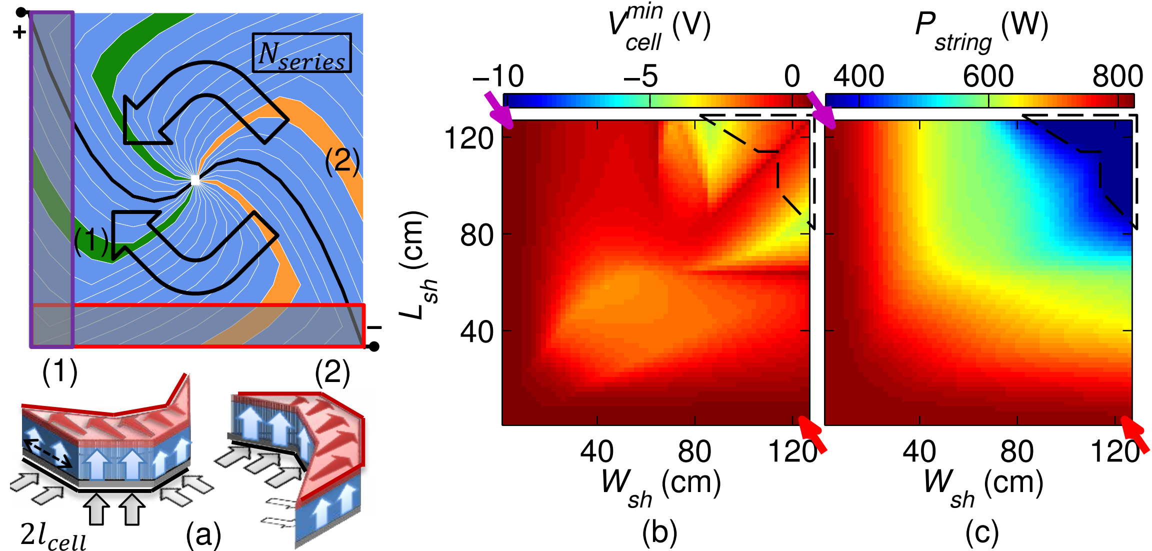

Fig. 5.16. (a) Schematic showing the spiral design of TFPV module, with N_{series} cells in series. Each cell consists of two half-cells (marked green e.g.) shaped like concave polygons, requiring curved terminals as shown, and resulting in the current flow direction marked by arrows. The schematic below shows 3D current flow pattern in half-cells with current flowing towards outer (1) and inner (2) edges. (b) Color plot of V_{cell}^{min} values for this spiral module, for various shadow sizes, shows the worst case value to be restricted to -4.2 V (see color bar). (c) The color plot of string output power P_{string} also shows marked improvement. The cases when external bypass turns on are highlighted by the dashed polygon. The directional symmetry of radial design is also retained (marked by arrows).

preserving module shape and size. Details regarding constructing this geometry are discussed in Sec. D.1.2 of appendix. These curved cells can be considered to be stretched and twisted forms of the triangles used in the radial design, arranged within the same rectangular module. Therefore, the current flow direction is also similar, as shown in Figure 5.16(a).

From the schematic in Figure 5.16(a) it is obvious that this spiral design retains the advantages of the radial design in terms of shade tolerance. This is validated from the circuit simulation result in Figure 5.16(b); which shows that the worst case

V_{cell}^{min} from shading in this spiral design is limited to -4.2 V, and the overall number of cases which result in reverse bias is also reduced. Some additional results for different shadow positions and orientations are discussed in Sec. 5.4.4, which affirm the robust shade tolerance of the spiral design in more general shading scenarios. Figure 5.16(c) also shows the improvement in string output power for the various shading scenarios; which also shows that external bypass diode is activated only for very large shadows. Therefore, with the spiral design it may be possible to avoid the external bypass diode altogether, enabling a truly monolithic TFPV module, and eliminating the considerable reliability issues associated with the external bypass diodes [212]. Moreover, from the schematic in Figure 5.16(a), it is apparent that due to the curved cell shape, the asymmetric shading problem cannot arise for rectilinear shadows of any orientation. Finally, we will show in Sec. 5.4.5 that the curvilinear cell shape also reduces overall resistive power loss compared to rectangular cells and improves module efficiency.

5.4.4 Effect of Shadow Position

So far, we have focused on edge shadows due to nearby objects [28], as they constitute the most probable shading scenarios. Although less likely to occur in practice, it is appropriate to evaluate other shade configurations that could be particularly detrimental to the module operation. As an illustrative example, we consider the case of shadow of width 2 cm covering the entire width/length of the modules, and oriented along the horizontal, vertical and diagonal directions (see Fig. 5.17). In this section, we evaluate to effect of position of these shadow for the three different designs.

Fig. 5.17(a) shows the effect of a long vertical shadow as a function of position. From Fig. 5.14 we saw that this was the best case scenario for rectangular geometry with no reverse stress, and all positions are identical (black line Fig. 5.17(a)). For the radial design, the long shadow in the middle covers two half cells (triangles) fully, which pushes them in reverse bias ($\approx$ -5 V, blue line Fig. 5.17(a)). For the

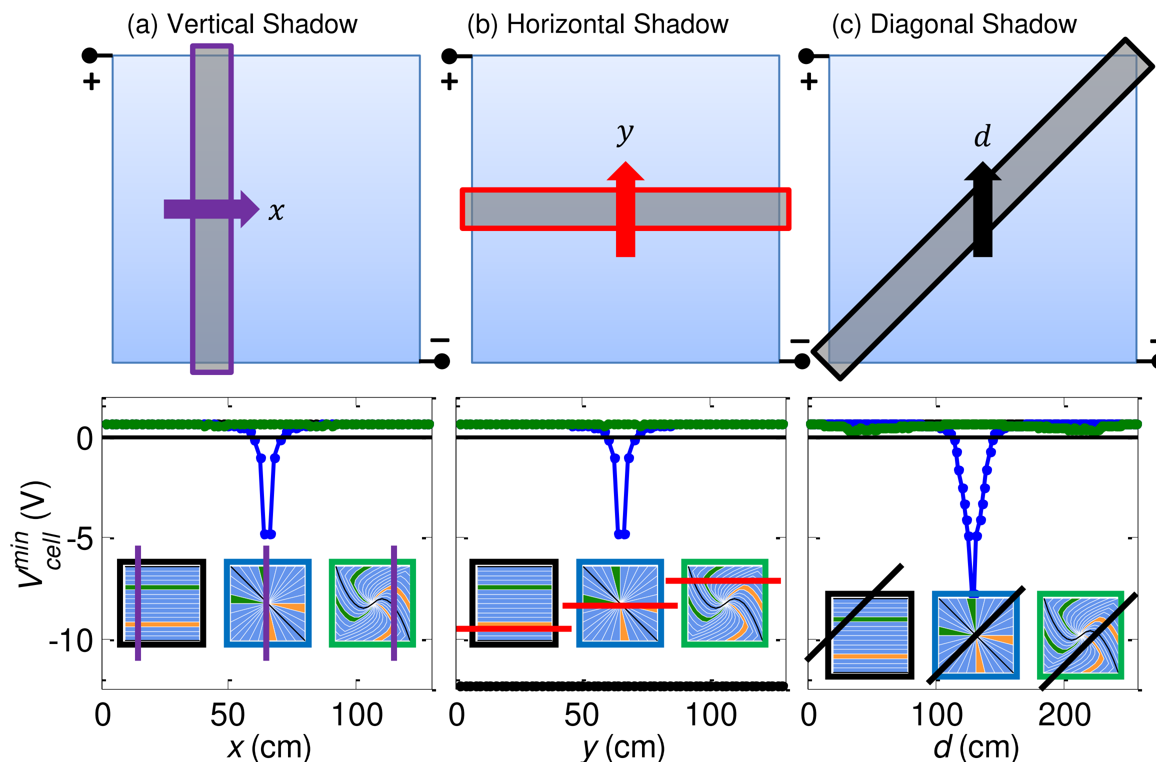

Fig. 5.17. Schematics showing the shading cases considered for the three designs, where shadow effect is evaluated as function of (a) horizontal, (b) vertical, and (c) diagonal orientations as shown.(a) Plot of V_{cell}^{min} vs. x position for long vertical shadow (best case for the rectangular geometry), comparing the three geometries (colors as shown in inset). (b) Plot of V_{cell}^{min} vs. y position for a horizontal shadow (worst case of rectangular design) comparing the three designs.(c) Plot of V_{cell}^{min} vs. position d for a diagonal shadow, which is the worst case for radial design. These results show that the spiral design works well in all cases and prevents shadow stress completely.

spiral design, however, there is no revers stress as V_{cell}^{min} is always positive and it only varies slightly with shadow position (green line Fig. 5.17(a)). Thus for these vertical shadows, the radial design actually performs worse (for specific cases) than the rectangular case, while the spiral design remains unaffected.

Next, Fig. 5.17(b) shows the results for a wide horizontal shadow as a function of vertical position (see top schematic in Fig. 5.17(b)), for the three designs. This is the

worst case scenario for rectangular design (as shown in Fig. 5.14), where 2 cells will be fully shaded and will go into reverse breakdown (≈ -12 V). Understandably, the response for the radial design is identical to the vertical shadow, owing to the radial symmetry. And, the horizontal shadow in the middle again results in the worst case stress of (≈ -5 V, blue line Fig. 5.17(b)). Finally, the spiral design again remains shade tolerant by effectively distributing the shade across many cells, and the cells stay in forward bias (green line Fig. 5.17(b)).

Finally, we consider a diagonal shadow intersecting the three types of modules at different positions, as shown in top schematic in Fig. 5.17(c). In this case, the V_{cell}^{min} for rectangular design shows slight variation, but remains positive as the shadow overlaps many cells (black line Fig. 5.17(c)). For the radial design, however, a diagonal shadow in the middle constitutes the worst case scenario, as it covers 2 cells almost completely, and pushes V_{cell}^{min} ≈-8 V (blue line Fig. 5.17(c)). The spiral design again ensures all cells remain in forward bias, as the shadow overlaps multiple cells (green line Fig. 5.17(c)).

From this analysis we can conclude that the spiral design effectively protects the cells, even for these worst case scenarios. Cells in the radial design, on the other hand, are protected for edge-shadows, but are pushed into reverse bias by long, rectangular shadows passing through the center of the module. We should note, however, that the worst case stress for radial design (≈-8 V) is still smaller than the worst case for rectangular structure (≈-12 V), where the shaded cells go into catastrophic reverse breakdown. This analysis of effect of long rectilinear shadows at different locations strengthens the case for shade tolerance of spiral design.

5.4.5 Module Efficiency Comparison

In this section, we evaluate how a change in cell shape affects the normal (no shade) operating performance of the module. We demonstrate that it is possible to achieve shade tolerance without a tradeoff in nameplate module efficiency, because of

reduced sheet resistance losses in non-rectangular cells of the shade tolerant designs. We also calculate and compare the dead area losses in different design to estimate the overall efficiency change for new designs.

In order to compare sheet resistance losses in cells with different geometries, we need to solve Eq. 4.1 numerically for all three geometries, and calculate the power dissipation per unit area in the sheet conductors using $|\vec{\mathcal{E}}_{xy}|^2/R_\square$. For making realistic comparison we assume typical values for a-Si:H technology in our simulations namely, $R_\square^{TCO} = 10\ \Omega/\square$ [58], and $J_{ph}^{mpp} = 15\ \text{mA/cm}^2$ [186]. The details regarding numerical calculation of the power dissipation in sheet resistors, have been discussed in Sec. 4.2.

Color plots at the top of Fig. 5.18 show the power dissipation per unit area in the TCO layer, obtained from the numerical solution to Eq. 4.1. The plots show the simulation results for the sub-module schematics shown in Figs. 5.14(a), 5.15(a), and 5.16(a), respectively. For the rectangular geometry, the power dissipation profile is identical for all cells. The dissipation per unit area increases monotonically towards the current collecting (top) edge of each cell. This is because the regions near the current collecting edge carry the total current generated in the area below, resulting in higher power loss per unit area. Using Eq. 4.4 for the rectangular geometry, we can get the total resistive power dissipation P_{dis}^{rec} =96 mW per cell.

For the two shade tolerant designs, the P_{dis} values will be different for each cell, because shape and orientation (and hence the current flow pattern) is different for each cell. As shown in the color plots in Fig. 5.18, the power dissipation per unit area in wider regions is higher than the thinner regions, as the current collecting edge near the wider areas collects more photocurrent. As a consequence, the wider triangles in the radial design (close to horizontal and vertical axes) dissipate twice the power compared to rectangular cells, while the dissipation in thin diagonal cells is almost equal to the rectangular case (compare the P_{dis}^{rad} values with P_{dis}^{rec} from the plot in Fig. 5.18).

This geometry dependence in resistive power dissipation is more interesting in the curvilinear cells of the spiral design; where the thinner regions near the center

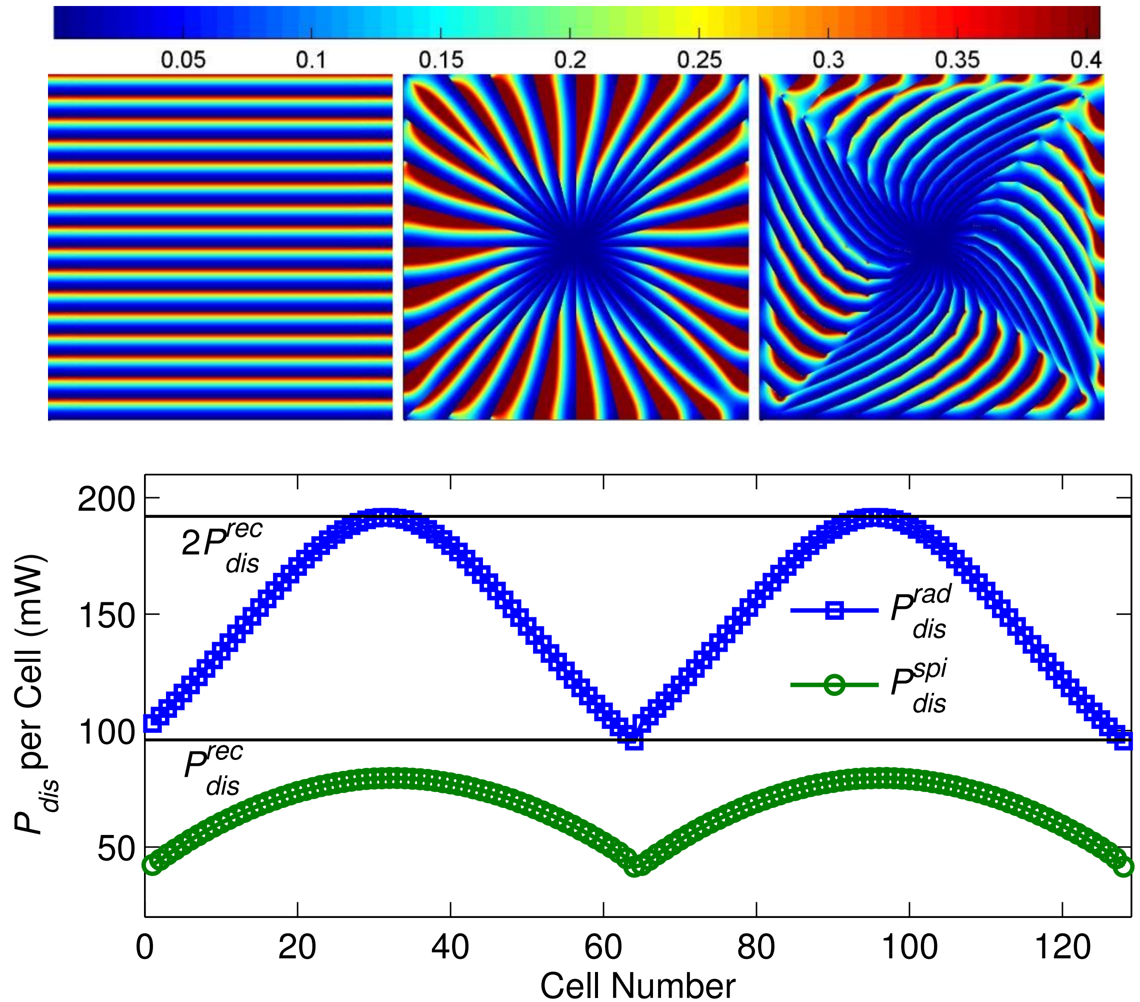

Fig. 5.18. PDE simulation results for rectangular, radial, and spiral sub-modules, showing distribution of resistive power dissipation per unit area in the TCO layer (color bar in mW/cm^2). Plot at the bottom shows power loss in each of the 128 cells for radial (P_{dis}^{rad}) and spiral (P_{dis}^{spi}) designs, compared to the dissipation in rectangular cells (P_{dis}^{rec}) which is same for all cells. The annotations highlight the fact that thin long cells near diagonals, have lower power dissipation (purple); while the wider cells near the center have significantly higher power dissipation (red), for both the designs.

dissipate less power compared to the wider areas towards the edges. Moreover, the pattern in P_{dis}^{spi} values across different cells is also the same, and the longer diagonal

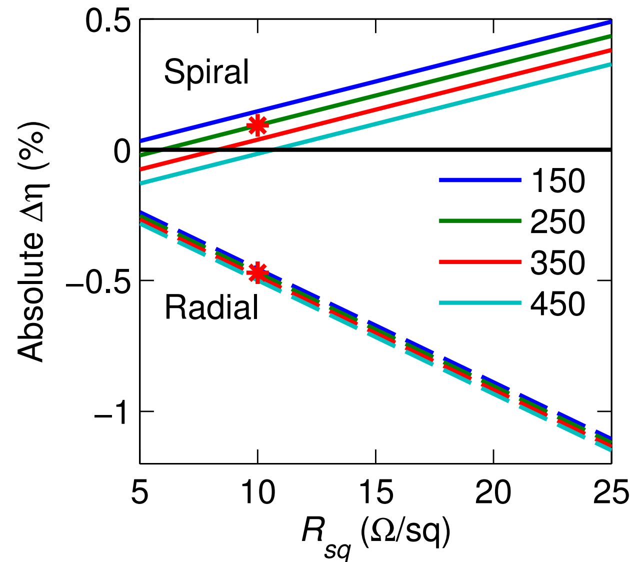

Fig. 5.19. Change in module efficiency compared to the rectangular design for the radial (dashed lines) and spiral (solid lines) designs, for different sheet resistance values and dead regions widths (legend in microns). The analysis shows, that spiral design usually improves the net module efficiency, except for very wide dead regions and/or very low sheet resistances. The filled symbols show the efficiency change for the state of the art parameters used in this study.

cells dissipate less power compared to wider cells near the middle. Overall, however, the cells in spiral design dissipate *less* power in sheet resistance compared even to the rectangular cells (see the P_{dis}^{spi} values in the plot in Fig. 5.18). Correspondingly, the total resistive loss in the spiral module is less than even the rectangular case. This reduction in P_{dis}^{spi} stems from the fact that the perimeter of these curvilinear polygonal cells is larger than the rectangular cells, while A_{cell} is the same. Therefore, the width of each cell is smaller (on an average) compared to rectangular cells, which reduces the overall power dissipation.

In order to compare the efficiency of shade tolerant designs, we must account for the increased 'dead area' due to longer scribe lines in the new designs. We can calculate the total length of scribes required for each design numerically. Using this estimate of dead area, along with calculation of the total power dissipation for different

$R_{\square}^{TCO} = 10\ \Omega/\square$ values, we can determine the exact change in module efficiencies as a result of shade tolerant design. For a-Si:H technology considered here with 9.8% cell efficiency (lab scale) [186], the absolute change in module efficiency ($\Delta\eta = \eta_{design} - \eta_{rect}$) is shown for radial (dashed lines in Fig. 5.19), and spiral (solid lines in Fig. 5.19) designs, as function of sheet resistance and dead region width. As expected, the module efficiencies for the radial design are always lower, owing to higher sheet resistance loss as well as more dead area loss. For the spiral design, however, the efficiency change is mostly positive, as the improvement in sheet resistance losses effectively compensates the active area loss due to longer scribe lines. Specifically, Fig. 5.19 highlights that the efficiency change is positive for the spiral design for current state of the art processes, where the dead region width is 250μ m [187], and TCO sheet resistance is 10 $\Omega/\square$ [47]. Furthermore, advanced techniques such as point-wise interconnection [187], are imminently suitable for the shade tolerant designs, and will further increase the efficiency gain for spiral designs by reducing the dead area loss even more.

5.4.6 Practical Considerations

In the previous sections, we have demonstrated that a geometrical approach to module design can not only alleviate the problem of partial shading in TFPV modules, but can also enhance the overall module performance. We believe this approach towards module design offers attractive improvements without requiring significant tradeoffs. We would like to emphasize that while the calculations presented here were done for a typical a-Si:H solar cell and module, the conclusions are equally valid for all monolithic TFPV technologies. For other TFPV technologies, the exact cell characteristics including the dark and light IV behavior and reverse breakdown voltages would change. Consequently, the exact values of V_{cell}^{min} will change depending on the reverse characteristics and breakdown voltage for the particular technology.

The general conclusions about the shadow size and orientations with respect to cell shape, however, will remain unchanged for any other thin film technology.

From a practical standpoint, laser scribing is the most suitable technique for manufacturing of these non-conventional cell geometries. Laser scribing has been used extensively for thin film Si technologies [213, 214], and it is being actively developed for other polycrystalline TFPV technologies [214–216]. We think it should be possible to adapt them for the proposed non-rectangular cell geometries, possibly through a combined motion of the laser head and rotation of the platform carrying the module to create the non-rectangular shapes. For the spiral design, a curvilinear bus bar will also have to be used, which may be accomplished by cutting the metal ribbon in desired shape. The center of the module in the shade tolerant design also needs to contain a small area for isolation, to prevent all the scribe lines from merging. Fortunately, this area can be as small as a couple of square centimeters to prevent any electrical shorts. This will also avoid high electrical or mechanical stresses in the center of the module, which may cause arcing or glass cracking in the long run. A potential cause of concern is that the longer scribe lines in radial and spiral designs may result in increased edge-shunting. It has been shown that for optimized laser scribing process, however, the edge shunts are not a major concern [217], and the random shunt formation across the cell surface is the dominant shunting mechanism [72].

Finally, we note that geometrical design in different guises has been used for improving the PV performance on different levels. The prominent examples of this include various light trapping schemes (at the cell level) [218], and the recent 3DPV approach to module arrangement (at the module level) [219]. We feel that the shade tolerant design proposed in this work is in the same vein, and utilizes geometry in a unique way to address an important reliability and performance issue in TFPV modules.

5.5 Conclusions

In this chapter, we analyzed the important performance and reliability issues of partial shading in thin film PV systems and modules. We began by exploring the origin of shadow stress in an intuitive manner. Next, we used 2D SPICE equivalent circuit simulation approach to examine the effect of partial shading unique to TFPV modules, and used IR thermal imaging to validate our predictions. After this validation, we used the SPICE model to understand the relationship between the shadow induced stress and the cell geometry and configuration. This insight was then used to provide technology independent geometrical solution for shade tolerant monolithic TFPV modules, and use detailed simulations to establish their advantages. The important insights from this chapter can be summarized as follows:

1. Shading at system level.
   (a) Reverse stress due to partial shading is a direct consequence of the mismatched current output in series connected cells and modules, and therefore is a concern for all PV technologies.
   (b) Only external bypass is possible for TFPV modules, which can limit output power loss for larger shadows, by preventing the total module voltage from becoming negative.
2. Partial shade in TFPV modules.
   (a) Partial shadows in TFPV modules typically cover only part of cell area due to unique cell geometry, resulting in the *unshaded* cell region dissipating more power than the shaded region itself.
   (b) The asymmetric stress in monolithic TFPV modules is a consequence of current and voltage rearrangement under partial shade, because the current must be continuous in series connected cells inside the module.

(c) The asymmetric power dissipation due to partial shading is applicable for all monolithically integrated TFPV technologies, and is verified for CIGS modules using IR thermal imaging during field operation.

(d) The 2D simulation can be used to show that geometry of overlap between the cell and the shadow is critical in determining the shade induced stress, with the thin *asymmetric* edge shadows constituting the worst case stress scenario.

(e) The simulations also show that external bypass diodes cannot protect individual cells from shadow stress, but limit the output power loss in the string for large area shadows.

3. Shade tolerant design

(a) The geometrical dependence of shadow stress suggests that a module which distributes the shadow over multiple cells will be able to avoid the worst case effects of partial shade.

(b) A module formed with triangular cells arranged radially, can preserve the module shape, and nominal output, while offering enhanced shade tolerance for majority shading cases.

(c) A spiral module design with polygonal cells offers the best shade tolerance for cells by eliminating all axes of symmetry for rectilinear shadows falling on a module.

(d) The module efficiency calculations show that while the shade tolerance is obtained at the cost of lower module efficiency for the radial design; the spiral design offers module efficiency *improvement* in addition to shade tolerance.

(e) The shade tolerant designs proposed here can be implemented with state of the art tools and manufacturing methods, making them an attractive solution for module design.

6. SUMMARY AND FUTURE WORK

6.1 Summary

In this work we developed comprehensive techniques for analyzing physical variability and reliability issues in thin film photovoltaics. Our approach relies on integrated device and circuit analysis for capturing the combined effect of physics and statistics on cell and module performance, and reliability. This combined insight led to propose technology agnostic practical solutions to important variability and reliability problems in TFPV modules. The key contributions of this work can be summarized as follows:

Chapter 2

In this chapter, we focused on the characteristics of an 'as-fabricated' TFPV cells, to understand its operation in light and dark.

- Even in absence of second order effects from trapped or injected charges, photocurrent in TFPV cells has two components namely, voltage dependent collection J_{photo}, and generation dependent recombination $J_{rec,G}$. In case of a-Si:H cells analytical expressions for these components were obtained under reasonable assumptions.
- Measured dark current in TFPV cells is often contaminated by symmetric, non-Ohmic, shunt current, which can be isolated using a simple subtraction scheme. This enables individual study of the bulk exponential diode current, and the parasitic shunt current.

- The non-Ohmic shunt exhibits identical voltage, temperature, and thickness dependencies in a-Si:H, CIGS, and OPV solar cells, and is modeled effectively by a local single carrier SCL current in parallel to exponential diode current.

- The physics of shunt conduction suggests that the origin of shunt formation in TFPV cells is the result of local metal incorporation through the thin emitter layers, resulting in a local MSM path responsible parasitic SCL shunt current.

- The physics of intrinsic photo and dark current components, as well as parasitic shunt current can be accurately captured in an equivalent circuit for the a-Si:H cells. This equivalent circuit, however, can be used effectively for other TFPV cells as well.

Chapter 3

In this chapter, we focus on statistical variation and long term degradation of TFPV cells.

- We showed that shunt current shows a universal log-normal distribution from cell to cell, regardless of TFPV technology of choice, and this trend can be verified using robust statistical methods.

- The statistics of shunt conduction are independently corroborated from analysis of shunt imaging techniques, which also show log-normal distribution of shunt magnitudes for different technologies.

- The analysis of shunt images reveals that the spatial distribution of shunt location follows Completely Spatially Random (CSR) process, suggesting uncorrelated shunt formation, in different TFPV technologies.

- We explore the consequences of reverse bias stress on TFPV cells and show that for a-Si:H cells, diode current I_D shows parametric power law degradation and

relaxation in time, with linear dependence on stress voltage, suggesting increase in midgap defect density in i-layer.

- On the other hand, we find that shunt current I_{SH} shows abrupt, non-volatile, metastable switching transitions with well defined thresholds in a-Si:H, and partially non-volatile changes in CIGS cells. This is a likely result of new shunts forming due to Al migration under electric field, and being destroyed by local heating.

Chapter 4

We incorporate the physics and statistics of TFPV to predict and control, module performance loss and variability, utilizing a combined device circuit modeling approach.

- We adapt a 2D distributed SPICE simulation framework for module simulations, to incorporate the physics and statistics of TFPV cells, in a larger scale simulation of cell or module operation.

- We use this simulation setup to demonstrate that microscopic grain variation, in polycrystalline TFPV cells, cause efficiency loss but cannot be responsible for performance fluctuation in laboratory scale cells, as the grain size distribution effects are averaged out for larger areas.

- A similar 2D simulation of module performance, incorporating the shunt magnitude and position statistics, shows that distribution of parasitic shunts and resistive losses in the sheet conductors can account for most of the cell to module efficiency gap in TFPV technologies.

- A detailed analysis of the effect of parasitic shunts in interconnected modules reveals that majority of shunt induced losses arise from the adverse effects of random shunts on their ‘good’ neighboring regions.

- Based on this insight, we provide an in-line, post-process technique for module efficiency improvement, which relies on limiting the effect of parasitic shunts on their neighboring regions; and demonstrate that this method can yield significant performance and yield improvements in realistic scenarios.

Chapter 5

We analyze the problem of partial shading in this chapter, and provide a geometrical solution the shading problem.

- We explore the problem of partial shading in series connected cells/modules to understand how it leads to reverse stress, owing to the series connected nature of PV systems.

- 2D circuit simulation approach is then used to illustrate the unique features of partial shading in TFPV modules, which experience higher stress in the *unshaded* portions of the partially illuminated cells, as a consequence of a rearrangement in cell current and voltage under shade.

- This asymmetric stress was then verified for an installed array of TFPV modules, using IR thermal imaging methods.

- We also use this simulation approach to examine the relation between cell and shadow geometry in determining the resulting shade induced stress, and illustrate the worst case scenarios.

- This analysis also showed the benefit of external bypass diodes in limiting string output power loss under shade, but revealed their inability to protect individual cells in a module from shadow stress.

- We then combined the system level shading simulations with device degradation studies to obtain quantitative estimates of long term panel performance degradation.

- Finally, we combine the insights on shading configurations and proposed geometrical design solutions capable of avoiding shading problem, and established their shade tolerance by combining computational geometry with equivalent circuit simulations.

6.2 Future Work

There are two major driving philosophies behind this work as a whole. The first is an integrated cell-module-system analysis for obtaining a coherent understanding of operation, manufacturing issues, and involved stresses. As shown in this thesis, this integrated view often enables new solutions for important problems in the PV technologies. The second aspect focuses on a technology agnostic view for TFPV as a whole, which focuses on the similarities in TFPV materials, structures, and manufacturing. This allows for adapting techniques and solutions from one technology to the other for mutual benefit. In the light of these viewpoints, we can suggest a few directions for further research on the manufacturing and reliability issues of TFPV technologies.

Photocurrent Model for TFPV cells

In chapter 2, we had created an equivalent circuit for a-Si:H cells in Sec. 2.6, using analytical solutions of semiconductor equation, under reasonable assumptions. This analysis, however, did not consider the effect of trapped or injected charges under illumination, which will modify the operation of the cells. While these effects have been studied individually in different materials [78, 88], a more generalized treatment for solar cells is lacking. Even if the transport equations cannot be solved in a compact form for all cell types, a unified look at the behavior of TFPV cells under light, and relating those characteristics to material and device parameters can yield valuable insight. This will not only allow a more realistic analysis of module performance by

using calibrated compact models for each cell type, but can also suggest improved characterization schemes for analyzing solar cell behavior.

Quantitative Image Analytics for TFPV

In Sec. 3.2.2, we showed the remarkable similarities in the statistical distribution of shunt magnitude and position across different PV technologies, obtained from analysis of image data from different spatial characterization techniques. This demonstrates that these imaging techniques can yield lot more information about the cell performance and variability, if the data is analyzed using quantitative and statistical techniques. This can have important consequences for in-line metrology in production environments because, it will enable automatic control, sorting, or processing of PV modules and cells, by using quantitative analytics on the imaging characterization for automated decision making.

Partial Shading as Diagnostic Tool

Finally, an interesting way of combining the work on parasitic defects, and partial shading, is by using controlled partial shading for characterizing the spatial distribution of defects in large area modules. This approach will involve measurement of module characteristics, under sequential shading of different magnitudes and locations. The data so obtained can then be mapped to obtain the local performance characteristics of individual cells or sub-cells, for quantifying the variability in manufacturing. This will allow a post-process method of spatial module characterization, without requiring expensive imaging equipment or analysis, which can be of considerable interest for the TFPV manufacturers.

LIST OF REFERENCES

LIST OF REFERENCES

[1] *sun worship*. Encyclopedia Britannica, 2013 (accessed July 25, 2013). `http://www.britannica.com/EBchecked/topic/573676/sun-worship`.

[2] J. H. Davies and D. R. Davies, "Earth's surface heat flux," *Solid Earth*, vol. 1, pp. 5–24, Feb. 2010.

[3] O. Morton, "Solar energy: a new day dawning? Silicon Valley sunrise.," *Nature*, vol. 443, pp. 19–22, Sept. 2006.

[4] K. Butti and J. Perlin, *A golden thread: 2500 years of solar architecture and technology*. Palo Alto: Cheshire Books, 1980.

[5] M. Thirugnanasambandam, S. Iniyan, and R. Goic, "A review of solar thermal technologies," *Renewable and Sustainable Energy Reviews*, vol. 14, pp. 312–322, Jan. 2010.

[6] H. Foundation, "The Last Straw Water Use by Power Plants in the Arid West The Land and Water," Tech. Rep. April, Hewlett Foundation, 2003.

[7] R. Cummerow, "Photovoltaic Effect in p-n Junctions," *Physical Review*, vol. 95, pp. 16–21, July 1954.

[8] P. Díaz, C. A. Arias, M. Gomez-Gonzalez, D. Sandoval, and R. Lobato, "Solar home system electrification in dispersed rural areas: a 10-year experience in Jujuy, Argentina," *Progress in Photovoltaics: Research and Applications*, vol. 21, pp. 297–307, Oct. 2011.

[9] M. A. Green, "The path to 25% silicon solar cell efficiency: History of silicon cell evolution," *Progress in Photovoltaics: Research and Applications*, vol. 17, pp. 183–189, May 2009.

[10] M. A. Green, K. Emery, Y. Hishikawa, W. Warta, and E. D. Dunlop, "Solar cell efficiency tables (version 40)," *Progress in Photovoltaics: Research and Applications*, vol. 20, pp. 606–614, Aug. 2012.

[11] ARPA-E, "$1/W Photovoltaic Systems: White Paper to Explore A Grand Challenge for Electricity from Solar," tech. rep., US Department of Energy, 2010.

[12] DOE, "Solar Energy Technologies Program - Multi Year Program Plan," tech. rep., 2008.

[13] K. L. Chopra, P. D. Paulson, and V. Dutta, "Thin-film solar cells: an overview," *Progress in Photovoltaics: Research and Applications*, vol. 12, pp. 69–92, Mar. 2004.

[14] D. Reynolds, G. Leies, L. Antes, and R. Marburger, "Photovoltaic Effect in Cadmium Sulfide," *Physical Review*, vol. 96, pp. 533–534, Oct. 1954.

[15] D. M. Chapin, C. S. Fuller, and G. L. Pearson, "A New Silicon p-n Junction Photocell for Converting Solar Radiation into Electrical Power," *Journal of Applied Physics*, vol. 25, p. 676, May 1954.

[16] D. Cusano, "CdTe solar cells and photovoltaic heterojunctions in IIVI compounds," *Solid-State Electronics*, vol. 6, pp. 217–218, May 1963.

[17] J. Perlin, *From space to earth : the story of solar electricity.* Ann Arbor, MI: Aatec Publications, 1999.

[18] M. D. Platzer, "U . S . Solar Photovoltaic Manufacturing : Industry Trends , Global Competition , Federal Support," tech. rep., Congressional Research Service, 2012.

[19] S. S. Hegedus and A. Luque, *Handbook of photovoltaic science and engineering.* Chichester [u.a.]: Wiley, 2003.

[20] S. Hegedus, "Thin film solar modules: the low cost, high throughput and versatile alternative to Si wafers," *Progress in Photovoltaics: Research and Applications*, vol. 14, pp. 393–411, Aug. 2006.

[21] W. A. Wohlmuth, "Thin Film CdTe Module Manufacturing," in *The International Conference on Compound Semiconductor Manufacturing Technology*, CSManTech, 2009.

[22] A. E. Delahoy, "Recent developments in amorphous silicon photovoltaic research and manufacturing at chronar corporation," *Solar Cells*, vol. 27, pp. 39–57, Oct. 1989.

[23] F. C. Krebs, T. Tromholt, and M. Jø rgensen, "Upscaling of polymer solar cell fabrication using full roll-to-roll processing.," *Nanoscale*, vol. 2, pp. 873–86, June 2010.

[24] M. Powalla, D. Hariskos, E. Lotter, M. Oertel, J. Springer, D. Stellbogen, B. Dimmler, and R. Schäffler, "Large-area CIGS modules: processes and properties," *Thin Solid Films*, vol. 431-432, pp. 523–533, May 2003.

[25] A. Goodrich, T. James, and M. Woodhouse, "Residential, Commercial, and Utility-Scale Photovoltaic (PV) System Prices in the United States: Current Drivers and Cost-Reduction Opportunities," Tech. Rep. February, National Renewable Energy Laboratory, Golden, CO, 2012.

[26] A. Goodrich, T. James, and M. Woodhouse, "Solar PV Manufacturing Cost Analysis : U . S . Competitiveness in a Global Industry," tech. rep., Stanford University: Precourt Institute for Energy, NREL, 2011.

[27] C. N. Jardine, G. J. Conibeer, and K. Lane, "PV-COMPARE: direct comparison of eleven PV technologies at two locations in northern and southern Europe," in *17th European Photovoltaic Solar Energy Conference and Exhibition*, (Munich, Germany), 2001.

[28] B. r. P. Jelle, C. Breivik, and H. D. Rø kenes, "Building integrated photovoltaic products: A state-of-the-art review and future research opportunities," *Solar Energy Materials and Solar Cells*, vol. 100, pp. 69–96, 2012.

[29] M. B. Schubert and R. Merz, "Flexible solar cells and modules," *Philosophical Magazine*, vol. 89, pp. 2623–2644, Oct. 2009.

[30] B. Kippelen and J.-L. Brédas, "Organic photovoltaics," *Energy & Environmental Science*, vol. 2, no. 3, p. 251, 2009.

[31] D. H. Rose, F. S. Hasoon, R. G. Dhere, D. S. Albin, R. M. Ribelin, X. S. Li, Y. Mahathongdy, T. A. Gessert, and P. Sheldon, "Fabrication procedures and process sensitivities for CdS/CdTe solar cells," *Progress in Photovoltaics: Research and Applications*, vol. 7, pp. 331–340, Sept. 1999.

[32] T. Minami, "Transparent conducting oxide semiconductors for transparent electrodes," *Semiconductor Science and Technology*, vol. 20, pp. S35–S44, Apr. 2005.

[33] C. Jeong, P. Nair, M. Khan, M. Lundstrom, and M. A. Alam, "Prospects for nanowire-doped polycrystalline graphene films for ultratransparent, highly conductive electrodes.," *Nano letters*, vol. 11, pp. 5020–5, Nov. 2011.

[34] J. van de Groep, P. Spinelli, and A. Polman, "Transparent conducting silver nanowire networks.," *Nano letters*, vol. 12, pp. 3138–44, June 2012.

[35] N. Romeo, A. Bosio, R. Tedeschi, and V. Canevari, "Back contacts to CSS CdS/CdTe solar cells and stability of performances," *Thin Solid Films*, vol. 361-362, pp. 327–329, Feb. 2000.

[36] J.-H. Yoon, J.-H. Kim, W. M. Kim, J.-K. Park, Y.-J. Baik, T.-Y. Seong, and J.-h. Jeong, "Electrical properties of CIGS/Mo junctions as a function of MoSe 2 orientation and Na doping," *Progress in Photovoltaics: Research and Applications*, 2013. doi: 10.1002/pip.2377.

[37] F. Yang, L. Zhang, T. Tanaka, Y. Zheng, F. Schimitt, R. Wang, A. Tso, K. Reinke, N. Hammond, M. Pandit, L. Li, L. Tsuei, Z. Yuan, and B. Shieh, "Uniform growth of a-Si / μc-Si Tandem junction solar cells over 5.7m2 substrates," in *Photovoltaic Specialists Conference (PVSC), 2009 34th IEEE*, pp. 1541–1545, 2009.

[38] M. Denhoff and N. Drolet, "The effect of the front contact sheet resistance on solar cell performance," *Solar Energy Materials and Solar Cells*, vol. 93, pp. 1499–1506, Sept. 2009.

[39] S. S. Hegedus and W. N. Shafarman, "Thin-film solar cells: device measurements and analysis," *Progress in Photovoltaics: Research and Applications*, vol. 12, pp. 155–176, Mar. 2004.

[40] M. Despeisse, C. Ballif, a. Feltrin, F. Meillaud, S. Fay, F.-J. Haug, D. Domine, M. Python, T. Soderstrom, P. Buehlmann, and G. Bugnon, "Research and developments in thin-film silicon photovoltaics," *Proceedings of SPIE*, vol. 7409, pp. 74090B–74090B–15, 2009.

[41] M. D. Irwin, J. Liu, B. J. Leever, J. D. Servaites, M. C. Hersam, M. F. Durstock, and T. J. Marks, "Consequences of Anode Interfacial Layer Deletion. HCl-Treated ITO in P3HT:PCBM-Based Bulk-Heterojunction Organic Photovoltaic Devices," *Langmuir*, vol. 26, pp. 2584–2591, Feb. 2009.

[42] Q. Guo, G. M. Ford, H. W. Hillhouse, and R. Agrawal, "Sulfide nanocrystal inks for dense Cu(In1-xGa(x))(S1-ySe(y))2 absorber films and their photovoltaic performance.," *Nano letters*, vol. 9, pp. 3060–3065, Aug. 2009.

[43] F. Kessler, D. Herrmann, and M. Powalla, "Approaches to flexible CIGS thin-film solar cells," *Thin Solid Films*, vol. 480-481, pp. 491–498, June 2005.

[44] B. Stanbery, "Copper Indium Selenides and Related Materials for Photovoltaic Devices," *Critical Reviews in Solid State and Materials Sciences*, vol. 27, pp. 73–117, Apr. 2002.

[45] T. Aramoto, F. Adurodija, Y. Nishiyama, T. Arita, A. Hanafusa, K. Omura, and A. Morita, "A new technique for large-area thin film CdS/CdTe solar cells," *Solar Energy Materials and Solar Cells*, vol. 75, pp. 211–217, Jan. 2003.

[46] P. Kumar, S. C. Jain, V. Kumar, S. Chand, and R. P. Tandon, "A model for the J-V characteristics of P3HT:PCBM solar cells," *Journal of Applied Physics*, vol. 105, no. 10, p. 104507, 2009.

[47] "Power series qs: Amorphous silicon thin film modules." `http://www.moserbaersolar.com/resources/thinfilms-english~QS-latest.pdf`.

[48] M. Gloeckler, A. L. Fahrenbruch, and J. R. Sites, "Numerical modeling of CIGS and CdTe solar cells: setting the baseline," in *Photovoltaic Energy Conversion, 2003. Proceedings of 3rd World Conference on*, vol. 1, pp. 491–494, IEEE, 2003.

[49] R. A. Street, "Currentinduced defect creation and recovery in hydrogenated amorphous silicon," *Applied Physics Letters*, vol. 59, pp. 1084–6, 1991.

[50] T. Tiedje, *Hydrogenated Amorphous Silicon - Electronic and Transport Properties*, vol. 21 of *Semiconductors and Semimetals*. Elsevier, 1984.

[51] R. Sokel and R. Hughes, "Numerical analysis of transient photoconductivity in insulators," *Journal of Applied Physics*, vol. 53, no. 11, p. 7414, 1982.

[52] R. S. Crandall, "Modeling of thin film solar cells: Uniform field approximation," *Journal of Applied Physics*, vol. 54, no. 12, p. 7176, 1983.

[53] E. A. Schiff, "Low-mobility solar cells: a device physics primer with application to amorphous silicon," *Solar Energy Materials and Solar Cells*, vol. 78, pp. 567–595 ST – Low–mobility solar cells: a device p, 2003.

[54] E. Malainho, M. I. Vasilevskiy, P. Alpuim, and S. a. Filonovich, "Dielectric function of hydrogenated amorphous silicon near the optical absorption edge," *Journal of Applied Physics*, vol. 106, no. 7, p. 073110, 2009.

[55] H. a. Atwater and A. Polman, "Plasmonics for improved photovoltaic devices.," *Nature materials*, vol. 9, pp. 205–13, Mar. 2010.

[56] N. Naghavi, D. Abou-Ras, N. Allsop, N. Barreau, S. Bücheler, A. Ennaoui, C.-H. Fischer, C. Guillen, D. Hariskos, J. Herrero, R. Klenk, K. Kushiya, D. Lincot, R. Menner, T. Nakada, C. Platzer-Björkman, S. Spiering, A. N. Tiwari, and T. Törndahl, "Buffer layers and transparent conducting oxides for chalcopyrite Cu(In,Ga)(S,Se)2 based thin film photovoltaics: present status and current developments," *Progress in Photovoltaics: Research and Applications*, vol. 18, no. 6, pp. 411–433, 2010.

[57] P. A. Basore, "Optimum grid-line patterns for concentrator solar cells under nonuniform illumination," *Solar Cells*, vol. 14, pp. 249–260, July 1985.

[58] M. K. Bhan, R. Kapil, I. S. Bajpai, R. Kumar, V. Jain, and S. Kumar, "Scaling single-junction a-Si thin-film photovoltaic technology to the next level," *Photovoltaics International*, vol. 7, pp. 101 – 106, 2010.

[59] S. Ku, S. Haas, B. E. Pieters, U. Zastrow, A. Besmehn, Q. Ye, and U. Rau, "Investigation of laser scribing of a-Si:H from the film side for solar modules using a UV laser with ns pulses," *Applied Physics A*, vol. 105, pp. 355–362, Sept. 2011.

[60] S. Silvestre, A. Boronat, and A. Chouder, "Study of bypass diodes configuration on PV modules," *Applied Energy*, vol. 86, pp. 1632–1640, Sept. 2009.

[61] R. Rösch, F. C. Krebs, D. M. Tanenbaum, and H. Hoppe, "Quality control of roll-to-roll processed polymer solar modules by complementary imaging methods," *Solar Energy Materials and Solar Cells*, vol. 97, pp. 176–180, Feb. 2012.

[62] M. Frei and D. Wang, "Performance and yield calculations for large-area thin-film modules through distributed modeling," in *2009 34th IEEE Photovoltaic Specialists Conference (PVSC)*, pp. 001708–001712, IEEE, June 2009.

[63] C. A. Wolden, J. Kurtin, J. B. Baxter, I. Repins, S. E. Shaheen, J. T. Torvik, A. A. Rockett, V. M. Fthenakis, and E. S. Aydil, "Photovoltaic manufacturing: Present status, future prospects, and research needs," *Journal of Vacuum Science & Technology A: Vacuum, Surfaces, and Films*, vol. 29, p. 030801, 2011.

[64] D.-H. Neuhaus and A. Münzer, "Industrial Silicon Wafer Solar Cells," *Advances in OptoElectronics*, vol. 2007, pp. 1–16, 2007.

[65] C. R. Osterwald and T. J. McMahon, "History of accelerated and qualification testing of terrestrial photovoltaic modules: A literature review," *Progress in Photovoltaics: Research and Applications*, vol. 17, pp. 11–33, Jan. 2009.

[66] N. Bosco, "Reliability Concerns Associated with PV Technologies," tech. rep., 2010 (accessed July 25, 2013). `http://www.nrel.gov/pv/performance_reliability/pdfs/failure_references.pdf`.

[67] R. Gaston, R. Feist, S. Yeung, M. Hus, M. Bernius, M. Langlois, S. Bury, J. Granata, M. Quintana, C. Carlson, G. Sarakakis, D. Ogden, and A. Mettas, "Product reliability and thin-film photovoltaics," *Proceedings of SPIE*, vol. 7412, pp. 74120N–74120N–15, 2009.

[68] M. Stutzmann, W. Jackson, and C. Tsai, "Light-induced metastable defects in hydrogenated amorphous silicon: A systematic study," *Physical Review B*, vol. 32, pp. 23–47, July 1985.

[69] R. M. Sullivan, "Shadow effects on a series-parallel array of solar cells," tech. rep., NASA Goddard Space Flight Center, Greenbelt, MD, 1965.

[70] A. Johansson, R. Gottschalg, and D. G. Infield, "Modelling shading on amorphous silicon single and double junction modules," in *Photovoltaic Energy Conversion, 2003. Proceedings of 3rd World Conference on*, vol. 2 of *Proceedings of 3rd World Conference on Photovoltaic Energy Conversion*, pp. 1934–1937, IEEE, 2004.

[71] J. Bauer, J.-M. Wagner, a. Lotnyk, H. Blumtritt, B. Lim, J. Schmidt, and O. Breitenstein, "Hot spots in multicrystalline silicon solar cells: avalanche breakdown due to etch pits," *physica status solidi (RRL) - Rapid Research Letters*, vol. 3, pp. 40–42, Mar. 2009.

[72] S. Dongaonkar, J. D. Servaites, G. M. Ford, S. Loser, J. Moore, R. M. Gelfand, H. Mohseni, H. W. Hillhouse, R. Agrawal, M. A. Ratner, T. J. Marks, M. S. Lundstrom, and M. A. Alam, "Universality of non-Ohmic shunt leakage in thin-film solar cells," *Journal of Applied Physics*, vol. 108, no. 12, p. 124509, 2010.

[73] S. Dongaonkar, K. Y, D. Wang, M. Frei, S. Mahapatra, and M. A. Alam, "On the Nature of Shunt Leakage in Amorphous Silicon p-i-n Solar Cells," *IEEE Electron Device Letters*, vol. 31, pp. 1266–1268, Nov. 2010.

[74] N. Tarr and D. Pulfrey, "The superposition principle for homojunction solar cells," *IEEE Transactions on Electron Devices*, vol. 27, pp. 771–776, Apr. 1980.

[75] F. Lindholm, J. Fossum, and E. Burgess, "Application of the superposition principle to solar-cell analysis," *IEEE Transactions on Electron Devices*, vol. 26, pp. 165–171, Mar. 1979.

[76] J. Hubin and A. V. Shah, "Effect of the recombination function on the collection in a p-i-n solar cell," 1995.

[77] S. S. Hegedus, "CurrentVoltage Analysis of a-Si and a-SiGe Solar Cells Including Voltage-dependent Photocurrent Collection," *Progress in Photovoltaics: Research and Applications*, vol. 5, pp. 151–168, May 1997.

[78] M. Gloeckler, C. Jenkins, and J. Sites, "Explanation of Light/Dark Superposition Failure in CIGS Solar Cells," in *Materials Research Society Symposium*, vol. 763, pp. 231–236, Materials Research Society, 2003.

[79] M. Gloeckler, J. R. Sites, and W. K. Metzger, "Grain-boundary recombination in Cu(In,Ga)Se[sub 2] solar cells," *Journal of Applied Physics*, vol. 98, no. 11, p. 113704, 2005.

[80] K. Decock, S. Khelifi, and M. Burgelman, "Analytical versus numerical analysis of back grading in CIGS solar cells," *Solar Energy Materials and Solar Cells*, vol. 95, pp. 1550–1554, 2011.

[81] G. T. Koishiyev and J. R. Sites, "Impact of sheet resistance on 2-D modeling of thin-film solar cells," *Solar Energy Materials and Solar Cells*, vol. 93, no. 3, pp. 350–354, 2009.

[82] K. Chakrabarty and S. N. Singh, "Depletion layer resistance and its effect on I-V characteristics of fully- and partially-illuminated silicon solar cells," *Solid-State Electronics*, vol. 39, pp. 577–581, 1996.

[83] A. Flat and A. Milnes, “Optimization of multi-layer front-contact grid patterns for solar cells,” *Solar Energy*, vol. 23, pp. 289–299, Jan. 1979.

[84] J. Pallares, R. Cabre, L. F. Marsal, and R. E. I. Schropp, “A compact equivalent circuit for the dark current-voltage characteristics of nonideal solar cells,” *Journal of Applied Physics*, vol. 100, no. 8, pp. 084513–5, 2006.

[85] K. Araki, “Novel equivalent circuit model and statistical analysis in parameters identification,” *Solar Energy Materials and Solar Cells*, vol. 75, pp. 457–466, Feb. 2003.

[86] J. Merten, J. Asensi, C. Voz, A. Shah, R. Platz, and J. Andreu, “Improved equivalent circuit and analytical model for amorphous silicon solar cells and modules,” *IEEE Transactions on Electron Devices*, vol. 45, no. 2, pp. 423–429, 1998.

[87] B. Ray, M. S. Lundstrom, and M. A. Alam, “Can morphology tailoring improve the open circuit voltage of organic solar cells?,” *Applied Physics Letters*, vol. 100, p. 013307, Jan. 2012.

[88] M. S. Anjan and M. Z. Kabir, “Modeling of currentvoltage characteristics of CdS/CdTe solar cells,” *Physica Status Solidi (a)*, vol. 208, no. 8, pp. 1813–1816, 2011.

[89] S. M. Sze and K. K. Ng, *Physics of semiconductor devices*. Hoboken, N.J.: Wiley-Interscience, 2007.

[90] M. Burgelman, P. Nollet, S. Degrave, and J. Beier, “Modeling the cross-over of the I-V characteristics of thin film CdTe solar cells,” in *Photovoltaic Specialists Conference, 2000. Conference Record of the Twenty-Eighth IEEE*, pp. 551–554, 2000.

[91] M. Igalson and C. Platzer-Björkman, “The influence of buffer layer on the transient behavior of thin film chalcopyrite devices,” *Solar Energy Materials and Solar Cells*, vol. 84, pp. 93–103, Oct. 2004.

[92] J. Tan, “Current transport in copper indium gallium diselenide solar cells comparing mesa diodes to the full cell,” *Solar Energy Materials and Solar Cells*, vol. 77, pp. 283–292, May 2003.

[93] J. Deng and C. R. Wronski, “Carrier recombination and differential diode quality factors in the dark forward bias current-voltage characteristics of a-Si:H solar cells,” *Journal of Applied Physics*, vol. 98, no. 2, p. 024509, 2005.

[94] H. Matsuura, A. Matsuda, H. Okushi, and K. Tanaka, “Dark current transport mechanism of p-i-n hydrogenated amorphous silicon diodes,” *Journal of Applied Physics*, vol. 58, no. 4, p. 1578, 1985.

[95] J. C. Nolasco, R. Cabre, J. Ferre-Borrull, L. F. Marsal, M. Estrada, and J. Pallares, “Extraction of poly (3-hexylthiophene) (P3HT) properties from dark current voltage characteristics in a P3HT/n-crystalline-silicon solar cell,” *Journal of Applied Physics*, vol. 107, no. 4, p. 044505, 2010.

[96] A. Sturiale, H. T. Li, J. K. Rath, R. E. I. Schropp, and F. a. Rubinelli, "Exploring dark current voltage characteristics of micromorph silicon tandem cells with computer simulations," *Journal of Applied Physics*, vol. 106, no. 1, p. 014502, 2009.

[97] K. R. Lord II, M. R. Walters, and J. R. Woodyard, "Investigation of shunt resistances in single-junction a-Si:H alloy solar cells," in *Amorphous Silicon Technolgoy, Material Research Society Symposium*, Amorphous Silicon Technology - 1994. Symposium, (Detroit, MI), pp. 729–34, Materials Research Society, 1994.

[98] M. David, "Statistical analysis of local shunts and their relationship with minority-carrier lifetime in multi-crystalline silicon solar cells," *Solar Energy Materials and Solar Cells*, vol. 65, pp. 445–451, Jan. 2001.

[99] B. Mazhari, "An improved solar cell circuit model for organic solar cells," *Solar Energy Materials and Solar Cells*, vol. 90, pp. 1021–1033, May 2006.

[100] T. J. McMahon, T. J. Berniard, and D. S. Albin, "Nonlinear shunt paths in thin-film CdTe solar cells," *Journal of Applied Physics*, vol. 97, no. 5, p. 054503, 2005.

[101] R. Martins, "Dependence of amorphous silicon solar cell performances on the lateral drift current," *Solar Energy Materials and Solar Cells*, vol. 45, pp. 1–15, Jan. 1997.

[102] R. Kind, R. van Swaaij, F. A. Rubinelli, S. Solentsev, and M. Zeman, "Thermal ideality factor of hydrogenated amorphous silicon p-i-n solar cells," *Journal of Applied Physics*, vol. 110, p. 104512, Nov. 2011.

[103] S. Dongaonkar and M. A. Alam, "PV Analyzer," Mar. 2011 (accessed July 24, 2013). `http://nanohub.org/resources/11073`.

[104] N. F. Mott and R. W. Gurney, *Electronic processes in ionic crystals*. New York: Dover Publications, 1964.

[105] A. Rose, "Space-Charge-Limited Currents in Solids," *Physical Review*, vol. 97, pp. 1538–1544, Mar. 1955.

[106] G. Paasch and S. Scheinert, "Space-charge-limited currents in organics with trap distributions: Analytical approximations versus numerical simulation," *Journal of Applied Physics*, vol. 106, no. 8, p. 084502, 2009.

[107] P. Mark and W. Helfrich, "Space-Charge-Limited Currents in Organic Crystals," *Journal of Applied Physics*, vol. 33, p. 205, Jan. 1962.

[108] A. R. Moore, "Electron and hole drift mobility in amorphous silicon," *Applied Physics Letters*, vol. 31, p. 762, Dec. 1977.

[109] W. Luangtip, S. Rotbuathong, P. Chindaudom, M. Horphatum, V. Patthanasetthakul, P. Eiamchai, and T. Srikirin, "Investigation of Aluminium Diffusion into an Amorphous Silicon Thin Film at High Temperature by ¡i¿In Situ¡/i¿ Spectroscopic Ellipsometry," *Advanced Materials Research*, vol. 55-57, pp. 449–452, 2008.

[110] M. Haque, H. Naseem, and W. Brown, "Aluminum-induced degradation and failure mechanisms of a-Si:H solar cells," *Solar Energy Materials and Solar Cells*, vol. 41-42, pp. 543–555, June 1996.

[111] K. Krishna, S. Guha, and K. Narasimhan, "Barrier height modification in heat-treated aluminium Schottky diodes on hydrogenated amorphous silicon," *Solar Cells*, vol. 4, no. 2, pp. 153–156, 1981.

[112] F. Schauer and O. Zmeskal, "Temperature dependent SCLC in amorphous silicon," *Journal of Non-Crystalline Solids*, vol. 164-166, pp. 537–540, Dec. 1993.

[113] T. Tiedje, J. Cebulka, D. Morel, and B. Abeles, "Evidence for Exponential Band Tails in Amorphous Silicon Hydride," *Physical Review Letters*, vol. 46, pp. 1425–1428, May 1981.

[114] S. Dongaonkar, K. Y., S. Mahapatra, and M. A. Alam, "Physics and Statistics of Non-Ohmic Shunt Conduction and Metastability in Amorphous Silicon pin Solar Cells," *IEEE Journal of Photovoltaics*, vol. 1, pp. 111–117, Oct. 2011.

[115] M. A. Green, "Thin-film solar cells: review of materials, technologies and commercial status," *Journal of Materials Science: Materials in Electronics*, vol. 18, pp. 15–19, Apr. 2007.

[116] K. Durose, J. D. Major, and Y. Y. Proskuryakov, "Nucleation and Grain Boundaries in CdTe/CdS Solar Cells," in *Materials Research Society Symposium Proceedings*, vol. 1165, Materials Research Society, 2009.

[117] S. Dongaonkar, S. Loser, E. J. Sheets, K. Zaunbrecher, R. Agrawal, T. J. Marks, and M. A. Alam, "Universal statistics of parasitic shunt formation in solar cells, and its implications for cell to module efficiency gap," *Energy & Environmental Science*, vol. 6, pp. 782–787, 2013.

[118] K. J. B. M. Nieuwesteeg, M. van der Veen, T. J. Vink, and J. M. Shannon, "On the current mechanism in reverse-biased amorphous-silicon Schottky contacts. I. Zero bias barrier heights and current transport mechanism," *Journal of Applied Physics*, vol. 74, p. 2581, Aug. 1993.

[119] P. P. Edwards, a. Porch, M. O. Jones, D. V. Morgan, and R. M. Perks, "Basic materials physics of transparent conducting oxides.," *Dalton transactions (Cambridge, England : 2003)*, pp. 2995–3002, Oct. 2004.

[120] S. S. Schmidt, *Microscopic properties of grain boundaries in Cu (In , Ga) Se 2 and CuInS 2 thin-film solar cells studied by transmission electron microscopy.* PhD thesis, Technischen Universitat Berlin, 2011.

[121] S. Dongaonkar, Y. Karthik, D. Wang, M. Frei, S. Mahapatra, and M. A. Alam, "Identification, Characterization and Implications of Shadow Degradation in Thin Film Solar Cells," in *Reliability Physics Symposium (IRPS), 2011 IEEE International*, (Monterey, CA), pp. 5E.4.1 – 5E.4.5, IEEE, 2011.

[122] S. Dongaonkar, E. Sheets, R. Agrawal, and M. A. Alam, "Reverse Stress Metastability of Shunt Current in CIGS Solar Cells," in *38th IEEE Photovoltaic Specialits Conference (PVSC 2012)*, (Austin, TX), pp. 000868–000872, IEEE, June 2012.

[123] L. Zhang, H. Shen, Z. Yang, and J. Jin, "Shunt removal and patching for crystalline silicon solar cells using infrared imaging and laser cutting," *Progress in Photovoltaics: Research and Applications*, vol. 18, pp. 54–60, Jan. 2010.

[124] S. W. Johnston, N. J. Call, B. Phan, and R. K. Ahrenkiel, "Applications of imaging techniques for solar cell characterization," in *34th IEEE Photovoltaic Specialists Conference (PVSC)*, pp. 000276–000281, IEEE, June 2009.

[125] J. Major, Y. Proskuryakov, K. Durose, and S. Green, "Nucleation of CdTe thin films deposited by close-space sublimation under a nitrogen ambient," *Thin Solid Films*, vol. 515, pp. 5828–5832, May 2007.

[126] M. Python, E. Vallatsauvain, J. Bailat, D. Domine, L. Fesquet, a. Shah, and C. Ballif, "Relation between substrate surface morphology and microcrystalline silicon solar cell performance," *Journal of Non-Crystalline Solids*, vol. 354, pp. 2258–2262, May 2008.

[127] H. Zhang, B. Gao, B. Sun, G. Chen, L. Zeng, L. Liu, X. Liu, J. Lu, R. Han, J. Kang, and B. Yu, "Ionic doping effect in ZrO[sub 2] resistive switching memory," *Applied Physics Letters*, vol. 96, no. 12, p. 123502, 2010.

[128] C. Hudaya, J. H. Park, and J. K. Lee, "Effects of process parameters on sheet resistance uniformity of fluorine-doped tin oxide thin films.," *Nanoscale research letters*, vol. 7, p. 17, Jan. 2012.

[129] E. S. Mungan, S. Dongaonkar, and M. A. Alam, "Bridging the Gap: Modeling the Variation due to Grain Size Distribution in CdTe Solar Cells," in *39th IEEE Photovoltaic Specialists Conference (PVSC)*, (Tampa, Florida), IEEE, 2013.

[130] B. Ray, P. R. Nair, and M. A. Alam, "Annealing dependent performance of organic bulk-heterojunction solar cells: A theoretical perspective," *Solar Energy Materials and Solar Cells*, vol. 95, pp. 3287–3294, Dec. 2011.

[131] R. W. Lof and R. E. I. Schropp, "Anomalous conductivity behavior of microcrystalline silicon," in *Photovoltaic Specialists Conference (PVSC), 2010 35th IEEE*, pp. 003735–003738.

[132] A. Virtuani, E. Lotter, M. Powalla, U. Rau, J. H. Werner, and M. Acciarri, "Influence of Cu content on electronic transport and shunting behavior of Cu(In,Ga)Se[sub 2] solar cells," *Journal of Applied Physics*, vol. 99, no. 1, p. 014906, 2006.

[133] O. Breitenstein, J. P. Rakotoniaina, M. H. Al Rifai, and M. Werner, "Shunt types in crystalline silicon solar cells," *Progress in Photovoltaics: Research and Applications*, vol. 12, pp. 529–538, Nov. 2004.

[134] T. Johnson, G. Ganguly, G. Wood, and D. Carlson, "Investigation of the Causes and Variation of Leakage Currents in Amorphous Silicon pin Diodes," in *Materials Research Society Symposium*, vol. 762, pp. 381–386, Materials Research Society, 2003.

[135] O. Breitenstein, J. Rakotoniaina, S. Neve, M. Green, and G. Hahn, "Lock-in thermography investigation of shunts in screen-printed and PERL solar cells," *Conference Record of the Twenty-Ninth IEEE Photovoltaic Specialists Conference, 2002.*, pp. 430–433, 2002.

[136] H. Straube and O. Breitenstein, "Infrared lock-in thermography through glass substrates," *Solar Energy Materials and Solar Cells*, vol. 95, pp. 2768–2771, Oct. 2011.

[137] S. Johnston, T. Unold, I. Repins, R. Sundaramoorthy, K. M. Jones, B. To, N. Call, and R. Ahrenkiel, "Imaging characterization techniques applied to Cu(In,Ga)Se[sub 2] solar cells," *Journal of Vacuum Science & Technology A: Vacuum, Surfaces, and Films*, vol. 28, no. 4, p. 665, 2010.

[138] D. Shvydka, J. P. Rakotoniaina, and O. Breitenstein, "Lock-in thermography and nonuniformity modeling of thin-film CdTe solar cells," *Applied Physics Letters*, vol. 84, pp. 729–731, 2004.

[139] S. Johnston, I. Repins, N. Call, R. Sundaramoorthy, K. M. Jones, and B. To, "Applications of imaging techniques to Si, Cu(In,Ga)Se¡inf¿2¡/inf¿, and CdTe and correlation to solar cell parameters," in *2010 35th IEEE Photovoltaic Specialists Conference*, pp. 001727–001732, IEEE, June 2010.

[140] O. Breitenstein, J. Bauer, P. P. Altermatt, and K. Ramspeck, "Influence of Defects on Solar Cell Characteristics," *Solid State Phenomena*, vol. 156-158, pp. 1–10, Oct. 2009.

[141] M. Kasemann, B. Walter, C. Meinhardt, J. Ebser, W. Kwapil, and W. Warta, "Emissivity-corrected power loss calibration for lock-in thermography measurements on silicon solar cells," *Journal of Applied Physics*, vol. 103, no. 11, p. 113503, 2008.

[142] *Log-normal distribution*. Wikipedia, the free encyclopedia.

[143] F. J. Massey Jr., "The Kolmogorov-Smirnov Test for Goodness of Fit," *Journal of the American Statistical Association*, vol. 46, pp. 68–78, Mar. 1951.

[144] A. Clauset, C. R. Shalizi, and M. E. J. Newman, "Power-Law Distributions in Empirical Data," *SIAM Review*, vol. 51, p. 661, Nov. 2009.

[145] O. Breitenstein, J. Bauer, and J. P. Rakotoniaina, "Material-induced shunts in multicrystalline silicon solar cells," *Semiconductors*, vol. 41, pp. 440–443, Apr. 2007.

[146] G. Brown, A. Pudov, B. Cardozo, V. Faifer, E. Bykov, and M. Contreras, "Quantitative imaging of electronic nonuniformities in Cu(In,Ga)Se[sub 2] solar cells," *Journal of Applied Physics*, vol. 108, no. 7, p. 074516, 2010.

[147] F. R. Runai, F. Schwable, T. Walter, A. Fidler, S. Gorse, T. Hahn, and I. Kotschau, "Imaging and performance of CIGS thin film modules," in *Photovoltaic Specialists Conference (PVSC), 2011 37th IEEE*, pp. 3399–3403, 2011.

[148] O. Breitenstein and M. Langenkamp, *Lock-in thermography: basics and use for functional diagnostics of electronic components*. Springer series in advanced microelectronics, Springer, 2003.

[149] K. Bothe, K. Ramspeck, D. Hinken, C. Schinke, J. Schmidt, S. Herlufsen, R. Brendel, J. Bauer, J.-M. Wagner, N. Zakharov, and O. Breitenstein, "Luminescence emission from forward- and reverse-biased multicrystalline silicon solar cells," *Journal of Applied Physics*, vol. 106, no. 10, p. 104510, 2009.

[150] V. Sittinger, F. Ruske, W. Werner, B. Szyszka, B. Rech, J. Hüpkes, G. Schöpe, and H. Stiebig, "ZnO:Al films deposited by in-line reactive AC magnetron sputtering for a-Si:H thin film solar cells," *Thin Solid Films*, vol. 496, no. 1, pp. 16–25, 2006.

[151] E. Miranda, E. O'Connor, and P. Hurley, "Analysis of the breakdown spots spatial distribution in large area MOS structures," in *2010 IEEE International Reliability Physics Symposium*, pp. 775–777, IEEE, 2010.

[152] A. M. Mathai, P. Moschopoulos, and G. Pederzoli, "Random points associated with rectangles," *Rendiconti del Circolo Matematico di Palermo*, vol. 48, pp. 163–190, Feb. 1999.

[153] M. A. Alam, D. Varghese, and B. Kaczer, "Theory of Breakdown Position Determination by Voltage- and Current-Ratio Methods," *Electron Devices, IEEE Transactions on*, vol. 55, no. 11, pp. 3150–3158, 2008.

[154] G. Alers, J. Zhou, C. Deline, P. Hacke, and S. Kurtz, "Degradation of individual cells in a module measured with differential IV analysis," *Progress in Photovoltaics: Research and Applications*, vol. 19, pp. 977–982, July 2010.

[155] C. V. Thompson, "Grain Growth in Thin Films," *Annual Review of Materials Science*, vol. 20, pp. 245–268, Aug. 1990.

[156] M. D. Irwin, D. B. Buchholz, a. W. Hains, R. P. H. Chang, and T. J. Marks, "p-Type semiconducting nickel oxide as an efficiency-enhancing anode interfacial layer in polymer bulk-heterojunction solar cells," *Proceedings of the National Academy of Sciences*, vol. 105, pp. 2783–2787, Feb. 2008.

[157] K. Ottosson, *The role of i-ZnO for shunt prevention in Cu (In, Ga) Se2-based solar cells*. PhD thesis, Uppsala University, 2006. `http://www.teknik.uu.se/asc/documents/theses/2006_Karin_Ottosson.pdf`.

[158] J. Bauer, O. Breitenstein, and J.-P. Rakotoniaina, "Electronic activity of SiC precipitates in multicrystalline solar silicon," *physica status solidi (a)*, vol. 204, pp. 2190–2195, July 2007.

[159] D. L. Staebler and C. R. Wronski, "Reversible conductivity changes in discharge-produced amorphous Si," *Applied Physics Letters*, vol. 31, no. 4, p. 292, 1977.

[160] M. A. Quintana, D. L. King, F. M. Hosking, J. A. Kratochvil, R. W. Johnson, B. R. Hansen, N. G. Dhere, and M. B. Pandit, "Diagnostic analysis of silicon photovoltaic modules after 20-year field exposure," in *Photovoltaic Specialists Conference, 2000. Conference Record of the Twenty-Eighth IEEE*, pp. 1420–1423, 2000.

[161] G. Jorgensen, K. Terwilliger, J. Delcueto, S. Glick, M. Kempe, J. Pankow, F. Pern, and T. McMahon, "Moisture transport, adhesion, and corrosion protection of PV module packaging materials," *Solar Energy Materials and Solar Cells*, vol. 90, pp. 2739–2775, Oct. 2006.

[162] B. Ray and M. A. Alam, "A compact physical model for morphology induced intrinsic degradation of organic bulk heterojunction solar cell," *Applied Physics Letters*, vol. 99, p. 033303, July 2011.

[163] G. J. Jorgensen and T. J. McMahon, "Accelerated and outdoor aging effects on photovoltaic module interfacial adhesion properties," *Progress in Photovoltaics: Research and Applications*, vol. 16, pp. 519–527, Sept. 2008.

[164] S. E. Shaheen, "Mechanisms of Operation and Degradation in Solution-Processable Organic Photovoltaics," in *Reliability physics symposium, 2007. proceedings. 45th annual. ieee international*, pp. 248–252, 2007.

[165] T. Yanagisawa and T. Kojima, "Behavior of a CuInSe2 solar module under light irradiation in light/dark cycle tests," *Solar Energy Materials and Solar Cells*, vol. 77, pp. 83–87, Apr. 2003.

[166] D. J. Coyle, H. A. Blaydes, R. S. Northey, J. E. Pickett, K. R. Nagarkar, R.-A. Zhao, and J. O. Gardner, "Life prediction for CIGS solar modules part 2: degradation kinetics, accelerated testing, and encapsulant effects," *Progress in Photovoltaics: Research and Applications*, vol. 21, pp. 173–186, Mar. 2013.

[167] T. A. Gessert, S. Smith, T. Moriatry, M. Young, S. Asher, S. Johnston, A. Duda, C. DeHart, and A. L. Fahrenbruch, "Evolution of CdS/CdTe device performance during Cu diffusion," in *Photovoltaic Specialists Conference, 2005. Conference Record of the Thirty-first IEEE*, pp. 291–294, 2005.

[168] S. Kjaer, J. Pedersen, and F. Blaabjerg, "A Review of Single-Phase Grid-Connected Inverters for Photovoltaic Modules," *IEEE Transactions on Industry Applications*, vol. 41, pp. 1292–1306, Sept. 2005.

[169] J. Major and K. Durose, "Study of buried junction and uniformity effects in CdTe/CdS solar cells using a combined OBIC and EQE apparatus," *Thin Solid Films*, vol. 517, pp. 2419–2422, Feb. 2009.

[170] S. Wendlandt, A. Drobisch, T. Buseth, S. Krauter, and P. Grunow, "Hot spot risk analysis on silicon cell modules," in *25th European Photovoltaic Solar Energy Conference and Exhibition (EU PVSEC)*, vol. 49, pp. 4002 – 4006, 2010.

[171] M. A. Alam, S. Dongaonkar, Y. Karthik, S. Mahapatra, D. Wang, and M. Frei, "Intrinisic reliability of amorphous silicon thin film solar cells," in *2010 IEEE International Reliability Physics Symposium*, pp. 312–317, IEEE, 2010.

[172] A. V. Shah, H. Schade, M. Vanecek, J. Meier, E. Vallat-Sauvain, N. Wyrsch, U. Kroll, C. Droz, and J. Bailat, "Thin-film silicon solar cell technology," *Progress in Photovoltaics: Research and Applications*, vol. 12, pp. 113–142, Mar. 2004.

[173] N. Kramer and C. van Berkel, "Reverse current mechanisms in amorphous silicon diodes," *Applied Physics Letters*, vol. 64, no. 9, p. 1129, 1994.

[174] R. V. R. Murthy, V. Dutta, and S. P. Singh, "Reverse Biased Annealing Studies in Hydrogenated Amorphous Silicon Solar Cells," *Japanese Journal of Applied Physics*, vol. 33, pp. L1581–L1583, Nov. 1994.

[175] G. Nostrand and J. Hanak, *Method of removing the effects of electrical shorts and shunts created during the fabrication process of a solar cell*. US Patent Office, Sept. 1979. US Patent 4,166,918 `www.google.com/patents/US4166918`.

[176] P. Lechner and H. Schade, "Photovoltaic thin-film technology based on hydrogenated amorphous silicon," *Progress in Photovoltaics: Research and Applications*, vol. 10, pp. 85–97, Mar. 2002.

[177] A. E. Owen, P. G. L. Comber, J. Hajto, M. J. Rose, and A. J. Snell, "Switching in amorphous devices," *International Journal of Electronics*, vol. 73, pp. 897–906, Nov. 1992.

[178] J. Won Seo, S. J. Baik, S. J. Kang, Y. H. Hong, J.-H. Yang, L. Fang, and K. S. Lim, "Evidence of Al induced conducting filament formation in Al/amorphous silicon/Al resistive switching memory device," *Applied Physics Letters*, vol. 96, no. 5, pp. 053504–3, 2009.

[179] R. Waser and M. Aono, "Nanoionics-based resistive switching memories.," *Nature materials*, vol. 6, pp. 833–40, Nov. 2007.

[180] J. Yang, M. Masuduzzman, J. Kang, and M. Alam, "SILC-based reassignment of trapping and trap generation regimes of positive bias temperature instability," in *2011 International Reliability Physics Symposium*, pp. 3A.3.1–3A.3.6, IEEE, Apr. 2011.

[181] S. Dongaonkar and M. A. Alam, "End to end modeling for variability and reliability analysis of thin film photovoltaics," in *2012 IEEE International Reliability Physics Symposium (IRPS)*, pp. 4A.4.1–4A.4.6, IEEE, Apr. 2012.

[182] S. Dongaonkar and M. A. Alam, "In-Line Post-Process Scribing for Reducing Cell to Module Efficiency Gap in Monolithic Thin Film Photovoltaics," *(Under Review)*.

[183] C. F. J. Wu, "Jackknife, Bootstrap and Other Resampling Methods in Regression Analysis," *The Annals of Statistics*, vol. 14, pp. 1261–1295, Dec. 1986.

[184] L. Nielsen, "Distributed series resistance effects in solar cells," *IEEE Transactions on Electron Devices*, vol. 29, pp. 821–827, May 1982.

[185] S. Dongaonkar and M. A. Alam, "Geometrical Design of Thin Film PV Module for Improved Shade Tolerance and Performance," *Progress in Photovoltaics: Research and Applications*, 2013. In Press - preprint `http://arxiv.org/abs/1303.4604`.

[186] S. Benagli and D. Borrello, "High-efficiency amorphous silicon devices on LPCVD-ZnO TCO prepared in industrial KAI-M R&D reactor," in *24th European Photovoltaic Solar Energy Conference and Exhibition*, no. September, pp. 21–25, 2009.

[187] S. Haas, S. Krumscheid, A. Bauer, A. Lambertz, and U. Rau, "Novel series connection concept for thin film solar modules," *Progress in Photovoltaics: Research and Applications*, vol. 21, no. 5, pp. 972–979, 2013.

[188] F. A. Rubinelli, J. K. Arch, and S. J. Fonash, "Effect of contact barrier heights on a-Si:H p-i-n detector and solar-cell performance," *Journal of Applied Physics*, vol. 72, no. 4, p. 1621, 1992.

[189] G. T. Koishiyev and J. R. Sites, "Effect of weak diodes on the performance of CdTe thin-film modules," in *2009 34th IEEE Photovoltaic Specialists Conference (PVSC)*, pp. 001978–001981, IEEE, June 2009.

[190] B. E. Pieters, "Spatial Modeling of Thin-Film Solar Modules Using the Network Simulation Method and SPICE," *IEEE Journal of Photovoltaics*, vol. 1, pp. 93–98, July 2011.

[191] S. Dongaonkar and M. A. Alam, *Shade Tolerant Thin Film Photovoltaic Panel*. US Patent Office, 2012. Appl. Num. 61/644,653.

[192] E. E. Gurrola, S. Dongaonkar, and M. A. Alam, *PVpanel Sim*. 2012 (accessed July 24, 2013). https://nanohub.org/tools/pvpanelsim.

[193] J. W. Bishop, "Computer simulation of the effects of electrical mismatches in photovoltaic cell interconnection circuits," *Solar Cells*, vol. 25, pp. 73–89, 1988.

[194] S. Dongaonkar, C. Deline, and M. A. Alam, "Performance and Reliability Implications of Two Dimensional Shading in Monolithic Thin Film Photovoltaic Modules," *IEEE Journal of Photovoltaics*, 2013. In Press - preprint http://arxiv.org/abs/1303.4445.

[195] S. Hegedus, D. Desai, and C. Thompson, "Voltage dependent photocurrent collection in CdTe/CdS solar cells," *Progress in Photovoltaics: Research and Applications*, vol. 15, pp. 587–602, Nov. 2007.

[196] A. Helbig, T. Kirchartz, R. Schaeffler, J. H. Werner, and U. Rau, "Quantitative electroluminescence analysis of resistive losses in Cu(In, Ga)Se2 thin-film modules," *Solar Energy Materials and Solar Cells*, vol. 94, pp. 979–984, June 2010.

[197] D. Levitan, "The Solar Efficiency Gap - IEEE Spectrum," 2012 (accessed July 25, 2013). http://spectrum.ieee.org/green-tech/solar/the-solar-efficiency-gap.

[198] S. Dongaonkar and M. A. Alam, *Thin Film Photovoltaic Panels and Repair Methods*. US Patent Office, 2013. Appl. Num. 13/761914.

[199] P. Nath, K. Hoffman, C. Vogeli, and S. R. Ovshinsky, "Conversion process for passivating current shunting paths in amorphous silicon alloy solar cells," *Applied Physics Letters*, vol. 53, no. 11, p. 986, 1988.

[200] Y. Roussillon, D. M. Giolando, D. Shvydka, A. D. Compaan, and V. G. Karpov, "Blocking thin-film nonuniformities: Photovoltaic self-healing," *Applied Physics Letters*, vol. 84, pp. 616–618 ST – Blocking thin–film nonuniformities:, 2004.

[201] F. J. Pern, F. Yan, L. Mansfield, S. Glynn, M. Rekow, and R. Murison, "Performance characterization and remedy of experimental CuInGaSe¡inf¿2¡/inf¿ mini-modules," in *Photovoltaic Specialists Conference (PVSC), 2011 37th IEEE*, pp. 2792–2797, 2011.

[202] O. Breitenstein, J. P. Rakotoniaina, and M. H. A. Rifai, "Quantitative evaluation of shunts in solar cells by lock-in thermography," *Progress in Photovoltaics: Research and Applications*, vol. 11, pp. 515–526, Dec. 2003.

[203] A. Woyte, J. Nijs, and R. Belmans, "Partial shadowing of photovoltaic arrays with different system configurations: literature review and field test results," *Solar Energy*, vol. 74, pp. 217–233, Mar. 2003.

[204] E. V. Paraskevadaki and S. A. Papathanassiou, "Evaluation of MPP Voltage and Power of mc-Si PV Modules in Partial Shading Conditions," *IEEE Transactions on Energy Conversion*, vol. 26, pp. 923–932, Sept. 2011.

[205] J. Bishop, "Microplasma breakdown and hot-spots in silicon solar cells," *Solar Cells*, vol. 26, pp. 335–349, Sept. 1989.

[206] M. Kasemann, B. Walter, and W. Warta, "Reliable hot-spot classification in 10 ms using ultra-fast lock-in thermography," *Progress in Photovoltaics: Research and Applications*, vol. 17, pp. 441–450, Nov. 2009.

[207] H. B. Exell, *The Intensity of Solar Radiation*. 2000 (accessed Jyly 24, 2013). `http://www.homer.com.au/webdoc/science/solar/SolarRadiationIntensity.html`.

[208] H. Denio, "Aerial Solar Thermography and Condition Monitoring of Photovoltaic Systems," in *InfraMation*, p. 040, Infrared Training Center, 2011.

[209] L. C. Hirst and N. J. Ekins-Daukes, "Fundamental losses in solar cells," *Progress in Photovoltaics: Research and Applications*, vol. 19, pp. 286–293, May 2011.

[210] M. A. Alam, B. Ray, M. R. Khan, and S. Dongaonkar, "The essence and efficiency limits of bulk-heterostructure organic solar cells: A polymer-to-panel perspective," *Journal of Materials Research*, vol. 28, no. 04, pp. 541–557, 2013.

[211] T. Shimizu, "Staebler-Wronski Effect in Hydrogenated Amorphous Silicon and Related Alloy Films," *Japanese Journal of Applied Physics*, vol. 43, pp. 3257–3268, June 2004.

[212] J. R. Sites, "Thin-film photovoltaics: What are the reliability issues and where do they occur?," in *Reliability Physics Symposium (IRPS), 2010 IEEE International*, pp. 494–498, 2010.

[213] S.-Y. Lien, C.-H. Hsu, and Y.-C. Ou, "Innovation and fabrication of 5.5 generation image-patterned translucent photovoltaic module by using laser scribing technology," *Progress in Photovoltaics: Research and Applications*, vol. 21, pp. 374–378, Nov. 2013.

[214] A. Compaan, I. Matulionis, and S. Nakade, "Laser scribing of polycrystalline thin films," *Optics and Lasers in Engineering*, vol. 34, pp. 15–45, July 2000.

[215] M. Rekow, R. Murison, T. Panarello, C. Dunsky, C. Dinkel, S. Nikumb, J. Pern, and L. Mansfield, "CIGS P1, P2, P3 Scribing Processes Using a Pulse Programmable Industrial Fiber Laser," in *25th European Photovoltaic Solar Energy Conference and Exhibition (EU PVSEC)*, (Valencia, Spain), pp. 2862 – 2871, 2010.

[216] G. Heise, A. Heiss, C. Hellwig, T. Kuznicki, H. Vogt, J. Palm, and H. P. Huber, "Optimization of picosecond laser structuring for the monolithic serial interconnetion of CIS solar cells," *Progress in Photovoltaics: Research and Applications*, vol. 21, pp. 681–692, Jan. 2013.

[217] J. García-Ballesteros, S. Lauzurica, C. Molpeceres, I. Torres, D. Canteli, and J. Gandía, "Electrical losses induced by laser scribing during monolithic interconnection of devices based on a-Si:H," *Physics Procedia*, vol. 5, pp. 293–300, Jan. 2010.

[218] A. Polman and H. A. Atwater, "Photonic design principles for ultrahigh-efficiency photovoltaics.," *Nature materials*, vol. 11, pp. 174–7, Mar. 2012.

[219] M. Bernardi, N. Ferralis, J. H. Wan, R. Villalon, and J. C. Grossman, "Solar energy generation in three dimensions," *Energy & Environmental Science*, vol. 5, no. 5, p. 6880, 2012.

[220] E. Yablonovitch, "Statistical ray optics," *Journal of the Optical Society of America*, vol. 72, no. 7, pp. 899–907, 1982.

APPENDICES

A. ANALYTICAL SOLUTION FOR P-I-N SOLAR CELL

Here we reproduce the analytical derivations of dark and light IV for a p-i-n solar cell, without bulk recombination as described in [51]; and also include the bulk recombination component as discussed in [86].

A.1 Semiconductor Equations

In order to solve the IV characteristics of solar cells, we must solve the Poisson equation

$$\frac{\partial^2 \phi}{\partial x^2} = -\frac{\rho}{\epsilon}; \tag{A.1}$$

in conjunction to the electron and hole continuity equations given as,

$$\frac{\partial n}{\partial t} = \frac{1}{q}\frac{\partial J_n}{\partial x} + G(x) - R(x), \tag{A.2}$$

$$\frac{\partial p}{\partial t} = -\frac{1}{q}\frac{\partial J_n}{\partial x} + G(x) - R(x). \tag{A.3}$$

Here, ϕ, n, and p are the variables to be solved; and G and R denote generation and recombination processes; and J_n and J_p are electron and hole currents given as,

$$J_n = q\mu_n \mathcal{E} n + qD_n \frac{\partial n}{\partial x}, \tag{A.4}$$

$$J_p = q\mu_p \mathcal{E} p - qD_p \frac{\partial p}{\partial x}. \tag{A.5}$$

Here, q is electron charge, μ_n and μ_p are the carrier mobilities, D_n and D_p are the carrier diffusion coefficients, and $\mathcal{E}$ is the electric field.

In case of a-Si:H p-i-n cells, we can simplify these equations for steady state solution in the i-layer. Since the i-layer does not have fixed charges, we can write the electric field as $\mathcal{E} \approx (V - V_{bi})/d$; where V_{bi} is the built-in potential of the p-i-n

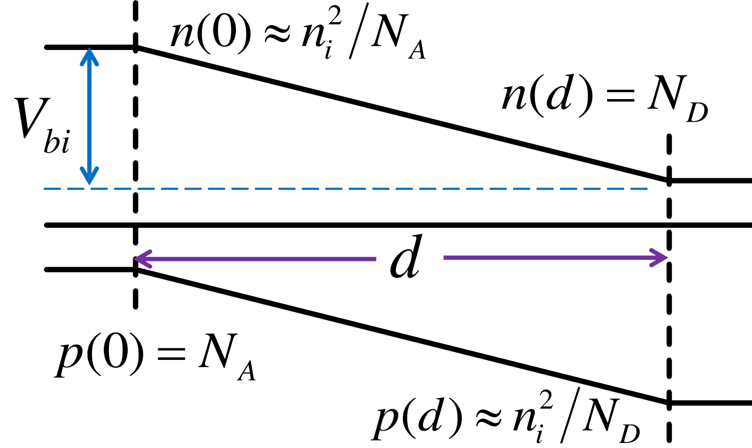

Fig. A.1. a-Si:H p-i-n solar cell band diagram, showing the thicknesses and built-in potential.

cell, and d is the thickness of i-layer, as shown in Fig. A.1. V_{bi} is generally a function of doping in p/n layers, as well as the contact work functions. In presence of ohmic contacts, it is solely determined by the doping densities N_D and N_A, and is given by $V_{bi} = (k_B T/q)\ln(N_A N_D/{n_i}^2)$. We further assume that equilibrium carrier densities are maintained at the ends of i-layer, as shown in Fig. A.1. These approximations allow us to simplify the transport equations in steady state as,

$$D_n \frac{\partial^2 n}{\partial x^2} + \mu_n \mathcal{E} \frac{\partial n}{\partial x} + G(x) - R(x) = 0, \tag{A.6}$$

$$D_p \frac{\partial^2 p}{\partial x^2} - \mu_p \mathcal{E} \frac{\partial p}{\partial x} + G(x) - R(x) = 0. \tag{A.7}$$

A.2 Solution without Recombination

This simplified equations still require two further approximations in order to solved fully namely, constant photogeneration in i-layer, and applicability of first order perturbation of calculating bulk recombination. The first approximation of constant generation in i-layer can be made because, typically, the light in the i-layer is absorbed after multiple bounces due to light trapping [220]. Therefore, generation rate is generally a weak function of distance, and can be approximated by an effective

generation rate, i.e. $G(x) \approx G_{eff}$ [52]. Secondly, we need a first order perturbation approach to account for bulk recombination $R(x)$. We will solve the equations by setting $R(x) = 0$, and then use carrier densities $n(x)$ and $p(x)$, so obtained to calculate the bulk recombination current. After these final approximations, and some normalizations we get

$$\frac{\partial^2 n}{\partial x^2} + \mathcal{E}_0 \frac{\partial n}{\partial x} + G_n = 0, \tag{A.8}$$

$$\frac{\partial^2 p}{\partial x^2} - \mathcal{E}_0 \frac{\partial p}{\partial x} + G_p = 0. \tag{A.9}$$

Here, $\mathcal{E}_0 = q\mathcal{E}/k_B T$ is the normalized electric field; and $G_n = G_{eff}/D_n$ and $G_p = G_{eff}/D_p$ denote normalized generation terms. The solution to these 2nd order homogeneous differential equations are given as,

$$n(x) = A_n e^{-\mathcal{E}_0 x} - \frac{G_n}{\mathcal{E}_0} x + B_n, \tag{A.10}$$

$$p(x) = A_p e^{\mathcal{E}_0 x} + \frac{G_p}{\mathcal{E}_0} x + B_p. \tag{A.11}$$

And, using equilibrium boundary conditions in A.1, we solve for values of B_n and B_p as

$$B_n = \frac{{n_i}^2}{N_A} \frac{(e^{qV/k_B T} - 1)}{(e^{\mathcal{E}_0 d} - 1)} + \frac{G_n d}{\mathcal{E}_0} \frac{e^{\mathcal{E}_0 d}}{(e^{\mathcal{E}_0 d} - 1)} \tag{A.12}$$

$$B_p = \frac{{n_i}^2}{N_D} \frac{(e^{qV/k_B T} - 1)}{(e^{\mathcal{E}_0 d} - 1)} + \frac{G_p d}{\mathcal{E}_0} \frac{1}{(e^{\mathcal{E}_0 d} - 1)} \tag{A.13}$$

Now, using Eq. A.4 and A.5, we can calculate the current density $J = J_n + J_p$ as, $J = q\mathcal{E}[\mu_n B_n + \mu_p B_p] - 2qG_{eff}/\mathcal{E}_0$. And, after substituting B_n and B_p from above, and simplifying we can find the current density J. We find that J separates into two terms, an exponential diode current J_{D1} (independent of G_{eff}), and a generation dependent photocurrent J_{photo} so that [51],

$$J_{D1} = q \left(\mu_p \frac{n_i^2}{N_D} + \mu_n \frac{n_i^2}{N_A} \right) \left(\frac{(V - V_{bi})/d}{e^{(q(V - V_{bi})/k_B T)} - 1} \right) \left[\exp\left(\frac{qV}{k_B T} \right) - 1 \right], \tag{A.14}$$

$$J_{photo} = qG_{eff} d \left[\coth\left(\frac{q(V - V_{bi})}{2k_B T} \right) - \frac{2k_B T}{q(V - V_{bi})} \right]. \tag{A.15}$$

A.3 Bulk Recombination

Having looked at the behavior of dark and light current without recombination, we use the $n(x)$ and $p(x)$ from previous solution to obtain bulk recombination current. The expression for electron and hole density given in Eqs. A.10 and A.11 can be approximated as,

$$p(x) \approx N_A e^{\mathcal{E}_0 x} + \frac{G_{eff}(x-d)}{D_p \mathcal{E}_0}, \tag{A.16}$$

$$n(x) \approx N_D e^{\mathcal{E}_0 (x-d)} - \frac{G_{eff} x}{D_n \mathcal{E}_0}, \tag{A.17}$$

for small applied bias $V < V_{bi}$. Now, we can calculate the recombination current by integrating the recombination profile as,

$$J_{rec} = \int_0^d R(x)dx \approx \int_0^d \min\left(\frac{n}{\tau_n}, \frac{p}{\tau_p}\right) \approx \int_0^{x_c} \frac{n(x)}{\tau_n} + \int_{x_c}^d \frac{p(x)}{\tau_p}. \tag{A.18}$$

Here, x_c denotes the point where recombination changes from electron limited to hole limited, so that we can get x_c by solving

$$\frac{n\left(x_c\right)}{\tau_n} \approx \frac{p\left(x_c\right)}{\tau_p}, \tag{A.19}$$

which will usually lead to a transcendental equation. But in simpler cases, when x_c is close to middle of i-layer, we can neglect the exponential terms in Eqs. A.16 and A.17. Then, the above equation can be solved to get x_c as [86]

$$x_c \approx d\frac{\mu_n \tau_n}{\mu_n \tau_n + \mu_p \tau_p}. \tag{A.20}$$

And the recombination current can be obtained in terms of x_c as

$$J_{rec} \approx \underbrace{\frac{qN_D}{\tau_n \mathcal{E}_0}\left(e^{\mathcal{E}_0 d} - e^{\mathcal{E}_0 (d-x_c)}\right) + \frac{qN_A}{\tau_p \mathcal{E}_0}\left(e^{\mathcal{E}_0 d} - e^{\mathcal{E}_0 x_c}\right)}_{J_{D2}} - \underbrace{\frac{G_{eff}}{2\mathcal{E}}\left[\frac{{x_c}^2}{\mu_n \tau_n} + \frac{(d-x_c)^2}{\mu_p \tau_p}\right]}_{J_{rec,G}}. \tag{A.21}$$

Note that the recombination current separates into a dark component J_{D2}, and more importantly, a *generation dependent* component $J_{rec,G}$. These can be further

simplified by assuming $\mu_n\tau_n \approx \mu_p\tau_p \approx \mu_{eff}\tau_{eff}$, which gives $x_c \approx d/2$, and for $V < V_{bi}$ we can obtain

$$J_{rec,G} \approx \frac{qG_{eff}d^3}{4\mu_{eff}\tau_{eff}(V_{bi}-V)}, \tag{A.22}$$

$$J_{D2} \approx q\frac{n_i}{\tau_{eff}}d\frac{2k_BT/q}{V_{bi}-V}\exp\left(\frac{qV}{2k_BT}\right). \tag{A.23}$$

Here, J_{D2} reduces to the familiar recombination current in a diode with ideality factor 2. Thus, we can account for all the current components in a TFPV cell, by calculating the following four components namely,

- ideal dark current J_{D1} with ideality factor 1,
- voltage dependent collection J_{photo},
- dark recombination current J_{D2} with ideality factor $\sim$2, and
- generation dependent recombination $J_{rec,G}$.

B. SPACE-CHARGE-LIMITED CURRENT IN SOLIDS

Here we derive the expression for space-charge-limited (SCL) current in solids. We will consider an ideal defect free semiconductor [104], as well as one with exponential distribution of shallow trap states [107].

B.1 Ideal Semiconductor - Mott-Gurney Law

In this section, we derive the SCL current in a defect free ideal semiconductor after [104]. The analytical solution can be obtained using the following assumptions

1. The semiconductor layer has no fixed or trapped charges (intrinsic and defect free).
2. Both contacts can inject/extract only one carrier (holes in this case).
3. The electric field at the injecting contact is always zero ($\mathcal{E}(0) = 0$).
4. The applied bias is large, so that diffusion current can be neglected.

With these assumptions, the steady state semiconductor equations in Sec. A.1 are simplified to

$$J_{SCL} = q\mu_p p\mathcal{E}, \tag{B.1}$$

and

$$\frac{d\mathcal{E}}{dx} = \frac{qp}{\epsilon}. \tag{B.2}$$

Here, J_{SCL} is the steady state SCL current, μ_p is hole mobility, $\mathcal{E}$ is the electric field, $p(x)$ is the hole concentration, ϵ is the semiconductor permittivity, and q is electron charge. Using Eq. B.1, we can write $p = J_{SCL}/q\mu_p\mathcal{E}$, and substitute it in Eq. B.2 to obtain

$$\frac{d\mathcal{E}}{dx} = \frac{J_{SCL}}{\epsilon\mu_p}\frac{1}{\mathcal{E}}. \tag{B.3}$$

This can be rearranged, and integrated from the injecting contact to an arbitrary point x inside the semiconductor, using the assumption (3) above to get

$$\int_0^{\mathcal{E}} \mathcal{E} d\mathcal{E} = \frac{J_{SCL}}{\epsilon \mu_p} \int_0^x dx, \tag{B.4}$$

which gives the electric field inside the semiconductor as

$$\mathcal{E}(x) = \sqrt{\frac{2J_{SCL}}{\epsilon \mu_p}} \sqrt{x}. \tag{B.5}$$

The band diagram in this situation is shown in Fig. B.1(a), which demonstrates the situation under single carrier (hole) injection. Finally, we write the electric field in terms of the potential inside the semiconductor as $\mathcal{E} = -d\phi/dx$ and integrate across the semiconductor layer thickness L to write

$$-\int_0^V d\phi = \sqrt{\frac{2J_{SCL}}{\epsilon \mu_p}} \int_0^L \sqrt{x} dx, \tag{B.6}$$

which when integrated and rearranged yields the SCL current expression as

$$J_{SCL} = \frac{9\mu_p \epsilon}{8} \frac{V^2}{L^3}, \tag{B.7}$$

which is known as the 'Mott-Gurney Law' [104].

B.2 With Exponential Distribution of Shallow Traps

In this section, we analyze the a semiconductor with exponential distribution of shallow traps near the given by

$$N_t = \frac{N_{t0}}{E_0} \exp\left(\frac{E_V - E}{E_0}\right), \tag{B.8}$$

as shown schematically in Fig. B.1(b), where E_0 denotes the characteristic energy of trap distribution. In presence of traps, we need to account for trapped as well as free charge in the Poisson equation, and an analytical solution can be obtained for the following additional assumptions

1. For the hole traps all states above E_F are assumed to be positively charged.

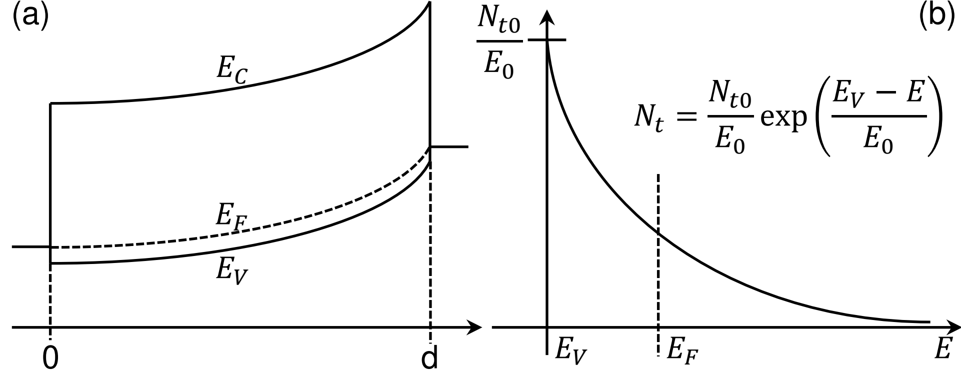

Fig. B.1. (a) Band diagram of an MSM structure with single carrier (hole) injection setup, showing the change in potential due to injected charge. (b) Schematic showing the exponential trap distribution (band tails) near the valence band edge.

2. In the region of interest the Poisson equation is dominated by the trapped charge.

This correction to the Mott-Gurney Law was first reported in [105], but we use the approach outlined in [107] to derive the relevant expression. In this scenario the number of charged traps at a given position can be calculated as

$$p_t(x) = \int_{E_V}^{\infty} \frac{N_{t0}}{E_0} \exp\left(\frac{E_V - E}{E_0}\right) dE. \tag{B.9}$$

Note that the upper limit of integration is assumed infinite, because in typical materials $E_0 \ll E_g$, where E_g is the semiconductor band gap. This integration yields

$$p_t(x) = N_{t0} \exp\left(\frac{E_V - E_F}{E_0}\right), \tag{B.10}$$

and the free carrier density is given by the usual Maxwell-Boltzmann statistics, so that the free carrier density

$$p_f(x) = N_V \exp\left(\frac{E_V - E_F}{k_B T}\right). \tag{B.11}$$

These relations allow us to write

$$p_f(x) = \frac{N_V}{N_{t0}^{\gamma}} p_t(x)^{\gamma}, \tag{B.12}$$

where $\gamma = E_0/k_BT$. Now using assumption (2) above we can write the Poisson and continuity equations as

$$\frac{d\mathcal{E}}{dx} \approx \frac{qp_t(x)}{\epsilon}, \tag{B.13}$$

and

$$J_{SCL} = q\mu_p p_f \mathcal{E}. \tag{B.14}$$

Then, using the relation between trapped and free charge we can get

$$\frac{d\mathcal{E}}{dx} \approx \frac{qN_{t0}}{\epsilon N_V^{1/\gamma}} p_f^{1/\gamma} = \underbrace{\frac{qN_{t0}}{\epsilon}\left(\frac{J_{SCL}}{q\mu_p N_V}\right)^{1/\gamma}}_{\Theta} \frac{1}{\mathcal{E}^{1/\gamma}}, \tag{B.15}$$

where the constants are collected as Θ. Rearranging the terms and integrating from 0 to arbitrary point x inside the semiconductor we get

$$\int_0^{\mathcal{E}} \mathcal{E}^{1/\gamma} d\mathcal{E} = \Theta \int_0^x dx, \tag{B.16}$$

which gives the electric field as

$$\mathcal{E} = -\frac{d\phi}{dx} = \left(\frac{\gamma+1}{\gamma}\Theta\right)^{\frac{\gamma}{\gamma+1}} x^{\frac{\gamma}{\gamma+1}}. \tag{B.17}$$

This is then integrated over the semiconductor layer thickness L to obtain the applied voltage as

$$V = \left(\frac{\gamma+1}{\gamma}\Theta\right)^{\frac{\gamma}{\gamma+1}} \frac{\gamma+1}{2\gamma+1} L^{\frac{2\gamma+1}{\gamma+1}}. \tag{B.18}$$

Finally, substituting the value of Θ from above and rearranging, we obtain the full expression of the SCL current in presence of shallow traps as

$$J_{SCL} = q\mu_p N_V \left(\frac{\epsilon\gamma}{qN_{t0}}\right)^{\gamma} \left(\frac{2\gamma+1}{\gamma+1}\right)^{\gamma+1} \frac{V^{\gamma+1}}{L^{2\gamma+1}}. \tag{B.19}$$

C. SHEET RESISTANCE AND ASYMMETRIC SHADOW STRESS

The following simulations show that the sheet resistance of TCO and metal contacts redistributes the voltage and current at the boundary between shaded and unshaded cells, but the asymmetry of partial shading effect is preserved even when sheet resistance is changed from $0.1\Omega/\square$ to $10\Omega/\square$. We will first show this for the sheet resistance values for our simulation of a-Si:H modules ($0.1\Omega/\square$), and also demonstrate for an extreme case where both contacts are TCO ($10\Omega/\square$).

C.1 Typical Scenario - Metal and TCO contacts

In this section, we consider the asymmetric shading in a-Si:H module and analyze the 2D current flow for $R_{\square}^{TCO} = 10\Omega/\square$, and $R_{\square}^{metal} = 0.1\Omega/\square$. Fig. C.1(a) shows the zoomed in color plot of the simulation results shown in Fig. 5.5(b). It shows the distribution of sub-cell voltages for 20 series connected cells, of which the left half of bottom 5 cells ($0 - 60cm$) are partially shaded. Fig. C.1(b) shows the sub-cell voltage across the width, for 4 cells, showing that the fully illuminated cells (cell 20, far from the shaded region, and cell 6, just next to the shaded region) in forward bias, while the partially illuminated (cell 1 and cell 5) cells in reverse bias.

Fig. C.1(b) shows that for partially illuminated cells away from the junction between shaded and unshaded cells (cell no. 1), the $V_{sub} = -8.47V$ across the whole width. For partially illuminated cell no. 5, however, V_{sub} changes from $-8.82V$ to $-8.01V$ along the width, but this difference is small compared to the overall reverse bias ($\sim -8V$). This slight asymmetry is a consequence of the redistribution of current from asymmetric flow in the partially illuminated cell no. 5, to a more symmetric flow in fully illuminated cell no. 6. This redistribution also affects the bias of the

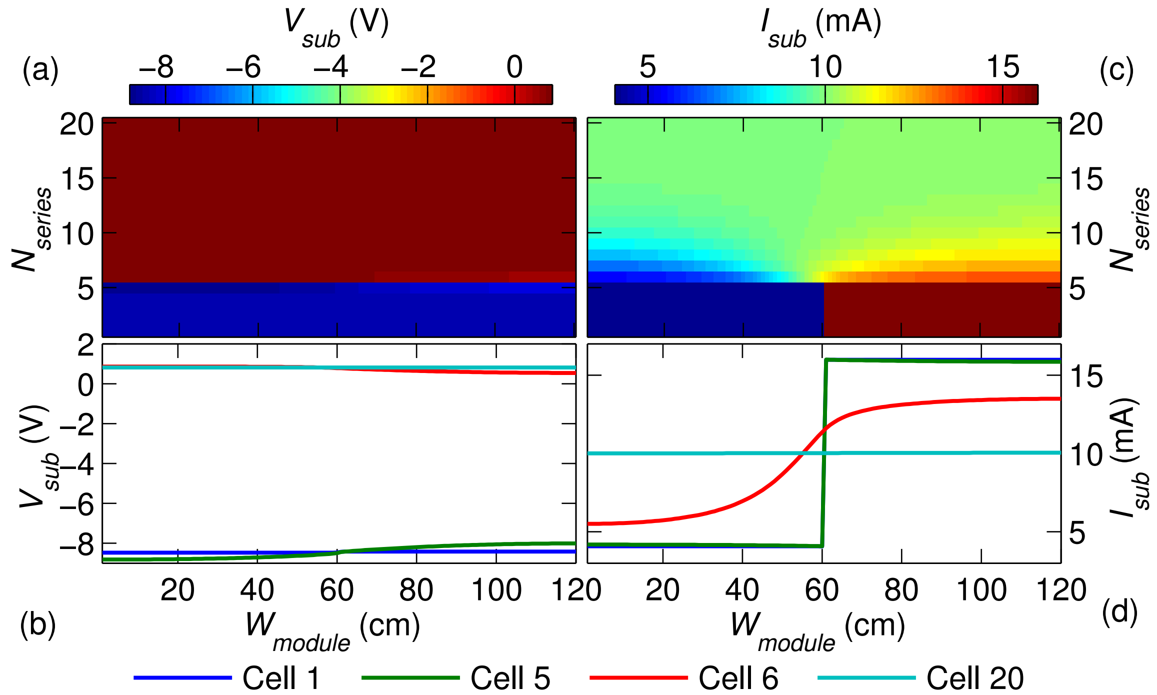

Fig. C.1. (a) Color plot of sub-cell voltages for 20 cells ($y - axis$), where left half of 5 cells at the bottom is shaded (color bar in V). (b) The sub-cell voltages across the cell width for 2 shaded cells (no. 1 and 5), and 2 unshaded cells (no. 6 and 20). (c) Color plot of sub-cell current for 20 cells ($y - axis$), where left half of 5 cells at the bottom is shaded (color bar in mA). (d) The sub-cell current across the cell width for 2 shaded cells (no. 1 and 5), and 2 unshaded cells (no. 6 and 20).

next cell, as evident by the change in V_{sub} values in cell no. 6 from $0.86V$ to $0.54V$ along the width. This asymmetry also goes away as we move away from the junction region as seen by the uniform V_{sub} value of $0.84V$ across cell no. 20.

This change in V_{sub} across the width happens because the asymmetric current in the partially illuminated cell cannot spread across the width of the next illuminated cell due to the sheet resistance of the metal contact. As seen in Fig. C.1(c), the sub-cell current I_{sub} in the 5 partially shaded cells show asymmetric current, which gradually becomes symmetric over next few fully illuminated cells. The asymmetric

I_{sub} distribution can be seen for cell no. 1 and 5 in Fig. C.1(d), which shows that the left half is supplying $\sim 4mA$ per sub-cell, and the right illuminated half is supplying $\sim 16mA$ per sub-cell, so that the total current through each cell (sum of I_{sub} along the width) is $0.004 \times 60 + 0.016 \times 60 = 1.2A$. This asymmetry is almost same all 5 partially illuminated cells. As a result of this asymmetry, however, the current does not become uniform immediately in the next few illuminated cells. Therefore, the current through the first fully illuminated cell (cell no. 6) is fairly non-uniform, changing from $5.51mA$ to $13.49mA$ along the width. This asymmetry is sequentially reduced over the next few cells (while keeping the total current $\sim 1.2A$ per cell), and the current becomes uniform ($I_{sub} = 10mA$ per sub-cell for cell no. 20) for cells away from the shaded region (see Fig. C.1(d)).

C.2 Translucent Module - TCO on Both Sides

These general observations about the asymmetric current flow, and reverse stress on the shaded hold true even for the extreme case where both contacts in the module are considered to be TCO with high sheet resistance so that $R_{\square}^{TCO1} = R_{\square}^{TCO1} = 10\Omega/\square$. Fig. C.2(a) shows that even though V_{sub} varies significantly across the width near the junction of shaded and unshaded regions (see cell 5 and cell 6); all regions of partially illuminated cells are in reverse bias (cell 1 and cell 5). Moreover, as seen from Fig. C.2(b), the qualitative features of V_{sub} variation are similar to those in the previous lower-resistance case shown in Fig. C.1. As expected however, the variation in the cells near the junction is higher, and V_{sub} shows larger variation along the width, changing from $-9.4V$ to $-4.9V$ for cell no. 5. This asymmetry disappears for cells away from this junction; e.g., as shown in Fig. C.2(b), V_{sub} values become quite uniform for cell 1 (shaded) and cell 20 (illuminated). Since the current redistribution in this case is more difficult due to higher $R_{\square}$ values, the voltage asymmetry in the first fully illuminated cell (cell 6) is also higher where V_{sub} changes from $0.86V$ to $-1.2V$ across the width. The larger asymmetry in V_{sub} for cell 6 is because the redistribution

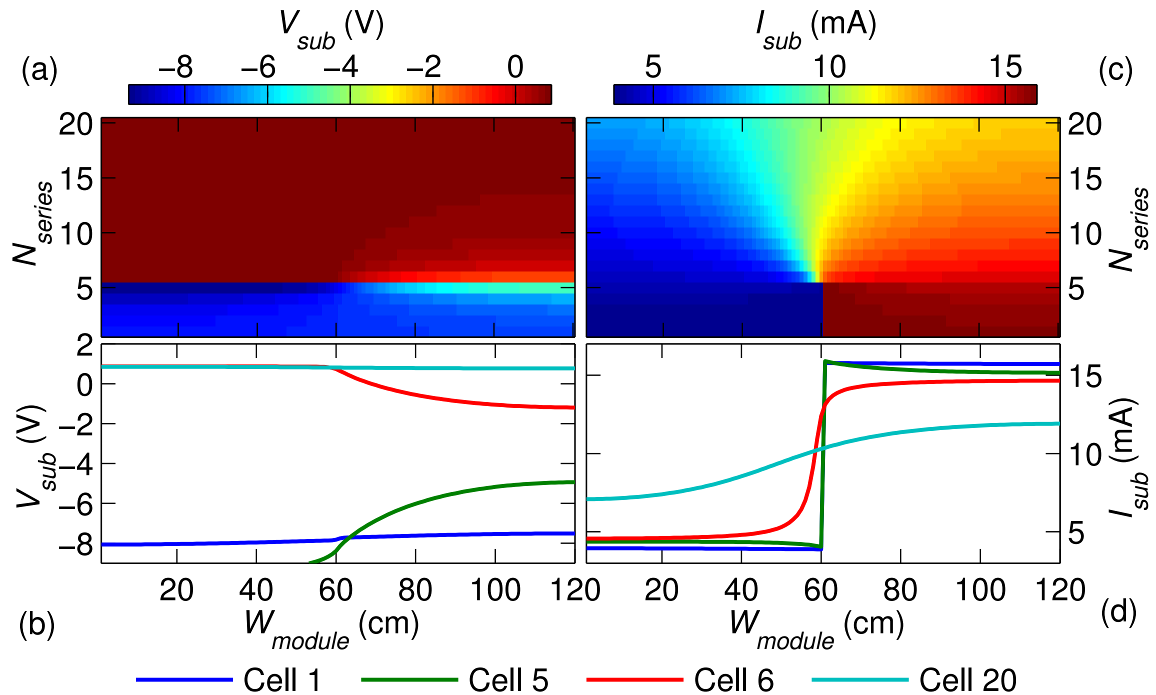

Fig. C.2. (a) Color plot of sub-cell voltages for 20 cells ($y - axis$), where left half of 5 cells at the bottom is shaded (color bar in V). (b) The sub-cell voltages across the cell width for 2 shaded cells (no. 1 and 5), and 2 unshaded cells (no. 6 and 20). (c) Color plot of sub-cell currents for 20 cells ($y - axis$), where left half of 5 cells at the bottom is shaded (color bar in mA). (d) The sub-cell currents across the cell width for 2 shaded cells (no. 1 and 5), and 2 unshaded cells (no. 6 and 20).

of current flow is more restricted in this higher $R_{\Box}$ case, and the rightmost sub-cells in fully illuminated cell 6 go into slight reverse bias to ensure current continuity.

The asymmetry is more clearly illustrated in the distribution of I_{sub} shown in Fig. C.2(c). Here also we see that asymmetric current flow in the 5 partially shaded cells, and this asymmetry forces the I_{sub} in the fully illuminated cells to become asymmetric as well. As seen in Fig. C.2(d), the ratio of I_{sub} between shaded and unshaded halves of cell no. 1 and 5 is almost same as the low $R_{\Box}$ case (i.e. $I_{sub} = 4mA$ for the shaded half and $I_{sub} =\sim 16mA$ for the unshaded half). Because of the high

$R_\square$ values however, the asymmetry induced in I_{sub} values in fully illuminated cells is much higher. As shown in Fig. C.2(d), the I_{sub} values in cell no. 6 changes from $4.6mA$ to $14.6mA$, almost same as cell no. 5. This is because the high $R_\square$ hinders the redistribution of current flow. As we move away from the shaded region however, I_{sub} becomes more uniform (e.g. I_{sub} for cell no. 20 changes from $7.1mA$ to $11.9mA$ along the width), but one needs to move ever farther away from the shaded region (cell no. 50 in this particular cell) before I_{sub} can become fully uniform.

C.3 Current Rearrangement in 2D

As the current flow distribution gradually changes from asymmetric in partially illuminated cells (cells 1 to 5) to symmetric in fully illuminated cells; the metal contacts of the cells facilitate the redistribution of the current. This results in lateral currents in the metal contacts, which ensure the current continuity. These lateral currents are limited by the sheet resistance of the metal contact. As shown in Fig. C.3(a) for $R_\square^{metal} = 0.1\Omega/\square$ case, there is a significant lateral current flow in the metal contact of cell 6 (first fully illuminated cell connected to the partially shaded cell 5). This current is flowing from right to left (negative sign), in order to increase the sub-cell current in the left half, while reducing the sub-cell current in the right half, so that the current continuity of I_{sub} can be maintained between cell 5 and 6 (see Fig. C.1(b)). Since the metal is conductive in this case, it allows for large horizontal current flow resulting in quicker realignment of current flow distribution. This horizontal current is maximum in the middle, which is consistent with the fact that the sub-cell current between cells 5 and 6 changes the most for sub-cells near the middle (see Fig. C.1(b)), while the sub-cell current at the edges homogenizes more gradually.

In case of TCO contacts on both sides, where $R_\square^{TCO} = 10\Omega/\square$, the horizontal current flow is much smaller (as shown in Fig. C.3(b)). This results in a more gradual realignment of current distribution through the fully illuminated cells, as seen in Fig. C.2(b). The overall current rearrangement pattern, however, remains

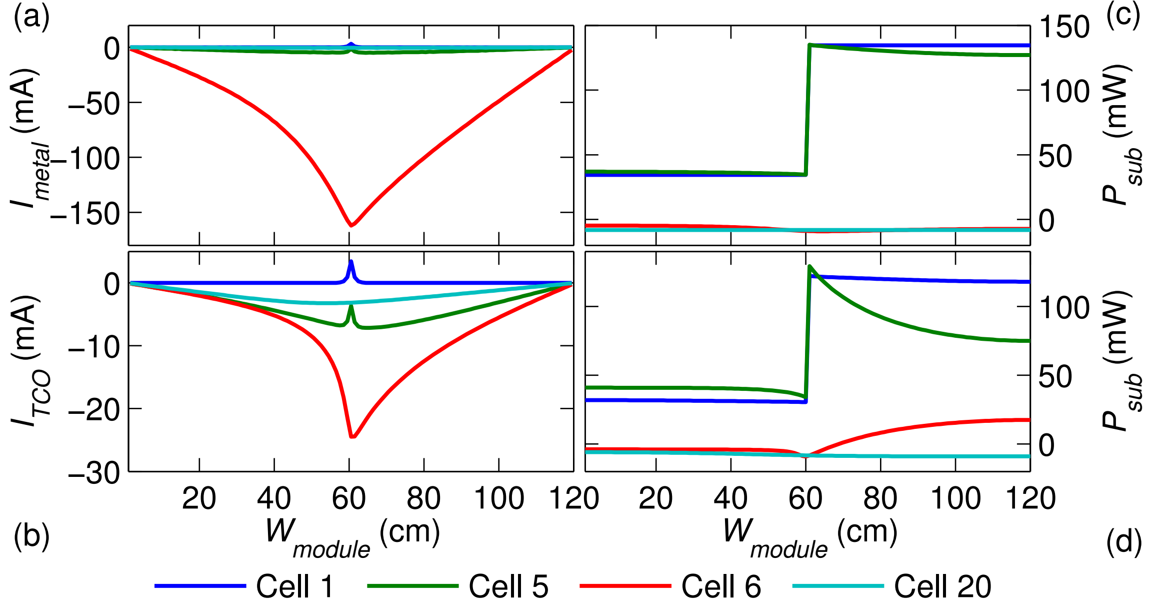

Fig. C.3. Horizontal current flow through the bottom (metal/TCO) contact of different cells for (a) $R_{\square}^{metal} = 0.1\Omega/\square$ case and (b) $R_{\square}^{TCO2} = 10\Omega/\square$ case, showing the horizontal current flow responsible for redistribution of sub-cell current between sub-cells of partially (cells 1 and 5) and fully (cells 6 and 20) illuminated cells. Sub-cell power output (or dissipation) for the 2 shaded cells (no. 1 and 5), and 2 unshaded cells (no. 6 and 20), for the typical case with $R_{\square}^{metal} = 0.1\Omega/\square$ (c) vs. high $R_{\square}^{TCO} = 10\Omega/\square$ on both contacts (d).

qualitatively identical to the metal contact case. The horizontal current is maximum at the junction of shaded and unshaded cells (i.e. cell 6), with the maximum value at the middle where the current rearrangement is most likely.

C.4 Asymmetric Shadow Stress

From the above simulations, we can see that even for very different sheet resistance values, the voltage across partially shaded cells remains roughly similar (see Figs. C.1(a)(b), C.2(a) (b)), while the current flow becomes asymmetric to preserve current continuity (Figs. C.1(c)(d), C.2(c) (d)). As a consequence, while the fully illuminated

cells continue to produce power, the partially shaded cells dissipate power. As shown in Fig. C.3(c), for the typical $R_\square$ values the sub-cells in the fully illuminated cells (cell no. 6 and 20) continue to produce power (negative P_{sub} in this convention) almost uniformly across the width. Moreover, not only all the sub-cells in partially illuminated cells (cell no. 1 and 5) are dissipating power (positive P_{sub}), but the dissipation is clearly asymmetric, where the unshaded (right) half dissipates 3 times more power than the shaded (left) half. These conclusions also hold for the P_{sub} distribution in high $R_\square$ case, as shown in Fig. C.3(d). There is however, greater penalty to be paid for the current rearrangement at the junction between shaded and unshaded cells, as discussed earlier, leading to some fully illuminated sub-cells in cell no. 6 dissipating power as well, while the dissipation in corresponding sub-cells in cell no. 5 is somewhat reduced. But, for cell no. 1 and 20, we can see the patterns in P_{sub} are almost identical to low $R_\square$ case in Fig. C.3(d).

We therefore conclude that the general conclusion about the 2D shadow stress is not affected by exact sheet resistance values. This is also the reason why it could be validated through infrared imaging of a different TFPV technology with different cell characteristics and sheet resistance values. Moreover, while the 1D approximation of the equivalent circuit used for shadow size and orientation analysis in Sec. 5.3.1, cannot account for the current/voltage redistribution across the cell width; it can accurately capture the worst case shadow stresses.

D. NON-RECTANGULAR MODULE GEOMETRIES

D.1 Construction of Module Geometries

D.1.1 Radial Geometry

In order to convert rectangular module geometry (schematic in Fig. D.1(a)) into a radial one, each rectangular cell must be modified into 2 triangles such that their total area is preserved. This means a rectangular cell with dimensions $l_{cell} \times w_{cell}$ is transformed into two triangles, each with base $2l_{cell}$ and height $w_{cell}/2$ (see Fig. D.1(b)). Note that for the rectangular geometry $l_{cell} = L_{module}/N_{series}$, and $w_{cell} = W_{module}$. Therefore, the above choice of triangular cell dimensions, also ensures that the module with triangular cells has the exact same dimensions as the one with rectangular

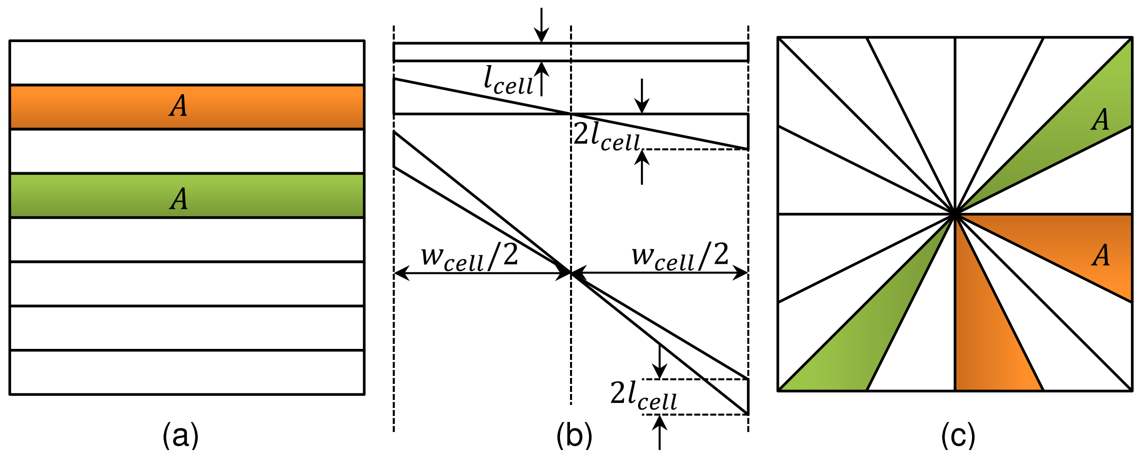

Fig. D.1. (a) Schematic of rectangular module with cell area A. (b) Transformation of each rectangular cell into two triangles, with different angles, keeping the base and height the same. The resulting triangles arranged in radial pattern to create the module with same dimensions, and same cell area.

cells, with same number of series connected cells; thereby ensuring that the output current and voltage of this redesigned module are exactly same as the rectangular case, as shown in Figure D.1(c).

D.1.2 Spiral Geometry

From the discussion in Sec. 5.4.2 we can see that a twisted cell geometry, where none of the cell edges are linearly aligned, will be ideally suited for shade tolerance. Any such design, however, must preserve the series connection, and the rectangular module geometry. We can construct one such geometry by creating a twisted version of the radial geometry. Fig. D.2 shows a step by step schematic representation of a single iteration of this construction method. This process when repeated recursively for multiple times results in the required spiral geometry.

Fig. D.2(a) shows the radial geometry with triangular half-cells of equal area, inside a square module of side w. The dotted square of side $w/2$ contains same radial pattern with half-cell area $A/4$. We then draw the dashed lines, as shown in Fig. D.2(b), which divides the triangles into two parts with equal areas $A/2$. Note

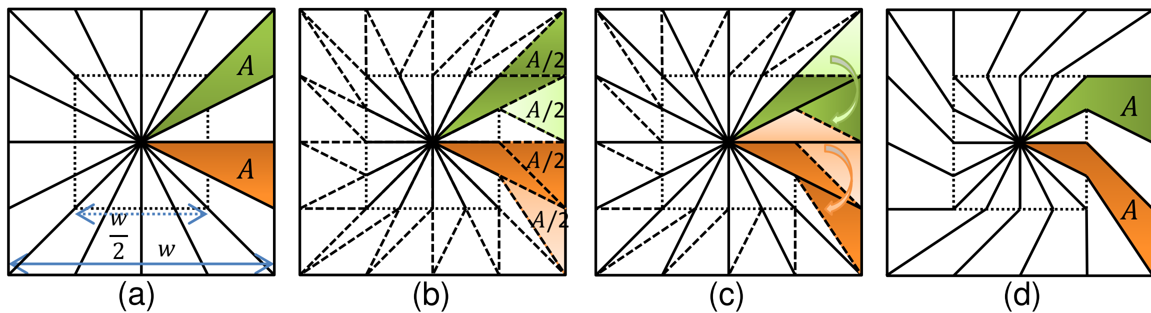

Fig. D.2. (a) Schematic of a square module with radial design showing two half-cells with equal areas. (b) The dashed lines are drawn as shown to bisect the triangle areas. (c) The successive triangles are exchanged so that triangles have one axis of bending. (d) This process repeated for all cells results in the spiral design with equal area half-cells, with once axis of twist.

that all these triangles at the outer edges are of equal areas. Therefore, in the next step, shown in Fig. D.2(c), we exchange these triangles in a clockwise fashion, without distorting the overall square module shape. Finally, we can merge these rotated shapes to create concave pentagons with same areas as the initial triangles (Fig. D.2(d)). This results in the required twisted module geometry, with one level of bending at $w/2$. In order to create a more curved polygonal we just repeat to larger number of iterations, so that the geometry is twisted at more points distance w/N apart.

D.2 Shading Simulation for Different Geometries

In order to simulate the behavior of a partially shaded module, we use a 1D equivalent circuit. We have shown in Sec. 5.3.1 that even for a shadow covering only a part of the cell area, the voltage developed across the shaded cell is quite uniform. Therefore, we can simplify the simulation of partially shaded module by creating a 1D equivalent circuit of N_{series} series connected cells. The photocurrent of each of these cells is determined by the amount of area shaded A_{sh}, and the photogeneration current in the shaded area ($J_{ph,sh}$). This method is applicable for any arbitrary cell or shadow shape; therefore, for N_{series} cells of a module with arbitrary shape and orientation C_i, and shadow of a give shape and size S we need to find their intersection and shaded areas as

$$A_{sh,i} = \mathcal{A}(C_i \bigcap S), \tag{D.1}$$

where $\mathcal{A}$ denotes the area of a given shape, and the intersection determines the region of cell C_i covered by the shadow S (see schematic in Fig. D.3(a)). Now, we can calculate the current output of each cell by using photogeneration in shaded ($J_{ph,sh}$) and unshaded regions (J_{ph}) as

$$J_{sh,i} = J_{ph,sh}A_{sh,i} + J_{ph}(A_{cell} - A_{sh,i}). \tag{D.2}$$

Here, we have assumed $J_{ph,sh} = 0.2J_{ph}$ for a typical case, but a more appropriate value based on the local weather and dust conditions can be used for a more accurate analysis. This can then be used to create the 1D circuit for the module with

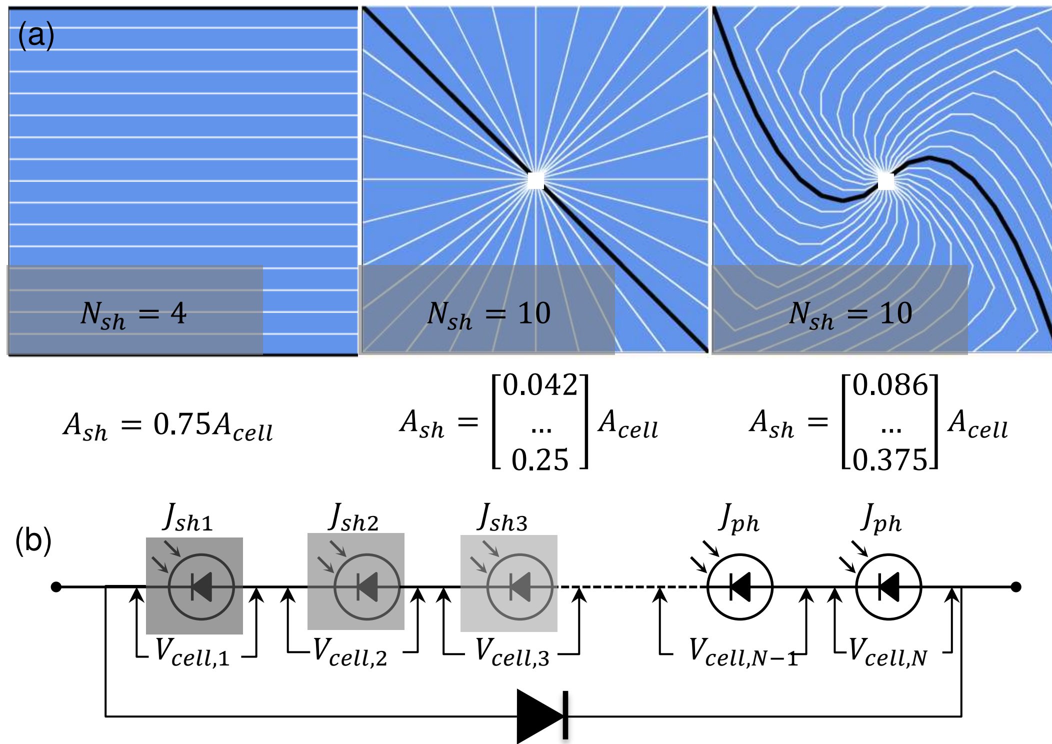

Fig. D.3. (a) Schematics showing the same size shadow on different module designs, showing the number of shaded cells (N_{sh}), and shaded areas $A_{sh,i}$ (identical for rectangular designs, but different for others). (b) Schematic of 1D equivalent circuit of the partially shaded module (with external bypass), using the calculated J_{sh} values from the respective A_{sh} values for each cell. The individual cell voltages are shown, and minimum V_{cell} is calculated at each shading condition for all the designs.

N_{series} solar cells with different photocurrent output (see Fig. D.3b)), each of which is represented by an appropriate equivalent circuit depending on the technology under consideration. We assume all cells have identical IV characteristics, with the photocurrent as the only varying parameter, depending on the amount of shading. We can simulate this partially shaded module, with external bypass diodes, in the string topology (Figure 5.3(a)) using SPICE, and obtain the operating voltage of each cell in the partially shaded module, for any given shadow dimensions. The minimum of these cell voltages (V_{cell}^{min}) is calculated for all possible shading configurations. This

value is compared for different designs, as a measure of its shade tolerance. From this simulation, we also obtain the DC power output of the string, for different shading conditions, and can identify when external bypass will turn on to clamp the loss in power output. Note that in the circuit simulation, the series resistances in the module equivalent circuit are not geometry dependent. While this is not strictly the case for non-rectangular cells, it has negligible impact on shadow effects. This is because, the current flow in the sheet conductors in the radial and spiral designs is two dimensional. Therefore, a single net resistance for whole cell cannot be used, and we must use a full continuity equation solution to determine the resistive dissipation in these cell geometries, as discussed in Sec. 5.4.5.

VITA

VITA

Sourabh Dongaonkar completed his B.Tech. in Electrical Engineering from the Indian Institute of Technology Kanpur, India in 2007. In 2007-08 he worked at the Global Markets Centre, Deutsche Bank, Mumbai, India as a quantitative analyst. Since 2008, he is a graduate student in the School of Electrical and Computer Engineering at Purdue University. His research interests are in analysis and design for variability and reliability in solar cells, and novel devices. He was the recipient of 2008 Ross Fellowship from Purdue University Graduate School. He has also received Best Student Presentation, and Best Poster Awards, at the 37th and 38th IEEE PVSC, respectively.